Title
A Heavy Flavor Tracker for STAR

Permalink
https://escholarship.org/uc/item/0cn2q79k

Author
Chasman, C.

Publication Date
2008-08-05

A Heavy Flavor Tracker for STAR

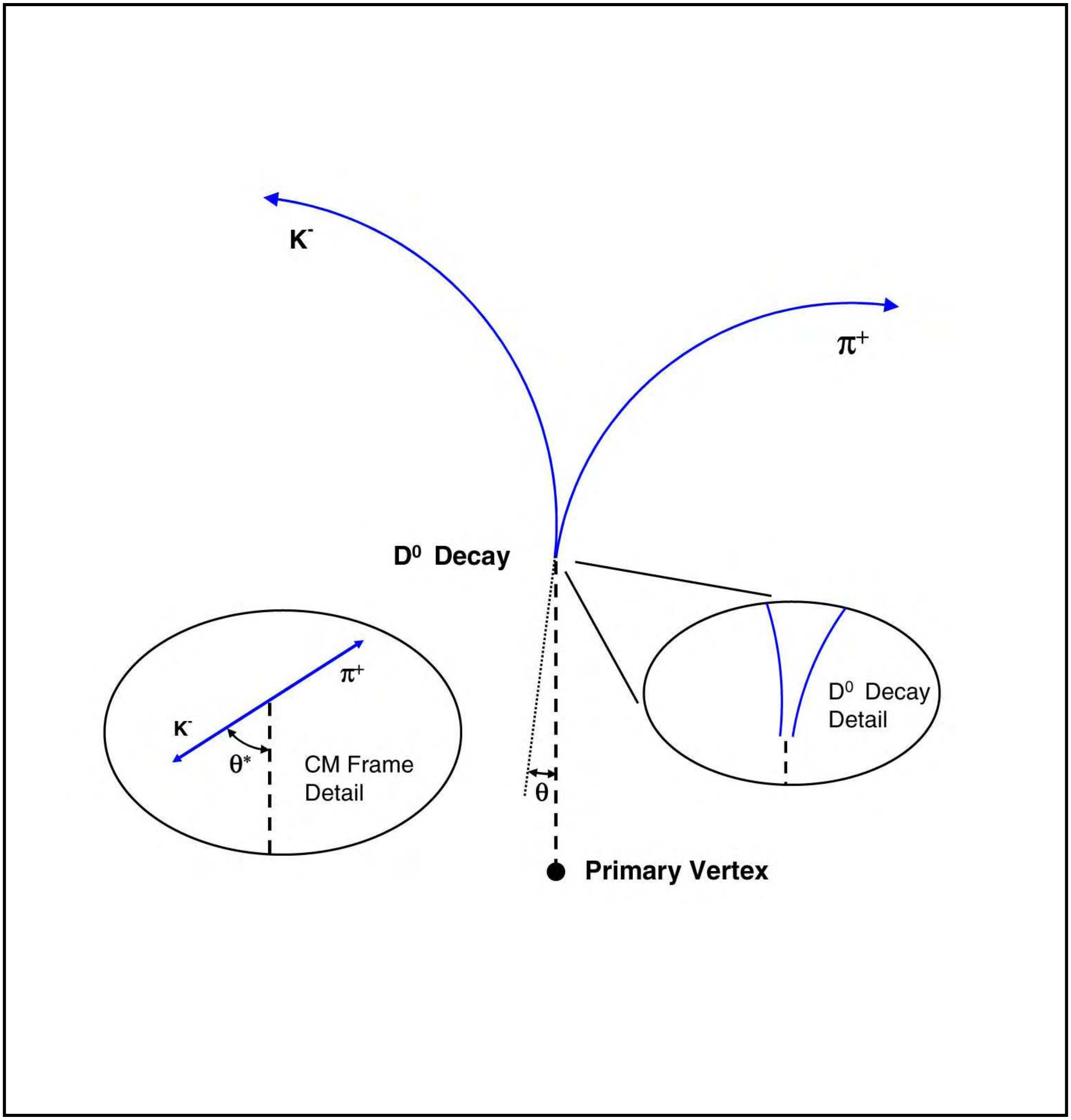

hft_final_submission_version

This page intentionally left blank

A Heavy Flavor Tracker for STAR

C. Chasman, D. Beavis, R. Debbe, J.H. Lee, M.J. Levine, F. Videbaek, Z. Xu
Brookhaven National Laboratory, Upton, NY 11973

S. Kleinfelder, S. Li
University of California, Irvine, CA 92697

R. Cendejas, H. Huang, S. Sakai, C. Whitten
University of California, Los Angeles, CA 90095

J. Joseph, D. Keane, S. Margetis, V. Rykov, W.M. Zhang
Kent State University, Kent, OH 43210

M. Bystersky, J. Kapitan, V. Kushpil, M. Sumbera
Nuclear Physics Institute AS CR, 250 68 Rez/Prague, Czech Republic

J. Baudot, C. Hu-Guo, A. Shabetai, M. Szelezniak, M. Winter
Institut Pluridisciplinaire Hubert Curien, Strasbourg, France

J. Kelsey, R. Milner, M. Plesko, R. Redwine, F. Simon, B. Surrow,
G. Van Nieuwenhuizen
Laboratory for Nuclear Science
Massachusetts Institute of Technology, Cambridge, MA 02139

E. Anderssen, X. Dong, L. Greiner, H.S. Matis, S. Morgan, H.G. Ritter, A. Rose,
E. Sichtermann, R.P. Singh, T. Stezelberger, X. Sun, J.H. Thomas, V. Tram, C. Vu,
H.H. Wieman, N. Xu
Lawrence Berkeley National Laboratory, Berkeley, CA 94720

A. Hirsch, B. Srivastava, F. Wang, W. Xie
Purdue University, West Lafayette, IN 47907

H. Bichsel
University of Washington, Seattle, WA 98195

This page intentionally left blank

Contents

List of Figures

List of Tables

1 Executive Summary

The STAR Collaboration proposes to construct a state-of-the-art microvertex detector, the Heavy Flavor Tracker (HFT), utilizing active pixel sensors and silicon strip technology. The HFT will significantly extend the physics reach of the STAR experiment for precision measurement of the yields and spectra of particles containing heavy quarks. This will be accomplished through topological identification of D mesons by reconstruction of their displaced decay vertices with a precision of approximately 50 μm in p+p, d+A, and A+A collisions.

The HFT consists of 4 layers of silicon detectors grouped into two sub-systems with different technologies, guaranteeing increasing resolution when tracking from the TPC and the Silicon Strip Detector (SSD) towards the vertex of the collision. The Intermediate Silicon Tracker (IST), consisting of two layers of single-sided strips, is located inside the SSD. Two layers of Silicon Pixel Detector (PIXEL) are inside the IST. The PIXEL detectors have the resolution necessary for a precision measurement of the displaced vertex.

The PIXEL detector will use CMOS Active Pixel Sensors (APS), an innovative technology never used before in a collider experiment. The APS sensors are only 50 μm thick and at a distance of only 2.5 cm from the interaction point. This opens up a new realm of possibilities for physics measurements. In particular, a thin detector (0.28% radiation length per layer) in STAR makes it possible to do the direct topological reconstruction of open charm hadrons down to very low p_T by the identification of the charged daughters of the hadronic decay.

1.1 Scientific Motivation

The primary motivation for the HFT is to extend STAR's capability to measure heavy flavor production by the measurement of displaced vertices and to do the direct topological identification of open charm hadrons. These are key measurements for the heavy-ion and spin physics programs at RHIC. Heavy quark measurements will facilitate the heavy-ion program as it moves from the discovery phase to the systematic characterization of the dense medium created in heavy-ion collisions as well as obtain a detailed measurement of the nucleon spin structure in polarized p+p collisions. The primary physics topics to be addressed by the HFT include heavy flavor energy loss, flow, and a test of partonic thermalization at RHIC. This program has been identified as key goals for the RHIC program in the Long Range Plan RHIC-II science program and in the RHIC mid-term scientific plan.

From a precise measurement of the spectra and the production ratios of D-meson states, we will be able to extrapolate to the total yield for charm quark production. Furthermore, the open charm production rate is high enough at RHIC that the coalescence process becomes relevant for Charmonium production. Knowledge of the total production cross section for charm quarks is essential as a baseline for J/ψ measurements. A meaningful answer to the question of whether the J/ψ mesons are suppressed or enhanced at RHIC requires knowledge of the charm production in heavy-ion reactions.

A heavy quark can be used to probe the properties of the medium created in heavy-ion collisions. The radiation of gluons is kinematically suppressed for heavy flavored quarks passing through the medium: thus they should lose less energy in the dense medium. An important measurement to be made with the HFT is R_{AA}, the ratio of charmed meson production in Au+Au collisions to the binary-scaled production rate in p+p or d+Au collisions (Section 2.5.1). Current measurements using non-photonic electrons as a measure of the abundance of charm and bottom hadrons indicate that the rate of energy loss for heavy quarks is unexpectedly high and inconsistent with our current understanding in pQCD models. Based on the non-photonic electron data the theory of heavy quark energy loss is uncertain and may be completely wrong, especially with regards to bottom.

Another important measurement to be made with the HFT is a measurement of the elliptic flow of D-mesons down to very low p_T values (Section 2.4.1). It is generally accepted that elliptic flow is established in the partonic phase. If charm quarks, with a mass much larger than the temperature of the system, undergo elliptic flow then it has to arise from many collisions with the abundant light quarks. Thus, flow of charm quarks can be taken as a probe for frequent re-scatterings of light quarks and is an indication of thermalization that may be reached in the early stages of heavy-ion collisions at RHIC. We believe that proof of thermalization constitutes the last step in the characterization of the strongly interacting matter created at RHIC. These important measurements require a very thin detector to push the measurement down to the lowest momenta where transverse elliptic flow is manifest.

Without the HFT upgrade the STAR experiment will not be able to execute the comprehensive heavy flavor program proposed here. However, STAR has been able to complete some initial charm measurements with the TPC alone, and with the data from the recent Run 7 STAR might be able to make an initial estimate for the B-meson contribution to the spectrum of the non-photonic electrons in Au+Au collisions.

1.2 Detector Concept

Both, the IST and the existing SSD use conventional strip technology. The PIXEL detector brings extremely high precision tracking capabilities to STAR with a resolution of 10 μm at the first layer of the detector, over a large pseudo-rapidity range, and with complete azimuthal angular coverage. This will enable STAR to perform high precision measurements of heavy-quark production over the broadest range of phase space, colliding system sizes and energies. It will exploit all of STAR's unique features including particle identification and tracking from the lowest to the highest p_T. In these respects, the HFT provides physics measurements that are unique at RHIC.

The PIXEL will surround the interaction vertex. It has two tracking layers composed of monolithic CMOS pixel detectors using 30 μm × 30 μm square pixels. These critical innermost tracking layers lie at radii of 2.5 cm and 7.0 cm, respectively, and these layers are active over 20 cm in z and have about 110 million pixels. The silicon chips for the detector will be thinned to 50 μm and will be mounted on low mass carbon fiber structures to minimize pointing errors generated by multiple Coulomb scattering.

Such a thin detector requires a correspondingly thin beam pipe. Therefore, we propose to build a new, 0.5 mm thick beryllium beam pipe for the STAR detector. The construction of such a thin beam pipe is challenging and it requires a unique design to enable the beam pipe to be handled during installation and bake-out.

2 The Physics of the HFT

2.1 Introduction

An important goal of high-energy nuclear physics is to understand Quantum Chromodynamics (QCD) at extreme temperatures and energy densities. Under these extraordinary conditions, we believe that the fundamental symmetries of QCD will reveal themselves: quarks and gluons will be the relevant degrees of freedom, color will be deconfined and chiral symmetry will be restored. Calculations within the framework of regularized lattice QCD predicts a fast crossover from ordinary nuclear matter into a deconfined and locally thermalized state of quarks and gluons called the Quark-Gluon Plasma[1] (QGP).

High-energy nuclear collisions can be characterized by three distinct phases: the initial phase where hard interactions between the partons of the incoming nuclei dominate, an intermediate phase where re-interactions between the constituents in the matter result in collectivity, and a final stage where hadronization, and chemical and thermal freeze-out occur. The matter produced in high-energy nuclear collisions can be investigated by studying the dynamics of the collective expansion of the bulk of the produced particles and by studying the interaction of the medium with penetrating probes such as leading particles and jets. In particular, the measurement of large elliptic flow,[2] and the observation of strong modifications of high p_T particle production, as measured by the ratio $R_{AA,}$[3] and the disappearance of the away side jet[4] have provided evidence for a high density and strongly interacting state of matter at RHIC.[5] The goal of our research program is to elucidate the nature of this matter and to determine if it is dominated by hadronic or partonic degrees of freedom.

Rare processes provide new ways to probe the medium generated in high-energy nuclear collisions. Bjorken[6] proposed that hard scattered partons (quarks and gluons) drawn from the incoming nuclei will interact with the medium in a density-dependent way. Bjorken's initial energy loss mechanism (elastic scattering) did not provide effects large enough to be observed, but medium-induced radiation (gluonic bremsstrahlung) can generate significant energy loss effects.[7,8] Hard parton scatterings can be experimentally reconstructed in elementary particle collisions ($e^+ + e^-$, $\bar{p} + p$) because the outgoing partons fragment into a collimated spray of energetic hadrons. The cluster of hadrons from the parton fragmentation is known as a jet. Jets can also be identified in high-energy nuclear collisions on a statistical basis; the modification of their properties may signal novel flavor dependent energy loss mechanisms in a dense medium by the parton that initiated the jet. Full jet reconstruction in heavy-ion collisions is exceedingly difficult but leading hadrons (i.e. high p_T hadrons, which typically carry a large fraction of the jet energy) and their correlations with other hadrons may provide the essential signals of partonic interactions in the medium.

Collective flow measurements have played a prominent role in understanding the physics of nuclear collisions because the magnitude and pattern of the collective motion is closely related to the equation of state (EOS) of the produced matter. If local equilibrium is achieved, we will be able to use hydrodynamic models to study the EOS and understand the degrees of freedom relevant for the basic constituents of the matter. Heavy quark (*c, b*) production provides some of the most important observables. Due to their large masses, *c* and *b* quarks are produced dominantly by the interactions of the initial incoming partons whereas lighter quarks are produced throughout the later stages of the evolution of a heavy-ion collision. Thus, the total yields of *c* and *b* quark production provide a direct connection to the initial state.

Due to their heavy mass and presumably small hadronic cross sections, charmed quarks are a sensitive probe for the frequency of interaction and therefore the degree of thermalization with constituents before hadronization. At high p_T, heavy quarks may be less suppressed than light quarks due to the "dead cone" effect and so high p_T probes are an additional way to study partonic energy loss. If charmed quarks participate sufficiently in re-scattering processes, they will develop flow (i.e. transverse radial and elliptic flow), which can be observed in charmed hadron momentum distributions. Finally, charmed quarks might achieve thermal equilibrium with the surrounding medium leading to statistical hadronization. In this case, the relative abundances of charmed hadrons might be significantly modified.

The study of the structure of nuclei and the nucleon is an important frontier in strong interaction physics. Despite considerable experimental and theoretical progress over the past several decades, many open questions remain. Striking examples include the observations by the European Muon Collaboration that partons in nuclei have different momentum distributions than partons in nucleons even when probed at high energy,[9] and that the contribution from quark spins to the proton spin is remarkably small.[10,11] The cross sections for heavy flavor production at RHIC receive large contributions from gluon-gluon fusion. The HFT will allow direct measurement of the total cross sections and their spin and nuclear dependence.

2.2 Initial Heavy Quark Production

Quarks are elementary particles, and, depending on the energy scale, there are two mechanisms that generate their masses with different degrees of importance: current quark masses are generated by the electroweak symmetry breaking mechanism (Higgs mass) and spontaneous chiral symmetry breaking leads to the constituent quark masses in QCD (QCD mass). The QCD interaction strongly affects the light quarks (u, d, s) while the heavy quark masses (c, b, t) are mainly determined by the Higgs mechanism, as shown in Figure 1. In high-energy nuclear collisions at RHIC, heavy quarks are produced through gluon fusion and $q\bar{q}$ annihilation.[12]

Heavy quark production is also sensitive to the parton distribution function. Unlike the light quarks, heavy quark masses are not modified by the surrounding QCD medium[13] (or the excitations of the QCD medium) and the value of their masses is much higher than the initial excitation of the system. It is these differences between light and heavy quarks in a medium that make heavy quarks an ideal probe to study the properties of the hot and dense medium created in high-energy nuclear collisions.

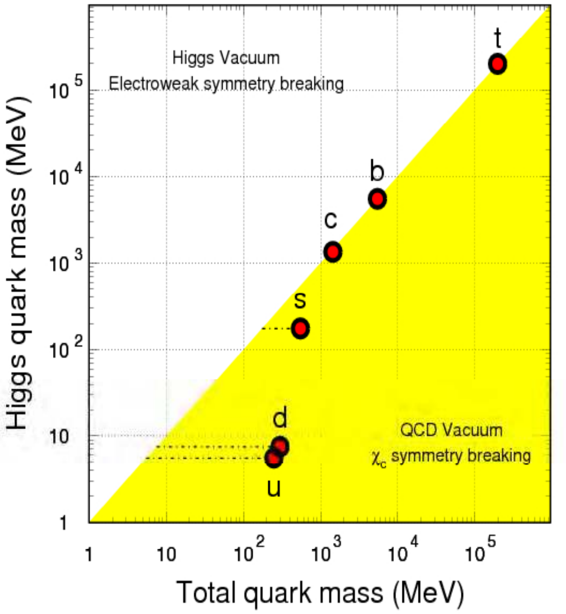

Figure 1: Higgs quark mass versus total quark mass.

Understanding the yield of charmed hadrons in hadron-hadron collisions requires a knowledge of the projectile and target parton distribution functions, the cross section for parton-parton interactions which generate charm quarks and the fragmentation functions for c(b) quarks into charmed (bottom) hadrons. The parton distributions within the proton can be extracted from electron-proton collisions while the cross-sections for gluon fusion and $q\bar{q}$ annihilation are calculated in a perturbative QCD framework up to next-to-leading-order (NLO).[14] However, the parton and gluon distribution functions within the nucleus, relevant for charm and bottom quark production at RHIC energies, are poorly understood[15] and thus leave room for precise measurements of charm cross sections in p+p, d+Au and Au+Au collisions. Perturbative QCD predictions for the cross section $\sigma(c\bar{c})$ and $\sigma(b\bar{b})$ in p+p collisions at $\sqrt{s_{NN}}$ = 200 GeV may be found in the literature[14] and they are in reasonably good agreement with the cross-sections measured at RHIC given that some of the theoretical calculations are uncertain by as much as 50% (see Table 1).

Experiment: $\sigma_{NN}(c\bar{c})$ = 900 - 1400 μb
Theory: $\sigma_{NN}(c\bar{c})$ = 289 - 445 μb
20 - 30 $c\bar{c}$ pairs per central Au+Au collision at $\sqrt{s_{NN}}$ = 200 GeV

Theory: $\sigma_{NN}(b\bar{b})$ = 1.64 - 2.16 μb
0.04 - 0.06 $b\bar{b}$ pairs per central Au+Au collision at $\sqrt{s_{NN}}$ = 200 GeV

Table 1: Cross sections for the production of charm and bottom.

The uncertainty in the theoretical cross-sections arises from a reasonable variation of quark masses (m_c = 1.2-1.5 GeV, m_b = 4.5-5.0 GeV), factorization and renormalization scales (μ_R and μ_F), and parton distribution functions (MRST, CTEQ, GRV). The number of underlying binary nucleon-nucleon collisions normalizes the cross section values. There are approximately 1000 binary nucleon-nucleon scatterings in each central Au+Au collision.

In heavy-ion collisions, final state interactions may also enhance charm production relative to the binary scaling of initial parton collisions and may also lead to additional production of charm via “thermal” processes. An analogous mechanism dominates strangeness production. The heavy quark channels should be greatly suppressed by the thermal factor due to the heavy quark mass ($m_c \approx$ 1.2 to 1.8 GeV, $m_b \approx$ 4.5 to 5.0 GeV),[16] making heavy quark production rates primarily sensitive to the dynamics of the initial collisions. This is especially true for the b quark. Figure 2 shows the calculated contributions to the total charm production at $y = 0$ for $\sqrt{s_{NN}}$ = 200 GeV, with an energy density of 3.2 GeV/fm^3 at the moment of thermal equilibration.

STAR and PHENIX have made measurements of charm production in Au+Au, d+Au, and p+p collisions at RHIC. The PHENIX data for Au+Au collisions suggests that the cross-section for open charm production is consistent with the expectations of pQCD. These results were derived from non-photonic single electron spectra[17] as shown in Figure 3. The STAR results show that the cross-section for open charm production in d+Au and Au+Au is consistent with binary collision scaling but the total yield may be larger than NLO pQCD models. Note, since we only measure the electrons and D^0s to extract the total charm cross-section, several assumptions such as the ratios of the neutral over charged D-mesons have to be used. Both the p_T integrated yield of dN/dy and the value of $\langle p_T \rangle$ of the measured D-meson spectrum are larger than the pQCD model predictions. The STAR results are obtained from a direct reconstruction of the open charm hadrons[18] as well as through single electron spectra.

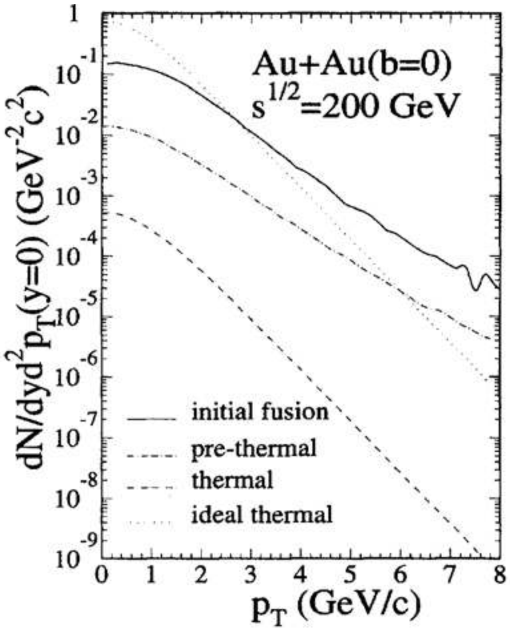

Figure 2: Contributions to charm production at RHIC energies. In the thermal calculation (dashed line), both gluon and quark fugacities are varying as a function of temperature. In the 'ideal thermal' calculation (dotted line), the system is assumed fully thermalized with both fugacities set to be unity. The distributions were calculated with an energy density of 3.2 GeV/fm^3 at the moment of thermal equilibration. The figure is from Reference [16].

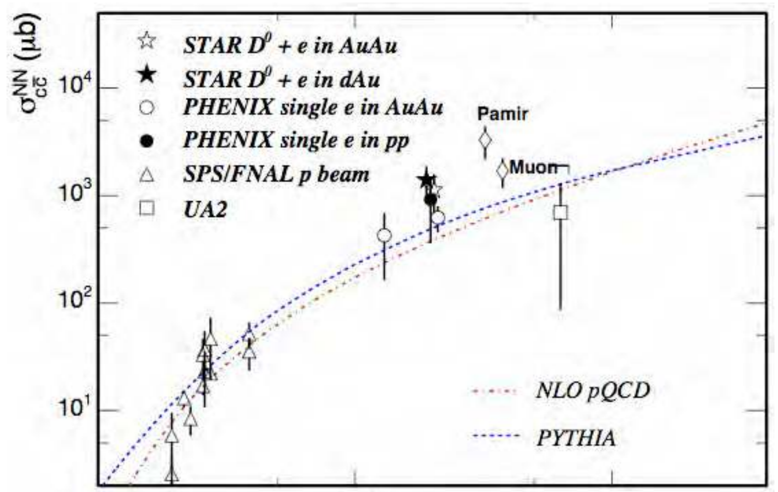

Figure 3: Total c$\bar{c}$ production cross-sections per nucleon-nucleon collision vs. collision energy. The dashed line depicts a PYTHIA calculation.[19,20] The dot-dashed line depicts a NLO pQCD calculation with MRST HO, m_c = 1.2 GeV/c^2, μ_F = 2m$_c$, μ_R = 2m$_c$.[21] The figure is adapted from References [18, 21].

2.3 The Need for Direct Topological Reconstruction of Open Charm

When direct measurements of heavy flavor hadrons are not possible, non-photonic electrons from heavy flavor decays can be used to study charm production. However there are serious limitations in such measurements. As shown by Batsouli, Kelly, Gyulassy, and Nagle in Reference [22], the decayed electron distributions are insensitive to the intrinsic shape of the D-meson transverse momentum distribution. Due to the decay kinematics and the light mass of the electrons and positrons, the dynamical information in the primary spectrum is washed out. This phenomenon is shown in Figure 4. There is a clear difference between the zero mean free path hydrodynamic flow prediction (solid) and the infinite mean free path pQCD PYTHIA calculations (dashed-line) for D-mesons; but the resulting electron spectra are nearly indistinguishable. In order to extract useful information about heavy flavor production in heavy-ion collisions, we have to measure the charm and bottom-hadrons by direct topological reconstruction. Single electron spectra are not sufficient.

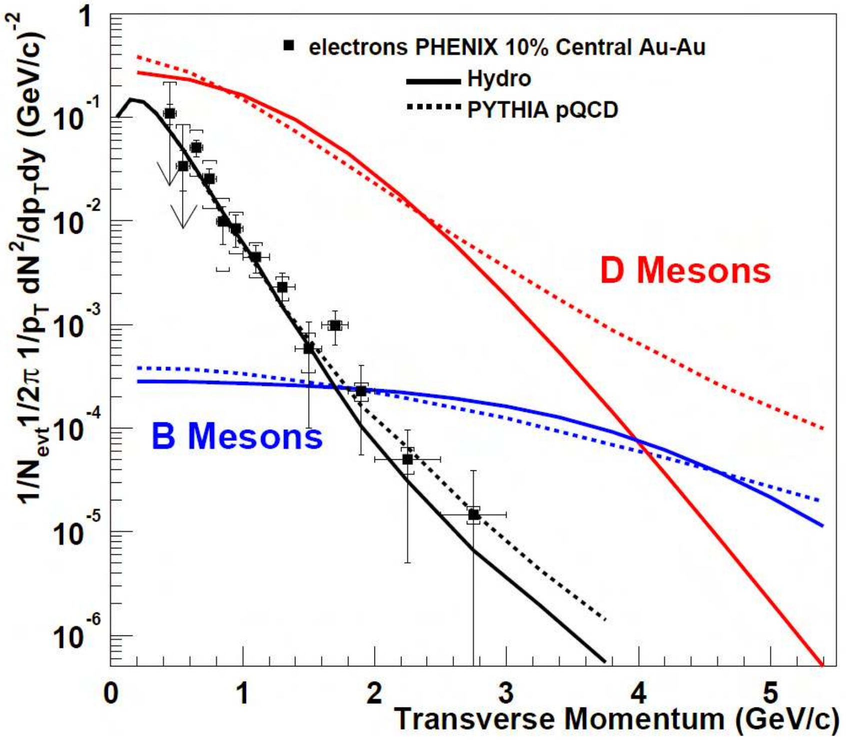

Figure 4: Solid- and dashed-curves represent the charm- (red) and bottom-hadron (blue) spectra from Blast-Wave and PYTHIA model calculations, respectively. The corresponding heavy flavor decayed electron spectra are shown as black curves. The data are the single electron distributions measured in 10% central Au+Au collisions at 130 GeV by the PHENIX collaboration. The figure is adapted from Reference [22].

The same conclusion is reached when doing the analysis of R_{AA} for heavy flavor spectra. Recall that R_{AA} is the ratio scaled by the number of binary collisions of the charm yield measured in heavy-ion collisions relative to the yield in p+p or d+Au. The nuclear modification factor, $R_{AA,}$ for D-mesons is shown in Figure 5. Two different models are presented. The figure shows that there are large differences in the two D-meson R_{AA} ratio curves but the corresponding decayed-electron R_{AA} curves are essentially identical for all p_T. These are theoretical curves without error bars. This suggests that it will not be possible to determine the heavy flavor R_{AA} from the decay electron R_{AA}. In addition, any electron measurement will have large systematic uncertainties at low momentum due to the large background from photonic electron production.[17,18] At higher p_T, electrons from B-meson decays will become more abundant making the electron measurement for charm physics even less realistic. This clearly calls for a direct measurement of heavy flavor hadrons, i.e. D- and B-mesons.

The proposed Heavy Flavor Tracker (HFT) will make these and other measurements by the direct topological reconstruction of the various charmed hadrons, including the D^+, D^-, D^0, D_s^+ and possibly Λ_c^+. Thus the HFT will enable us to dramatically reduce the systematic uncertainties that are inherent in single electron spectra.

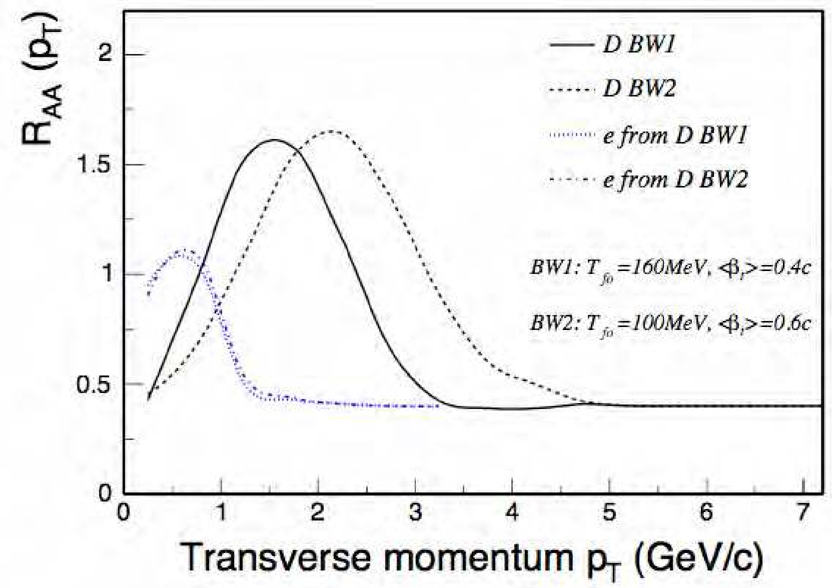

Figure 5: Nuclear modification factor R_{AA} of D-mesons assuming a hydro-dynamically inspired parameterization with a collective flow velocity of $<\beta_r>$ = 0.4*c* and 0.6c for D-mesons. The corresponding electron decay-spectra are shown by the blue dashed (1) and (2) lines.[23]

2.4 Probing Medium Thermalization: Charm Quark Re-interactions

RHIC data on light flavor hadrons strongly suggests that partonic collectivity has been achieved in heavy-ion collisions. The successful measurement of partonic collectivity is a necessary step toward the discovery of a QGP. However, this is not sufficient until we also address the issue of thermalization.

Collectivity in heavy-ion reactions is addressed by studying flow. Many important measurements of transverse radial and elliptic flow of identified hadrons, containing light quark flavors (*q* = *u, d, s*), have been performed at RHIC. The main conclusions from these studies are that the systems created in ultra-relativistic Au+Au collisions exhibit strong collective expansion. Compared to measurements at SPS energies, the degree of collectivity is stronger. In addition, the spectra suggest that at RHIC the multi-strange hadrons (Ξ and Ω) freeze-out at a higher temperature and lower collective velocity than the lighter hadrons. However, a significant amount of elliptic flow is also observed for multi-strange baryons. The elliptic flow of the multi-strange baryons is comparable to the amount of flow observed for the non-strange baryons and is in good accord with the valence quark scaling hypothesis that describes the non-strange quark bearing mesons and baryons well.[24] These results have been interpreted as an indication that sizeable partonic collectivity develops at RHIC. Details of these studies can be found in the literature.[2,25,26,27,28]

The key question then is whether or not charm quarks flow. If the elliptic flow of charm were comparable to the elliptic flow of the lighter quarks, this would be a clear indication of a thermalized state of matter because, in analogy to Brownian motion, it takes many interactions with lighter quarks and gluons, to cause a heavy quark to acquire the collective motion of the bulk matter.

Theoretical calculations indicate that thermalization may be reached at RHIC at temperatures of 0.3 to 0.5 GeV[29] and that the duration of the equilibrium period may be of the order of 5 to 10 fm/c.[30,31] Thermal production of $c\bar{c}$ pairs is suppressed due to their large masses, however, charmed hadrons may still be produced in a thermalized fashion if the c and $\bar{c}$ quarks become embedded in a thermalized bath of light quarks. The relative probability of creating different charmed hadrons will be driven by the properties of the medium which is providing the additional quarks necessary to form the hadrons. The relative yield of various charmed hadrons is thus sensitive to the properties (temperature and chemical potentials) of the light quark medium and these hadron yields must be measured in order to achieve a full understanding of the medium.

The transverse momentum distributions of hadrons are particularly important. They reflect the dynamic evolution of the system and yield indirect information about different stages of the collision. After hadronization is complete and inelastic collisions cease, the particle abundances are fixed. This is commonly referred to as chemical freeze-out. Later when elastic interactions cease, the particle momenta become fixed; this is referred to as kinetic freeze-out. The evolution of the system is recorded in the p_T spectra because, for most particle species, transverse *radial* flow is accumulated throughout the whole collision history while transverse *elliptic* flow is believed to saturate at early times in the collision sequence.

Thus charmed hadron flow is an indicator of thermalization due to the heavy quark interactions with light quarks and gluons. If thermalization takes place, it is reached during the partonic stage of the collision. In order to test the question of thermalization experimentally, we propose to measure the charmed hadron transverse radial and elliptic flow. The combination of the open charm spectra and v_2 will allow us to determine the collective properties of the charm quarks and the probable degree of thermalization of the light quarks.

2.4.1 Elliptic Flow

In non-central heavy-ion collisions the overlap region of the colliding nuclei is spatially deformed. It has the shape of an ellipse in the transverse plane. Through many re-scatterings, pressure gradients will be built up and the initial-state spatial anisotropy will be transformed into a final-state momentum space anisotropy. Notice that re-scattering is a sufficient condition for the development of these anisotropies and thermalization is not required. Theoretically, the largest momentum anisotropies are obtained in the hydrodynamic limit[32] where there is a zero mean free path, leading to instantaneous local thermal equilibrium.

The momentum space anisotropy leads to an azimuthal variation of the transverse-momentum distributions relative to the reaction plane. The azimuthal anisotropy can be quantified by the coefficients of a Fourier decomposition. The largest contribution comes from the second Fourier coefficient $v_2(p_T, y)$, the *elliptic flow coefficient.* In the time evolution of elliptic flow, the strong spatial deformation decreases because the matter begins to expand more rapidly in the direction of the shorter axis of the ellipsoid.[33] As the spatial deformation disappears, the build-up of flow due to pressure gradients ceases. Elliptic flow is thought to be a signal that develops in the early stages of a collision. RHIC data[2,34,35] show that in semi-central Au+Au collisions, elliptic flow reaches the hydrodynamic limit for transverse momenta up to 2 GeV/c and this suggests early thermalization[32] at a time of $\tau = 0.6$ fm/c. Thus, information about the equation of state[36] can be determined from a measurement of elliptic flow. If all hadron species experience the same anisotropic flow, their v_2 coefficients should obey simple hydrodynamic relations[36] and exhibit a characteristic mass dependence. As an example, Figure 6 (top) shows the measured elliptic flow of strange hadrons up to, and including, the multiply strange Ξ baryon. At low momentum, all particles exhibit a linear rise in v_2 and a clear mass ordering appears from the lower mass kaon to the heavier Ξ. The bottom plot in Figure 6 shows the measured elliptic flow versus transverse momentum, where both axes are scaled with the number of valence quarks. Quark coalescence models predict a universal scaling of v_2/n versus p_T/n at intermediate momentum where quark recombination is assumed to be the dominant hadron production mechanism. In such models collectivity – the elliptic flow of constituent quarks – is intrinsically built in. The analyses indicate that collectivity is established at the partonic level.

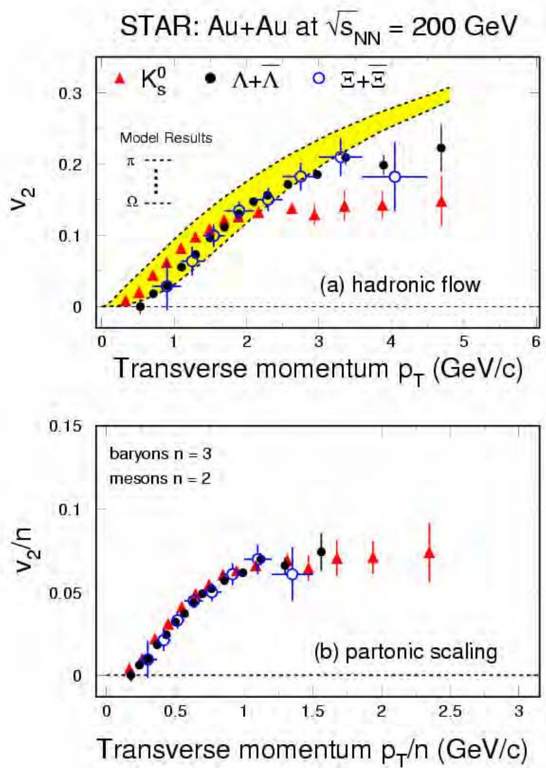

Figure 6: Elliptic flow of strange hadrons at RHIC as measured by the STAR detector. The top panel demonstrates typical hydro-dynamical mass ordering up to a p_T of less than 2 GeV/c and saturation at larger momenta. The bottom panel shows the scaling of elliptic flow with the number of valence quarks in the saturation region (baryons, n=3; mesons, n= 2).

Charm quarks are abundantly produced at RHIC energies. Due to their high mass and small interaction cross section, the strength of elliptic flow of heavy flavor hadrons may be a good indicator of thermalization occurring at the partonic level. If all quarks in heavy flavor hadrons flow with the same pattern as the quarks in the light flavor hadrons, this indicates frequent interactions between all quarks. Hence, thermalization of light quarks is likely to have been reached through partonic re-scattering.

Figure 7 shows a first indication of charm particle elliptic flow at RHIC measured in the inclusive electron channel.[37] The predictions assume elliptic flow for the light quarks as determined by fits to experimental data. The data support the idea that the heavy charm quarks might flow. As shown in the figure, the uncertainties are rather large especially at low transverse momentum where hydrodynamic behavior should occur. A precise measurement of directly reconstructed open charm hadrons to low momentum is essential to confirm and further quantify elliptic flow of the charm quarks.

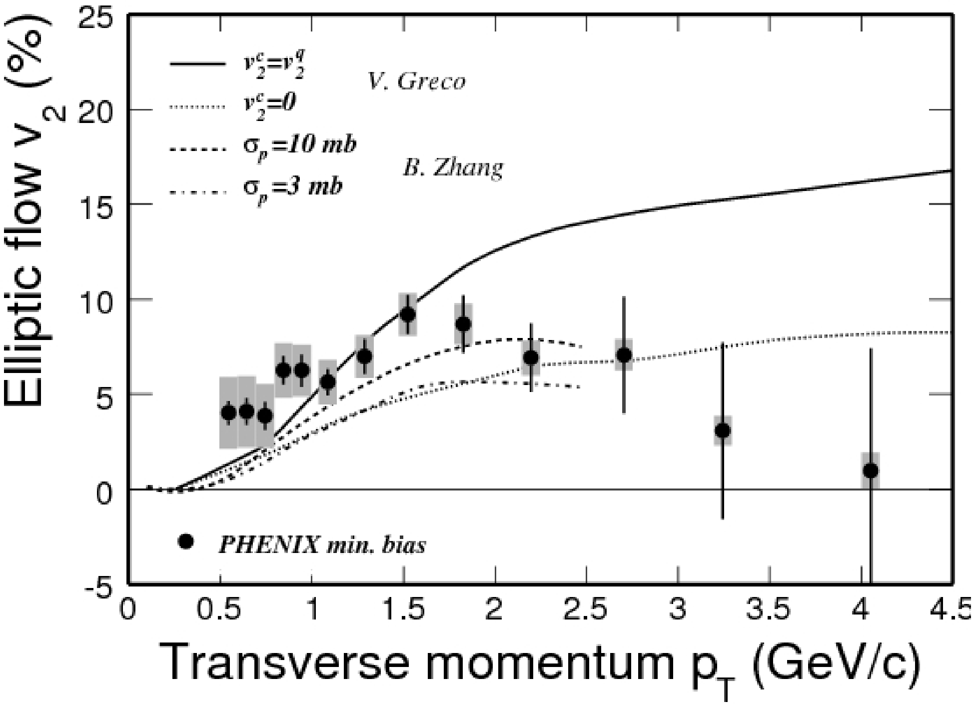

Figure 7: Non-photonic electron elliptic flow at RHIC. Circles represent data of non-photonic electron v_2 from PHENIX.[37] Statistical errors are shown as solid lines and the open boxes indicate the size of the systematic errors. The solid-line represents the results from Greco[38] et al. where similar v_2 distributions for c- and u-quarks are assumed.

2.4.2 Charm Hadro-Chemistry

Hadronic yields and their ratios have been measured from AGS to RHIC energies and have been successfully described by statistical models.[39,40] The relevant parameters are the chemical freeze-out temperature T_{ch} and the chemical potentials μ_i for conserved quantum numbers, i.e. net strangeness, charge, and baryon number conservation.[41] The extracted chemical freeze-out temperature T_{ch} is higher than the kinetic freeze-out temperature T_{fo} extracted from momentum spectra.[42] Chemical freeze-out occurs before kinetic freeze-out.

Charm quarks are dominantly produced in initial parton-parton scatterings.[21] Thermal production of charm quarks is suppressed due to their large mass. In the case of sufficient re-scatterings, initially produced charm quarks might thermally (but not chemically) equilibrate with the surrounding medium. This means their momentum distribution can be described by a temperature parameter consistent with the spectra of light quarks, while the total abundance of charm quarks is determined by the initial parton collision dynamics.

Some models predict statistical hadronization of charm quarks[43,44] with large changes in open and hidden charm production relative to p+p collisions with a strong centrality dependence.[45] Statistical coalescence implies that charm quarks travel over significant distances, e.g. in a QGP. Therefore, a consistent description of precision data by these models would be an indication of deconfinement.[45]

Measuring the total charm and bottom yields requires measuring the yields of several different hadrons. Indeed, charm quarks may fragment into a variety of hadrons as shown in the first column of Table 2. These fragmentation ratios have recently been compiled[46,47] using *e-p* and e^+-e^- collision data. The ratios are found to be independent of the collision energy and the collision system (e-p or e^+-e^-). They are likely to be the same in p+p collisions at mid-rapidity where the HFT can be used to detect charmed particles at RHIC. Note that the ratios calculated using PYTHIA[19] (shown in the third column of Table 2) differ significantly from the measured ratios. To avoid any uncertainties in the charm yield measurement, these ratios will have to be measured also in p+p collisions at RHIC energies.

	e-p and e^+-e^- average	PYTHIA	Statistical coalescence
$f(\mathrm{c} \rightarrow D^+)$	0.232	0.162	0.21
$f(\mathrm{c} \rightarrow D^0)$	0.549	0.639	0.483
$f(\mathrm{c} \rightarrow D_s^+)$	0.101	0.125	0.182
$f(\mathrm{c} \rightarrow \Lambda_c^+)$	0.076	0.066	0.080
$f(\mathrm{c} \rightarrow J/\psi)$		0.006	0.057

Table 2: Charm quark fragmentation functions. The left column is from References [46,47]. The right column is from Reference [45]. The D^+ and D^0 yields include feed-down from D^{*+} and D^{*0} decays.

The effect of statistical coalescence is shown in the last column of Table 2 (see Reference [45]). The calculation assumes that charm quarks statistically coalesce with the lighter quarks, (i.e. according to the temperature and chemical potential of the light-quark system). The temperature and chemical potential are set so that the light hadron yields at RHIC are reproduced. The number of charm quarks present in the system is set by pQCD calculations and this is reflected by a charm-chemical potential in the statistical coalescence model. These results show that statistical coalescence increases the yield of the D_s^+-meson by 80% and the J/ψ yield by a factor of 10 compared to PYTHIA while the yield of D^0 and D^+ decrease slightly. Thus, the ratios D_s^+/D^0, D_s^+/D^+ and $J/\psi / D^0$ are very sensitive probes of thermal charm hadron production.

With the HFT we will be able to precisely measure the ratio of D_s^+ to D^+ yields because most of the systematic errors in the individual spectra cancel out when they are reconstructed in very similar decay channels: $D^+ \rightarrow K^- \pi^+ \pi^+$ and $D_s^+ \rightarrow K^- \pi^+ K^+$. A precise measurement of the total charm production (mostly carried by open charm mesons) will also serve as a baseline for J/ψ enhancement/suppression measurements, which have been suggested as a possible signature for QGP formation.[45]

2.5 Probing the Density of the Medium: Heavy Quark Energy Loss

In order to develop collective flow in heavy-ion collisions, there must be frequent interactions between the constituents of the medium. These interactions will cause energy loss for the energetic partons that are traversing the medium. The amount of energy loss will depend on the distance traveled in the medium.

Results on the nuclear modification factor R_{AA} indicate that the rate of energy loss for heavy-quarks in central Au+Au collisions is surprisingly similar to that for the light-quarks (u, d, s).[48] This experimental observation contradicts our early understanding of the pQCD interactions of energetic partons in a hot and dense medium where much less energy loss was expected for heavy-quarks compared to the light ones.[49,50,51] Since there have been no directly reconstructed heavy quark hadron distributions from RHIC experiments so far, non-photonic electrons in the transverse momentum range $4 < p_T < 10$ GeV/c were used for these heavy-quark studies. The analysis of non-photonic electron p_T distributions is complicated by an unknown mixture of charm and bottom contributions. A possible way to disentangle these effects is a direct topological reconstruction of charmed-hadron distributions and a measurement of charmed hadron angular correlations.

2.5.1 R_{AA} and Energy Loss

The discovery of a factor of 5 suppression of high p_T hadrons ($5 < p_T < 10$ GeV/c) produced in Au+Au collisions at RHIC and the disappearance of the away-side jet has been interpreted as evidence for jet quenching.[3,52,53,4] This effect was predicted to occur due to radiative energy loss of high energy partons that propagate through a dense and strongly interacting medium.[54] The energy loss of heavy quarks is predicted to be significantly less compared to light quarks because of a suppression of gluon radiation at angles $\Theta < M_Q/E$, where M_Q is the heavy quark mass and E is the heavy quark energy.[50] This kinematic effect is known as the "dead cone" effect. The suppression of small angle radiation has the advantage that the heavy quark fragmentation function and the spectrum of light particles produced in association with the heavy quarks can be calculated perturbatively.

Figure 8 shows the result for the ratio of charm (H) to light (L) quark suppression from QCD calculations assuming a size of about 5 fm for the static medium traversed by the fast quark. For transverse momenta $p_T > 7.5$ GeV/c this ratio is predicted to be about 2 due to the smaller energy loss of the heavy quark. In the case where heavy quarks suffer the same amount of energy loss as light quarks, this ratio would be one. This ratio is exponentially sensitive to the density of color charges in the medium, and so the measurement of nuclear modification factors of open charm mesons at large p_T is a promising tool for the study and further characterization of QCD matter at RHIC.

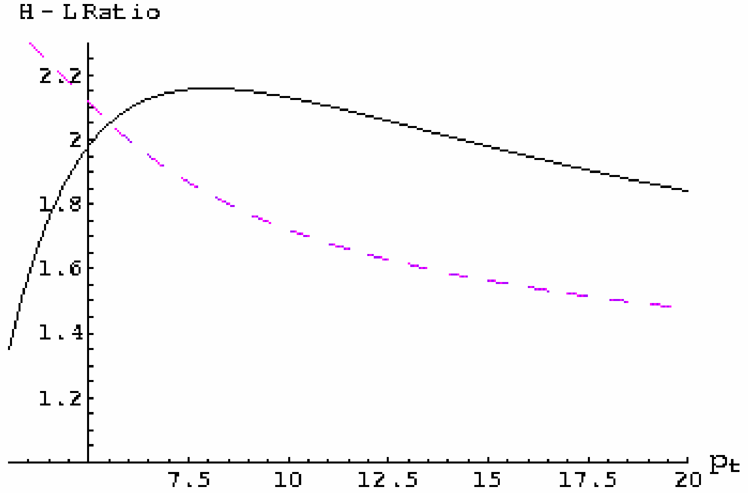

Figure 8: The ratio of suppression factors for charm (H) and light (L) quarks. The solid line represents results from calculations with unrestricted gluon radiation, while the dashed line is based on calculations with a cut on gluon energies ω > 0.5 GeV. The size of the static medium traversed by the fast quark is assumed to be 5 fm. The figure is from Reference [50].

Figure 9 shows the R_{AA} for non-photonic electrons[55,56,57] from STAR and PHENIX. The data extend up to transverse momenta of about 10 GeV/c. The suppression factor for single electron spectra is in the range of 0.2-0.3 which is almost exactly the same as the suppression factor observed for charged hadrons and pions[58,52] (i.e. light quarks). Using an unrealistically large initial gluon density of $dN_g/dy = 3500$, Djordjevic, Gyulassy, Vogt, and Wicks have done a pQCD calculation[59] including gluon radiative energy loss, which can barely reproduce the electron R_{AA} (blue line in Figure 9). The model ignores the contributions from bottom hadrons. When bottom is added the model cannot describe the data at all (yellow band in Figure 9). The model with bottom over-predicts the data by a factor of 2 to 3. Note that for light-quark hadrons, like pions, a gluon density of about 1000 has been used to reproduce the observed R_{AA}. These results are a serious challenge to our understanding of both the mechanism for heavy quark production and the mechanism for energy loss in a hot and dense medium. In order to resolve these important issues, we have to do direct topological reconstruction of open charm. It is experimentally and theoretically too difficult to make definite conclusions from the measurements of non-photonic electrons due to the complications from the mixing of the electrons from D and B decays and the smearing of the decay kinematics. In addition, changes in the hadro-chemistry could cause the R_{AA} for electrons to give a distorted view of the charm quark R_{AA}.

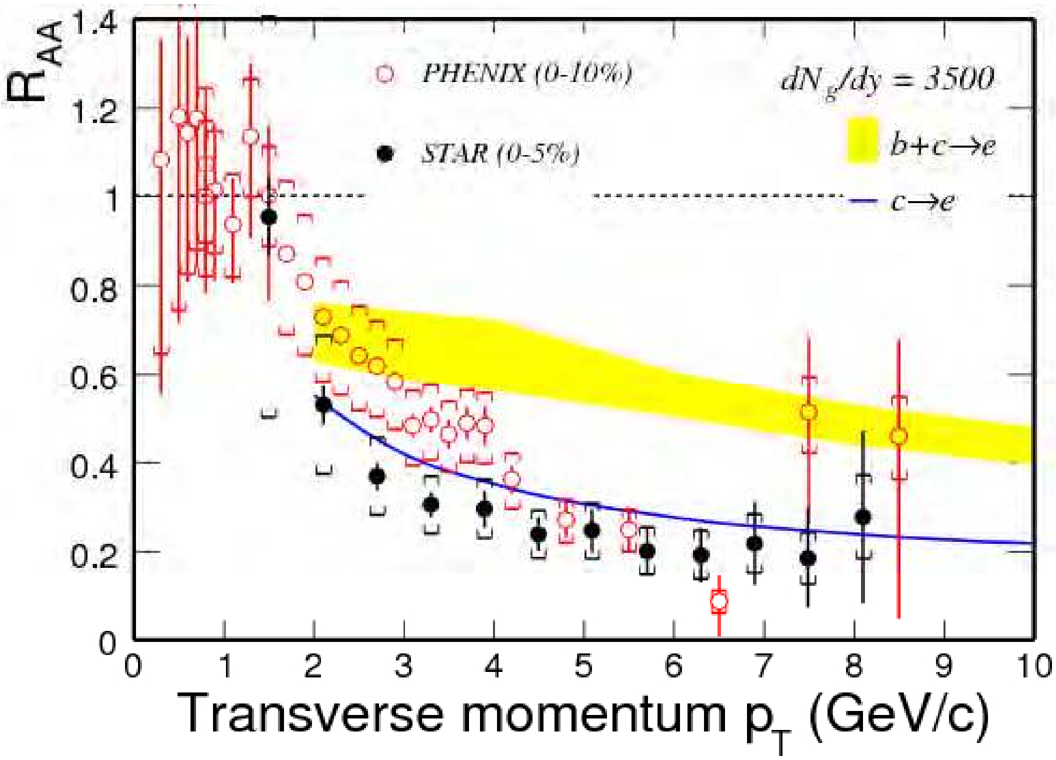

Figure 9: Non-photonic electron R_{AA} in central Au+Au collisions from STAR (filled circles, top 5%) and PHENIX (open circles, top 10%) from References [48,55,56,57]. Theoretical predictions for electrons from charm hadrons are shown as blue line and electrons from charm and bottom decays are shown as yellow band. In these calculations, the initial gluon density was assumed to be unrealistically large (see Reference [59]).

Extracting the heavy flavor production cross sections from semi-leptonic decays is a serious challenge. Experimentally, it is very difficult to reject the photonic electrons generated in the detector material. In addition, as shown in Figure 10, the correlation between parent and daughter p_T is very broad and the higher the p_T the broader the correlation. In order to study the properties of the hot and dense medium (low p_T region) and test the pQCD predictions in the strongly coupled regime (at high p_T), one must directly measure the heavy flavor hadron distributions.

2.5.2 Charm Angular Correlations

Correlations between charmed hadrons are another way to separate the effects of charm and bottom production. The correlation between D-mesons is defined as the normalized pair distribution $C(\Delta\phi) = N(p_1,p_2)/N_0$, where p_1 and p_2 are the momenta of the charmed hadrons and N_0 is the total number of pairs. Similar to jet production, heavy-quark production requires a large momentum transfer, so we expect a distinct back-to-back correlation for the quarks (and mesons) as shown by the open-circles in Figure 11. In this calculation, the PYTHIA (v6.2) event generator was used with the default set of parameters. As one can see there is a clear back-to-back correlation for the D-mesons. We propose to utilize this distinct correlation to study the charm-quark energy loss in high-energy nuclear collisions.

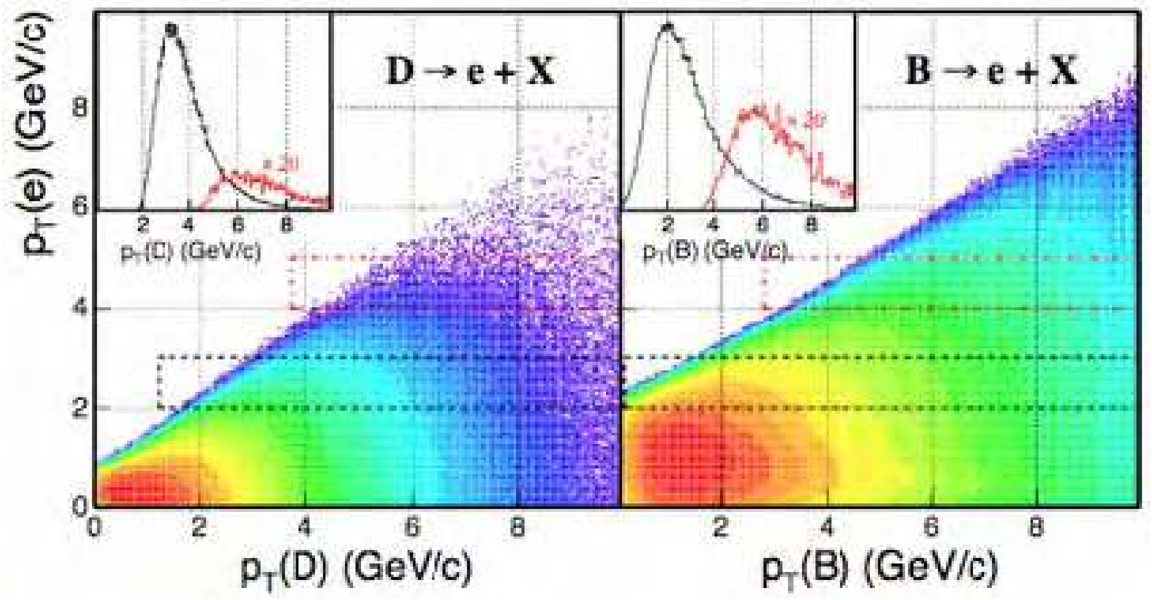

Figure 10: p_T distributions of electrons from semi-leptonic decay of heavy flavor mesons (left D-mesons, right B-mesons) as a function of parent p_T. The inserted plots represent the projections to the corresponding heavy flavor distributions. The widths of the electron p_T windows are indicated by dashed boxes.

Now let us consider a few potential observables. For example, when a charm quark interacts with the medium, it will lose energy and the original angular correlation pattern, as shown in Figure 11, will be modified. We show angular smearings of $<\sigma_\phi> = \pi/4$ and $\pi/2$. In addition, the change in the angular correlation depends on the nature of the interaction. Most of the (quasi)elastic scatterings are directed in a narrow cone in the forward direction[60] while the inelastic scatterings, such as the gluon radiative energy loss[49], will lead to a much wider smearing in the final correlation. In the inelastic scattering scenario,[49,51] the energy loss occurs deep inside the plasma and the final correlation function reflects the hot/dense properties of the medium. On the other hand, the resonant scattering happens near T_c.[60] Although both scenarios lead to sizable energy-loss, the angular correlations may allow us to distinguish these two different mechanisms in high-energy nuclear collisions. In order to perform the measurement, a large acceptance for the reconstructed charmed hadrons is required. The proposed HFT will be necessary for this study.

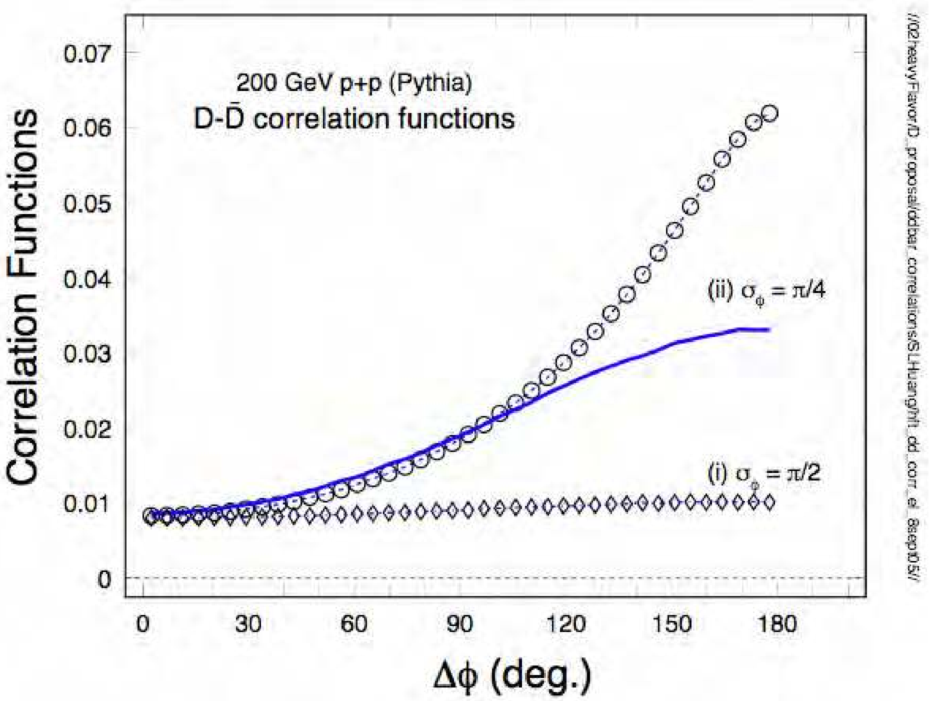

Figure 11: D-meson correlation functions for 200 GeV p+p collisions. A clear back-to-back correlation in the angular distribution of charmed mesons is observed (shown by the open circles). The solid line and the diamonds represent the results with angular smearing for σ_ϕ of π/4 and π/2, respectively.

Recently, the measurements on charm production by the Belle Collaboration[61] show a surprisingly large cross-section for J/ψ production in √s = 10.6 GeV e^++e^- collisions. Even more surprising is the fact that $c\bar{c}$ pairs accompany more than half of the observed J/ψ's. This result contradicts our current understanding for J/ψ production in the pQCD framework, as discussed in References. [19,62,63,64], and implies a different production mechanism for heavy-quarks in elementary collisions.[65] As proposed in Reference [65], gluon fragmentation is increasingly important for collisions at higher bombarding energies and so RHIC energies are very interesting. In elementary collisions, the main difference between the new and the conventional processes lies in the angular correlation of the produced charmed hadrons. With the proposed HFT and STAR EMC (Electro-Magnetic Calorimeter), we will be able to study the correlation of D-mesons to further understand pQCD in p+p collisions. We will also study the correlation of D-mesons in high-energy nucleus-nucleus collisions, were the gluon density is high.[59,66] This might enhance the effects observed in elementary p+p collisions. These studies will certainly shed light on the production mechanisms for charm and charmonium at RHIC.

As mentioned earlier, heavy-quark production leads to a back to back correlation between particle and anti-particle. This correlation is also reflected in their decay products, such as the electron pairs. In this case, it causes the background in the intermediate invariant mass region[67] ($1 < m_{ee} < 3$ GeV/c^2) to have a correlation too. Here m_{ee} is the invariant mass of the electron pair. This creates a significant background for a low mass vector meson analysis. Using the HFT to measure the correlated electron pairs will greatly reduce the background for vector meson and charm measurements via non-photonic electron spectra.

2.5.3 Baryon – Meson Ratios

In the intermediate p_T region ($2 < p_T < 6$ GeV/c) baryon yields are known to be enhanced compared to meson yields in Au+Au collisions. The enhancement is found to be proportional to the collision centrality. These observations have been confirmed by both R_{AA} and v_2 measurements. The results are usually explained by a hadronization mechanism involving collective multi-parton coalescence rather than by independent vacuum fragmentation. The success of the coalescence approach implies deconfinement and possibly thermalization of the light quarks prior to hadronization. Since Λ_c is the lightest charmed-baryon and its mass is not far from the other D-mesons, it will be very interesting to measure the R_{AA} of Λ_c and compare it with the R_{AA} of the other charmed mesons in order to see if there is a meson-baryon difference. Theories about heavy quark deconfinement and collectivity can be tested with these comparisons. In addition, due to the different branching ratios for the semi-leptonic decays, the measurement of Λ_c spectra will help us understand the surprising suppression observed in the non-photonic electrons. In this case, even if charmed quark production scales with the number of binary collisions, an increase in the ratio Λ_c/D-mesons similar to that seen for the Λ/kaon ratio will lead to a suppression of about 20% in non-photonic electrons ($1 < p_T < 5$ GeV/c) for central Au+Au collisions.[68]

2.6 Probing Chiral Symmetry of the Medium: Vector Mesons

Dilepton measurements of vector mesons in the invariant mass region below 1 GeV in relativistic heavy-ion collisions have attracted great interest as a possible signature of chiral symmetry restoration via observations of modifications of the vector meson masses. These measurements are challenging as the lepton production processes are rare and backgrounds from leptonic decays of hadrons as well as from photon conversions are large. In addition, the observed leptons are produced during the full evolution of the colliding system.

Despite the experimental difficulties, low and intermediate mass dileptons have been measured at the CERN-SPS and an excess of radiation above the hadron cocktail has been observed in the invariant mass region of $0.2 < M_{ee} < 0.6$ GeV/c^2 in semi-central Pb + Au collisions.[69,70] Under the assumption that the hadronic phase at RHIC is short the experimental measurement of photons and dileptons from thermal radiation might result in a clear signature. This is in contrast to measurements at lower energies where the hadronic phase is more pronounced. Recently, NA60 has measured the dimuon spectra around the ρ mass region for central In+In collisions.[71] Detailed energy dependence of the dilepton invariant mass has been calculated in Reference [72]. From SPS to RHIC energies the hadronic phase has little energy dependence on the dilepton yields while the QGP phase increases its dilepton radiation significantly from SPS to RHIC.

Clean electron identification is made possible by the measurement of charged particle energy loss in the TPC gas (dE/dx), and the measurement of charged particle velocity with the time-of-flight system. The observed electrons are, to a large extent, background. They originate from photons converting into electron-positron pairs, $\gamma \rightarrow e^+ e^-$, in the detector material, from π and η Dalitz decays, and from semi-leptonic decay of heavy quark hadrons. The large acceptance of the STAR TPC makes it possible to reduce π^0 and η Dalitz decay background by a factor of 3 (single track) by measuring both electrons of the pair. The PIXEL detector of the HFT makes it possible to reject conversion background originating outside the inner PIXEL detector by requiring hits in the PIXEL detector of the HFT. In addition, the HFT makes it possible to reject physics background from semi-leptonic decays of heavy quark hadrons. Correlated semi-leptonic decays of open charm form the dominant source of background at intermediate mass.[73,74] This background originates from a secondary vertex that is displaced by about 100 μm that can be measured with the high resolution provided by the HFT.

Figure 12 summarizes the dielectron invariant-mass distributions of background and signals. The signals of medium-modified vector mesons and thermal QGP radiation (black curve) are from calculations of Reference [75] folded with the STAR acceptance. The uppermost (red) curve is the total dielectron invariant-mass spectrum with year 2004 configuration. This is obtained from the single-inclusive electron spectrum measured in 200 GeV Au+Au collisions with the assumption of electron PID from full TOF coverage. The gray curve is the charm e^+e^- distribution after applying the HFT distance of closest approach cut (DCA < 80 μm). The dot-dashed line is from Dalitz decays from π^0 and η in the TPC after rejection. The net result is a signal-to-background ratio that, even in the continuum region, is around (or better) than 1/10, which is very comparable to the NA60 measurements for central In+In collisions.[71] The standard method of dealing with the residual background is by mixed-event methods. This has been used by CERES and NA50/NA60 at the SPS and will be used both in PHENIX and STAR.

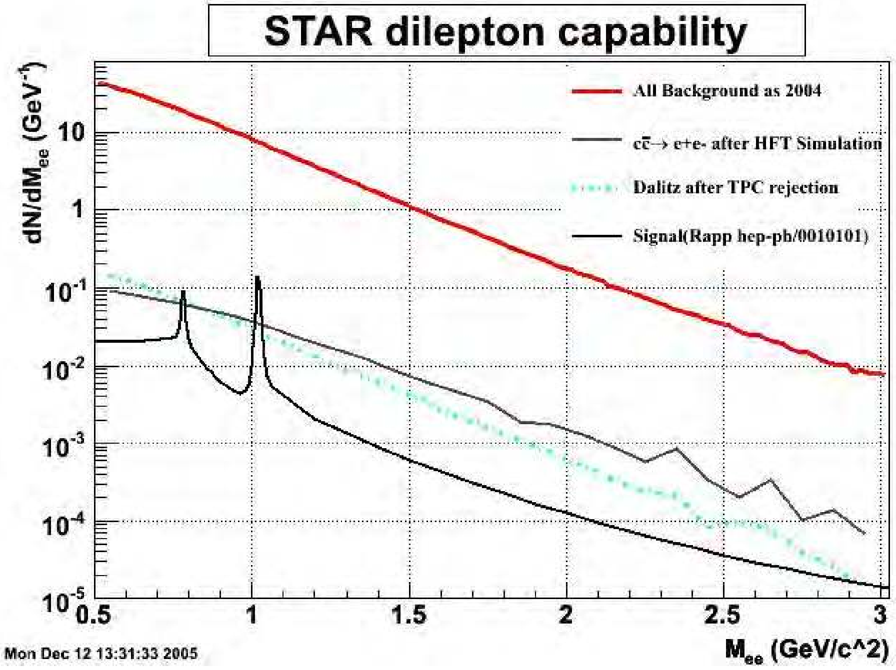

Figure 12: Di-electron invariant mass spectrum from 200 GeV Au+Au collisions. The continuous solid black curve represents the model prediction of Reference [73] using the full STAR acceptance. The red curve at the top is the total di-electron invariant mass spectrum seen with the 2004 configuration of STAR. The full TOF coverage is assumed for electron identification. Dalitz decays from π^0 and η after rejection from TPC are shown as the dashed-dotted curve. Electrons from charm decay are shown as the gray curve. The HFT is used to reconstruct open charm.

With the upgrade we expect to detect 6K φ and 22K ω decays in 200 million recorded central Au+Au collisions. These are to be compared with the numbers presented by NA60[71] in central In+In collisions: about 6K for the ω and about 10K for the φ.

2.7 Probing Cold Nuclear Matter

The measurement of charm production in d+Au collisions yields essential baseline data for the relativistic heavy-ion program at RHIC.

In relativistic heavy-ion collisions heavy flavor is expected to be produced via initial gluon fusion.[76] In the absence of nuclear effects the observations in relativistic heavy-ion collisions would thus scale with the number of binary collisions. Deviations from this scaling result from the partonic structure of the nucleus and from the high-energy-density phase following the collision. Detailed measurements in p+p collisions establish the underlying cross sections and kinematic distributions for hadrons containing heavy flavor for the free nucleon. Collisions of d+Au nuclei allow the study of nuclear modification and intrinsic k_T distributions.

Charm and bottom production in d+Au collisions at RHIC is dominated by gluon-gluon scattering contributions, and their measurement is thus a direct probe of gluon structure in the nucleus. Mid-rapidity STAR measurements of charm production are sensitive to the transition region between anti-shadowing and shadowing as illustrated in Figure 13, whereas measurements of bottom probe anti-shadowing. They are complementary to fixed target measurements, which probe larger momentum fractions *x*, and to future measurements at the LHC and at an Electron-Ion Collider (EIC), which probe smaller *x*.

Yield estimates for an inclusive D-meson measurement show that sensitivity can be obtained within 1 to 2 weeks of data taking at RHIC-II luminosities. Correlation measurements give additional insights and provide constraints on the kinematics of the colliding partons, but require considerably higher integrated luminosities.

Precise insight in the nuclear parton distributions leads to deeper understanding of the mechanisms associated with nuclear binding and has applications in neutrino experiments, in addition to forming crucial reference data for the heavy-ion physics program.

2.8 Probing the Nucleon

Heavy flavor production has received considerable attention since many measurements suggested discrepancies with next-to-leading-order (NLO) Quantum Chromodynamics (QCD) evaluations. New evaluations and better measurements have reduced the discrepancies to a level where, in several cases, they are no longer significant.[77] For example, the evaluations for the inclusive hadro-production of D^0, D^+, D^{*+}, and D_s^+ have been reconciled with CDF measurements at 1.96 TeV center-of-mass energy.[78] HERA-B has recently presented preliminary results of their open charm measurements at 42 GeV center-of-mass energy.[79]

Data in the intermediate center-of-mass energy region remain scarce. Pioneering open charm measurements have been made, without detection of the displaced vertex, by STAR and PHENIX using p+p, d+Au, and Au+Au collisions at 130 and 200 GeV center-of-mass energy. Theory in the form of NLO[80] and First-Order-Next-to-Leading-Log (FONLL) QCD calculations[81] undershoots the results, particularly at large transverse momenta p_T.[82] In contrast, inclusive jet, hadron, and photon production are well described at RHIC energies[83] by NLO calculations and suitable choices of parton distribution and fragmentation functions.

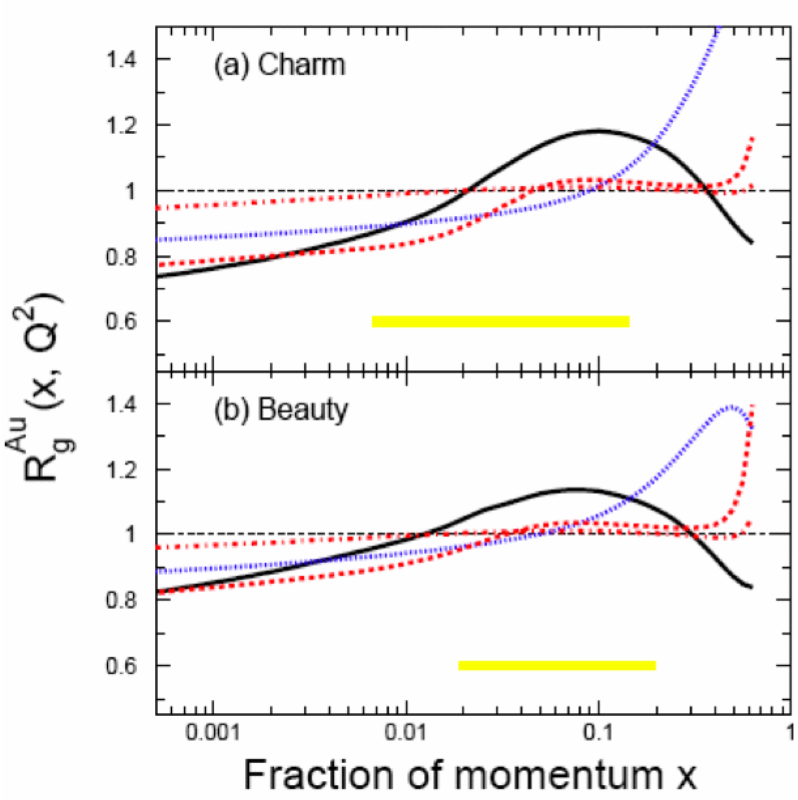

Figure 13: Model evaluations of the ratio R_g^{Au} of gluon momentum distributions of a Au nucleus compared to the nucleon as a function of the gluon momentum fraction x. The continuous, dotted, dashed, and dashed-dotted lines show the parameterizations by Eskola,[84] Hirai,[85] and De-Florian (2x),[86] respectively. The bands indicate the x-range that can be probed by mid-rapidity STAR measurements of charm and bottom production in 200 GeV center-of-mass energy collisions.

Figure 14 shows the NLO pQCD predictions of charm (red lines) and bottom (black lines) total cross-sections, as a function of center-of-mass energy, in hadronic p+p collisions. In the calculations, renormalization scale and factorization scale were chosen to be equal.[80] Large uncertainties exist in the factorization scales in current pQCD calculations for heavy flavor production, thus emphasizing the need for reference measurements. Future measurement of mid-rapidity cross-sections of charm- and bottom-hadrons by the combination of topologically reconstructed charm-hadrons and decay-electrons in 200 and 500 GeV p+p collisions at RHIC should provide stringent benchmarks within the 100 – 1000 GeV range for improved theoretical evaluations. In addition, these results are crucial reference data for quarkonium measurements in heavy-ion collisions at both RHIC and the LHC.

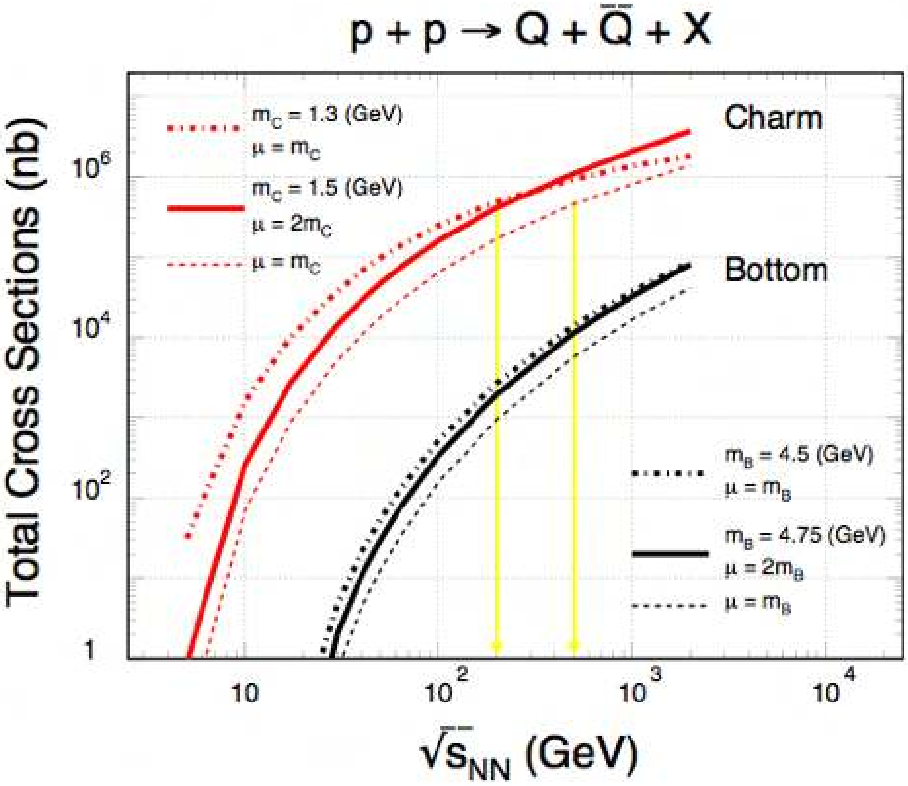

Figure 14: NLO pQCD predictions of charm (red lines) and bottom (black lines) for the total p+p hadro-production cross sections versus center-of-mass energy. The vertical lines indicate the 200 GeV and 500 GeV center-of-mass energies for polarized p+p collisions at RHIC.

In the future, as part of the spin physics program, RHIC will collide polarized protons also at a higher center-of-mass energy of 500 GeV. Large integrated luminosities are projected for both 200 and 500 GeV polarized proton beam operation. Direct reconstruction of open charm using displaced vertexing techniques will thus allow detailed measurement of the cross sections for open charm and open bottom production at two center-of-mass energies, as well as their spin dependences, with a single experiment.

The spin dependence is illustrated in Figure 15, showing a leading-order (LO) evaluation of the charm and bottom total cross section asymmetry for proton collisions with equal and opposite helicity configurations.[87] In LO it involves the densities of polarized gluons in the colliding proton beams and the partonic scattering asymmetry. Different gluon polarization parameterizations produce a large spread in the calculated cross section asymmetry. The partonic scattering asymmetry is calculable and has the unique property that it changes sign with increasing transverse momentum.[88] At RHIC energies, the relatively small size of the cross section asymmetry thus involves a partial cancellation and more sizable *negative* asymmetries are expected in LO for e.g. the longitudinal double spin asymmetry A_{LL} for electrons from heavy flavor decay. This is illustrated in

Figure 16, which shows the average partonic asymmetry for bottom production in polarized proton collisions at 500 GeV center-of-mass energy in comparison with the average partonic asymmetry for prompt photon production, which is part of the STAR baseline spin physics program. The evaluation of NLO contributions has recently been completed.[89] Detailed study of the differential spin cross section asymmetry constitutes a test of the spin structure of the QCD matrix elements, unless gluon polarization in the polarized nucleon is found to be exceedingly small. Conversely, if QCD corrections are under control and the absolute gluon polarization in the polarized nucleon is sizable, then heavy flavor production will give sensitivities that are comparable to those from the prompt-photon production reaction channel.

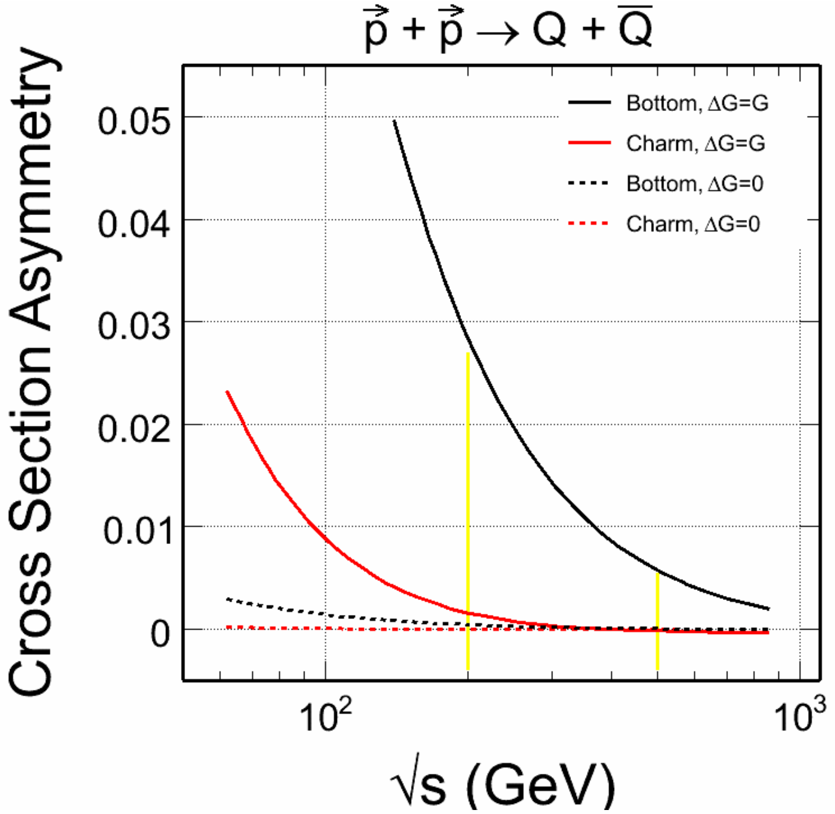

Figure 15: LO evaluation of the total cross section asymmetry for equal and opposite proton beam helicities for charm (red lines) and bottom (black lines) for two gluon polarization scenarios. The yellow vertical lines indicate the 200 GeV and 500 GeV center-of-mass energies for polarized p+p collisions at RHIC.

Other possibilities for the spin, heavy-flavor physics program, at future very high integrated luminosities at RHIC-II may include the measurement of the transverse double-spin asymmetry A_{TT}, which is sensitive to the transversity structure in the proton,[90] and at 500 GeV center-of-mass energy the measurement of the parity violating spin asymmetry A_L in charm-associated W production, which is sensitive to strange quark polarization in the nucleon.[91]

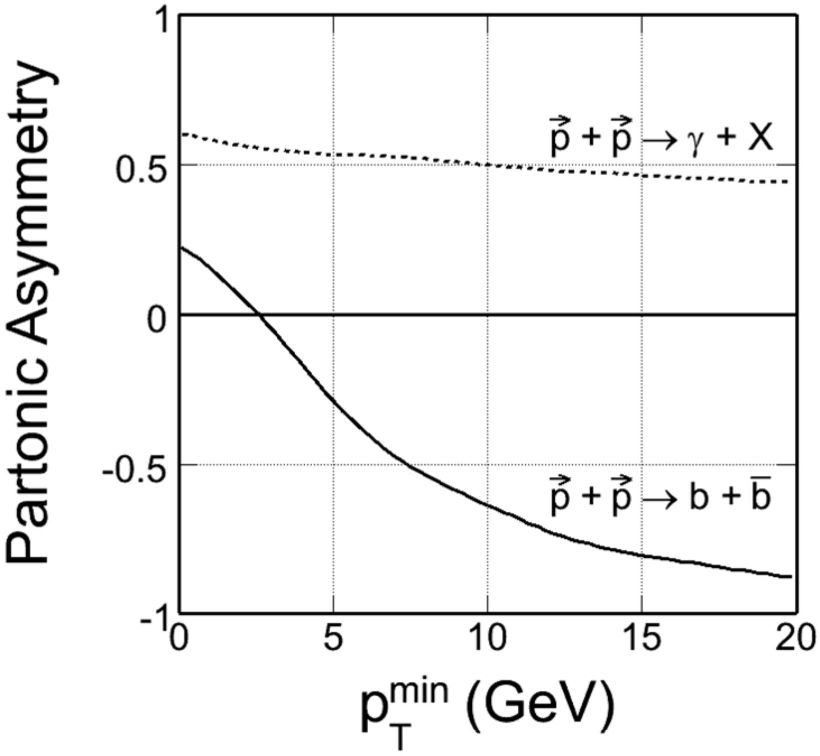

Figure 16: LO evaluation of the average partonic asymmetry for bottom production (continuous curve) and prompt-photon production (dotted curve) in polarized p+p collisions at 500 GeV center-of-mass energy versus the minimum accepted transverse momentum.

3 HFT Overview and Simulation

3.1 STAR and the HFT Detector System

STAR[92] was designed to make measurements of hadron production over a large solid angle, and it features detector systems for high precision tracking, momentum analysis and particle identification (see Figure 17). It is the only experiment at RHIC which measures the full azimuth in ϕ and tracks particles from 100 MeV/c to 20 GeV/c. Therefore, it is well suited for both characterization of heavy-ion collisions event-by-event and also for the detection of hadron jets.

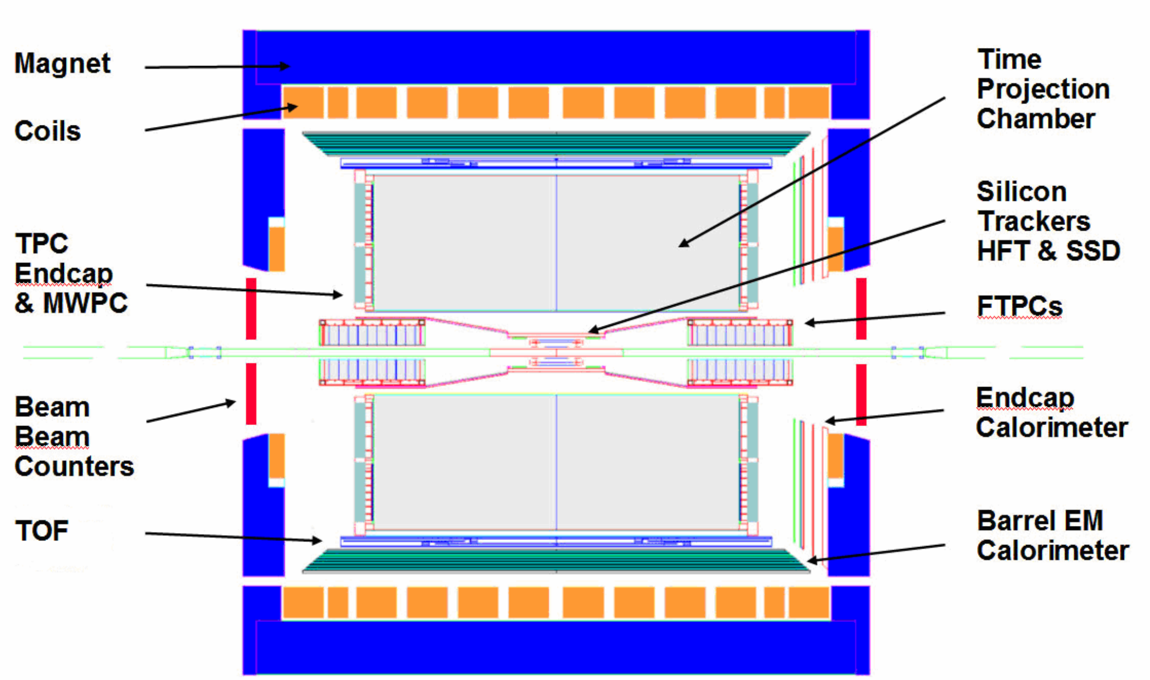

Figure 17: The STAR detector at RHIC is shown as it will be after the TOF and HFT upgrades. The TPC is 4.2 meters long and 4 meters in diameter. Heavy Ion beams enter from the left and right while collisions take place in the center of the detector.

By adding a Heavy Flavor Tracker (HFT) to STAR, we will be able to measure neutral and charged particles with displaced vertices that decay 100 µm, or less, from the primary vertex. The high spatial resolution of the tracker will allow us to study parent particles with a very short lifetime, such as the D^0 meson. The addition of the HFT will extend STAR's unique capabilities even further by providing direct topological identification of hadrons containing charm and bottom and for non-photonic electrons decaying from charm and bottom hadrons. Thus, the HFT is the enabling technology for making direct charm and bottom measurements in STAR.

The STAR detector is equipped with a Silicon Vertex Tracker (SVT), which was designed to make measurements of weakly decaying hyperons, but the SVT is too thick to provide event-by-event charm identification because of multiple scattering. Furthermore, the SVT electronics cannot operate at speeds much higher than 100 Hz, making it incompatible with the DAQ1000 upgrade which is underway. Therefore, the Collaboration decided after extensive review to remove the SVT after Run 7.

At the present time, the STAR detector has modest capabilities to measure secondary decay vertices that are displaced from the primary vertex. To make these measurements, we use the TPC and the SSD to determine the position of the primary vertex to a precision of approximately 100 μm in a central collision while the resolution for a secondary decay vertex is about 500 μm.

For example, it is possible to use this technique to identify the K_S^0 because a K_S^0 decays into two pions with a mean lifetime of 0.896×10^{-10} seconds and it has a characteristic decay distance of 2.68 cm. Since its decay distance is so much greater than STAR's vertex pointing resolution, this particle can be easily identified. Similarly, the decay of strange and multi-strange baryons, such as the Λ, Ξ, and Ω can also be identified.

The addition of the HFT to STAR will improve the single track pointing resolution by a factor of 20, and thus the HFT can be used to measure very short-lived particles by increasing the resolution for finding secondary decays near the vertex.

STAR has several mid-rapidity tracking detectors that are essential for the best performance of the HFT including the Time Projection Chamber[92] (TPC) and the Silicon Strip Detector[93] (SSD). The TPC and SSD are existing detectors, which are shown in Figure 17. At the time of HFT installation, a new Time-of-Flight detector (TOF) will be available and it will cover 2π in azimuth. The TOF detector will replace the Central Trigger Barrel (CTB), which is currently a simple array of scintillators without TOF information. The new TOF detectors will lie outside of the TPC and they will extend the PID region where kaons, pions, and protons can be separated from less than 1 GeV/c to well above 1 GeV/c.

The design of the HFT tracking system is dependent on the performance of the existing detectors in STAR. For example, using an outside-in tracking algorithm, the measurements in the TPC define a path that has a very narrow angular divergence as it is projected forward to the inner detectors. (The TPC can measure up to 45 points along the track between a radius of 190 cm and 60 cm.) Thus the TPC defines a nearly parallel-beam path, but the transverse dimensions of the projected track are relatively large. It is approximately 1 mm × 1 mm when it leaves the TPC.

The SSD is located at a radius of 23 cm and measures an intermediate space point between the vertex and the TPC with a resolution of 30 μm in the r-ϕ direction and 800 μm in the z direction. The SSD is an ideal companion to the TPC tracking system because it provides a pinhole through which the TPC tracks must pass and thereby reduces the transverse dimensions of the projected path of the particle without changing the angular divergence of the path very much. In fact, the angular divergence of the projected path after passing through the SSD is limited only by Multiple Coulomb Scattering (MCS) in the Si strips and so it is important that the SSD is very thin (1% radiation length).

In the remainder of this chapter, we present simulations of the performance of the HFT and show how it can be used to improve the performance of the TPC plus SSD tracking system.

3.2 The Design Parameters for the HFT

The Heavy Flavor Tracker consists of two sub-detectors: a silicon pixel detector (PIXEL) and an intermediate silicon tracker (IST). Both detectors lie inside the radial location of the SSD. The primary purpose of the SSD-IST-PIXEL detector is to provide graded resolution from the TPC into the interaction point and to provide excellent pointing resolution at the interaction point for resolving secondary particles and displaced decay vertices. The TPC will point at the SSD with a resolution of about 1 mm, the SSD will point at the IST with a resolution of about 300 μm, the IST will point at the PIXEL with a resolution of about 200 μm, and the PIXEL detector will point at the vertex with less than 50 μm resolution. A schematic view of the proposed detector layout is shown in Figure 18 and a perspective view is shown in Figure 19.

The Silicon Strip Detector (SSD) lies at a radius of 23 cm. It was built using 20 ladders of 67 cm length with double-sided wafers having 95 μm × 4.2 cm strips crossed at an angle of 35 mrad. The strips are oriented so as to improve the r-ϕ resolution the most. For tracks at mid-rapidity, the SSD detector material amounts to ~1% radiation length. Although the SSD is not discussed further in the main body of this write-up, its projected performance has been included and used in the simulations described below. The SSD is described in more detail in Appendix I – The Silicon Strip Detector (SSD).

The IST is a strip detector that is designed to match the high resolution of the PIXEL detector with the courser resolution of the TPC and the SSD. The IST sits inside the SSD. In order to provide the required graded resolution between the SSD and the PIXEL layers, two high rate conventional silicon barrel layers will be installed at radii of 17 cm (IST2) and 12 cm (IST1). The IST layers provide space-points in the z and r-ϕ directions, thereby reducing the number of possible candidate tracks that can be connected with hits on the outer layer of the PIXEL detector. This is particularly important in a high multiplicity environment.

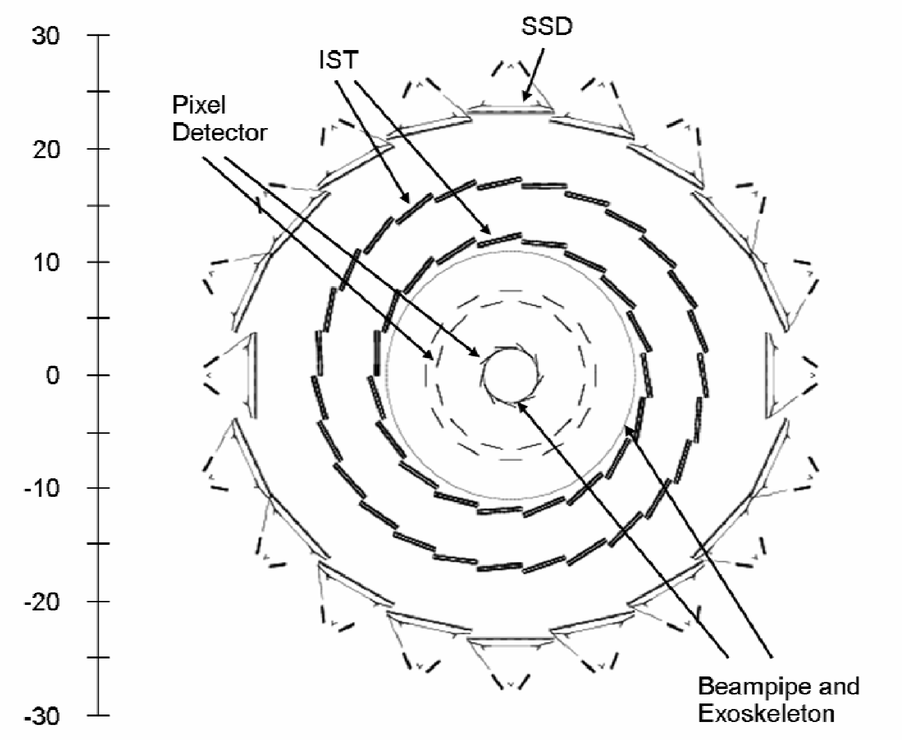

Figure 18: A schematic view of the Si detectors that surround the beam pipe. The SSD is an existing detector and it is the outmost detector shown in the diagram. The IST lies inside the SSD and the PIXEL lies closest to the beam pipe. The beam pipe and its exo-skeleton are also shown.

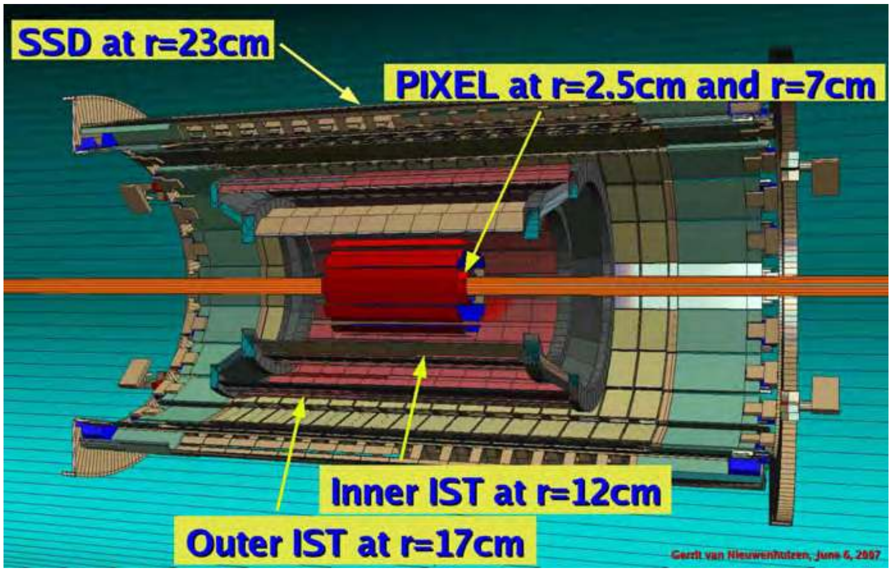

Figure 19: An oblique view of the proposed geometry for the STAR mid-rapidity tracking upgrade. From the outer to the inner radius, the detectors are the SSD (brown), the two IST layers (pink and brown), the two PIXEL layers (red), and the beam pipe (orange).

Each of the IST layers will be assembled from ladders. The outer layer lies at a radius of 17 cm, and consists of 27 ladders of 52 cm length. The inner layer, at a radius of 12 cm, consists of 19 ladders of 40 cm length. These and the other parameters for the IST are shown in Table 3. The ladders will carry commercially available 300 μm thick, 4 cm long, single-sided silicon strip sensors mounted on high thermal conductivity carbon-type material as a core and 100 μm Kapton hybrids. The detector material budget is ~0.75% radiation length for the inner and ~1.5% radiation length for the outer layer, including hybrids, ladder material, and the support structure.

The IST uses 60 μm × 4.0 cm strips in the outer layer and 60 μm × 2.0 cm strips in the inner layer. The resolution of each strip is assumed to be 1/√12 times the width of the strip, or about 17 μm. Two layers of single-sided strip detectors on the outer barrel of the IST are crossed by 90 degrees to give good resolution in the z direction and in the r-ϕ direction. The strips on the inner layer are oriented to give the best resolution in the r-ϕ direction.

Total number of strips/channels	692,480
Number of barrels	2
Number of ladders	46
Outer barrel (27 ladders)	r = 17 cm
Inner barrel (19 ladders)	r = 12 cm
Detector module active area	4 cm × 4 cm
Thickness (outer)	1.5 % X_0
Thickness (inner)	0.75 % X_0
Strip dimension (outer)	60 μm × 4 cm
Orientation of strips (outer)	best resolution in z and r-ϕ
Strip dimension (inner)	60 μm × 2 cm
Orientation of strips (inner)	best resolution in r-ϕ
Resolution of one strip	17 μm
Pseudo-rapidity coverage	± 1.2 units

Table 3: Selected parameters for the IST. These parameters were used in the simulation of the physics performance of the system.

The PIXEL detector is a low mass detector that will be located very close to the beam pipe. It will be built with two layers of silicon pixel detectors: one layer at 2.5 cm average radius and the other at 7.0 cm average radius. The outer layer will have 24 ladders and the inner layer will have 9 ladders; for a total of 33. Each ladder contains a row of 10 monolithic CMOS detector chips and each ladder has an active area of 19.2 cm × 1.92 cm. The CMOS chips contain a 640 × 640 array of 30 μm square pixels and will be thinned down to a thickness of 50 μm to minimize Multiple Coulomb Scattering (MCS) in the detector. The effective thickness of each ladder is 0.28% of a radiation length. See Table 4.

The PIXEL detector will achieve maximum vertex resolution by lying as close as possible to the interaction point without residing inside the RHIC beam pipe. But to locate the detector at 2.5 cm radius will require a new, and smaller, beam pipe. This new design also presents us with the opportunity to make the beam pipe thinner (0.5 mm). The new Be beam pipe, which will reduce the MCS scattering that occurs in front of the HFT, is an essential part of the proposal and its design will be discussed in Section 6.2.

Number of pixels	135,168,000
Pixel dimension	30 μm × 30 μm
Resolution of one pixel	9 μm
Detector chip active area	19.2 mm × 19.2 mm
Detector chip pixel array	640 × 640
Number of ladders	33
Ladder active area	192 mm × 19.2 mm
Number of barrels	2
Outer barrel (24 ladders)	r = 7.0 cm
Inner barrel (9 ladders)	r = 2.5 cm
Frame read time	0.2 msec
Pseudo-rapidity coverage	± 1.2 units
Thickness: Si on ladder (w/Al cable)	0.28 % X_0
Beam pipe thickness	0.5 mm or 0.14 % X_0

Table 4: Selected parameters for the PIXEL detector. These parameters were used in the simulation of the physics performance of the system.

3.3 A Simple Estimate of Detector Performance

A great deal can be learned about the detector by using a pocket-formula. The goal is to design a very high resolution tracking detector that is limited only by the multiple Coulomb scattering (MCS) in the various detector layers. Assuming an outside-in tracking algorithm, the pointing resolution of the HFT is determined by the layers of the PIXEL detector and the ultimate resolution does not depend strongly on the IST, SSD, or TPC. These other detectors are needed to associate the PIXEL detector hits with a projected track in a high hit-density environment, and do it with high efficiency, but otherwise these detectors do not play a large role in determining the pointing accuracy of the HFT. In fact, in an MCS limited system, the pointing resolution at any point along a track can be estimated by knowing the resolution and MCS from the previous two layers of tracking detectors.

The single track pointing resolution for a two layer detector telescope has three terms which are shown in Equation 1. The first two terms represent the pointing accuracy associated with the detector position resolution. The third term represents the error due to the MCS in the layer closest to the target.

Thus:

$$(1) \qquad \sigma^2 = \frac{\sigma_1^2\, r_2^2 + \sigma_2^2\, r_1^2}{\left(r_2 - r_1\right)^2} + \frac{\theta_{mcs}^2\, r_1^2}{\sin^2(\theta)} ,$$

where r_1 and r_2 are the radii of the two detectors, σ_1 and σ_2 are the resolution of the detectors, θ is the tilt angle of the track with respect to the detector, and θ_{mcs} is the width of the multiple Coulomb scattering angular distribution in the first layer of the tracker (corresponding to r_1, the inner layer).

θ_{mcs} is momentum dependent and is given approximately by

$$(2) \qquad \theta_{mcs} = \frac{13.6\,(MeV/c)}{\beta\ \ p}\sqrt{\frac{x}{X_0}} ,$$

where the thickness of the detector is measured in radiation lengths, *p* is the particle momentum, and $\beta = p/E$. So, for example, the multiple scattering width at 750 MeV/c for a kaon passing through a 0.28% thick Si detector is ~1.2 mrad. This is a useful number because it represents the MCS for the average kaon from $D^0 \rightarrow K^- + \pi^+$ decay. It is precisely these kaons that must be tracked with high precision in the PIXEL detector.

Using these formulae and the parameters in Table 4, we can estimate the pointing resolution of the PIXEL detector. Not including multiple Coulomb scattering in the beam pipe, the predicted resolution of the detector will be approximately 30 μm for 750 MeV/c kaons. A more complete prediction is shown in Figure 20. Once again, the point of reference is 750 MeV/c because this represents the mean momentum of a kaon from the decay of a D^0. The calculations shown in the figure are for 'straight up tracks', meaning that the tilt angle of the track is perpendicular to the surface of the detector.

It is worth noting that the resolution of each pixel is so high (~9 μm) that the predicted pointing resolution of the detector is dominated by MCS and is not determined by the individual pixel resolution. Thus, the pointing resolution of the detector is not sensitive to modest changes in the radial location of the Si layers or the resolution of each pixel.

It is possible to simulate the performance of the full TPC+SSD+IST+HFT system by iterative application of equations [1] and [2], but it is tedious. Billoir developed a better technique.[94] The essential ingredients of Billoir's method are shown schematically in Figure 21. Consider a series of detector elements with finite resolution and a finite thickness for Multiple Coulomb Scattering in each element. Billoir introduces a 5×5 information matrix that represents MCS in a layer of the detector, and another matrix for a measurement with resolution σ at the given layer, and finally a matrix to represent the propagation of a particle over the distance between two layers.

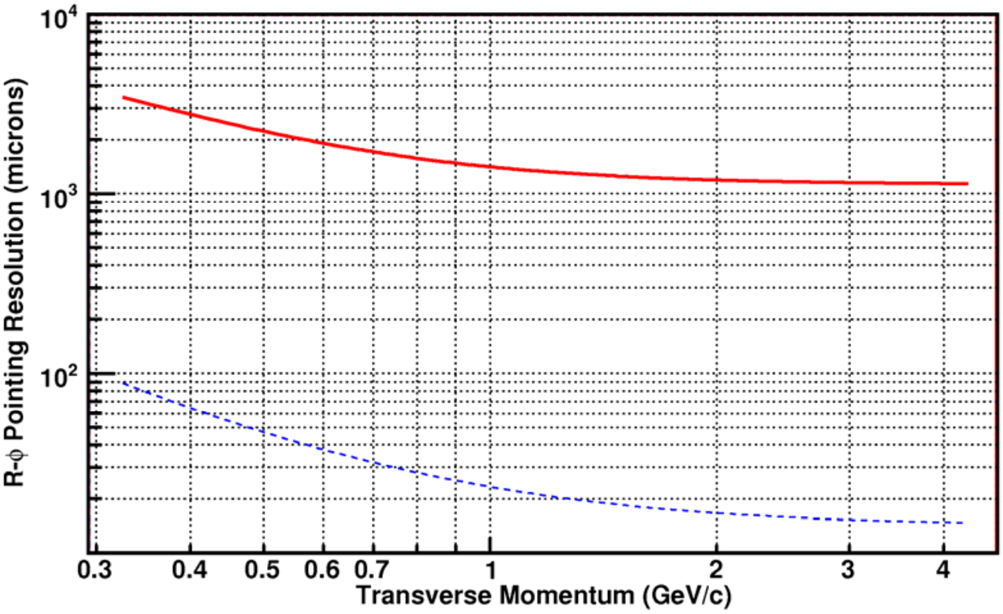

Figure 20: The dotted blue line shows the predicted resolution for tracking kaons in the PIXEL detector as a function of p_T based on equations (1) and (2). The beam pipe is not included in these calculations and the tracks are assumed to travel perpendicularly to the detector layers. The pointing resolution of the TPC at the vertex, acting alone, is shown for comparison in red. The purpose of the SSD and the IST detectors is to provide graded resolution between the TPC and the PIXEL detector.

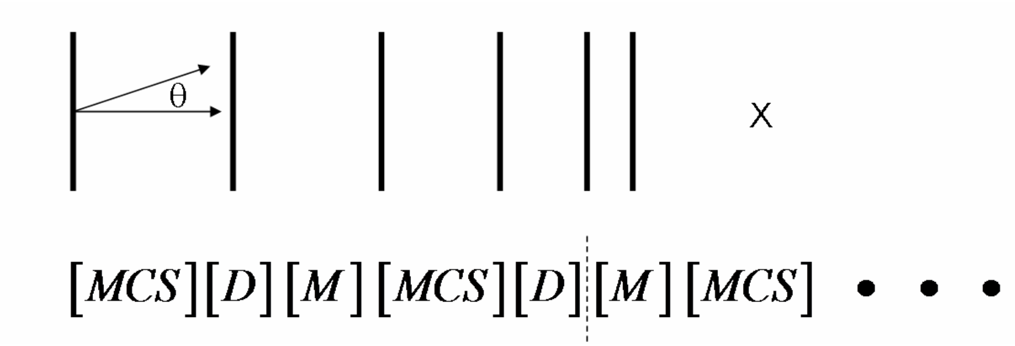

Figure 21: Billoir's method uses a recursion relation among information matrices; three matrices for each active layer in a detector system. The 'x' marks the vertex position in a hypothetical collider detector and we assume outside-in tracking (left to right). The recursion relation follows the track of a particle from the outside of the detector – in towards the vertex. [MCS] represents the recursion relation acting upon the multiple Coulomb scattering matrix, [D] represents propagation between two layers, and [M] represents the measurement at a layer with resolution σ.

The performance of a particular detector system can be calculated by applying a recursion relation among the matrices for each layer. After many non-commutative matrix operations, the result is applied to a basis state vector describing a particle traveling through space with finite momentum. Symbolically, the procedure looks like beam transport dynamics, but of course, it is different.

Billoir's method of matrices is a Kalman Filter[95] and, in fact, it is the Kalman Filter that is implemented in the STAR tracking software. The only difference between the 'hand calculations' presented in Figure 20 and Figure 22 and the automated results delivered by the STAR tracking software is that the hand calculations track a particle from the outside – in. The STAR reconstruction software tracks a particle from the outside – in *and* from the inside – out, and finally averages the results of the two calculations.

Billoir's method is nearly exact. The only significant approximation that is made is that the method assumes that the magnetic field is constant between two layers. This is not a limitation because in STAR's case the magnetic field is uniform everywhere and, in the more general case, the method can still be used by introducing pseudo-layers frequently enough to accommodate a changing magnetic field.

An interesting comment on this procedure revolves around the fact that matrix multiplication is not commutative. It is necessary to stop Billoir's recursion relation at the appropriate point because the procedure does not allow you to back-up along a track. So for example, to know the pointing resolution at a particular detector element (the target), we should apply the recursion relation to the appropriate matrices but stop after applying the D matrix that represents transport to the target layer. As illustrated in Figure 21, the calculation should stop at the dashed line if, for example, we are interested in knowing the pointing resolution on the third detector layer from the left. (If we apply the recursion relation to the measurement matrix (M) at the third layer, then we will only learn about the measurement resolution of the third layer rather than the pointing resolution to it.)

Using these tools we can simulate the HFT as it is embedded in the STAR detector. Typical results are shown in Figure 22. The calculations underlying Figure 22 include the 45 rows of the TPC, its inner field cage (a source of MCS), the SSD, the IST, the PIXEL detector layers and the beam pipe. The solid blue line represents the pointing resolution of the full system at the vertex. The dashed blue line is the same line shown in Figure 20 and it represents the theoretical limit of the pointing resolution for a two layer pixel detector without other elements such as the beam pipe to induce extra multiple Coulomb scattering. We can clearly see the effect of the beam pipe below 2 GeV/c. Above 2 GeV/c, an interesting thing happens: the track inside the TPC is long so that it provides a very tight angular constraint and it exceeds the angular resolution constraints imposed by the PIXEL detector at high p_T even though the PIXEL detector has 30 μm elements. This is only visible at high p_T when MCS is small and no longer dominates the resolution calculations in the PIXEL detector.

The red line in Figure 22 represents the pointing resolution of the TPC acting alone, at the vertex. Obviously, the pointing resolution of the TPC is not sufficient to find hits on a detector close to the vertex that is segmented into 30 μm pixels. Intermediate tracking layers with graded resolution between the TPC and the PIXEL detector are required in order to enable the association of tracks found in the TPC with hits on the PIXEL detector. That is precisely why we must use additional layers of tracking between the TPC and the PIXEL detector. The number of intermediate layers, and the required resolution of each layer, is a function of the anticipated hit density on the pixel detectors and the number of events piled-up in a single PIXEL detector readout cycle.

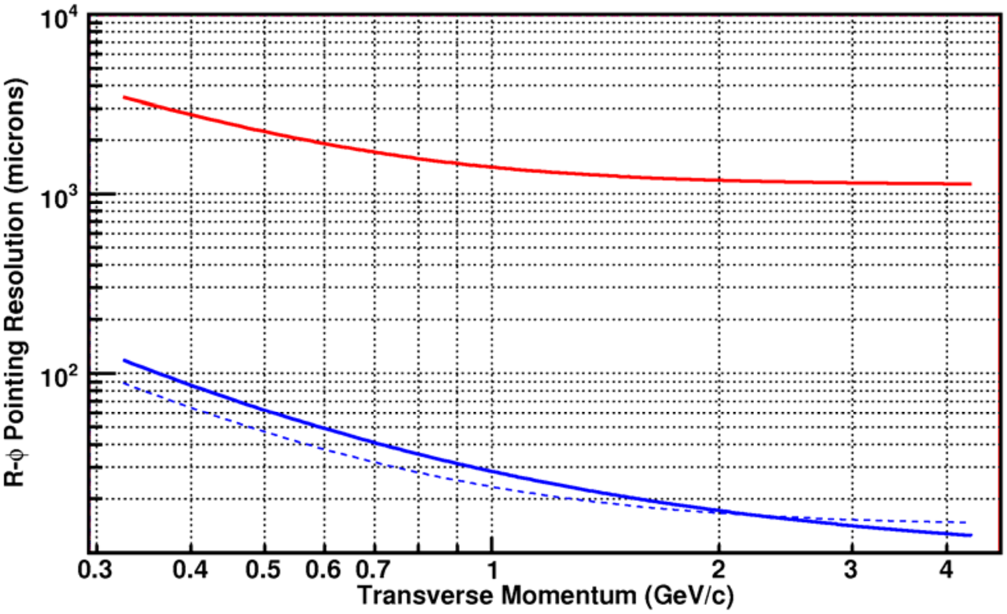

Figure 22: Billoir's method is used to calculate 'by hand' the pointing resolution at the vertex by the TPC+SSD+IST+PIXEL detectors (solid blue line). The agreement between the hand calculations and the ideal case is very good. The dashed blue line is the same idealized performance line shown in the previous figure. The pointing resolution of the TPC (red), acting alone, is also shown as a reference.

Table 5 shows the pointing resolution of the TPC+SSD+IST+PIXEL detectors at intermediate points along the path of a kaon as it is tracked from the outside going in. These calculations were done using Billoir's method and the quoted resolutions are for √[(r-ϕ resolution) + (z resolution)] when the r-ϕ and z resolutions can be different.

Graded Resolution from the Outside - In		Resolution(σ)
TPC pointing at the SSD	(23 cm radius)	~ 1 mm
SSD pointing at IST-2	(17 cm radius)	~ 330 μm
IST-2 pointing at IST-1	(12 cm radius)	~ 225 μm
IST-1 pointing at PIXEL-2	(7 cm radius)	~ 200 μm
PIXEL-2 pointing at PIXEL-1	(2.5 cm radius)	~ 70 μm
PIXEL-1 pointing at the vertex		~ 40 μm

Table 5: The calculated pointing resolution of the TPC+SSD+IST+PIXEL detector at intermediate points along the path of a 750 MeV kaon as it is tracked from the outside – in. The intermediate pointing resolution is used to resolve ambiguous hits on the next layer of the tracking system.

A more detailed look at the resolution of the system is shown in Figure 23. The top panel shows the r-ϕ pointing resolution and the bottom panel shows the z pointing resolution at different places in the system. The beam pipe is included in the calculations. Due to the different geometry of the detectors, the r-ϕ and z resolutions are different in different places but, typically, the average pointing resolution improves for layers at smaller radii.

The red line (top) in Figure 23 shows the pointing resolution of the TPC (acting alone) at the vertex, while the black line shows the pointing resolution of the TPC onto the SSD. The pointing resolution onto the SSD is better because the SSD is closer to the TPC than the vertex.

The remainder of Figure 23 is devoted to showing the pointing resolution of the system at each layer of the system. A detailed examination of the figure shows an alternating pattern of improvement in the resolution of the system of proposed detectors. For example, the SSD detector has an asymmetric resolution of approximately 27 μm in the r-ϕ direction and 750 μm in the Z direction. The resolution of the TPC+SSD pointing at IST2 is shown by the green line in the figures. The r-ϕ and z resolution are also different for the proposed IST detectors; so for example, IST2 has a resolution of approximately 11,500 μm in the r-ϕ direction and 17 μm in the z direction. The yellow line in the figures shows the resolution that can be achieved by the TPC+SSD+IST2 pointing at IST1 and, because of the underlying characteristics of each detector, the ordering of the yellow and green lines are reversed in the two panels of the figure. The same story plays itself out for IST1 (magenta line), but the figure returns to a simply ordered pattern with the addition of the PIXEL layers because these detectors are symmetric systems with 9 μm resolution in both directions.

The red line and the dashed blue lines are shown for reference and are duplicated from the previous figures. Additional details are included in the figure caption.

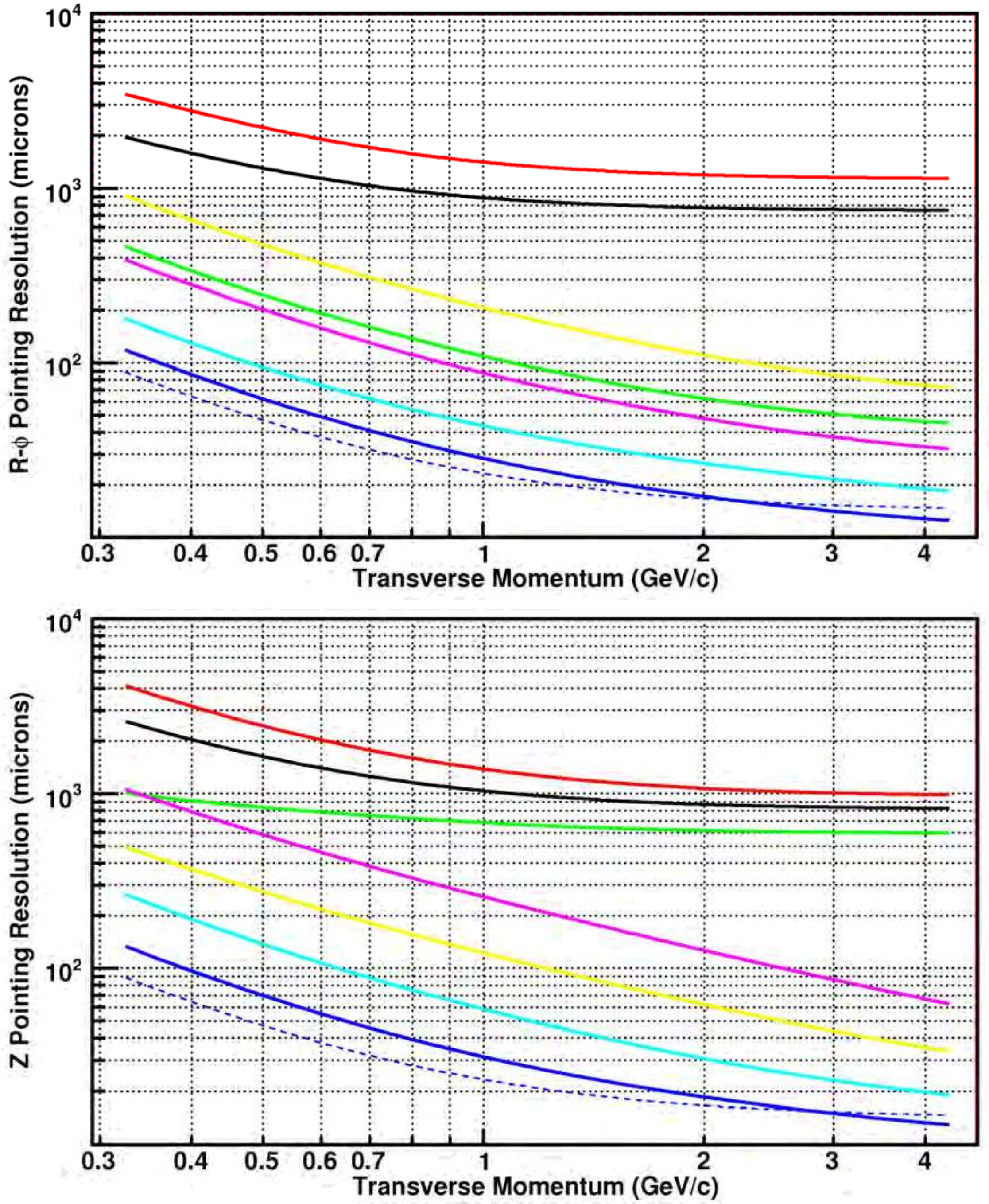

Figure 23: The pointing resolution of each element of the HFT detector system (σ); where the r-ϕ and z pointing resolutions are plotted separately (top and bottom, respectively). The calculations assume a kaon passing through the system. Data at 750 MeV/c is a useful line of reference to guide the eye. The pointing resolution of the TPC onto the vertex is shown by the red line. The pointing resolution of the TPC onto the SSD is shown by the black line. The TPC+SSD pointing at IST2 is shown in green. The TPC+SSD+IST2 pointing at IST1 is yellow, TPC+SSD+IST2+IST1 pointing at PIXEL2 is magenta, TPC+SSD+IST2+IST1+PIXEL2 pointing at PIXEL1 is cyan, and the full system TPC+SSD+IST2+IST1+PIXEL2+PIXEL1 pointing at the vertex is blue. The blue dashed line is the idealized HFT performance from Equation 1; without beam pipe or other sources of MCS.

3.3.1 Comparison of the 'Hand Calculations' and GEANT Simulations

Billoir's method, as applied by STAR, is what we call the 'Toy Model' in Figure 24. The Toy Model is a very fast method to optimize a new detector configuration. However, the method includes several assumptions that should be checked to ensure that the results are reliable. We have cross-checked many of its predictions with GEANT simulations. The pointing resolution predicted by the Toy Model, another simplified tracking simulation called the 'Toy Simulation' and the primary STAR GEANT simulation are compared in Figure 24.

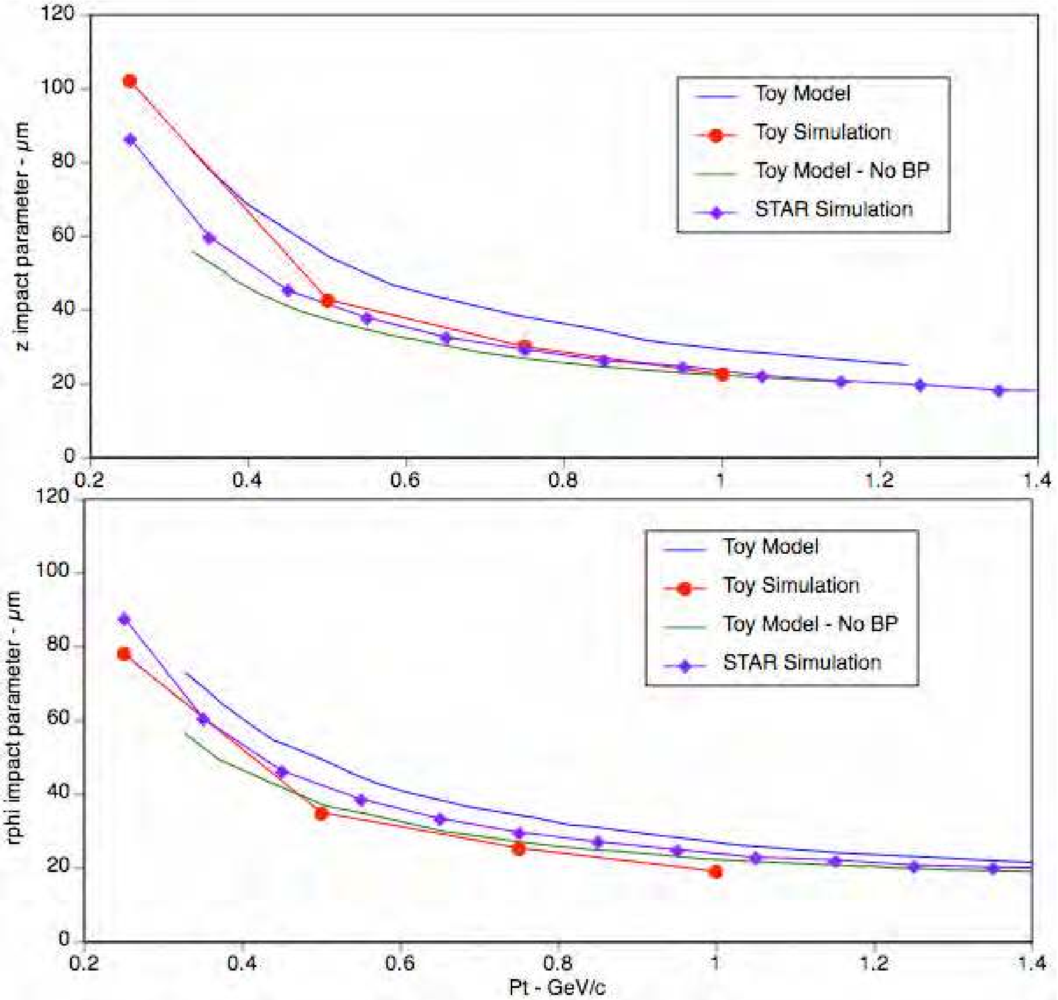

Figure 24: Comparison of three different types of simulations to determine the pointing resolution at the vertex. The three methods are the Toy Model, a Toy Simulation, and the full STAR Simulation. Each method has different assumptions and slightly different parameters but overall, the agreement is good. In the figure's legend, BP is short hand for "beam pipe".

The ‘Toy Simulation’ consists of a simple analysis of GEANT data. Muon tracks were generated by GEANT, at various p_T bins, from the center of the detector. Tracks were digitized using the GEANT hits and then an estimate of the resolution of each detector was used to smear the hits. Tracks were then selected which had at least 15 TPC hits and no less than a total of two IST and SSD hits. Using a simple track finding algorithm, the momentum was calculated and then used to project the track from the two PIXEL hits back to the event vertex. These two hits and the measured momentum were used to calculate the distance of closest approach at the vertex.

The ‘STAR Simulation’ used the same GEANT hit generation method but now with the full STAR analysis package. In this case, central events provided the tracks. Pion tracks were required to have at least 15 TPC hits, but there was no requirement for the other HFT detectors. Using these reconstructed tracks, the distance of closest approach to the GEANT vertex was determined for different p_T bins.

Results from all three methods can be viewed in Figure 24. The figure shows remarkable similarity between all three calculations. Because each method has slightly different assumptions, the small systematic differences are expected. The fact that the STAR simulation agrees with the Toy simulation and the Toy model demonstrates that the full pointing ability of the HFT arises from the two pixel layers. Also, there is no significant difference in pointing resolution for Central and isolated tracks. Because of the close agreement for each of the approaches shown by these and other simulations, we are comfortable with the idea that they can be used to predict the performance of the HFT.

3.3.2 Comparison of the ‘Hand Calculations’ and a Real Detector

The STAR Silicon Vertex Tracker (SVT) is a detector in STAR that been recently retired. However, its design and performance is well understood and thus we can compare the measured performance of the detector to the predictions of the hand calculations in order to test the quality of the predictions. The parameters for the SVT, based on as-built drawings and real data, are shown in Table 6.

Number of barrels	3
Outer barrel (16 ladders)	r = 14.7 cm
Middle barrel (12 ladders)	r = 11.0 cm
Inner barrel (8 ladders)	r = 6.9 cm
Thickness (outer)	1.75 % X_0
Thickness (middle)	1.75 % X_0
Thickness (inner)	1.0 % X_0
Resolution in the r-ϕ direction	50 µm
Resolution in the z direction	40 µm
Be Beam Pipe (4 cm radius)	0.28 % X_0

Table 6: Selected parameters for the SVT. These parameters were used in the simulation of the SVT based on the measured performance of the system in-situ at STAR.

The predicted performance of the SVT detector system is shown in Figure 25 and Figure 26. The system is MCS limited, so even though the detector resolution on each layer is 50 µm in the r-ϕ direction and 40 µm in the z direction, the pointing resolution at the vertex is worse than these numbers might suggest. At 750 MeV/c, the pointing resolution is predicted to be about 200 µm in the r-ϕ and in the z direction.

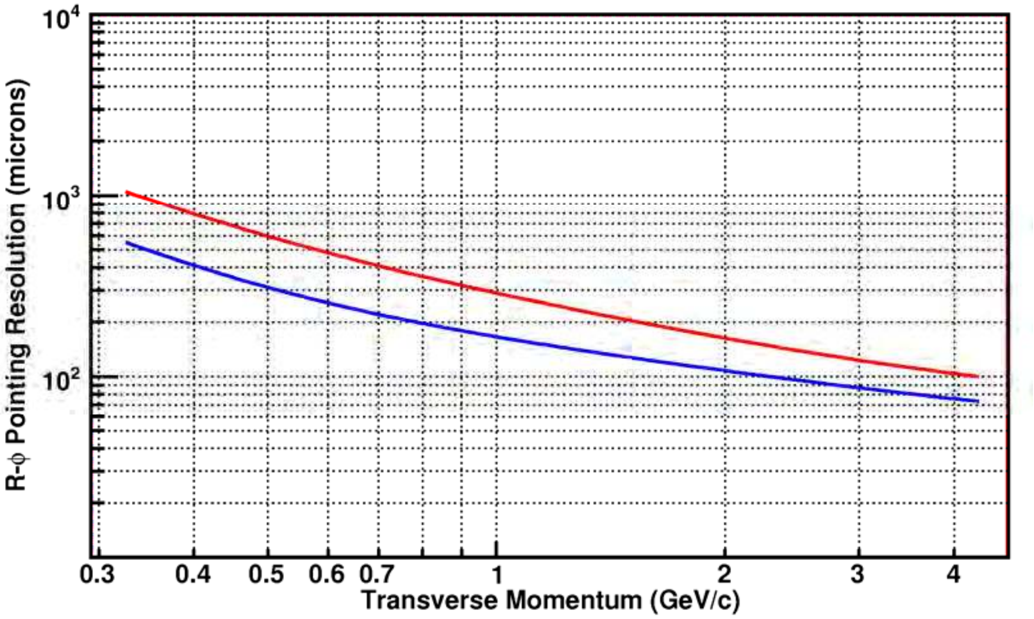

Figure 25: The predicted pointing resolution of the TPC+SSD+SVT at the vertex in the r-ϕ direction. The blue line shows the pointing resolution for all three SVT layers. The red line shows the effective resolution if the first layer of the detector is not hit and only layers 2 and 3 have hits.

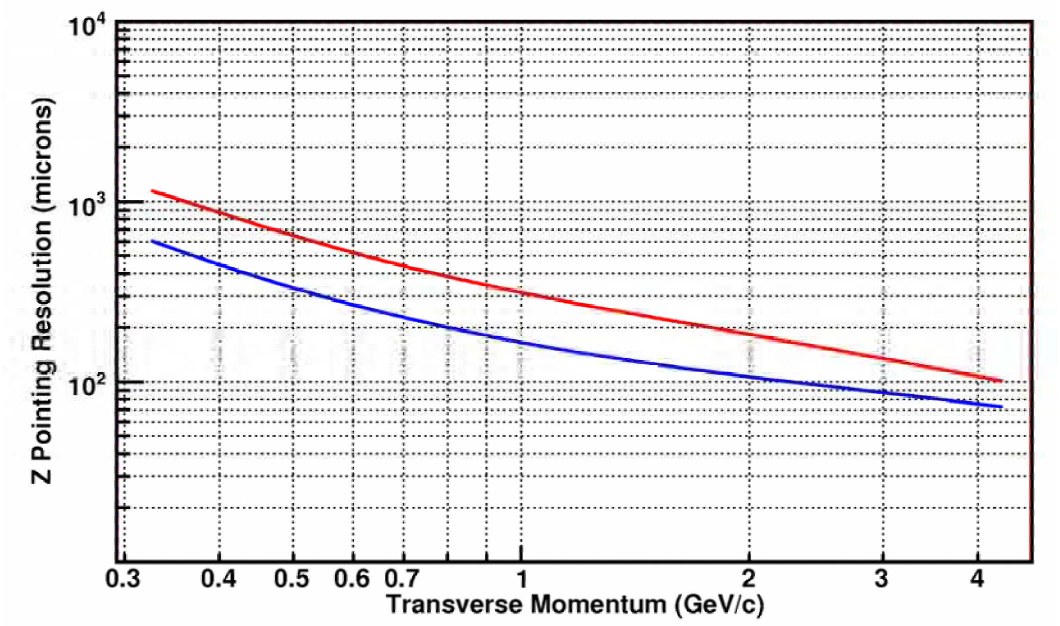

Figure 26: The predicted pointing resolution of the TPC+SSD+SVT at the vertex in the z direction.

This is in very good agreement with the measured performance of the detector in-situ at STAR which is 200 μm at 1 GeV/c. It also means that it should be possible to find D^0s with the SVT, but the software reconstruction efficiency is not expected to be very high due to the relatively poor pointing resolution that is supposed to pick out a non-vertex decay with $c\tau \approx 125$ microns.

3.4 Hit Density at the Front Surface of the PIXEL Detector

Table 5 and Figure 23 illustrate the need for intermediate tracking detectors and how they help pick out the correct hit on the PIXEL detector to be associated with the tracks from the TPC. Once the correct hit is found on the PIXEL detector, the intermediate tracking detectors have completed their mission. But extending the TPC tracks in towards the vertex will turn out to be a difficult problem because the PIXEL layers are close to the interaction vertex and they suffer a significant density of hits in central Au+Au collisions. A TPC track can easily point at several hits on the PIXEL layers that lie within the pointing accuracy of the TPC (acting alone). If the association is done incorrectly, the track is corrupted and becomes part of the background noise that must be eliminated by other means in the physics analysis (such as combinatorial background subtraction). Before considering this problem further, let us explore the hit density on the front surface of the PIXEL detectors to see how difficult it can be to associate hits with tracks.

All of the detector elements in the HFT experience a high multiplicity of hits, per event, but the PIXEL layers experience the highest hit densities because they lie closest to the vertex. Also, the PIXEL detector is not a triggered device but rather is continually active for a fixed period of time (the frame readout rate) and therefore records all particles that pass through it during its readout time. This means that in tracking the events of interest there will be extraneous hits and pileup in the detector due to other collisions at earlier or later times, tracks from beam gas showers, in addition to hits from other background sources. The real density of extraneous hits that can be tolerated will depend on the pointing accuracy of the tracking system and how precisely tracks can be projected onto the PIXEL detector from the TPC+SSD+IST as well as on the details of the track reconstruction algorithms. The hit density on the PIXEL detector also depends on the frame readout rate, the beam luminosity, the interaction cross sections and background rates from outside sources.

To start the discussion, consider the sources for the tracks that enter a detector. The number of tracks passing through a detector is a sum of several terms:

$$\frac{dN}{dA} = \textit{Central Collision Rate} + \textit{Integrated MinBias} + \textit{UPC electrons} + \textit{Background}$$

Let's consider the terms listed in this equation, beginning with the Central Collision Rate. A central Au+Au collision has a multiplicity of about 700 charged particles per unit of pseudo-rapidity. The density of hits on the detector can be calculated by translating dN/dη into the flat space of the detector.[96]

$$\frac{dN}{dz} = \frac{dN}{d\eta} \times \frac{d\eta}{dz} \qquad \text{where} \qquad \frac{d\eta}{dz}(r,z) = \frac{1}{\sqrt{r^2+z^2}}$$

So for a central event centered under the PIXEL detector, the hit density on the front face of the detector (z = 0 and 2.5 cm radius) is:

$$\frac{dN}{dA}(Central) = \frac{dN}{dz} \times \frac{1}{2\pi r} = \frac{700}{2\pi r^2} = 17.8\, cm^{-2}$$

The parameters assumed for these calculations are shown in Table 7.

Au+Au Luminosity (RHIC-II)	80 x 10^{26} $cm^{-2}s^{-1}$
dn/dη (Central)	700
dn/dη (MinBias)	170
MinBias cross section	10 barns
MinBias collision rate (RHIC-II)	80 kHz
Interaction diamond size, σ	15 cm
Integration time for Pixel Chips	200 μsec

Table 7: Luminosity and other RHIC II parameters that determine the particle flux on the HFT. The minbias hadronic cross-section for Au-Au collisions at RHIC is 7.0 barns. We have used the

total cross-section, including photo-dissociation, in order to be conservatively on the high side for rate calculations and detector simulations.

The central collision hit densities for all of the detectors in the HFT system are shown in Table 8. The simple formula described above is in good agreement with the hit densities thrown by HIJING and propagated by GEANT through a realistic description of the HFT. The reasons for agreement are both interesting and complex, but essentially the idea is that low p_T particles which have a radius of curvature that is too small to reach the next detector layer are (coincidentally) replaced by the additional particles that are produced by weak decays and hadronic interactions in the material of the different detector layers. Thus, the flux of particles through the PIXEL, IST, and SSD detectors is nearly constant.

The PIXEL detector uses Si chips that have a finite integration time (200 μsec) so we must add a contribution from the integrated minimum-bias collision events to the central collision densities shown in Table 8. We call these events minimum-bias 'pileup'. We should also include the hit density due to Ultra Peripheral Collisions (UPC) and other background rates.

	Radius	Simple Formula $\lvert\eta\rvert = 0$	Monte Carlo $\lvert\eta\rvert < 0.2$	Monte Carlo $\lvert\eta\rvert < 1.0$
PIXEL1	2.5 cm	17.8 cm^{-2}	19.0 cm^{-2}	15.0 cm^{-2}
PIXEL2	7.0 cm	2.3 cm^{-2}	2.4 cm^{-2}	2.0 cm^{-2}
IST-1	12.0 cm	0.77 cm^{-2}	0.88 cm^{-2}	0.69 cm^{-2}
IST-2	17.0 cm	0.38 cm^{-2}	0.43 cm^{-2}	0.34 cm^{-2}
SSD	23.0 cm	0.21 cm^{-2}	0.23 cm^{-2}	0.19 cm^{-2}

Table 8: The density of hits on each layer of the HFT and SSD from one central Au+Au collision.

The integrated minimum-bias hit density on the PIXEL detector is, in fact, larger than the central collision hit density. One compensating factor is that the minimum-bias events come from all over the interaction diamond vertex and so not all of them lie directly under the detector. The average rate can be calculated by integrating over the Gaussian shape of the diamond and multiplying by the number of minimum-bias collisions that occur during the integration time of the detector.

So, for example:[96]

$$\frac{dN}{dA}(MinBias, z, r, \sigma) \quad = \quad \frac{dN}{d\eta} \times \frac{1}{2\pi\, r} \times ZDC \times \tau \times \int_{-a}^{a} \frac{1}{\sqrt{2\pi}\,\sigma}\; e^{\frac{-z_0^2}{2\sigma^2}}\; \frac{d\eta}{d(z - z_0)}\; dz_0 \ ,$$

where ZDC rate is the number of minimum-bias collisions per second, τ is the integration time of the PIXEL detector, and *a* is a practical limit on the extent of the interaction diamond along the z axis. The ZDC minimum-bias interaction rate for RHIC II luminosities will be 80 kHz and the integration time for the detector discussed in this proposal is 200 µsec (see Table 7).

Reducing this equation yields:

$$\frac{dN}{dA}(MinBias, z, r, \sigma) \quad = \quad \frac{2720}{2\pi\, r} \times \int_{-a}^{a} \frac{1}{\sqrt{2\pi}\,\sigma}\; e^{\frac{-z_0^2}{2\sigma^2}}\; \frac{1}{\sqrt{r^2 + (z - z_0)^2}}\; dz_0 \ .$$

This integral is not easily evaluated by hand and so we quote the results achieved by numerical integration and tabulate them in Table 9. For example, the integrated yield of hits on the front face of the PIXEL detector is 23.5 hits per cm^2.

	PIXEL-1 Inner Layer	PIXEL-2 Outer Layer
Radius	2.5 cm	7.0 cm
Central collision hit density	17.8 cm^{-2}	2.3 cm^{-2}
Integrated MinBias collisions (pileup)	23.5 cm^{-2}	5.2 cm^{-2}
UPC electrons	19.9 cm^{-2}	0.8 cm^{-2}
Totals	**61.2 cm^{-2}**	**8.3 cm^{-2}**

Table 9: Integrated hit loading on the PIXEL detector and associated pileup in Au+Au collisions.

Ultra-Peripheral Collisions (UPC) are a copious source of low momentum electrons. They are created by the coherent interaction between the strong electromagnetic fields that occur when two nuclei ‘miss’ each other in an ultra-relativistic collision. The nuclei do not interact via the strong interaction, but they do interact electromagnetically (see Figure 27). A pair of virtual photons that are emitted by the colliding nuclei create the electrons and therefore the electrons have very low momenta and the momenta are determined (mostly) by the uncertainty principle. Since the characteristic radius of a Au nucleus is 7 fm, the characteristic transverse momentum for the electrons is 70 MeV/c or less. These electrons will enter the PIXEL detector and interact with it, leaving a hit in the detector. A precise calculation of the UPC electron spectrum is quite tedious and beyond the scope of this proposal; however, we will utilize the estimates provide by Hencken, Baur, and Trautmann.[97]

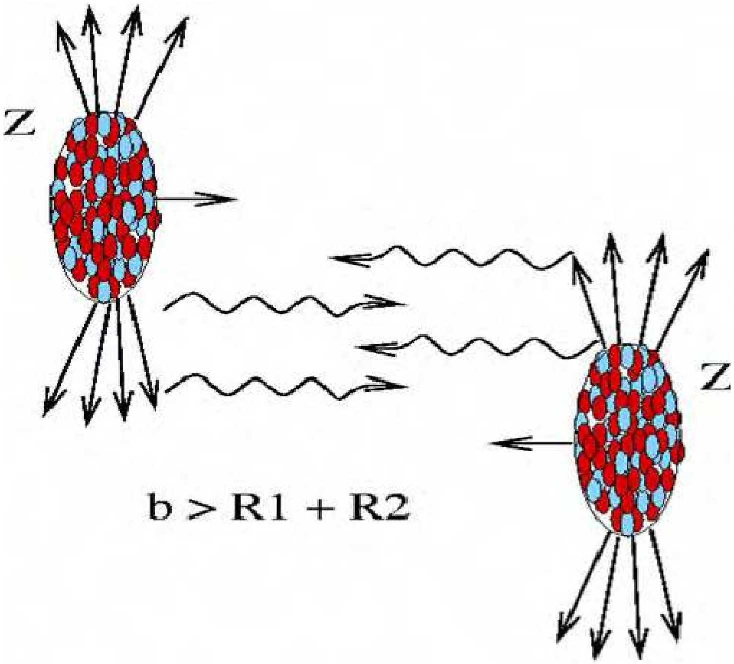

Figure 27: UPC electrons are created when nuclei 'miss' each other (geometrically) but still interact via long range fields that are generated by the highly Lorentz contracted nuclei at RHIC energies.

The abundance of UPC electrons is large and is approximately equal to the number of particles from minimum-bias hadronic collisions. However, due to the low momentum of the electrons, they do not extend to large radii inside the STAR detector and so we parameterize their abundance based on GEANT simulation files produced by Hencken et al. We assume that the UPC rate is equal to the integrated minimum-bias hadronic rate at 1.5 cm radius and drops to zero at 8 cm radius; and further we assume that the UPC electrons pileup in the PIXEL detector in a manner that scales with the integrated minimum-bias rate. The variation of the UPC rate with the radius is shown in Figure 28.

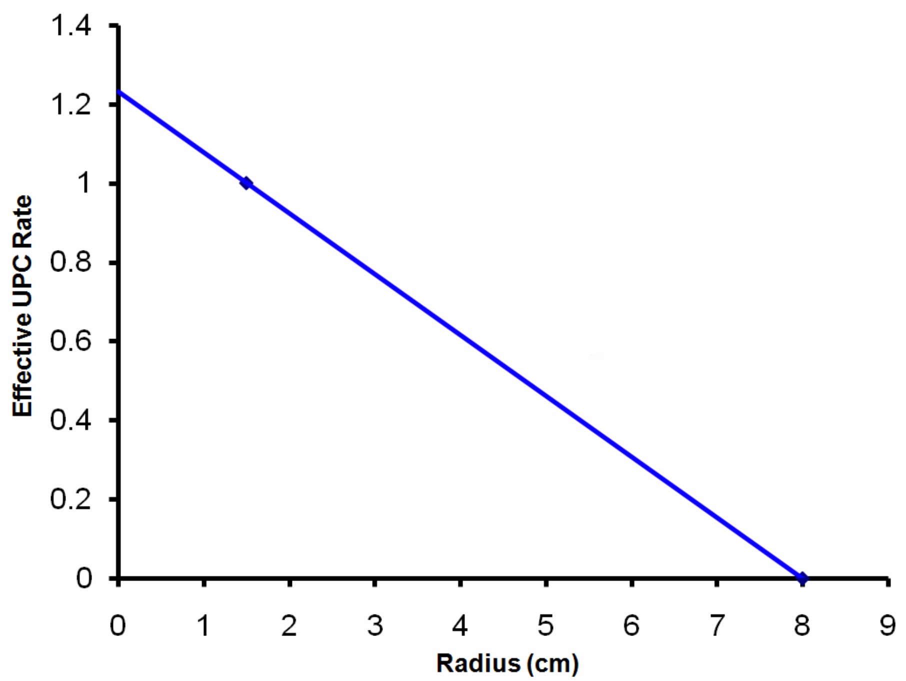

Figure 28: The assumed rate of UPC electrons at different radii. The vertical axis shows the effective multiplier; this rate is multiplied by the minimum-bias pileup rate to yield the total UPC hit density.

The IST and the SSD are fast detectors and they lie at relatively large radii. Therefore, they do not pileup multiple events from out-of-time minimum-bias collisions and they do not see the UPC electrons. Thus, we do not include the minimum-bias pileup nor the UPC electrons in the sample of particles that hit these fast detectors.

Finally, we should say a few words about the background rates in the STAR detector. We know that we see tracks in the TPC that are (probably) due to beam gas interactions that occur upstream of the STAR detector. The number of these tracks is typically equal to the number of global tracks in the TPC; hence doubling the load on the TPC. This rule of thumb may or may not apply at the small radius where the HFT lies. The background events that appear in the HFT are probably fewer in number than what appear in the TPC; however it is difficult to estimate this number due to the number of unknowns in how the background is produced in the STAR environment. Therefore, we have undertaken a vigorous program to measure the track densities near the interaction point using a prototype pixel detector to get a definitive answer to this question. Future simulation efforts will include the background rates measured in the STAR environment.

3.4.1 Track Finding and Efficiency in a High Multiplicity Environment

The primary goal of the SSD and the IST detectors is to provide hits on tracks at intermediate radii so that the track reconstruction software can follow a track from the

TPC to the PIXEL detector and correctly associate a hit on each PIXEL layer with the track. This is a challenging task because the transverse dimensions of the predicted track can be quite large, in relative terms, and there will be several candidate hits that can be associated with the track at each layer. However, only one is the right hit that will allow the track to be extended to the next layer in the tracking system and thus find the next good hit. In our previous discussions we focused on the hit densities on the PIXEL layers, however the ambiguities in associating hits with tracks exists in all of the Si layers of the system and the success of the system depends on the hit densities on each layer as well as the pointing resolution of the outer detectors onto each layer. We will discuss the errors and efficiency for making the correct hit associations, below.

The probability of correctly associating a hit with a track was recently reviewed by Howard Wieman, Gene Van Buren, and Victor Perevoztchikov[98,99,100]. The essential idea is that we have several hits on each layer of the detector. We also have a predicted track that has been projected onto the layer which needs to be associated with one of those hits. The probability of making the correct hit association is (using a weighted chi-square fit):

$$P(good) = \frac{1}{1+S} \qquad \text{where} \qquad S = 2\pi\,\sigma_x\,\sigma_y\,\rho$$

σ_x is the convolution of the detector resolution and the projected track error in the 'x' direction, σ_y is the convolution of the detector resolution and the projected track error in the 'y' direction, and ρ is the density of hits on the layer of interest.

With a minor rearrangement of terms, it is easy to show that:

$$P(bad) = \frac{S}{1+S} \qquad \text{and when S is small} \qquad P(bad) \approx 2\pi\,\sigma_x\,\sigma_y\,\rho$$

P(bad) is the probability that the wrong hit lies closer to the centroid of the predicted track than the correct hit and so it is a measure of the inefficiency of the system. This definition of inefficiency is intuitive and very appealing because the inefficiency is proportional to the number of ambiguous hits found inside an ellipse. The dimensions of ellipse are defined by the pointing resolution of the system up to that point, $\pi\,\sigma_x\,\sigma_y$, times the density of hits, ρ, times two. The not-so-obvious factor of two is related to the fact that Wieman et al. assume a Gaussian probability distribution for the track errors and these distributions extend to infinity.

σ_x and σ_y are Gaussian errors in two orthogonal dimensions. They are the errors that are incurred in making a measurement of the distance between the point where the predicted track intersects the detector and the location of a candidate-hit. σ_x and σ_y are a convolution of two other terms:

$$\sigma_x = \sqrt{\sigma_{xp}^2 + \sigma_{xd}^2} \qquad \text{and} \qquad \sigma_y = \sqrt{\sigma_{yp}^2 + \sigma_{yd}^2}$$

In this equation σ_{xd} is the resolution of the detector while σ_{xp} is the error in the location of the predicted track. Both variables are in the 'x' direction (see Figure 29).

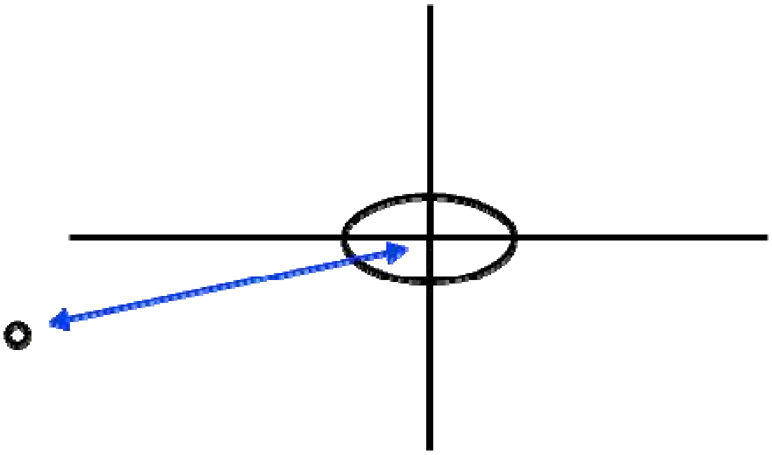

Figure 29: An illustration of how to associate a hit with a predicted track that has been projected on the detector from the outside; it is essential to measure the distance between the two in order to estimate the probability that the association is the correct one. After the association is made, the track will be refit and projected onto the next layer in the detector system. The small circle on the left is a representation of the hit; it has errors σ_{xd} and σ_{yd}. The large ellipse in the center of the diagram represents the projected track. It has errors σ_{xp} and σ_{yp}.

These calculations can be carried out, layer by layer in the HFT, from the TPC in towards the vertex in order to estimate the overall efficiency for correctly associating hits with tracks. If the association is correct at each point, then we have a good track. If the association is wrong, the track becomes a ghost track and is part of the background that has to be removed from the signal. The calculations are simple to execute, and intuitively obvious, when the errors are symmetric and the detector resolution is smaller than the projected track error. However, it gets complicated when the errors are asymmetric and the detector resolution is long in one dimension and the projected track error is long in the other. The cross terms result in lower detector efficiencies because the largest terms dominate in the quadrature sum.

3.4.2 The Efficiency of the HFT and its Sensitivity to Pileup

Figure 30 shows the calculated efficiency of the HFT detector using the tools outlined above. The calculations assume that the detector was exposed to central Au+Au collisions, but without pileup or other background tracks. The calculations include all of the existing and proposed detectors (i.e. TPC+SSD+IST2+IST1+PXL2+PXL1) and, in particular, the calculations assume a factor of 0.75 for the combined acceptance of the TPC and SSD. Thus the curves in Figure 30 cannot exceed the 75% mark, by definition.

The solid blue line in the figure is the single track efficiency for finding a kaon in the HFT. The efficiency at 750 MeV/c is a good figure of merit for a single track. The dashed blue line is the D^0 efficiency. In this case the efficiency at 1.3 GeV/c is the relevant figure of merit.

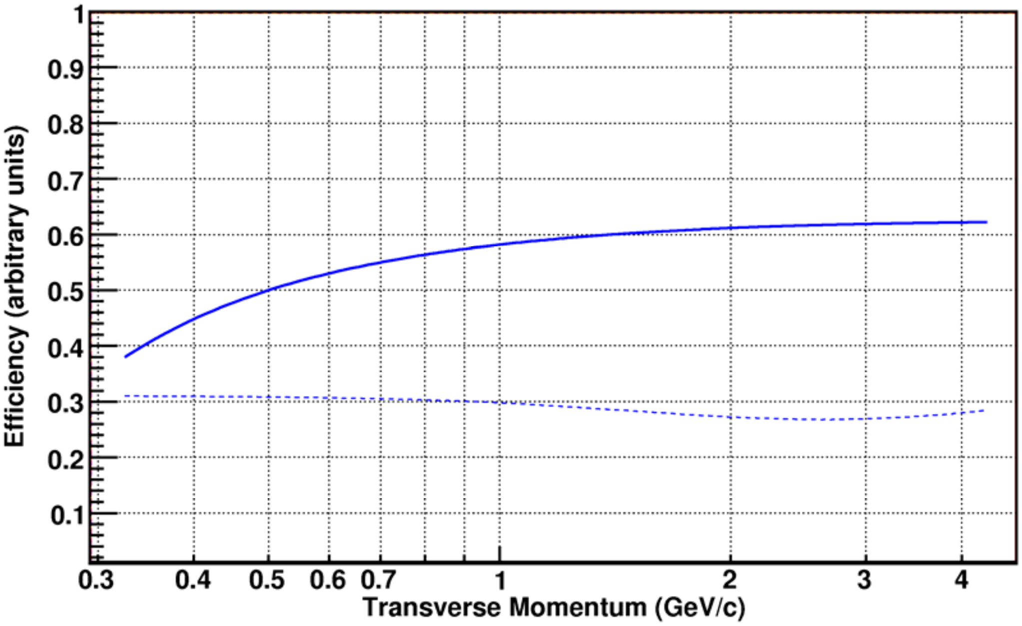

Figure 30: The predicted efficiency of the HFT detector is shown above. The solid blue line is the single track efficiency for finding kaons in the detector. The dashed blue line is the efficiency for finding the D^0 meson; the D^0 efficiency is derived from the single track efficiencies by integrating over the Lorentz kinematics of the two daughter particles.

The principle source of inefficiency in these calculations is IST2 because it suffers from a high number of ambiguous hits due to the 4 cm length of the strips ($\sigma \approx 1.15$ cm) in one dimension, and the asymmetric resolution of the SSD ($\sigma \approx 750$ μm) in the other. Using these numbers in the efficiency equations from the previous section, and using a density of hits equal to 0.38 per cm^2 an efficiency of 82% for the IST2 detector is obtained. This, combined with the assumed acceptance of the TPC+SSD, defines the upper bound on the single track efficiency shown in Figure 30.

The input parameters that underlie the calculations in Figure 30 are identical to the input parameters that have gone into the Monte Carlo simulations that will be presented in subsequent chapters of this proposal. As a result, the single track efficiencies shown in Figure 30 are comparable to the Monte Carlo results shown in Figure 32; and the D^0 efficiencies are comparable to the Monte Carlo results shown in Figure 37. The net result is that the single track efficiencies found by the hand calculations and the Monte Carlo methods are in reasonable agreement except at low p_T, while the D^0 reconstruction efficiencies differ by about a factor of two at all p_T. Due to the peculiarities of the Lorentz decay kinematics of the D^0 meson, the discrepancies between the D^0 efficiencies can be attributed to the differences between the single track efficiencies at low p_T and can be explained, in part, by the fact that the STAR reconstruction software does not yet produce track residuals that are comparable to the detector resolution at each layer. The track residuals and the detector resolutions often differ by a factor of two. Clearly more work is required, but we are confident that we are moving in the right direction.

Finally, in closing this section, it is worth noting that the PIXEL layers are operating at 99% efficiency in the example quoted above. Therefore, we do not expect minbias pileup to be a problem because doubling or tripling the density of hits on the PIXEL layers will only cause their efficiencies to drop to 97%, or so. Thus, the Monte Carlo results shown in the next section are probably a reasonable representation of the performance of the HFT even though we have not yet been able to include pileup and other backgrounds in the Monte Carlo simulations.

3.5 Monte Carlo Simulations for Au+Au Collisions at 200 GeV

The STAR experiment has an extensive simulation framework which can accurately predict the performance of the HFT detector. This framework involves several software packages working together to produce the final results. We will give a general overview of the simulation chain in order to place the results and predictions contained in this document in a broader context.

The philosophy of the HFT simulations is to use as much standard STAR software as possible. For instance, we use the standard STAR simulation package with modifications for the new beam pipe design and the introduction of the HFT to generate events, and for track reconstruction we use the newest STAR tracking software package.

The simulation framework has three stages:

1. The simulation of the physics under study: for example a central Au+Au interaction at $\sqrt{s} = 200$ GeV
2. The simulation of produced particles as they interact with the detector and physical structures of the experiment
3. The simulation and digitization of signals in the detector

The goal of the simulation software package is to use the same analysis methods on both the simulated and real data, and to predict the performance and optimize the design of the detector, as well as to optimize the methods for future data analysis.

A primary goal of the simulation effort will be to reproduce the signal to background characteristics that are to be expected in real data. However, we have not yet achieved that goal. All of the simulations presented in sections 3.5, 3.6 and 3.7 are for multiplicity densities that correspond to the primary track rate from central Au+Au collisions (0-3 fm impact parameter) at 200 GeV. Our simulations do not include UPC electrons, the minimum-bias event pileup due to the finite integration time of the PIXEL detector, nor other backgrounds. Since the efficiency for finding a D^0 in the HFT depends on the density of hits on these detectors, this may be a source of inefficiency that is not yet included in our simulations.

3.5.1 Physics Simulations

The simulations presented in this chapter focus on the reconstruction of the D^0 meson in an environment similar to what we expect to see in the real experiment. The background events for these studies were Au+Au central events created with the HIJING event generator.

The physical interaction between daughter particles and the material of the detector, as well as signal digitization, are simulated using the STAR implementation of the GEANT simulation package.[101] This package is used in STAR and is a standard analysis tool which includes a detailed understanding of the TPC response function; including dead areas and realistic detector resolutions and responses.

For both the SSD and HFT detectors, GEANT reports the exact crossing point of the particle through the detector to the track reconstruction software. Realistic detector resolutions are used to smear the perfect position information, and the resulting simulated hits are used in tracking. For the PIXEL detector, for example, the hits were smeared by 8.6 μm in both ϕ and z. We ignore the effects of cluster overlap in the PIXEL detector because we expect these effects to be relatively unimportant because the occupancy, even in a central Au+Au event, is very small on a per pixel basis.

3.5.2 Reconstruction

Reconstruction of the simulated events is handled by the usual framework implemented in STAR to unite the various tracking detectors. With the current STAR algorithm, the tracker follows a series of hits in the TPC and silicon detectors, and refits the track after every new hit is added. These tracks (called "global" tracks) are then passed to the vertex finder, which reconstructs the event vertex. The global tracks are extended to the resulting reconstructed vertex, and, if the fit is successful, the new track is stored and labeled as a primary track.

The efficiency of the track reconstruction package to find and correctly associate HFT hits is defined as

$$\varepsilon = \frac{Tracks(reconstructed)}{Tracks(MonteCarlo)}$$

where the reconstructed tracks are matched to their corresponding Monte Carlo track at the hit level. Tracks that do not match, or which only partially match, to a Monte Carlo track, do not contribute to the numerator in this equation.

The HFT allows us to improve the final vertex position resolution to be about 6 μm for the highest multiplicity events, while in the most general case the vertex resolution follows the functional form

$$\sigma = \frac{136\mu m}{\sqrt{N_{ch}}} + 2.7\ \mu m \quad \text{in y and} \quad \sigma = \frac{89\mu m}{\sqrt{N_{ch}}} + 3.3\ \mu m \quad \text{in z,}$$

where N_{ch} is the multiplicity of charged particles in the detector acceptance. The vertex resolution functional form follows Poisson statistics, as expected. This functional form is drawn as a line to guide the eye in Figure 31.

3.5.3 Primary Track Reconstruction Performance

The performance of the HFT was simulated using tracks from central Au+Au collisions at $\sqrt{s_{NN}}$ = 200 GeV which were generated by the "HIJING" code. The simulated tracks and events were processed through GEANT and, finally, a detailed response function for the TPC and the SSD were applied to the data (aka "the slow simulator"). These response functions take into account physical effects in the detectors and the subsequent electronics. We used a fast simulator (less detailed than the slow simulator) to describe the performance of the PIXEL and IST layers.

Note that the TPC has a geometric acceptance of slightly less than 90% due to sector gaps and other construction details. Similarly the SSD has a geometric acceptance of slightly less than 90%. Together they are only about 75% efficient and so the absolute efficiency calculations in this proposal will not rise above the 75% level. Both of these acceptance factors are included in the GEANT simulations and in the hand calculations (presented earlier). However, all of the new detectors (PIXEL and IST) are assumed to have 100% acceptance and so any inefficiency seen in these layers is due to tracking, occupancy and ambiguity issues, alone.

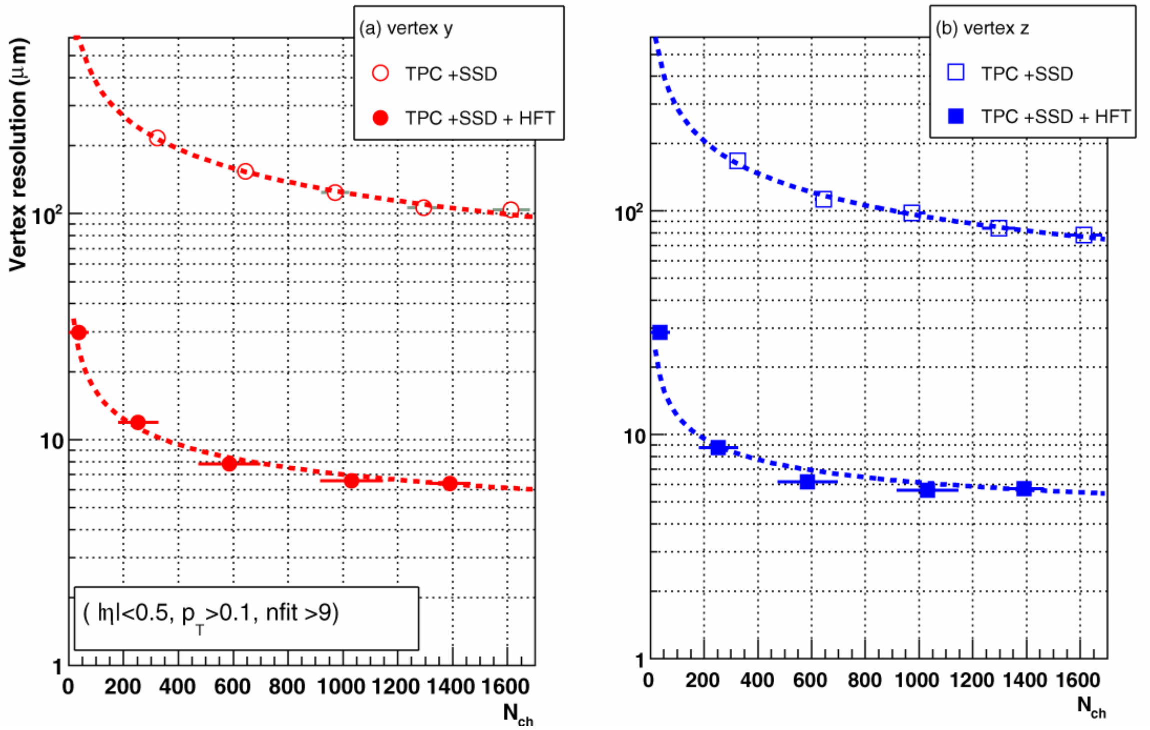

Figure 31: Vertex resolution σ(MC Vertex Position – Reconstructed Vertex position) as a function of Nch, the number of charged tracks in the reconstructed event. The PIXEL refit vertex shows an order of magnitude improvement over the previously reconstructed primary vertex. a) Vertex resolution in y vs. N_{ch}. b) Vertex resolution along the beam direction. Best resolution is $v_y = 6.5$ µm, $v_z = 5.5$ µm.

Tracks with at least 15 hits in the TPC and 2 hits in the PIXEL detector were reconstructed with the STAR inner-tracker code. Figure 32 shows the efficiency for tracking pions and kaons with $|\eta| < 1.0$. Note that these are absolute efficiencies so that the TPC tracking efficiency limits the efficiency of the PIXEL at low p_T while the geometric acceptance of the TPC (and SSD) limits the efficiency to 75% at high p_T.

At low momentum, the (in)efficiency is dominated by multiple Coulomb scattering, the magnetic field and dE/dx. At high momentum, the acceptance of the detectors is quite uniform. Thus the absolute efficiency for STAR tracking in Au+Au collisions with the HFT is above 50% at momenta above 1 GeV/c. Simulations using mono-energetic pions show that the efficiency stays approximately constant up to 20 GeV/c.

The differences between the pion and kaon lines in Figure 32, at low $p_{T,}$ are due to dE/dx and the decay of the kaon. At high $p_{T,}$ the two lines merge but you can still see the effects of kaon decay up to about 3 GeV/c because the STAR TPC is 2 meters in diameter and the unboosted cτ for the decay of a charged kaon is 3.7 meters.

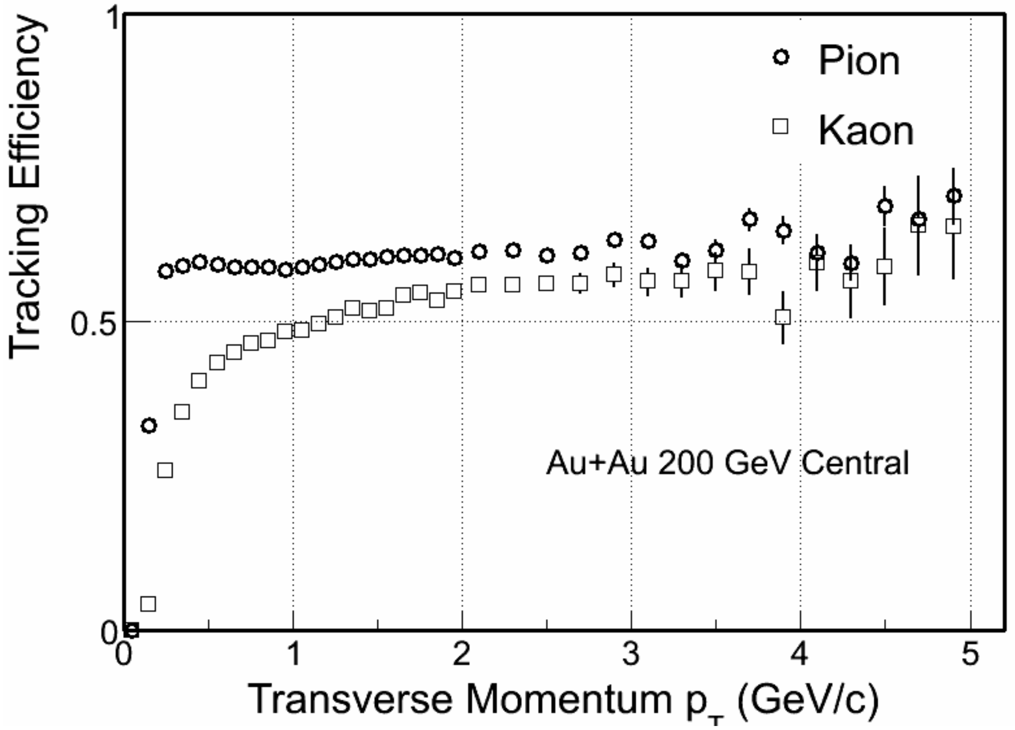

Figure 32: The efficiency for finding tracks in central Au+Au collisions in the STAR TPC, and the PIXEL detector. Finite acceptance effects for the TPC and SSD are included in the simulations. Accepted tracks have more than 15 TPC hits and 2 PIXEL hits that match to a single track. The quoted efficiency is for $|\eta| < 1.0$ and for tracks coming from the primary vertex with $|v_z| < 5$ cm. The difference between the pions and kaons at low p_T is due to dE/dx and the decay of the kaon.

3.6 Open Charm Reconstruction Simulation

As previously discussed, particles containing charm and bottom quarks are the probes relevant for the main thrust of our physics program. Charm and bottom quarks occur in a wide variety of hadrons, and these hadrons decay into a large number of different channels. To demonstrate the power of the HFT, we have simulated the $D^0 \rightarrow K^- \pi^+$ decay. Table 10 displays some of the properties of the D^0 and other charm hadrons.

In the Monte Carlo simulation, we embedded ten D^0s in each central Au+Au event. The input D^0 has a flat distribution in p_T and η in order ensure enough statistics at large momentum but this technique required us to normalize the signal and background to the real total cross-sections and p_T distributions. To be conservative, we have assumed that the total production cross-section for charm is 560 μb and this corresponds to the lower limit of the measurements by STAR and PHENIX. To scale the cross-section to mid-rapidity we used the results from PYTHIA.[19] The transverse momentum of the real distribution of the charm hadrons follows a power law with $<p_T>$ = 1 GeV/c where the power is 11. The distributions of the reconstructed D meson signal and background were then scaled to match the expected D-meson production rates per central Au+Au collision.[45]

Particle	**Decay Channel**	**cτ (μm)**	**Mass (GeV/c^2)**
D^0	$K^- \pi^+$ (3.8%)	123	1.8645
D^+	$K^- \pi^+ \pi^+$ (9.5%)	312	1.8694
D_s^+	$K^+ K^- \pi^+$ (5.2%) $\pi^+ \pi^+ \pi^-$ (1.2%)	150	1.9683
Λ_c^+	$p K^- \pi^+$ (5.0%)	59.9	2.2865

Table 10: Open charm hadron properties

Figure 33 shows that we can identify secondary vertices that are displaced from the primary vertex by less than 100 μm because the primary and secondary vertices are separated by more than their respective widths.

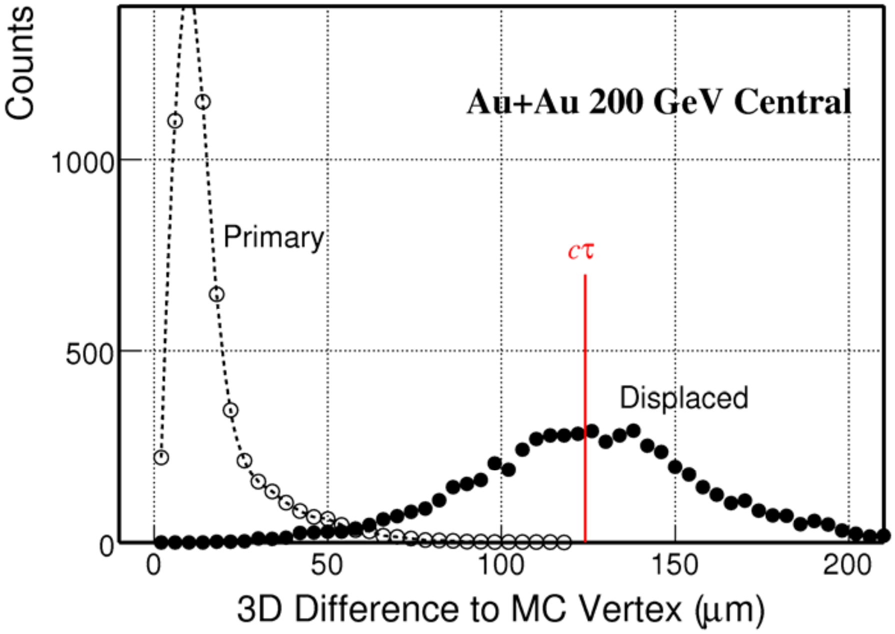

Figure 33: The open circles show the primary vertex resolution in central Au+Au collisions. The solid circles show the D^0 secondary decay-vertex resolution. The mean decay distance, cτ = 123 μm for the D^0, is shown to guide the eye. These data were generated by Monte Carlo simulations and so the curves illustrate the absolute magnitude of the 3 dimensional distances from the Monte Carlo vertex to the reconstructed vertex. Each D^0 decay length was scaled by the appropriate βγ factor to provide a universal peak for the purposes of the illustration.

The primary vertex peak shown in the figure is the result of combining the information from several hundred tracks while the secondary vertex peak is the result of comparing two particles at a time (a π and a K).

3.6.1 D^0 Reconstruction

The HFT detector allows us to identify a D^0 decay-vertex by reconstructing the trajectory of its two daughters. Figure 34 shows the topology of the decay.

The following selection criteria were used to separate the D^0 signal from background:

- The distance of closest approach DCA between the daughter tracks and the primary vertex (PV)
- Isolation cuts on $\cos(\theta)$, with θ being the angle between the D^0 momentum (vector sum of the two daughter momenta) and the vector joining the primary vertex to the D-meson decay vertex
- The distance of closest approach, $DCA_{\pi K}$, between the two daughter tracks
- The difference, Δm, between the reconstructed invariant mass and the D^0 rest mass

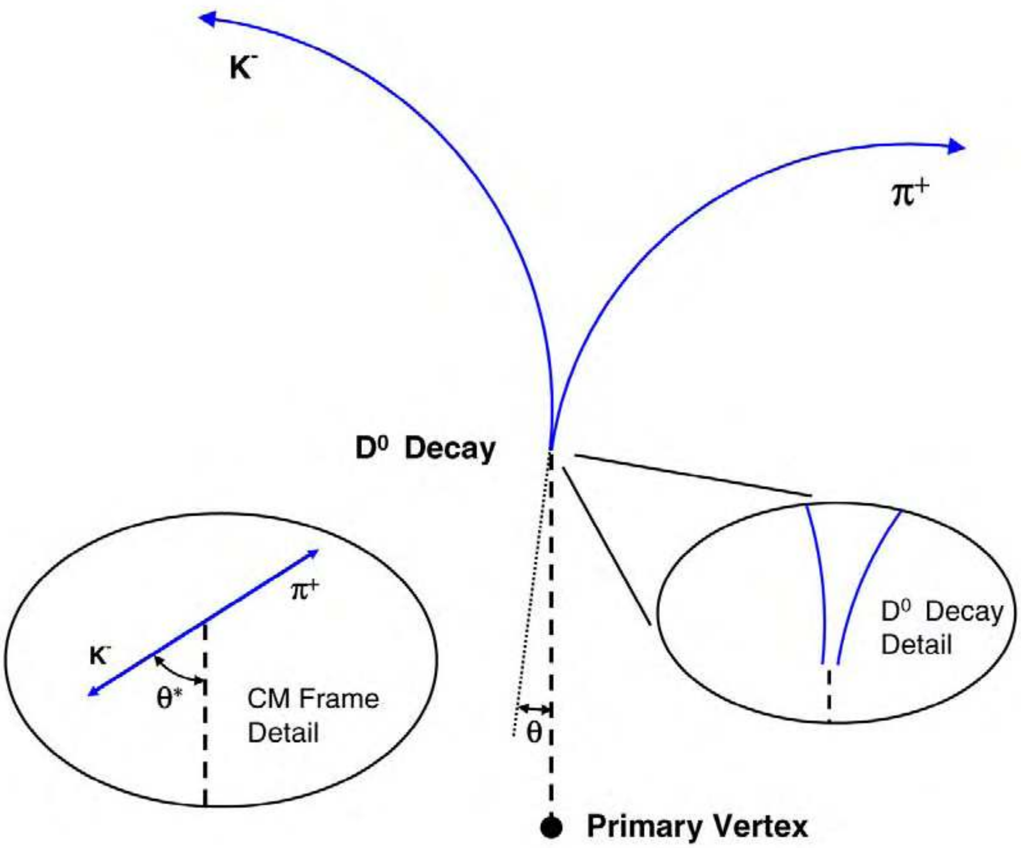

Figure 34: The topology of a D^0 decaying to a kaon and a pion. Isolation cuts to identify the D^0 from the background tracks are described in the text.

The selection of proper cuts is very important in order to reduce the background. The applied cuts for D^0 reconstruction were determined based on prior experience with D^0 simulation and track reconstruction (see Table 11) and are not momentum dependent. Using momentum dependent cuts would most likely improve the D^0 finding efficiency.

Cuts	**D^0**
TPC hits	> 15
Pseudo-rapidity range	± 1.0
PIXEL hits	2
DCA (primary vertex)	$\geq 50\ \mu m$
$DCA_{\pi K}$	$\leq 50\ \mu m$
$\cos(\theta)$	≥ 0.98
Δm	$\leq 35\ MeV/c^2$

Table 11: The cuts for the D^0 reconstruction and efficiency analysis are shown.

Charged decay daughters were identified by their Monte Carlo ID. This means that we are assuming 100% PID efficiency for the daughter particles. In reality, we expect that about 90% of all tracks at intermediate p_T can be identified by the combination of dE/dx in the TPC and the timing information from the TOF detector.

Comparisons of signal and background distributions for various cut variables are shown in Figure 35 along with the final cut values that were applied to the data.

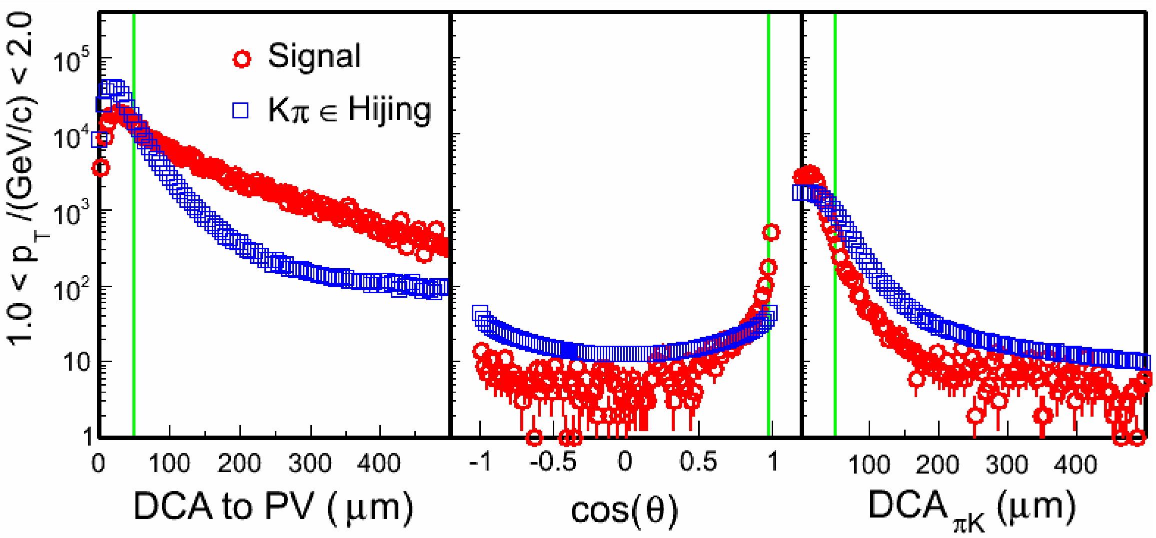

Figure 35: The distribution of quantities used to distinguish signal from background for the D^0 in the p_T range 1 - 2 GeV/c. The D^0 signal is shown in red (circles), while the background is shown in blue (squares). Central Au+Au collisions without other backgrounds are assumed for the rate of background primary tracks. The vertical green lines show the topological cuts that were applied to the data; for example, the DCA to the primary vertex is cut at 50 μm.

Figure 36 shows the reconstructed D^0 signal. It is interesting to note that the signal cannot be distinguished from the background without making topological cuts on the data and this shows that the pointing resolution of the HFT is essential to distinguish the signal from the background in this environment.

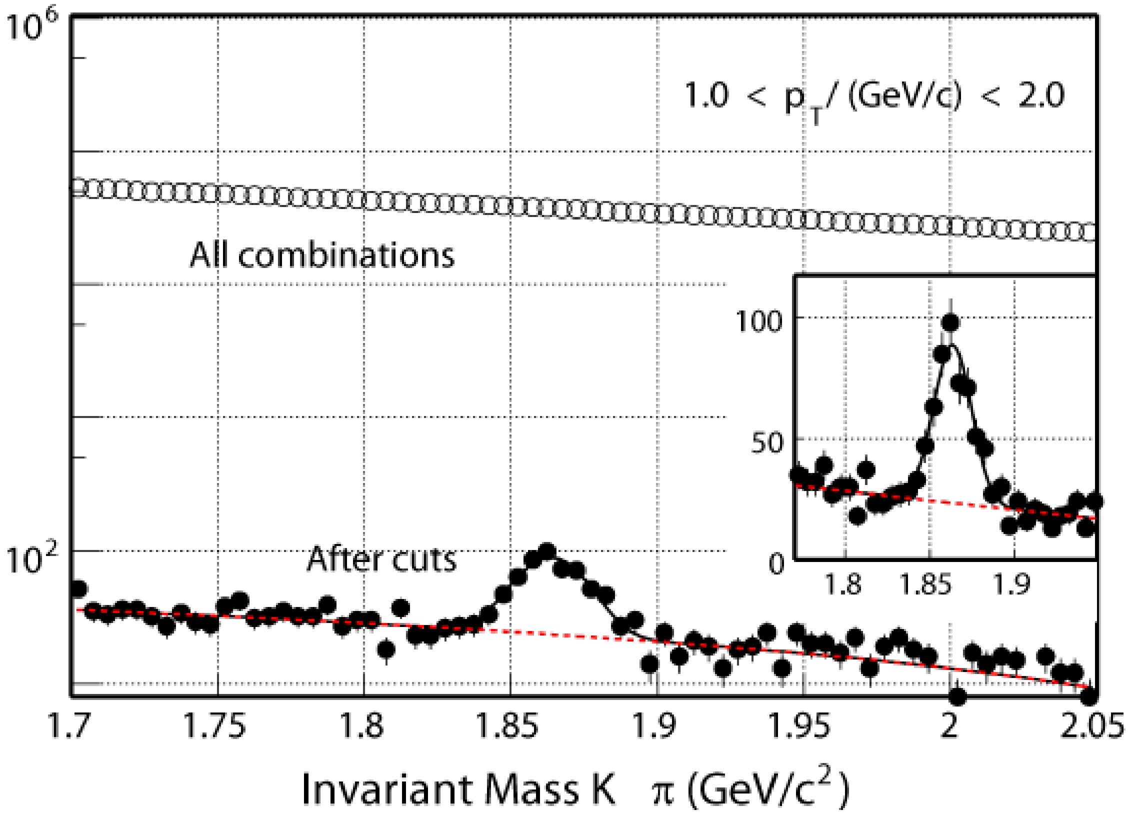

Figure 36: The D^0 signal, after cuts, is shown by the solid black circles. The original spectrum, before software cuts, is shown by the line of open circles. The dashed red line shows the background that was fit from outside the interval 1.3 to 1.9 GeV/c^2. The D^0 peak is shown on a linear scale in the inset figure.

Once we have made the topological and other cuts on the data, we can study the efficiency for reconstructing the D^0s. The overall efficiency takes into account the acceptance, single track efficiency and D^0 reconstruction efficiency. Figure 37 shows the efficiency for identifying the D^0 given a flat spectrum as the input. The red squares show the probability that both daughters from the D^0 decay were reconstructed with 2 PIXEL hits and more than 15 TPC hits. The black circles show the probability for identifying the D^0 from these daughters with the cuts listed in Table 11. The decrease at low p_T is due to the lack of boost from the parent particle and so the pool of candidates for the daughter tracks can be contaminated by the primary tracks; which dilutes the signal and increases the background.

Figure 38 shows the significance of the signal for 100 Million central events, which we expect to be able to acquire in two weeks of running during the RHIC II era. The signal significance is directly related to the precision with which we can make a D^0 flow measurement.

Once we have identified a D^0 signal, and we know the efficiency for recording the signal, the only step left is to remove the flat p_T dependence of the D^0 spectrum that went into the Monte Carlo simulation. We do this by scaling the signal, and the background, by the true cross-section and real p_T dependence of the signal in order to derive the physics results shown in the next section.

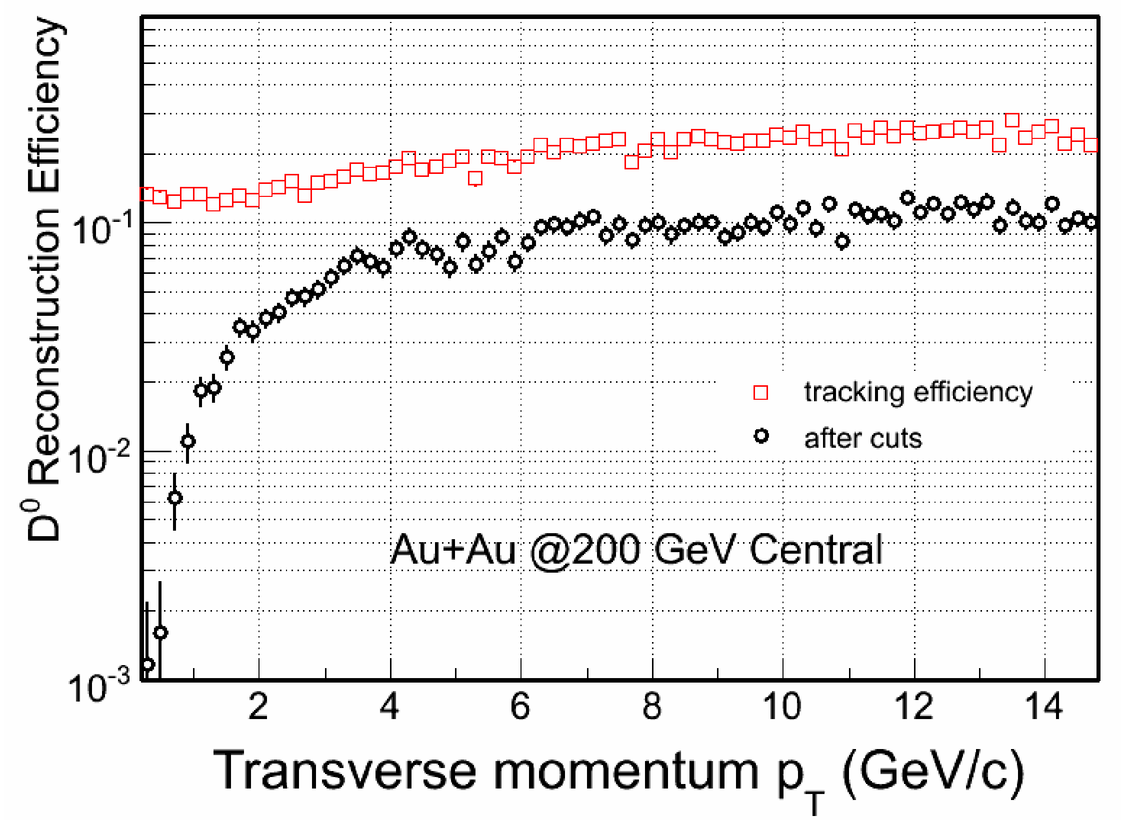

Figure 37: The yield of reconstructed D^0s divided by the simulated D^0 yield (which was flat). The red squares show the maximum possible efficiency for reconstructing a D^0 based upon the single track efficiencies for the daughter particles. The black circles show the efficiency for actually finding these D^0s after applying the topological cuts. Note, however, that UPC electrons and pileup from minimum-bias events are not yet included in the simulation.

3.7 Charm Elliptic Flow

A precision measurement of charm elliptic flow is one of the main goals for the HFT program. The measurement is necessary to understand the degree of thermalization in the partonic phase of a relativistic collision. In order to study the sensitivity of the HFT for this kind of measurement, we will focus on the capability of the HFT to measure the flow of the D^0-meson.

In order to simulate measurements on minimum-bias Au+Au collisions, we rescaled the yield of the D^0 signal from our simulated central Au+Au data by the number of binary collisions, and the background by the number of participants (squared). And to make a rate estimate relevant for the charm v_2 measurement, we need to make further assumptions about the magnitude and the p_T dependence of the anisotropy of the flow distributions. Models of D^0 flow with and without charm quark flow[38], represent the two extremes that are possible and thus bracket the expected measurement range. This is shown in Figure 39. With the known efficiency, and the anticipated signal to background ratios, the statistical errors on a proposed measurement can be calculated. Table 12 and Figure 39 show the errors that can be achieved in the measurement of D^0 v_2 (p_T) with 100 million Au+Au minimum bias events. So, for example, the D^0 v_2 (p_T) can be measured up to p_T ~ 5 GeV/c with an absolute error of about 0.02 using the proposed STAR HFT.

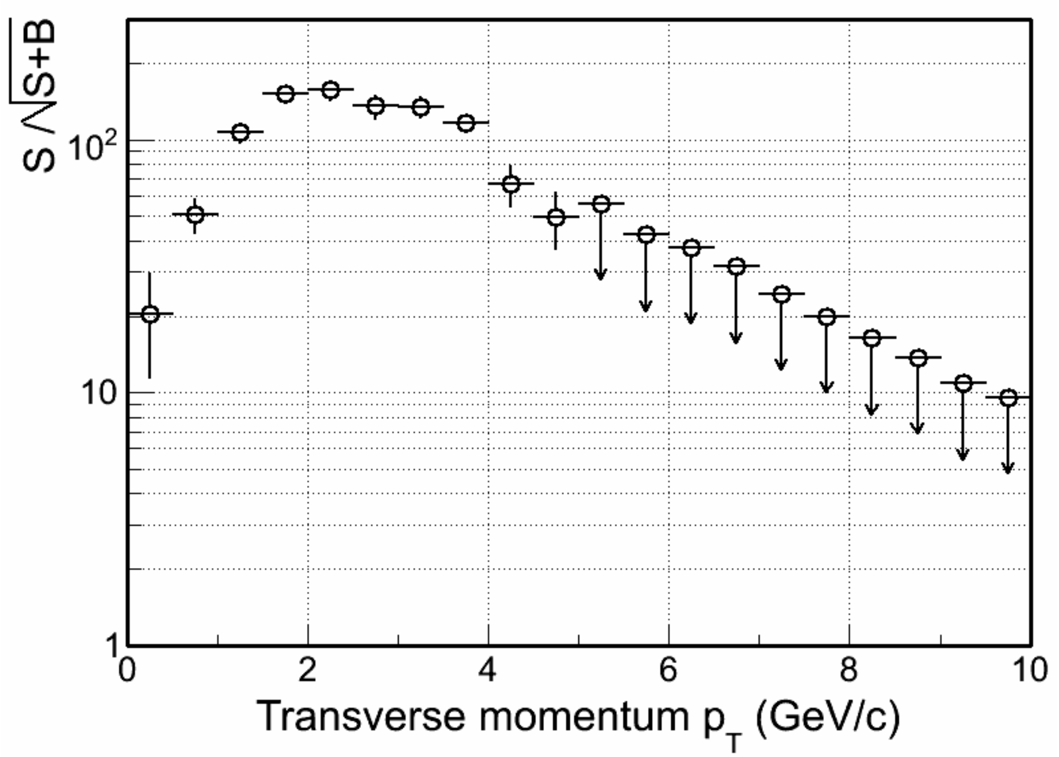

Figure 38: The expected significance of the D^0 measurement with 100 M central events as a function of p_T. For p_T above 5 GeV/c, the upper limit on the signal significance is shown because we do not have sufficient statistics to properly estimate the background. UPC electrons and pileup of minimum-bias events during the integration time of the PIXEL detectors are not included in this simulation.

p_T (GeV/c)	Δp_T (GeV/c)	v2 error
0.75	0.5	0.027
1.25	0.5	0.003
2.0	1.0	0.005
3.0	1.0	0.007
4.0	1.0	0.010
5.0	1.0	0.016

Table 12: An estimate of the absolute value of the v_2 errors using 100 M minimum-bias events.

As mentioned earlier, the assumptions in the model[38] are extreme limits. In order to test the thermodynamic behavior of the D-meson, the most important region is $p_T < 3$ GeV/c, because at higher p_T other dynamical effects will become important (e.g. jet correlations). From the figure, we can conclude that the proposed STAR HFT detector will be able to make precise v_2 measurements in the transverse momentum region $0.81 < p_T < 4$ GeV/c. As we have done with the hadrons from the light-flavor sector,[5] the combined analysis of the D-meson spectra and v_2 distributions will allow us to explore the thermodynamic nature of the medium created in heavy-ion collisions at RHIC.

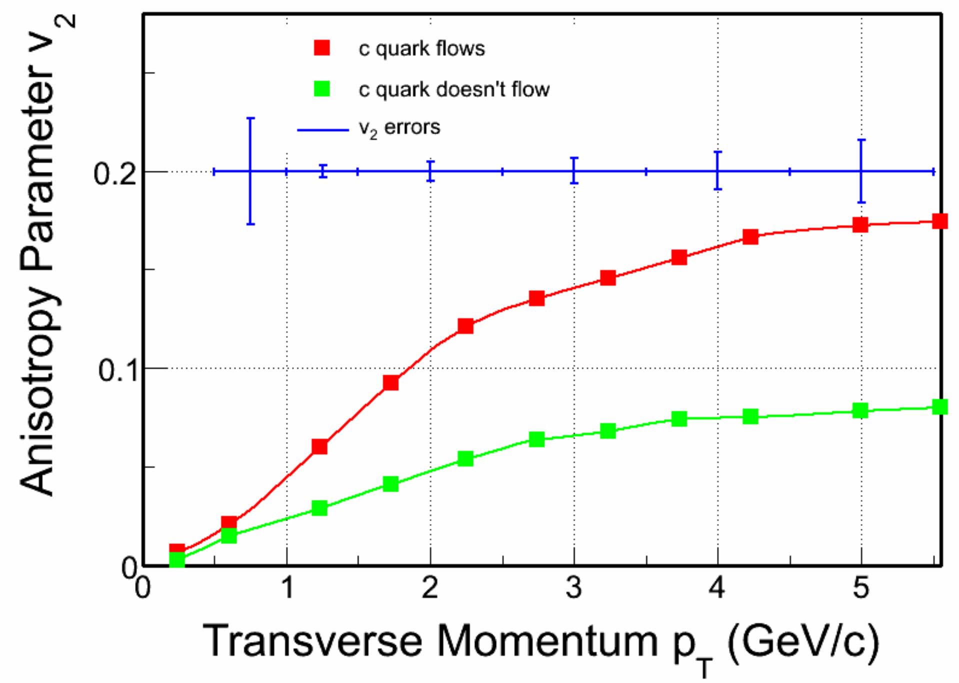

Figure 39: Charm meson flow. The green line describes the expected magnitude of the v_2 parameter if only the light quarks in the D^0 exhibit flow. The red line illustrates how the flow parameter can increase if the charmed quarks also flow. The blue error bars shown at the top of the figure show the anticipated errors of measurement in 100 M Au+Au minimum-bias events.

3.8 Monte Carlo Simulations for p+p Collisions at 200 GeV

The charm measurements in p+p collisions provide an important base line for the heavy ion measurements and are used, for example, to form the nuclear modification factor R_{AA}. We simulated p+p collisions at 200 GeV with the PYTHIA generator. To enhance the signal, we selected only those processes that create charm pairs (MSEL = 4) in the event generator. The background simulations are not fully implemented yet, and so the results reported here only include the background processes in the event generator itself which are rather small. However, to give an order of magnitude estimate for the background, we expect the pileup hit densities to be about the same as the pile-up in minbias Au-Au collisions (to within a factor of 2, coincidentally).

The events generated by PYTHIA were run through the full STAR detector GEANT based simulation package and were reconstructed using the standard STAR tracking algorithms.

Figure 40 shows the primary vertex resolution compared to the displaced vertex resolution for D^0 mesons and shows that the two peaks are separated by a distance that is comparable to their width.

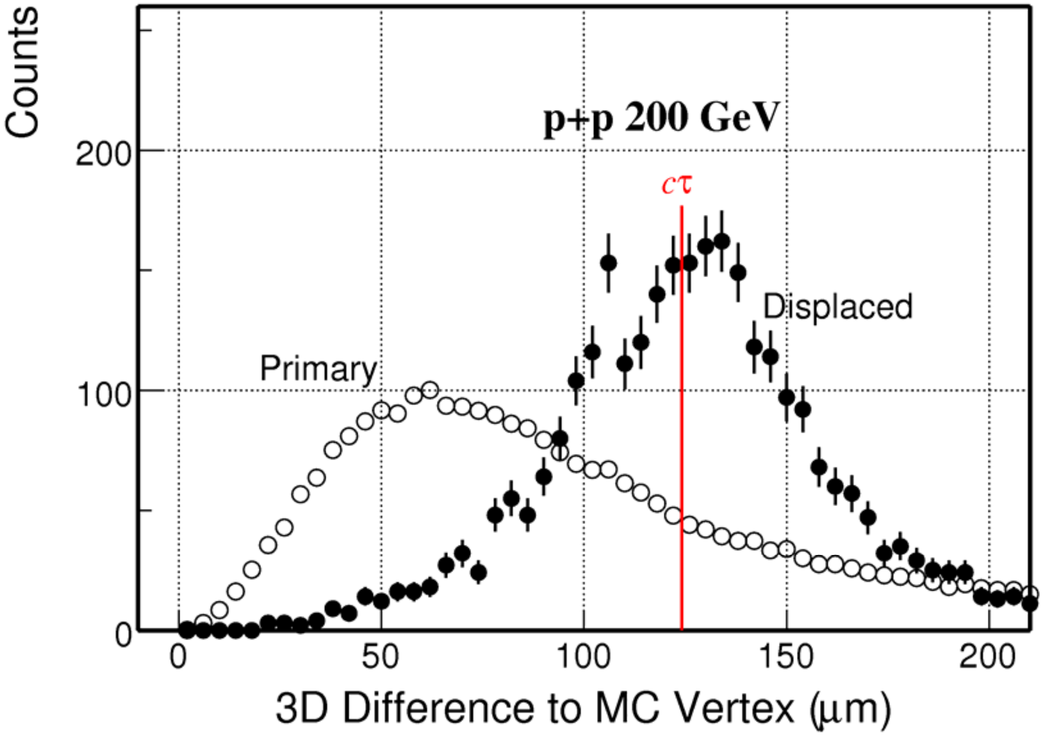

Figure 40: The open circles show the primary vertex resolution in p+p collisions. The solid circles show the simulated D^0 secondary decay-vertex resolution. The mean decay distance, cτ = 123 μm for the D^0, is shown to guide the eye. These data were generated by Monte Carlo simulations and so the curves illustrate the absolute magnitude of the 3 dimensional distances from the Monte Carlo vertex to the reconstructed vertex. Each D^0 decay length was scaled by the appropriate βγ factor to provide a universal peak for the purposes of the illustration.

In Figure 40, the D^0 vertex was reconstructed using a re-fit daughter track helix assuming perfect hit resolution in the PIXEL detector (the procedure can still be improved and this would result in an even narrower peak). Note that the primary vertex data in the figure did not go through the re-fit algorithm and this is why the primary vertex distribution is broader than the secondary vertex distribution.

Figure 41 shows the single-track efficiency for pions and kaons with 2 PIXEL hits and more than 15 TPC hits. The figure suggests that the single track efficiency in p+p collisions is higher than Au+Au collisions. This is, no doubt, due to the lower multiplicity per event in p+p collisions.

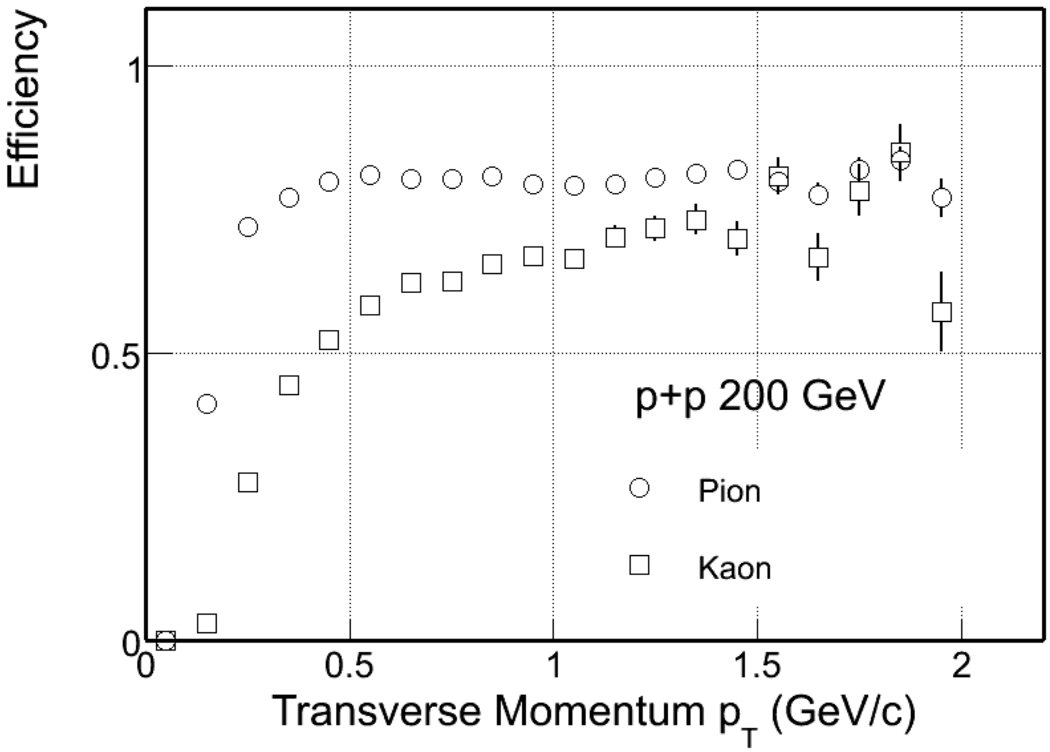

Figure 41: The efficiency for finding tracks in p+p collisions in the STAR TPC and PIXEL detectors. Accepted tracks have more than 15 TPC hits and 2 PIXEL hits that match to a single track. The quoted efficiency is for particles with $|\eta| < 1.0$ and coming from the primary vertex with $|v_z| < 5$ cm.

The D^0 reconstruction efficiency is shown in Figure 42. Although the backgrounds have not been fully simulated yet, the figure suggests that the efficiency for reconstructing D^0s in p+p collisions is relatively large (~30%). The expected rate of pile-up hits at PIXEL layers in pp running with RHIC-II luminosity shouldn't exceed the values for AuAu. Therefore we expect small to negligible impact of possible ambiguous hits on D0 reconstruction in pp."

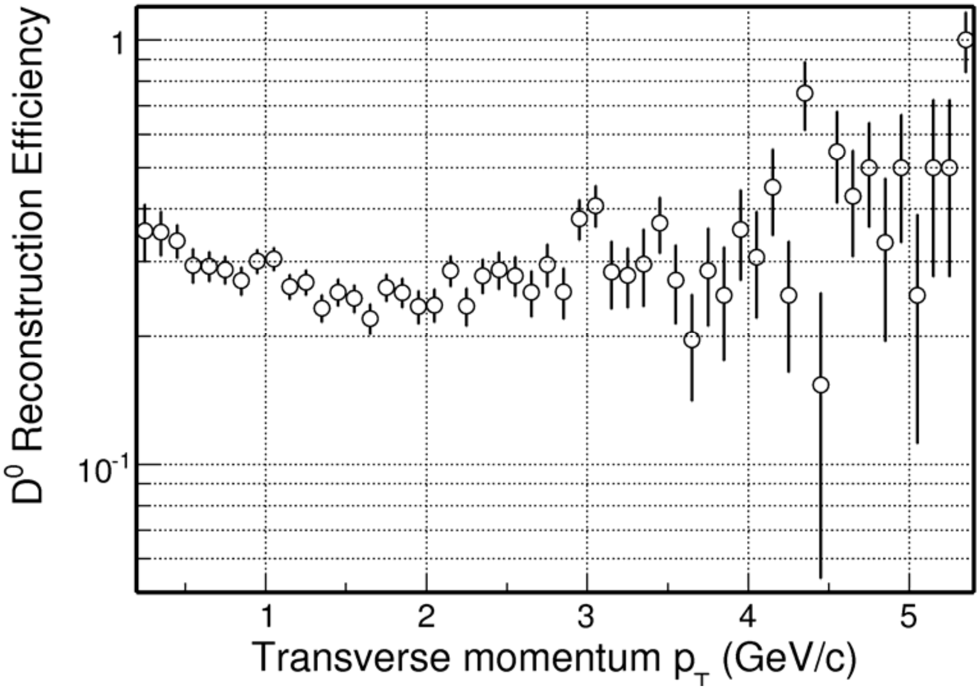

Figure 42: The figure shows the absolute yield of D^0s from simulated p+p collisions seen in the TPC and PIXEL detectors divided by the flat D^0 spectrum which was input to the calculation. The open symbols show the maximum efficiency for reconstructing a D^0 based upon the acceptance, quality cuts and single track efficiencies for the daughter particles; however, the software cuts to constrain the decay kinematics have not been applied because the background and other effects have not yet been fully implemented.

To reach an adequate level of significance, topological cuts on the data presented in Figure 42 will be necessary, and this may drop the calculated efficiency by up to a factor of 2. With this information we can estimate our ability to make certain key physics measurements especially where the background is low, such as at intermediate and high p_T.

Table 13 shows the estimated relative statistical errors that can be achieved in an R_{AA} measurement for D^0s with one RHIC year of Au+Au running and one year of p+p running.

The assumptions underlying these calculations presume that the non-singly diffractive cross-section is 30 mb, and dN/dy for the D^0 at mid-rapidity is 0.002. Further, we assume 30% D^0 reconstruction efficiency at all transverse momenta; and the p_T shape of the D^0 spectrum follows the power law function mentioned earlier with $<p_T>$ = 1 GeV/c and a power of 11.

Under these assumptions, Table 13 indicates that an accurate R_{AA} measurement can be made in the intermediate and high p_T interval from 4 to 10 GeV/c.

P_T (GeV/c)	Δp_T (GeV/c)	R_{AA} relative error (%)
4.5	1.0	1.0
5.5	1.0	1.8
6.5	1.0	2.8
7.5	1.0	4.3
8.5	1.0	6.4
9.5	1.0	9.3

Table 13: The estimated statistical errors on R_{AA} that can be achieved with 1.0 pb^{-1} of analyzed p+p collision data. We assume a vertex width of ± 15 cm vertex. The simulations presented here do not include minimum-bias background.

4 The Pixel Detector (PIXEL)

4.1 Introduction

The STAR heavy flavor physics program requires a thin, fast, detector that can operate in a relatively high radiation environment. A precision flow measurement requires determining transverse momenta down to 150 MeV/c. To reach this low threshold requires a very thin pixel detector in order to maintain precise tracking without degradation by multiple Coulomb scattering. It is difficult to meet all of these requirements using the "usual" techniques currently employed in high-energy physics experiments.

The emergence of CMOS sensor technology offers a new perspective on high precision charged particle tracking and vertex finding. This technology can provide the performance parameters required by the PIXEL. Recent developments have shown that CMOS technology is capable of excellent spatial resolution and charge collection efficiency, together with satisfactory radiation tolerance.

4.1.1 Choice of Technology

We have evaluated the available technologies in detail. At this time, there are four good technologies that can be used for thin vertex detectors: Charge Coupled Devices (CCD), Active Pixel Sensors (APS), Hybrid Pixels, and DEPleted Field Effect Transistor structure (DEPFET). Each of these devices has strengths and weaknesses. We have evaluated these technologies and selected APS as our choice for the PIXEL detector.

CCDs

At SLAC, the SLD collaboration built and successfully operated a pixel vertex detector,[102] VXD3, based on CCD technology.[103] But since silicon is damaged by radiation and CCDs require that the charge be transferred from one pixel to another, CCDs are more susceptible to radiation than other vertex devices. Charge in the end row of a CCD chip, for example a 1000 × 1000 array, must be transferred through more than 1000 pixels before being digitized. Therefore, any small loss in charge transfer produces large signal losses and signal sharing. The SLD vertex detector ran at a relatively low radiation intensity because that is the nature of the SLAC Linear electron Collider (SLC), so the SLC CCD could tolerate the radiation environment. In addition, the complexity of the clocking makes the readout slow. This was suitable for the SLC where it only had to be operated at 2 Hz.

CCDs require significant power to clock the charge around the chip because high capacitance electrode structures covering the whole chip must be voltage switched. This becomes a power versus speed trade off with consequences in the mass budget because liquid cooling is usually required. In any case, cooling is a complication for CCD operation. For instance, VXD3 used LN_2 gas to cool the device but because the ladders were operated far below room temperature, elaborate mechanical and alignment systems were needed to achieve the excellent resolution of about 30 μm for determining the impact parameter. An outer heated jacket was needed to prevent condensation and the cooling system added extra complications and created additional mass.

Finally, to fabricate CCDs requires specialized knowledge, is expensive, and requires a long learning curve to become familiar with its details. Currently, there is a group studying whether the limitations of the process can be overcome to use this technology at a future electron collider.[104]

Hybrid Pixels

At the Large Hadron Collider (LHC)[105] the three major experiments decided to use a hybrid technology where the sensor is bump bonded to a read-out chip. The hybrid technology has the disadvantage that the pixel size is much greater than a CCD pixel and two chips have to be layered on top of each other. The two chips and their interconnection are much thicker than can be done in CCD technology.

DEPFET

The Munich MPI Semiconductor Laboratory has recently invented[106] and continues to be the leader in the use of DEPFETs.[107] This concept is based on the combination of the sideward depletion, as used in a semiconductor drift detector with a field effect transistor to collect the charge. The MPI Group has a conceptual design for a detector for the Linear Collider but much development is needed to make a realistic device. DEPFETs require a very special process and MPI is the only producer of this device so any development must be done within that institute.

Active Pixel Sensors

APS devices have been used as photon detectors since late 1960s.[108] They have recently surpassed CCDs in the photography market because of their lower cost and lower demand for power. Power consumption is important in a particle detector application because a detector that can be air cooled is overall thinner than a detector that requires water cooling. The IPHC group in Strasbourg France has done a great deal of research on these detectors, taking them from small prototypes to large arrays of successful detector elements. Table 14 presents a detailed listing of the CMOS sensor program.

Chip	Year	Process (µm)	Epi. (µm)	Pitch (µm)	Pixels	Comments
MIMOSA-1	1999	AMS 0.6	14	20	4k	thick epitaxial layer
MIMOSA-2	2000	MIETEC 0.35	4.2	20	4k	thin epitaxial layer
MIMOSA-3	2001	IBM 0.25	2	8	32k	deep sub-mm
MIMOSA-4	2001	AMS 0.35	no	20	4k	low dopant substrate
MIMOSA-5	2001	AMS 0.6	14	17	1M	real scale 1M pixels
MIMOSA-6	2002	AMIS 0.35	4.2	28	3k	fast column parallel readout internal data sparsification
MIMOSA-7	2003	AMS 0.35	no	25	1k	fast column parallel readout internal data sparsification. (photoFET)
MIMOSA-8	2003	TSMC 0.25	~8	25	4k	fast column parallel readout internal data sparsificaton
MIMOSA-9	2004	AMS 0.35 opto	~14	20 30 40	7k	tests diodes/pitch/leakage current
MIMOSA-9 (no epi)	2004	AMS 0.35 opto	no	20 30 40	7k	tests diodes/pitch/leakage current
MIMOSA-10 (MIMOSTAR-1)	2004	TSMC 0.25	~8	30	16k	first prototype for STAR PIXEL
MIMOSA-11	2005	AMS 0.35 opto	~14	30	7k	radiation tolerant structure
MIMOSA-12 (Mosaic 1)	2005	AMS 0.35 high resistive	no	35	0.6k	multi-memory pixels (FAPS)
MIMOSA-13 (Mosaic 2)	2005	AMS 0.35 high resistive	no	20	1.4k	fast column readout
MIMOSA-14 (MIMOSTAR-2)	2005	AMS 0.35 opto	no	30	16k	second prototype STAR PIXEL
MIMOSA-15	2005	AMS 0.35 opto	~14	20 30	7k	multi-purpose tracker-imager
MIMOSA-20 (MIMOSTAR-3)	2007	AMS 0.35 opto	~14	30	200k	half-size of the STAR PIXEL sensor
SUC 1	2003	AMIS 0.35	4.2	25 35	4k	radiation tolerant structure (SUCIMA project)
SUC 2	2003	AMS 0.35	no	40	2k	low dopant substrate (SUCIMA project)
SUC 3	2003	AMIS 0.35	4.2	20	8k	radiation tolerant structure (SUCIMA project)
SUC 4 Mtera	2004	AMS 0.35	14	150	12.5k	Hadron therapy/beam monitor. (SUCIMA project)
SUC 5	2004	AMIS 0.35	4.2	30	65k	proton dosimetry (SUCIMA project)

Table 14: APS chips that the IPHC group has produced in the past 5 years (Reference [109]).

APS technology is our preferred technology for the PIXEL and we are working with the Strasbourg group to design and utilize this technology in our detector.

4.2 Main Features and Performance of CMOS Active Pixel Sensors

CMOS sensors are manufactured using industry-standard CMOS technology. This offers low fabrication costs and fast turn-around times in their development. The key element of this technology, for our purposes, is the use of an n-well/p-epi diode to collect the charge through thermal diffusion, which is generated by the impinging particles in the thin epitaxial layer underneath the read-out electronics,[110] schematically shown in Figure 43. An attractive feature of these sensors is that they allow fabrication of System-on-Chips (SoC) by integrating signal processing micro-circuits (amplification, pedestal correction, digitization, discrimination, etc.) on the detector substrate. Moreover, a CMOS substrate can be thinned down to a few tens of microns because the active region is less than 20 μm thick.

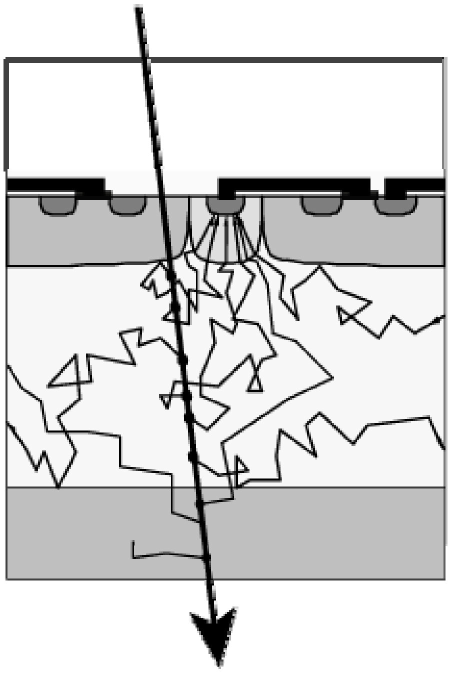

Figure 43: Epitaxial Silicon used as a sensor. In this design, a primary ionizing particle creates free charges in the epitaxialy grown Si layer that is a few tens of microns thick and a few electrons in the bulk layers. The liberated charges are then free to diffuse towards a potential well structure at the top of the sensor where they are extracted and read out into a DAQ system.

The ability of these sensors to provide charged particle tracking is now well established.[111] The IPHC group, at Strasbourg, has built a series of these sensors, which they called MIMOSA.[112] Similarly, the LBNL/UCI group has also built and successfully tested these sensors. The MIMOSA line of detectors has explored different CMOS fabrication processes and key parameters of the charge sensing system, and the results demonstrate that a detection efficiency of ~ 99% and a single point resolution of ~2 μm can be achieved using a pixel pitch of 20 μm. The prototypes also show that digitizing the charge with a small number of ADC bits does not degrade the resolution significantly (the measured reduction was ~ 2.5–3 μm) while the double hit resolution is ~ 30 μm.

The radiation tolerance of the sensors to bulk damage[113] was also investigated. No significant performance loss was observed up to fluences close to 10^{12} n_{eq} cm^{-2}. As far as ionizing radiation damage is concerned, the real potential of this technology is still being explored, but it is already established that it stands up to more than 100 kRad.

Most of the R&D at IPHC was performed with small prototypes (a few mm^2) containing a few thousand pixels. Figure 44 shows a full size prototype (i.e. ~3.5 cm^2) called MIMOSA-5. It is composed of ~ 1 million pixels per chip, and it was fabricated on a 6 inch wafer, as shown in the figure. The wafers were thinned down to 120 μm before the chip was cut and diced into individual, reticle sized, detector elements.

Tests at the CERN-SPS confirmed that MIMOSA-5 performed as well as the smaller prototypes: a 99% detection efficiency was observed with ~ 2 μm single point resolution. The prototypes were operated with a read-out time of 25 ms, which was limited by the maximum operation frequency of the read-out board (i.e. 10 MHz). The chip was actually designed for a 4 times faster read-out speed. The LBNL group has tested several of these chips at the LBNL Advanced Light Source (ALS) and has measured the expected Landau spectrum on each.

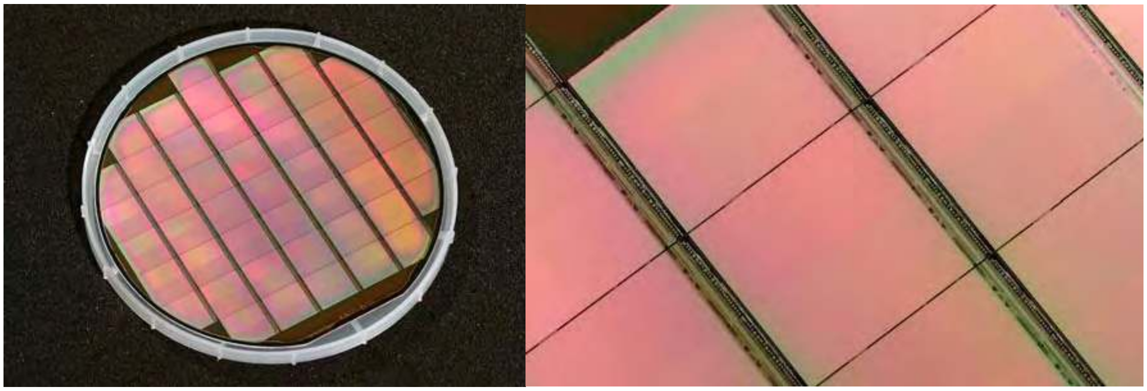

Figure 44: Wafer of reticle size sensors (left) and zoomed-in view of individual chips (right).

After MIMOSA-5, several fabrication processes were explored, aiming to find the process providing the smallest leakage current. In general, several parameters underlying the sensor performance depend on features specific to each fabrication process and so the process specific characteristics need to be explored in parallel with the development of the chip architecture.

For instance, a new fabrication technology, relying on a lightly doped substrate but exhibiting no epitaxial layer was investigated with two different prototype chips. Further IPHC tests show that a detection efficiency of 99.9% can be achieved with this technology, as well as a single point resolution of about 2.5 μm.[114] A major advantage of this technology is that a large signal can be generated because the charges are collected from several tens of microns of Si instead of from ~ 10 μm in an epitaxial layer. The extra charge makes it well suited to applications with substantial electronic noise.

4.3 Thinning

Up to now, tested MIMOSA-5 chips have been thinned down to 120 μm thickness. This operation was successful and we have not found any degradation of the sensor parameters. In the PIXEL, the MIMOSTAR thickness will be 50 μm. Thinning a 6 or 8 inch wafer down to this thickness is not expected to be a problem, since the process is an industry standard technique. We have demonstrated that 50 μm sensors are mechanically stable and can be assembled into ladders. We have used low-yield MIMOSA-5 wafers to make these investigations and have successfully thinned detectors to 50 μm.[115] Our colleagues at the LBNL light source (ALS) have just characterized several MIMOSA-5 chips in the 1.5 GeV/c electron beam and have subsequently thinned them. Tests of the thinned chips are completed. No degradation of signal from thinned chips was found.

4.4 Additional R&D

CMOS sensors have been developed in Strasbourg since 1999 for various applications, which range from vertex detectors for subatomic physics, to bio-medical imaging (e.g. beam monitoring for oncotherapy, dosimeters for brachyotherapy) and operational dosimetry (e.g. control of ambient radon and neutron radiation levels in nuclear plants).

Several application domains call for SoCs providing fast read-out speed (meaning signal treatment and data flow reduction integrated on the chip), high radiation tolerance, minimal material budget and low power dissipation. Developments for the STAR upgrade will thus benefit from the synergy with the R&D for other applications, in terms of fabrication process exploration, development of fast signal processing architectures, radiation tolerance investigations, and other improvements. More information on the activities and achievements of the Strasbourg team are available in Reference [116].

Starting with an IPHC design, the LBNL/UCI group has built several generations of APS sensors. These devices were built in the 0.25 μm process at TSMC. These ICs have been tested using different sources, i.e. ^{55}Fe, 1.5 GeV accelerator electrons and a scanning electron microscope. Figure 45 shows one of the sensors that has 16 different test structures.

Our measurements have confirmed the IPHC results that APS sensors can measure charged particles with excellent spatial resolution.[117,118] Figure 46 shows several 1.5 GeV electrons recorded at LBNL's Advanced Light Source.

To study the effects of radiation, we have exposed the chips to protons at LBNL's 88" Cyclotron. Afterwards, we measured the change in leakage current and pulse height. The tests show that there was a modest change with an irradiation of 300 kRad. What was most interesting is that after 6 months the device self annealed. Therefore, the effect of gradual radiation is much less than that of an acute exposure.[119] These radiation measurements are complementary to the neutron exposures studied by the IPHC group.

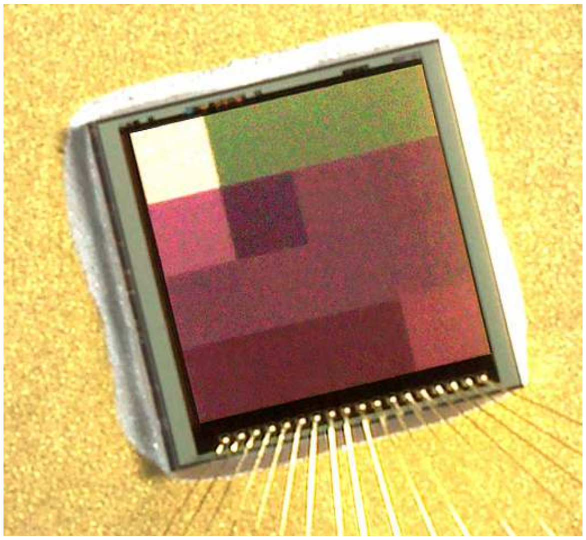

Figure 45: An APS Sensors developed by the LBNL/UIC group. The picture shows 16 separate test structures. Each structure has a 36 × 36 array of 20 µm pixels.

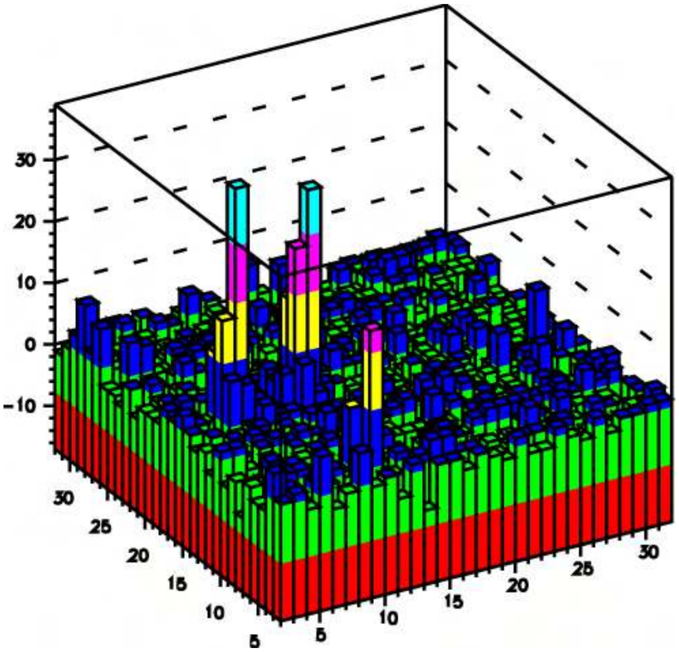

Figure 46: Plot of one event taken with 1.5 GeV electrons. Each bin represents one pixel and the height is proportional to the measured charge. Several electron hits can be identified.

We also completed a study on the effects of varying the pixel pitch. We built and tested a sensor with 5, 10, 20 and 30 μm spacing. Our tests show that to first order the charge collection was identical when comparing the central pixel to the charge collected on its neighbors.[120] As the pixel spacing decreases, more total charge is collected. This observation can be explained by the fact that as pixel spacing becomes smaller, the charge is collected by the diode faster, so there is less time for it to recombine. This implies that we can easily extrapolate our measurements at 20 μm spacing to the selected spacing of 30 μm for MIMOSTAR.

We have been looking at several other techniques to improve APS sensors. It is clearly desirable to speed up the readout as well as reduce the signal spreading to multiple pixel diodes. Concentrating the signal onto a single diode would improve signal to noise.

We can increase the fraction of charge collected by a single pixel using the photo-gate technology. In principle, this technology allows us to use a large area photo-gate for charge collection, without increasing the capacitance, because the charge is transferred from the photogate region to a low capacitance diode. Even though we have demonstrated the sensitivity of the photo-gate structure to X-rays, we have not achieved the expected performance of the device. The transfer time required for moving electrons from the photo-gate to the drain appears to be very long (several ms). We believe this undesirable signal delay is consistent with surface traps at the $Si0_2$ silicon boundary. Studies to find a way to avoid this delay have been studied in a SBIR proposal.

Correlated double sampling (CDS) is a standard technique that is used to remove the fixed pattern noise and KTC noise introduced by the reset transistor. Its main drawback is the required read out and storage of a full frame of data. To avoid doing CDS, we have produced a clamp circuit[121] that reduces the reset noise by a factor of 3**.**

Two generations of "active reset chips" have been fabricated and tested. In this approach the pixel voltage is reset to the empty level with a feed back amplifier potentially reducing fixed pattern noise and the KTC noise associated with a passive reset switch. Preliminary testing shows some noise reduction, but not the full potential improvement. We will make design changes to this circuit and fabricate a new sensor.

To explore how charge is collected on a sensor as a function of position, we tested a device at LBNL's National Center for Electron Microscopy. Using the scanning electron microscope, we have been able to position the beam on a pixel with precision of about 1 μm. This allows us to explore algorithms for determining the position of an incoming particle by relating how charge is shared among neighboring pixels. The results show that we can easily obtain the position of the incoming electron by weighting the charge collected from nearby pixels.

We have collaborated with colleagues at UC San Diego on the suitability of using an APS sensor in an electron microscope.[122] We have studied the response of electrons from energies of 100 keV to 300 keV. Results show that single electrons can be detected with a good signal-to-noise ratio. This technique is well suited for this application as it overcomes problems for traditional CCDs that suffer radiation damage. Excellent pictures of proteins have been taken. Using APS devices is very appealing for different types of applications.

We continue to try to further improve the devices. We have fabricated a sensor with different diode sizes. We have used this device to understand the effect of diode size on signal to noise. The tests show that the smallest diode that meets the design rules produces the best signal to noise.

Recently, we submitted an IC design without an epi-layer. We have received the sensor and are in the process of testing it. Simulations show that we should be able to collect more charge from the process.

Our main effort is in studying ways to reduce the sampling time. In the current MIMOSTAR design, the sensor is always sensitive to radiation. We will design a sample-and-hold circuit to see if we can reduce the time window during which the detector is sensitive. If we could gate such a sensor, then pileup effects of out of time interactions would be significantly reduced.

4.5 MIMOSTAR Sensor Design

Based on our experience with CMOS technology, a new series of chips, MIMOSTAR, have been fabricated. The first chip in the series is also called MIMOSA-10, which indicates its place in the evolution tree of CMOS sensors. Its most significant design parameters are:

- Pixel pitch: 30 µm
- Passive forward bias diode in place of reset switch
- Additional details can be found in Reference [123].

The goal of the MIMOSTAR series is to provide a full-scale prototype that is suitable for evaluating the performance of a CMOS sensor in a collider environment.

Since the read-out speed requirement for this prototype is modest, the chip's architecture is based on relatively slow signal processing at the pixel level. This low speed requirement enables us to quickly implement this sensor, while at the same time we are independently developing a sensor that fulfills STAR's requirements. Its design favors moderately low noise and modest power consumption. On the other hand, high speed signal processing is needed at the chip level (i.e. after amplification and multiplexing) due to the need for short integration times and limited shot noise.

The chip includes JTAG based remote control functionality (e.g. bias setting, test settings, etc.). The power dissipation of this architecture is estimated to be slightly more than 50 mW (i.e. less than 15 mW/cm^2), which can easily be cooled with air.

The IPHC group has studied MIMOSTAR-1, which was fabricated in the TSMC 0.25 μm process. They showed that the conventional controls work (via the JTAG controller), and that the bias circuits work and exhibit linear response via their DACs. The analog performance of the chips has been tested and the gain on the pre-amplifiers was about 3.5 at the two 10 MHz outputs. However, due to the inherent properties of the TSMC process, the charge collected on the n-diode could not hold the collected charge long enough for it to be read out. Our group at Berkeley Lab observed a similar effect with another chip designed in collaboration with UCI, which also was fabricated in the TSMC 0.25 process.

Consequently, we decided to switch to the AMS 0.35 OPTO process, in which the passive forward bias diode reset circuit has already been demonstrated to work. A new chip, MIMOSTAR-2, has been fabricated, passed ^{55}Fe tests, and then tested in DESY's 5 GeV electron beam. A radiation tolerant design and a standard design showed efficiency greater than 99.7% at a temperature of 40 C. The radiation tolerant design showed a very small increase in noise at 40 C when it was exposed to 23 kRad of ^{60}Co.

4.6 The Path to a CMOS Pixel Detector

With the research and development done at IPHC and LBNL, we are confident that we can build a CMOS sensor appropriate for RHIC-II luminosities. To achieve this goal, we have identified a series of steps that must be taken before we can design and build the final PIXEL sensor. In the next subsections, we will describe the different R & D steps necessary to achieve this ultimate goal.

4.6.1 MIMOSTAR-3 – a Half Sized Chip

MIMOSTAR-3, which is half the size of the final sensor, continues the work done on MIMOSTAR-2. It is made up of 640 × 320 pixels and uses the AMS 0.35 OPTO technology. The chip has two analog outputs implemented on the same side of the sensor. Each output runs in parallel at 50 MHz so the total time for readout is 2 ms.

Once these chips have been qualified, they will be incorporated on a ladder for a full function test in STAR. As a ladder will be half the final size, significant tests will be able to be done.

4.6.2 MIMOSTAR-4 – a Full Sized Chip

Using the experience gained from building and testing MIMOSTAR-3, we will design and manufacture a full sized sensor that can be used in a full sized ladder prototype. This chip will be twice the size of MIMOSTAR-3, so it will be 640 × 640 pixels. It will have 2 analog outputs on one side running at the same speed of MIMOSTAR-3, so it will take 4 ms to read out all of the pixels. The fabrication of this chip will be done in a production run.

Table 15 shows how the measured performance of the MIMOSA-5 sensor compares to the specifications of MIMOSTAR-4. Most of the requirements (granularity, radiation tolerance, thinning, read-out speed, power dissipation, and sensor size) have already been demonstrated with MIMOSA-5. Some effort is still needed to achieve a higher read-out speed and higher yield during thinning. Moreover, since the sensors will be operated at room temperature, special attention will be given to the magnitude of the leakage current in order to keep the corresponding shot noise at an acceptable level.

Parameter	MIMOSTAR-4 specifications	MIMOSA-5 performance
Detection efficiency	> 98% at 30 – 40° C	~99% ≤ 20° C
Single point resolution	< 10 μm	~2 μm
Granularity (pixel pitch)	30 μm	17 μm
Read-out time	4 ms	24 ms (< 20 ms possible)
Ionizing radiation tolerance	3.7. krad/yr*	> 100 krad
Fluence tolerance	2×10^{10} n_{eq}/cm^2	≤ 10^{12} n_{eq}/cm^2
Power dissipation	< 100 mW/cm^2	~10 mW/cm^2
Chip size	~2 × 2 cm^2	1.9 × 1.7 cm^2
Chip thickness	~50 μm	120 μm

Table 15: Comparison between MIMOSA-5 characteristics and MIMOSTAR-4 specifications.

4.6.3 The Ultimate Sensor

A next generation CMOS IC is needed to meet the requirements of the high intensity at RHIC-II. At these higher luminosities, we need to read out the chip to match the 1 ms readout time of the TPC and to have the chip sensitive for a much shorter time to reduce

---

* Estimate based on RHIC achieving an average Au+Au luminosity of 1.0×10^{27} $cm^{-2}s^{-1}$ for 21 weeks at 60% efficiency. T. Roser, W. Fischer, A. Drees, H. Huang, V. Ptitsyn, “RHIC Collider Projections (FY2006-FY2008). July 19, 2005. http://www.agsrhichome.bnl.gov/AP/RHIC2004/RhicProjections.pdf

the effect of pileup. The goal of our R&D program is to find a sensor that can meet the specifications listed in Table 16.

This sensor will be the same size as MIMOSTAR-4. It will have the same pitch, 30 μm, and pixel array, 640 x 640 μm. It also will be thinned to 50 μm. A specific architecture needs to be developed for this design. Based on our experience, we have a good description for this sensor. The device has an active time period much shorter than the readout time. The active period of time is strobed by the STAR trigger, followed by a 1 ms period to read out the full number of pixels.

The general organization of the chip relies on columns processed in parallel. The chip operation includes a continuous cycling over the array with an integration time of 100 to 200 μs. There will be in-pixel storage of the integrated charges, but at this time it is not clear whether CDS can be done “on chip”.

The details of the signal processing, i.e. ADC or double threshold discrimination for zero suppression are still open and need to be studied with real data. Studies on this chip will commence this year.

4.7 Mechanical Support Structure

Simulations have shown that for good D-meson identification in the high track density environment of Au+Au collisions, it is important to minimize the scattering thickness of the beam pipe and the first detection layer. This requirement has been the primary driver of the current design. By using APS technology we can use thinned silicon with modest connection requirements to minimize the support electronics and cable thickness. In addition, the low power nature of these devices allows a mechanical design that is air-cooled which helps to minimize scattering material in the track path. Several conceptual designs have been considered. We present the design that is currently the focus of our investigations.

In recognition of difficulties encountered in previous experiments, we are adopting design requirements for rapid insertion and removal of the vertex detector, rapid calibration and calibration transfer and multiple detector copies. By addressing these issues early in the design cycle the requirements can be met without major cost impact.

Our mechanical design makes significant use of carbon composite material, which has nearly the same radiation length as beryllium. This allows us to take advantage of the extensive work going on at LBNL for the ATLAS pixel detector.

Since the design of the original STAR detector system, there has been significant progress in tools available for mechanical work. Very powerful low cost 3D CAD programs are now available which allow complex modeling with moving parts and direct interfacing to CNC machines and rapid prototyping. These tools provide the means to tackle the more complex mechanical designs required for rapid insertion and alignment (SolidWorks)..

Ladder active area	2 cm × 20 cm
Pixel size	30 μm × 30 μm
~Pixel mapping on the ladder	640 × 6400
Minimum operating distance from beam	1.5 cm
Power	≤200 mW/cm^2
Operating temperature	≥30 °C
Integration time[†]	≤0.2 ms
Mean silicon thickness	≤100 μm
Readout time	≤1 ms
Efficiency (min I)[‡]	≥98%
Accidental cluster density	≤22/cm^2
Binary readout, number of threshold bits[§]	1 or 2
Radiation tolerance [**]	≥171 krad
Number of conductors supporting the ladder (10 chips/ladder)[††]	≤140
Triggered readout, maximum trigger delay[‡‡]	2 μs

Table 16: Silicon requirements for maximum average Au+Au RHIC luminosity of 7.0 × 10^{27} Hz/cm^2 or 2.5 nb^{-1}/week.

[†] The time that a pixel is sensitive to tracks, this determines amount of pileup.

[‡] Efficiency after cluster filter on binary threshold information from the detector

[§] To satisfy both the efficiency and accidental requirements it is expected that some off chip cluster analysis will be required. Depending on signal to noise either one or two thresholds will be needed.

[**] 4 year operation at maximum RHIC luminosity for a running period of 21 weeks/year see: W. Fisher, T. Roser, I. Ben-Zvi, A Fedotov, 16-Mar-2005. http://www.phenix.bnl.gov/phenix/WWW/publish/leitch/rhicii-forward/RHIC_II_Luminosity_Roser.pdf

[††] This requirement addresses the radiation thickness of the flex cable that is part of the thin ladder structure. The current proto-type ladder that uses the MIMOSA5 chips has this many conductors. At the end of the ladder there can be additional mass for cables, drivers and cooling.

[‡‡] The short integration time allows operation of the pixel detector like any other STAR detector, namely one frame associated with one interaction event only. The STAR trigger is delivered 1.6 μs following the collision.

4.8 Support Carriage for Rapid Installation and Removal

A conceptual design has been developed for the support carriage that will permit rapid insertion and removal without moving other detector components. This system is shown in Figure 47 as it will be positioned for operation in the STAR detector system. The PIXEL detector is a small detector at the center of the STAR system. Additional layers of tracking (not shown), the IST and the SSD, lie outside of the PIXEL detector. As shown, the mechanical support and electronic service for the PIXEL detector is located on one end only. The transparent tan structure in Figure 47 represents the support structure that will be permanently installed and supported by the exiting West cone. This provides support for the PIXEL detector and its electronics that slide in as a unit. The structure also supports the middle of the beam pipe so that in fine tuning position the PIXEL detector and beam pipe move as a unit. The detector system shown in Figure 47 allows for rapid removal and replacement while maintaining reproducible position through the use of fully defined kinematic mounts. For simplicity, several existing STAR structures are not shown in the figure.

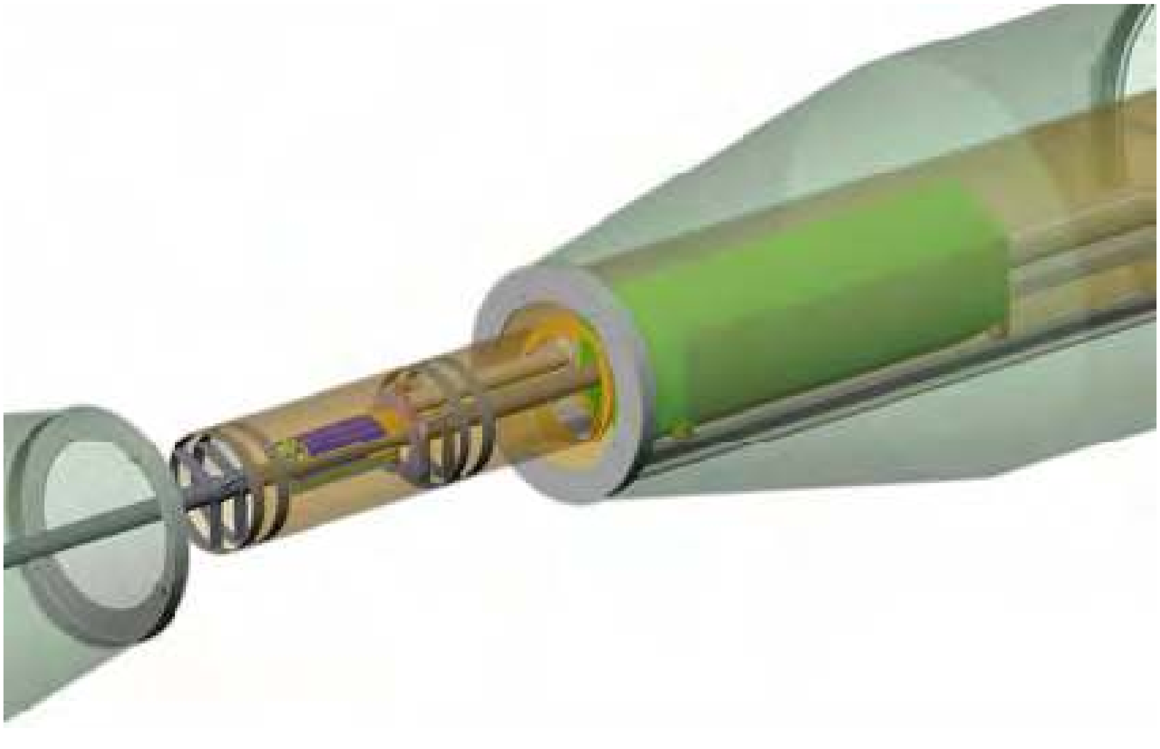

Figure 47: The PIXEL is shown integrated with the STAR inner detectors cone assembly.

A close up view in Figure 48 shows the PIXEL detector ladder arrangement. There are two tracking layers. The design shown in this figure consists of ALICE style thin carbon beams that supports 3 or 4 detector ladders each, one inner radius ladder and two or three outer radius ladders. The ladders are composed of thinned detector chips mounted on a flex PC cable that is backed by a thin carbon composite layer. The carbon beam structures are arranged in three modules with three beams per module.

A cut away view of this PIXEL detector structure is shown in Figure 49. The cooling fin elements which are out of the tracking area provide additional air cooling for the driver heat load at the end of the ladders. Also shown is the 3-point kinematic support for each of the three modules. These kinematic mounts define precise reproducible positions for the ladders.

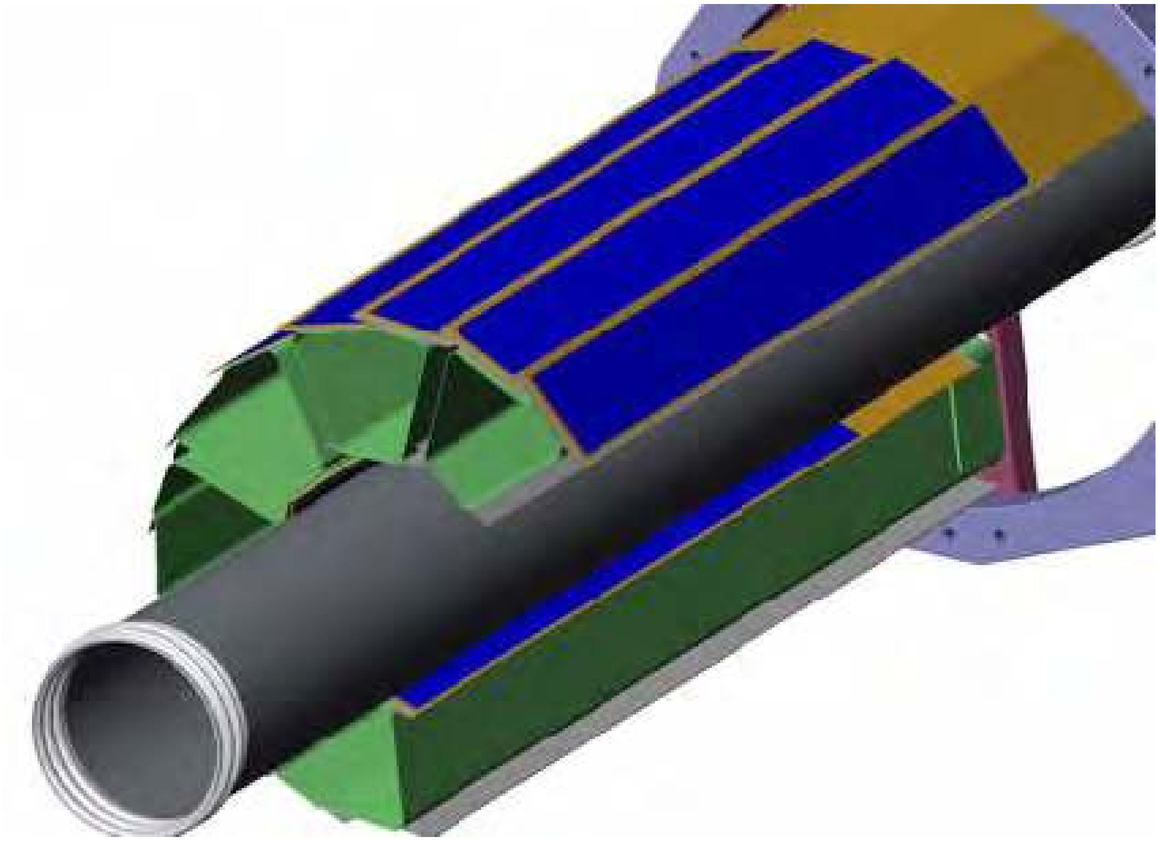

Figure 48: Close up view of the PIXEL ladders. The system is composed of three separate modules, one of which is removed in this illustration.

During installation and withdrawal the modules open up in a controlled path to clear the beam pipe and beam pipe support structures.

4.8.1 Position Alignment and Calibration

The required position resolution of better than 10 μm is a significant challenge for calibration and alignment. The detector system is small and so it permits a design with a single kinematic support to define a reproducible position centered on the STAR system.

With the proposed mechanical design the detector system can be moved as a unit between the visual coordinate measuring system and the docking support in the STAR experiment without disturbing the relative PIXEL ladder positions. The detector silicon will be patterned with a fiducial grid in the top aluminum connection layer. This fine-grained grid will be mapped in 3D with a visual coordinate measuring machine.

The pixel-to-pixel mapping will be preserved through transfer and docking in the middle of the STAR detector system. The calibration burden by track matching will be limited to determining the 6 parameters defining the location of the vertex detector unit within the other STAR detectors. It is expected that success of this approach will require careful temperature control. Further analysis and measurements will quantify this requirement.

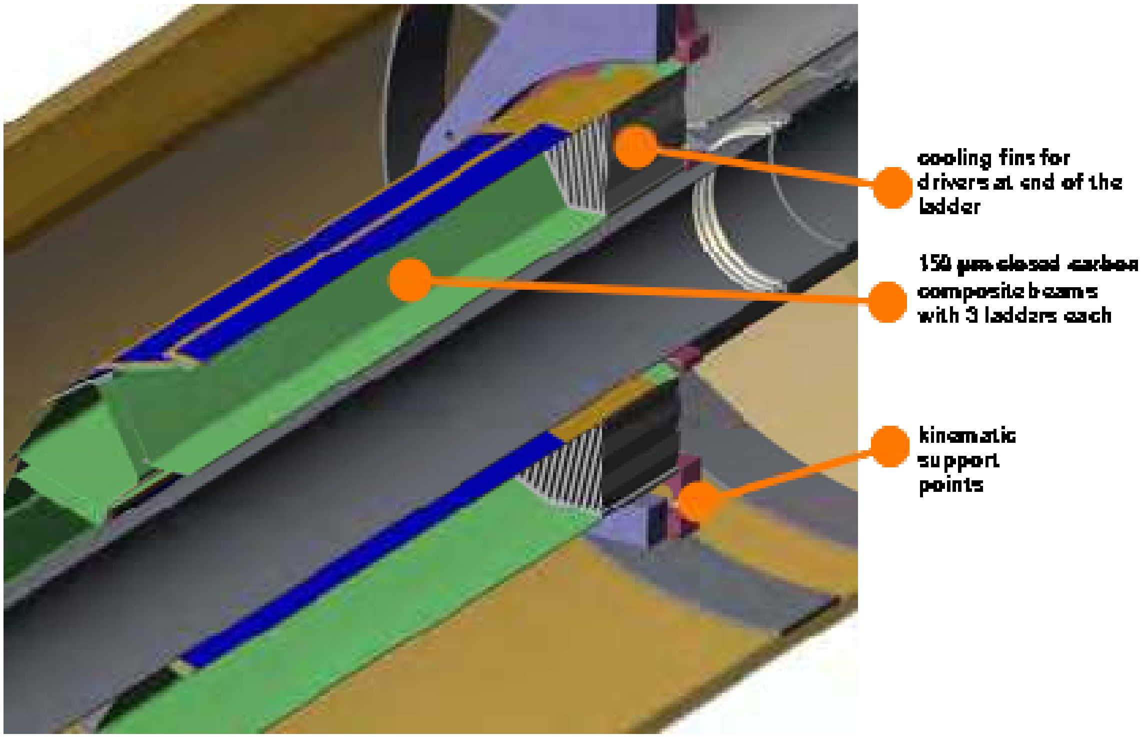

Figure 49: Detector support structure with kinematic mounts to insure repeatable detector positioning.

4.9 Ladder Design and Fabrication

Several ladder designs have been evaluated. One design was composed of thinned silicon on a flex PC Kapton cable bonded to thin composite structure with two skins separated by carbon foam. The radiation thickness of this structure is characterized in Table 17. Analysis of this design shows thermal distortion in excess of our desired goal of 20 microns or less. We are now analyzing the design illustrated in Figure 48 and in Figure

49. This is based on the ALICE design and should provide a more stable rigid structure while maintaining comparable radiation thickness.

Material	Si equivalent (μm)	Material thickness (μm)	% X_0
Beryllium beam pipe	133	500	0.14
Silicon	50	50	0.053
Adhesive	13.4	50	0.014
Cable Assembly	83.9	125	0.089
Adhesive	13.4	50	0.014
Carbon Composite	103	3200	0.11
Total for **one ladder**	264	3475	0.282

Table 17: Materials in the beam pipe and the first detector layer with their total thickness and radiation length. For details see Reference [124].

It was found with test structures that it is relatively straightforward to make wire bonds on these thinned devices where vacuum chucks maintain the sandwich as a flat firm surface. A method to bond the silicon sandwich has been developed using DuPont Pyralux LF thermally activated acrylic sheet adhesive. Advantages of using sheet adhesive include fixed bondline thickness and ease of handling. Other bonding methods including low viscosity epoxies are also under investigation.

A complete ladder using silicon-sandwiches has not been produced yet but we have tested fabrication methods that use a uni-layer silicon structure. We have used vacuum chuck fixturing to butt-join chips side by side against a straight edge and have then bonded to Kapton with Pyralux. This bonded structure was then bonded at room temperature to the carbon beam using Hysol EA9396 aerospace epoxy.

A few μm thick protective polymer, Parylene, will be used to protect the exposed wire bonds and to control the spread of carbon dust. The Parylene coating process is available in the electronics industry. The coating material is applied at the molecular level by a vacuum deposition process at ambient temperature. The thickness is well controlled and it is uniform without pinholes, so protection can be achieved without compromising detector thickness. Application at room temperature avoids introducing stresses that distort the ladder shape.

4.9.1 Detector Radiation Length

Multiple scattering in the beam pipe and the first inner layer of the vertex detector sets the intrinsic limit of precision for vertex resolution. The radiation thickness for an inner ladder and the beam pipe is given in Table 17. The detector ladder is placed at an angle and is quite close to the interaction point so particles pass through the material at varying angles. This results in path length through the materials that is greater than the thickness. Table 17 also shows the thickness and radiation length of a ladder and the beam pipe.

4.9.2 Expected Radiation Exposure

RHIC luminosity projected to 2008 with the assumptions of a 21 week running period and a 60% operating efficiency for Au+Au give a radiation dose of approximately 3.7 kRad/year. This calculation can be found on the web.[125] The materials that we anticipate using in the PIXEL detector are the same as used in much higher radiation environments like the ATLAS pixel detector. One exception is the acrylic adhesive, which exhibits excellent radiation resistance (Radiation Index ~5).[126] Our structure should not exhibit any mechanical degradation from the absorbed dose.

4.10 Ladder Mechanical Tests

4.10.1 Load Distortion Tests

Figure 51 shows an early prototype ladder and detector carrier that we have built. Figure 50 shows a cross-sectional view of the ladder. The mechanical tests have shown that the stiffness and bending characteristics of the assembly are acceptable. For these and similar tests,[127] the ladder's mechanical structure was supported on one end and the surface contours were measured with and without a 10 gram end load using the vision measuring machine at LBNL. The deflection profile is shown in Figure 52 along with the calculated deflection for a simple triangular closed beam. The stiffness is within 20% of expectations from an engineering model. The measured fundamental frequency of the ladder is 140 Hz while the engineering model gives a resonant frequency of 135 Hz and a Q of 45.[128] We have measured the vibrational environment at the STAR detector and it is dominated by low frequencies and so we anticipate that the ladders with the stiffness of our test structure will maintain a relative position to each other of better than a micron.[129]

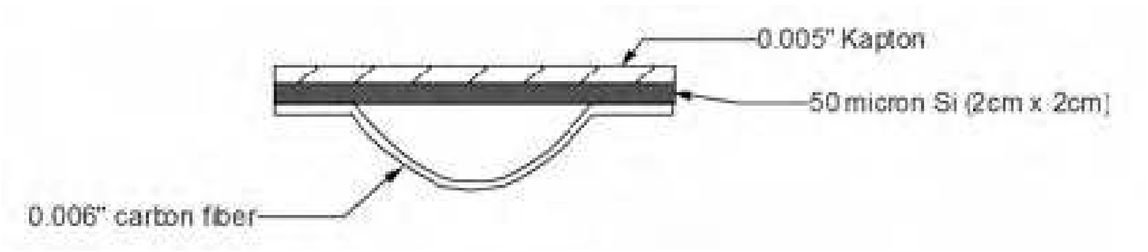

Figure 50: A cross-section of the prototype detector ladder showing its structure and materials.

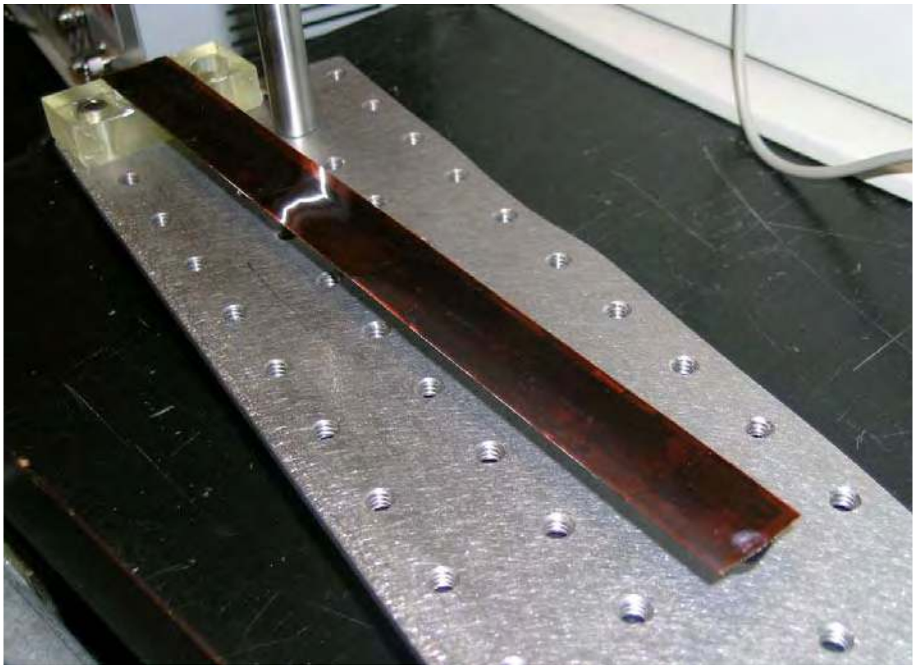

Figure 51: Early prototype ladder and detector carrier.

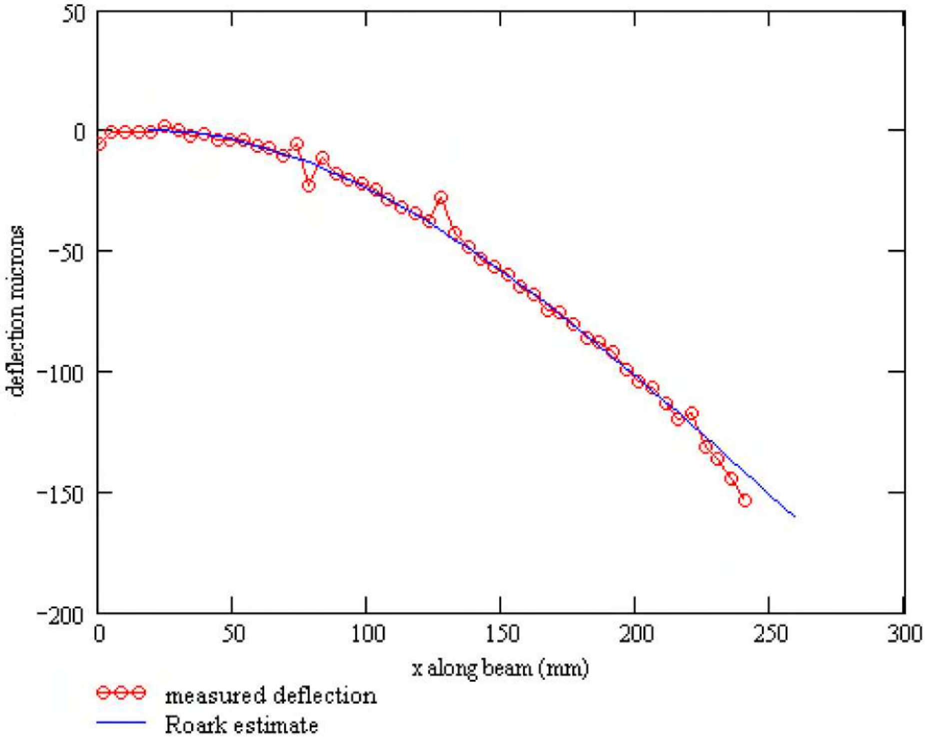

Figure 52: Measured bend of a silicon/carbon composite ladder test structure and the calculated bend shape. The ladder was rigidly supported at one end with a 10 gram weight placed on the other.

4.10.2 Thermal Distortion Tests

We have measured thermally generated deflections using TV holography.[130] This tool, available to us, courtesy of the ATLAS Pixel project, provides a rapid visual distortion map on the sub micron scale. This is proving to be a useful tool for identifying and understanding different design parameters. Measurements are done on structures thermally isolated in a transparent box as shown in Figure 53. This tool will also be used to test the stability of the final detector.

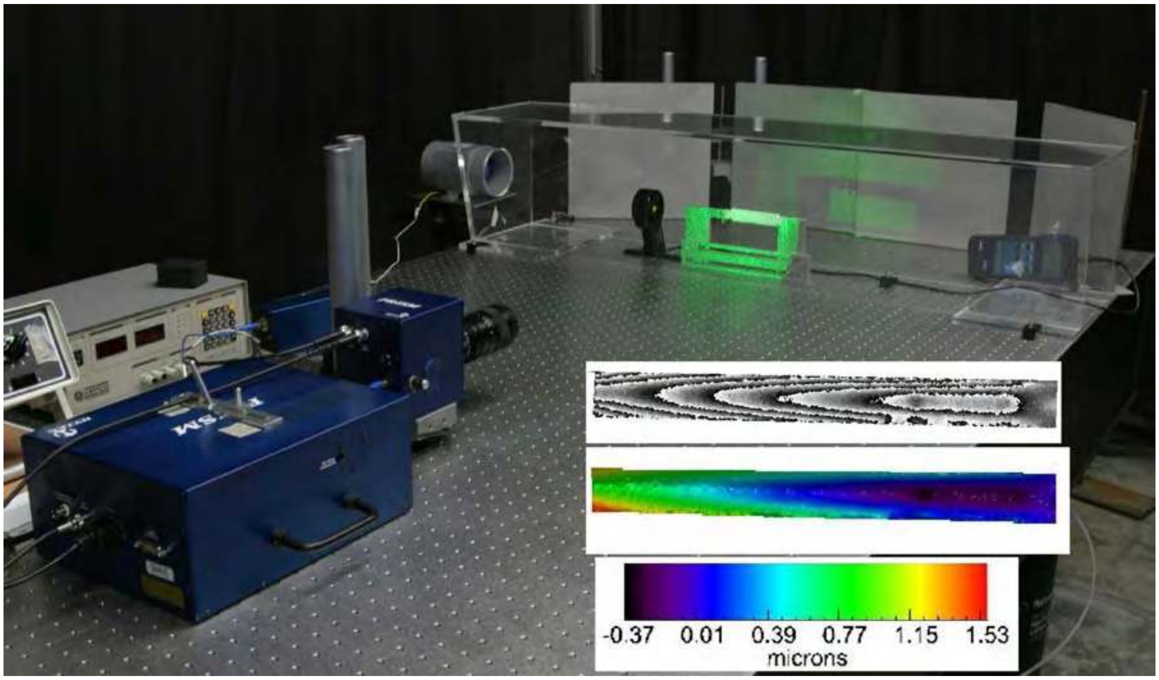

Figure 53: TV Holography system viewing test ladder in a small transparent wind tunnel. Inset shows diffraction pattern with color map of the surface displacement.

4.10.3 Cooling Measurements

In the interest of low mass, the detector system is being designed to use air cooling for the detector structure in the active tracking volume. A small wind tunnel has been constructed (see Figure 53) to evaluate the cooling capacity of air and the design of the system. Measurements with resistive heated ladder test structures and thermocouple readouts show that air velocities on the order of 1 m/s are sufficient to handle power levels of 150 mW/cm^2. This setup, with its thermal camera, will be used to check operating silicon-ladder-devices to evaluate localized heating issues. In addition to cooling tests the wind tunnel is being used to evaluate the vibration stability of the ladder design under the required wind flow conditions. The amplitude of cooling air driven vibrations in the ladder is measured with non-contact capacitive probes[131] and if necessary specific vibration modes can be monitored with the TV holography system. The vibration induced by the air cooling gives an acceptable positional location σ of 1.6 μm. The low mass ladder structure is the critical design element requiring vibration testing, but the full detector structure will be evaluated with this system as well.[132] Additional information on the cooling studies is available on the web.[133]

4.11 Cabling

Connection to the detector readout chips will be done with an aluminum Kapton cable. The cable is part of the ladder and is located underneath the pixel chip. It will carry power, clock, analog signals and control. We have found a commercial vendor that makes aluminum cables with vias. Fabrication tests have been done with 0.35 mil aluminum with 1 mil Kapton plus two 1 mil acrylic adhesive layers. Wire bonding tests with this material have been successful.

Figure 54 shows the prototype for a PIXEL readout cable. The prototype is an active cable with a buffer and differential amplifier for each sector of 10 MIMOSA-5 detectors. The final detector readout cable will not have the components shown, will be narrower, and will be slightly wider than the detectors themselves to allow wire bonding. The cable in the figure uses a copper conductor on a 25 μm Kapton insulator. The final cable will be a 4-layer low-mass aluminum conductor cable with a radiation length equivalent of 84 μm of Si. The prototype has been successfully tested and is working in our prototype ladder readout system. Additional and more recent information on cable and ladder developments may be found on the web.[134]

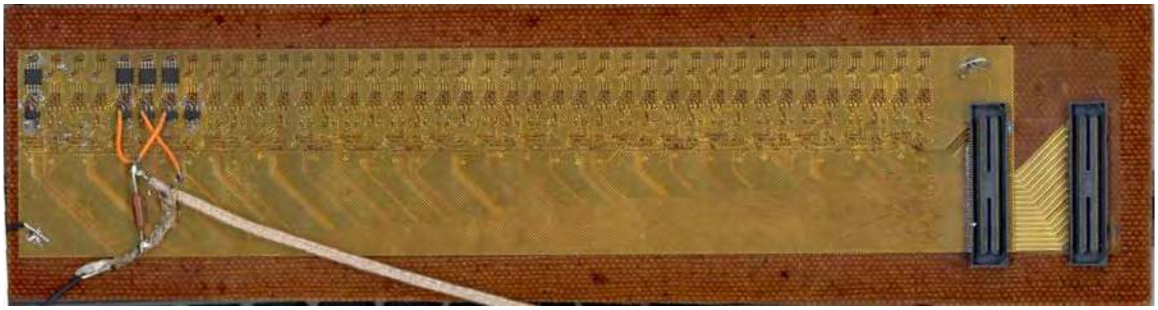

Figure 54: A prototype readout cable for the PIXEL.

Figure 55 shows a mechanical prototype with 4 MIMOSA-5 detectors glued to the Kapton cable assembly with a thin acrylic film adhesive. The adhesive has a bond line of 50 μm. The MIMOSA is relatively flat in horizontal direction but has a “dish” shape in the vertical (y) direction. The magnitude of these distortions is, however, quite small. The largest deviation from a linear fit in y is only ± 6 μm. This low rate of deformation will allow us to make a minimum number of measurements of the detector positions on the ladders in order to locate the individual pixel position to the required accuracy by a parameterized location function.[135]

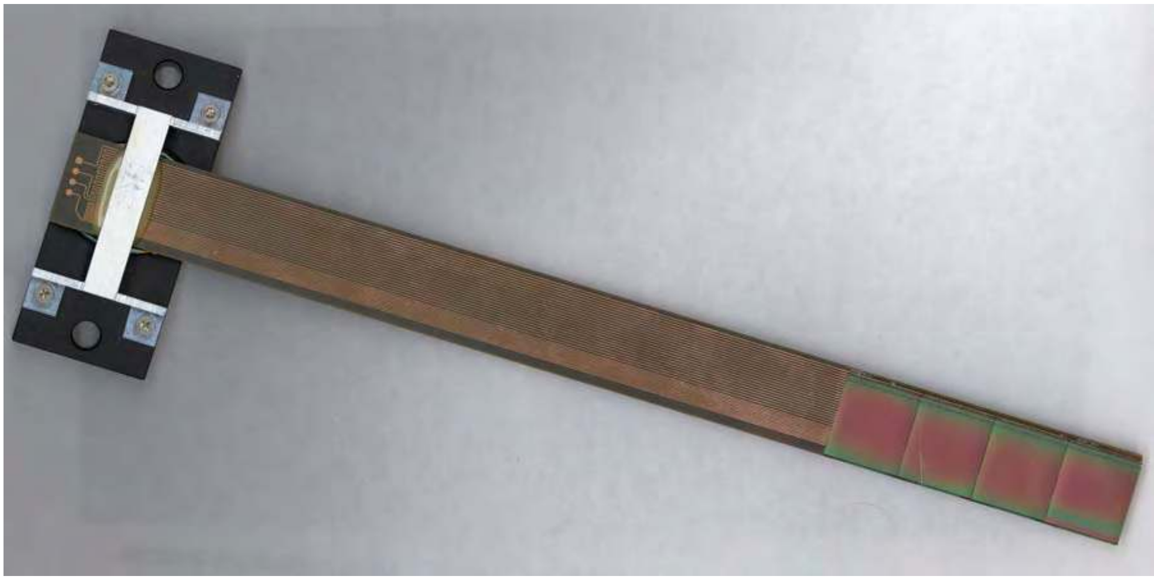

Figure 55: Mechanical Prototype with 4 MIMOSA-5 detectors glued to the Kapton cable assembly.

4.12 Data Acquisition and Readout

We are designing the readout and data acquisition system for the PIXEL in two stages. These stages follow the development of the silicon sensors in our project. The initial prototype readout system is designed to read out the MIMOSTAR-4 detectors which have analog outputs and a 4 ms readout time. The second stage is for use with the final Ultimate series sensors, which have a digital output and a 1 ms readout time but only a 200 μs integration time. The goal of the first stage is to develop much of the infrastructure for doing cluster finding and data sparsification, the interfaces to trigger and DAQ and the mechanical readout structures and assemble a working prototype detector with the MIMOSTAR-4 sensors. The second stage would make use of the development that we have done with the prototype detector and integrate the Ultimate series sensors with a developed readout system.

4.13 Requirements and Prototype Design

The requirements for the prototype and final readout system are very similar. They include:

- Triggered detector system fitting into existing STAR infrastructure and interfaces to the existing Trigger and DAQ systems.
- Deliver full frame events to STAR DAQ for event building at approximately the same rate as the TPC.
- Reduce the total data rate of the detector to a manageable level (< TPC rate).

We have designed the prototype data acquisition system to read out the large body of data from the individual MIMOSA-4 sensors, to digitize the signals, to perform data compression, and to deliver the sparsified data to an event building and storage device. A summary of the specifications and requirements is provided in Table 18.

Total number of pixels	1.35×10^8
Number of pixels per chip	640×640
Pixel readout rate (analog output)	2×50 MHz / chip
Readout time per frame	4 ms
Frame integration time	4 ms
Noise after correlated double sampling	10 e^-
Maximum signal	900 e^-
Dynamic range after correlated double sampling	8 bits
Total sensor power consumption (24 33 ladders)	90 132 W

Table 18: Prototype Stage Requirement Summary - constraints for the MIMOSTAR-4 APS.

Digitizing the analog signal on each pixel into a 12 bit digital signal yields approximately 1.2 Gb/s per sensor chip when read out in 4 ms. Thus, the total front end data rate is ~50.7 GB/s. Clearly, the volume of data must be reduced before being passed to the DAQ event builder and written to storage.

Data compression is achieved by performing correlated double sampling (CDS) i.e. subtraction of two consecutive frames followed by zero suppression. CDS cancels out fixed pattern and reset noise and reduces 1/f noise. The fixed pattern noise corresponds to the spread of the baseline voltage in all pixels. It has been measured on the MIMOSA-5 chip to be 2000 electrons. The noise remaining after CDS must be on the order of 14 e^- to guarantee an efficiency of greater than 98%. The maximum signal is estimated from dE/dx calculation and by measuring how the charge spreads over pixels. The signal can be truncated above 900 e^- without compromising either the efficiency or the position resolution, so 8 bits is a sufficient dynamic range for signal storage. A synchronous cluster finding algorithm and the reduction of the data to addresses of cluster center pixels reduce the data to a manageable rate.

4.14 Architecture for the Prototype System

The basic flow of a ladder data path starts with the APS sensors. A PIXEL ladder has 10 MIMOSTAR-4 APS chips each with a 640 by 640 pixel array. Each chip is divided in half with two sectors each containing a separate analog, differential current output buffer. The chips are continuously clocked at 50 MHz and the data is read out, running serially through all the pixels connecting them to the output buffer. This operation is continuous during the operation of the MIMOSTAR detectors on the PIXEL ladder. Analog data are carried from the two 50 MHz outputs in each sensor in parallel on a low mass ladder flex printed circuit board to discrete electronics at the end of the ladder and out of the low mass detector region. This electronics performs current-to-voltage conversion and contains buffers and drivers for the clocks and other control signals needed for ladder operation.

Each MIMOSTAR detector requires a JTAG connection for configuration of the chip, power, ground and a 50 MHz readout clock. These signals and power as well as the analog outputs and synchronization and marker signals from the detectors are carried via a low mass twisted pair cable from the discrete electronics at the end of the ladder to the readout electronics located about 1 meter from the PIXEL ladders. There is one readout board per PIXEL ladder. A functional diagram of a PIXEL ladder and a description of the data flow are shown in Figure 56.

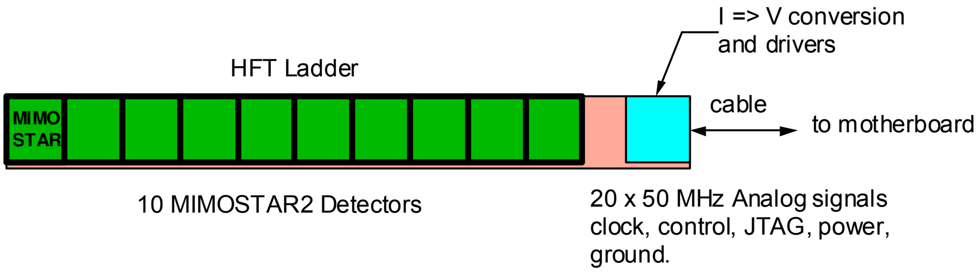

Figure 56: Ladder Layout - sketch of the readout-topology on a detector ladder. This figure shows the ten APS and the corresponding current to voltage conversion and driver electronics. The drivers will be located out of the low mass region of the detector and may require additional cooling.

The readout electronics currently consist of a motherboard and daughter card configuration. A functional block diagram is shown in Figure 57. There are 3 daughter cards per motherboard and each daughter card is capable of servicing 4 of the MIMOSTAR sensors on the ladder. The analog signals are carried to the daughter cards where they are digitized with a 12-bit ADC at 50 MHz. Following digitization, ADC values are passed synchronously to an FPGA for CDS. Performing CDS requires that a data sample be stored for each pixel of the detector. This requirement drives the need for external RAM on the daughter cards. After CDS and pedestal subtraction, 8 bits are used to represent the data. The data is then transferred to the next stage for hit finding and data reduction.

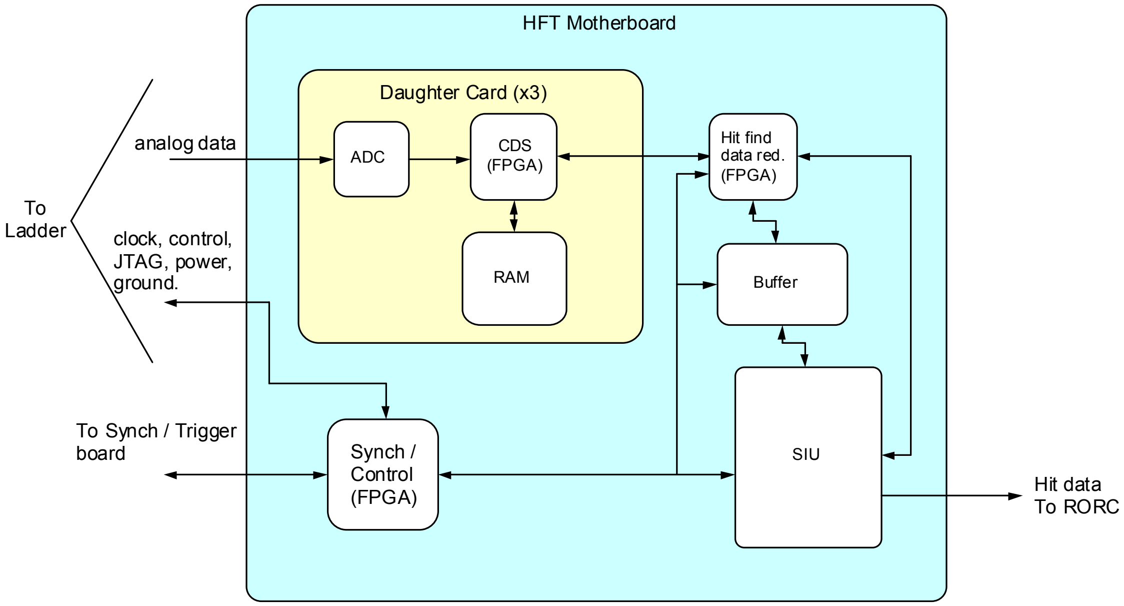

Figure 57: Prototype DAQ Layout: schematic of DAQ system for a single MIMOSTAR-4 ladder. Analog data is carried as differential current on the low mass cable at 50 MHz. The signals are driven in parallel over short (~1m) twisted pair cables to the motherboard. Analog to digital conversion, CDS and data reduction are performed in the Motherboard/Daughter cards. The reduced hit data is transferred digitally to the SIU and carried to Linux based readout PCs via an optical fiber. Control, synchronization, and event ID tagging are accomplished in the Control/Trigger FPGA on the motherboard.

The 8-bit data data exiting the CDS stage are resorted on the fly to be a traditional raster scan through the pixels of the sector. This stream of rasterized data can then be passed to the cluster finder. We are currently investigating methods of hit finding and data reduction for use on the motherboard. A simple readout of the address of a center pixel high threshold hit with the surrounding 8 pixels meeting additional cluster selection criteria such as at least 1 cell over the low threshold is our default approach. This can be implemented in an FPGA and run as a pipeline filling the output buffer with center pixel address values. A simple example of an FPGA logic diagram that accomplishes this can be seen in Figure 58. We are also investigating a number of cluster selection methods including summing algorithms around different thresholds and center pixel determination by geometric pattern with high and low thresholds. A preliminary study of some simple cluster finding algorithms that can be implemented in FPGA shows promising results for efficiency and noise rejection. A sample of these results is shown in Figure 59 and Figure 60 where one can see that the efficiency and fake hit rate for a low threshold crossing in one of the surrounding 8 pixels of a 9 pixel cluster candidate is comparable to a much more complex ADC sum for a reasonable range of cuts and provides greater than 99 percent efficiency with an accidental rate of less than 10^{-4}.

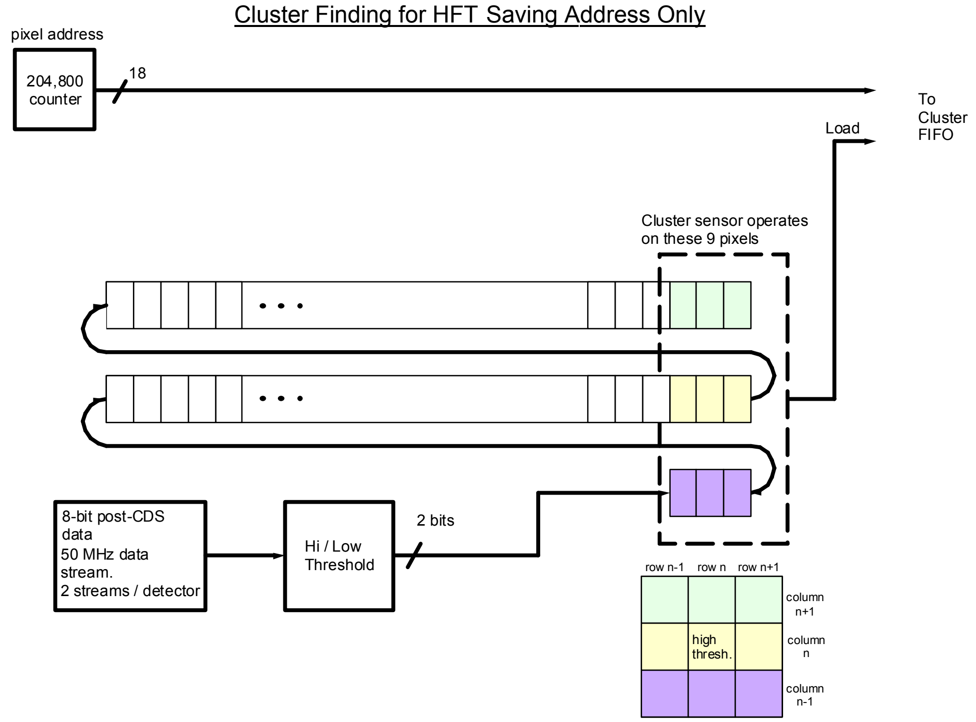

Figure 58: A simple cluster finding algorithm for the PIXEL detector. ADC data from two MIMOSTAR detector columns + 3 pixels are sent to a high/low threshold discriminator. The resulting 2 bits are fed sequentially in an 2-bit wide shift register. The center pixel of a 3 × 3 pixel window is compared to a high threshold with each clock tick. If the threshold is exceeded, the additional cluster identification criteria are checked for the 3 × 3 pixel window. If the results meet the critera for a cluster, the center pixel address is stored into a readout FIFO.

The reduced data are then buffered and transferred to the STAR DAQ system over a high-speed bi-directional fiber link. We intend to use the Source Interface Unit (SIU) and Readout Receiver Cards (RORC) developed for ALICE as our optical link hardware to transfer data to and from the STAR DAQ system. These links have been chosen as the primary readout connections for the new STAR TPC FEE. Leveraging existing hardware and expertise in STAR allows for a faster and more reliable design than developing our own custom solution. The complete system consists of a parallel set of ladder readouts consisting of 33 separate chains.

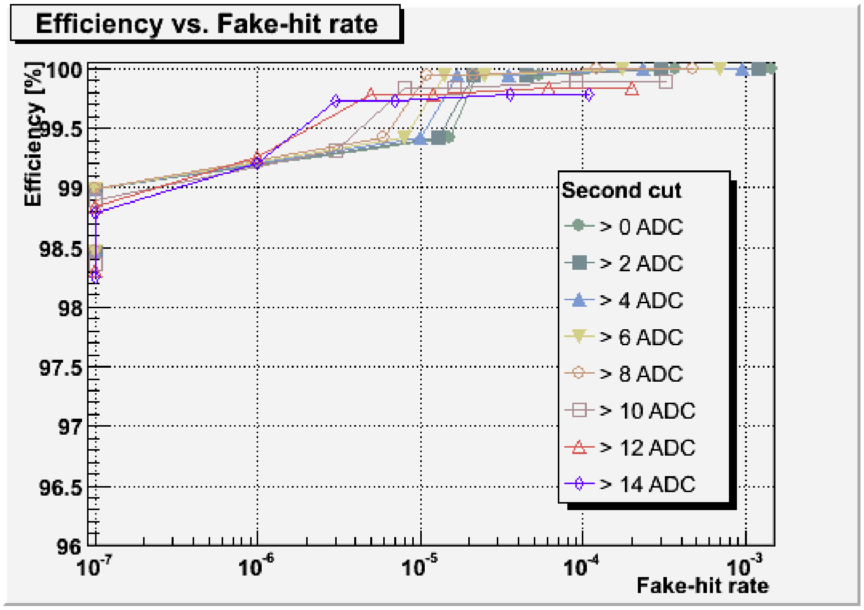

Figure 59: Efficiency versus accidentals and fake hit rate as a function of cuts for a standard cluster finding algorithms run on cluster data from a MIMOSA5 detector. Note that some parameter combinations of this algorithm are already over 98% efficient with consisting of a accidentals rate of 1-2 hits / cm^2 high center pixel ADC and a sum of the surrounding eight pixels in a 3 × 3 pixel box. Center pixel ADC cut runs from 15 to 8 and is denoted by the markers. The color of the line denotes the cut on the 8 surrounding pixel sum.

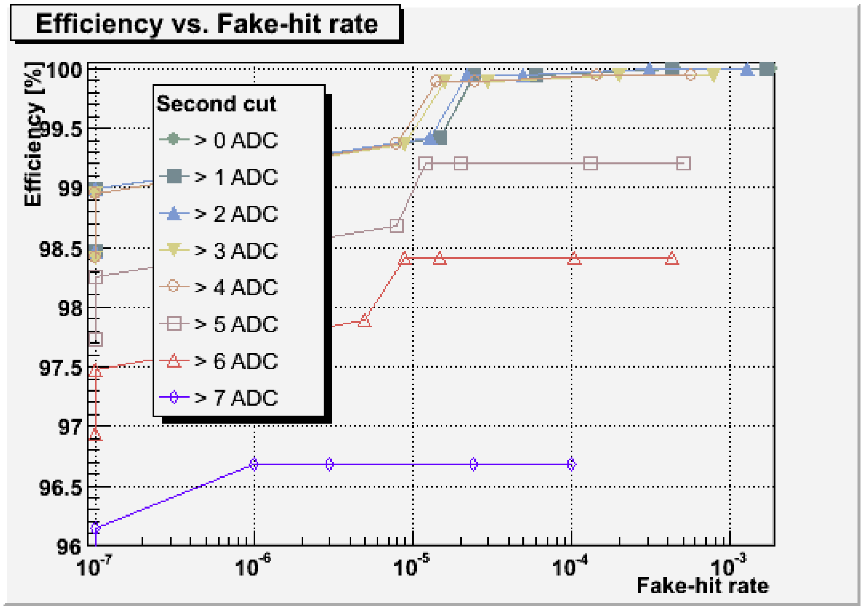

Figure 60: Efficiency and fake hit rate as a function of cuts for the proposed cluster finding algorithm with a high threshold crossing in the center pixel and a low threshold crossing in any of the surrounding eight pixels in a 3 x 3 pixel box. For a reasonable range of cuts, this algorithm is quite comparable to the traditional ADC sum method.

4.15 Data Synchronization, Readout, and Latency

The readout of the prototype PIXEL sensors is continuous and hit and cluster finding is always in operation during the normal running of the detector. The receipt of a trigger initiates the saving of the found clusters into a FIFO for 1 frame (204,800 pixels). The PIXEL detector as a whole will be triggered via the standard STAR TCD module. Since 4 ms are required to read out the complete frame of interest, the data will be passed to DAQ for event building ~ 4 ms after the trigger is received. We will provide multiple buffers that will allow the capture of temporally overlapping complete frames. This will allow us to service multiple triggers within the 4 ms readout time. A functional block diagram of this system is shown in Figure 61. In this system, the cluster data is fanned out to 5 Event FIFOs. A separate Event FIFO is enabled for the duration of one frame upon the receipt of a trigger from the TCD. Subsequent triggers enable additional event FIFOs until all of the event FIFOs are full and the system goes busy. The resulting separate complete frames are then passed to STAR DAQ as they are completed in the Event FIFOs. This multiple stream buffering gives a system that can be triggered up to the expected rate of the STAR TPC (approximately 1 kHz) after the DAQ1K upgrade. This will result in the duplication of some data in frames that overlap in time, but our data rate is low and the duplication of some data allows for contiguous event building in the STAR DAQ, which greatly eases the offline analysis. In addition, synchronization between the ladders/boards must be maintained. The PIXEL will receive a clock via the standard STAR TCD and will derive its internal clocks from the RHIC strobe. We will provide functionality to allow the motherboards to be synchronized at startup and any point thereafter.

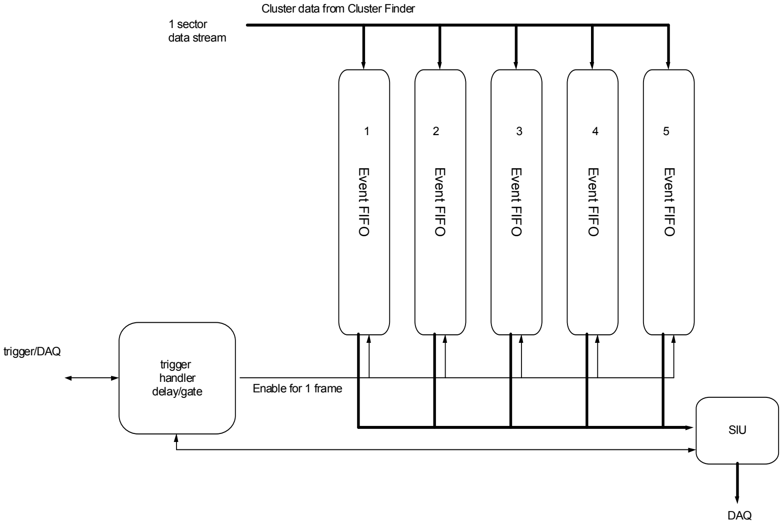

Figure 61: Multiple event FIFOs are fed in parallel from the cluster finder. A separate Event FIFO is enabled for one frame upon the receipt of a trigger from the TCD. The resulting separate complete frames are then passed to STAR DAQ as they are completed in the Event FIFOs.

4.16 Data Rates for the Prototype RDO

The ADC data rate from each 640 × 640 MIMOSTAR detector is approximately 4.9 Mb per frame or 1.2 Gb/s. The total rate of raw ADC data entering the processing chain in the detector is thus approximately 50.7 GB/s. After CDS, the data can be represented by 8 bits. Pixel addressing within a sector requires 18 bits. The sector-in-ladder address will be accomplished as address words in the data stream. Ladder address will be added at the DAQ receivers. This covers the address space to map the detector pixel space. Each cluster word stored in the FIFO contains the 18 address bits of a cluster central pixel. Combining this with the occupancy per layer, the average number of pixels per cluster, the overhead for event format and headers and the readout rate of 1 kHz (with data duplication in the event FIFOs) gives an event size of 285 kB and data rate from the detector of 285 MB/s. Figure 62 shows this graphically. The parameters used for the data rate calculation are shown in Table 19.

Item	Number
Bits/address	18
Inner ladders (r=2.5 cm)	9
Middle ladders (r=6.5 cm)	12
Outer ladders (r=7.5 cm)	12
MIMOSTAR sensors per ladder	10
Average hits/sensor, inner (2.5), $L = 10^{27}$	212
Average hits/sensor, outer (6.5), $L = 10^{27}$	43
Average hits/sensor, outer (7.5), $L = 10^{27}$	35
Average Pixels / Cluster	2.5
Trigger rate	1 KHz

Table 19: Data rate calculation parameters. Note that the hit rates are normalized to $L = 10^{27}$. This is for comparison over different readout scenarios that happen at different times. The number should be scaled appropriately to RHIC II luminosities for final hit densities.

4.17 Requirements for the Ultimate Design

The Ultimate series of APS detector will incorporate several changes from the previous MIMOSTAR versions. The primary changes include on-pixel CDS and a two level programmable discriminator applied to the CDS output for each chip. The Ultimate chip will be read out digitally in 2 bit words per pixel through 4 LVDS outputs per chip. The control functions for the chip are still via the JTAG interface. A summary of basic requirements is given below:

Physical

- 640 x 640 pixels with 30um pitch.
- Minimum of 3 fiducial marks / chip for optical survey purposes.
- All bonding pads located along 1 side of chip.
- Two bonding pads per I/O of the chip for probe testing before sensor mounting.

Electronic

- Continuous cycling 100-200 µs integration time.
- Trigger input reads out the previous 200 µs integration window.
- On chip CDS for the pixels.
- On chip JTAG programmable discriminator thresholds, biases, etc.
- 4 LVDS readout channels / chip with a full readout time of less than 1 ms.
- JTAG programmable testing modes.
- Appropriate flags for readout synchronization, e.g. first pixel marker.
- Synch input to start chip function.
- Signal/Noise > 9 at operating temperature of 30 degrees C.
- Maximum average power dissipation of 100 mW/cm^2.

This system readout is different from the previous MIMOSTAR-4 based readout but most components are the same.

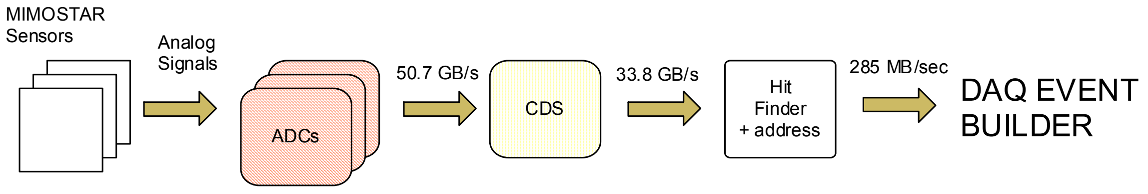

Figure 62: Data rates at the various stages of the Prototype MIMOSTAR-4 readout chain.

4.18 Architecture for the Ultimate System

In this system, much of the functionality of the daughter cards has been moved into the Ultimate sensors themselves. The correlated double sampling and dual level discriminator functionality are now integrated onto the sensor and there are 4 LVDS readout lines per chip. The rest of the system, however, remains substantially the same. A revised functional block diagram is shown below in Figure 63.

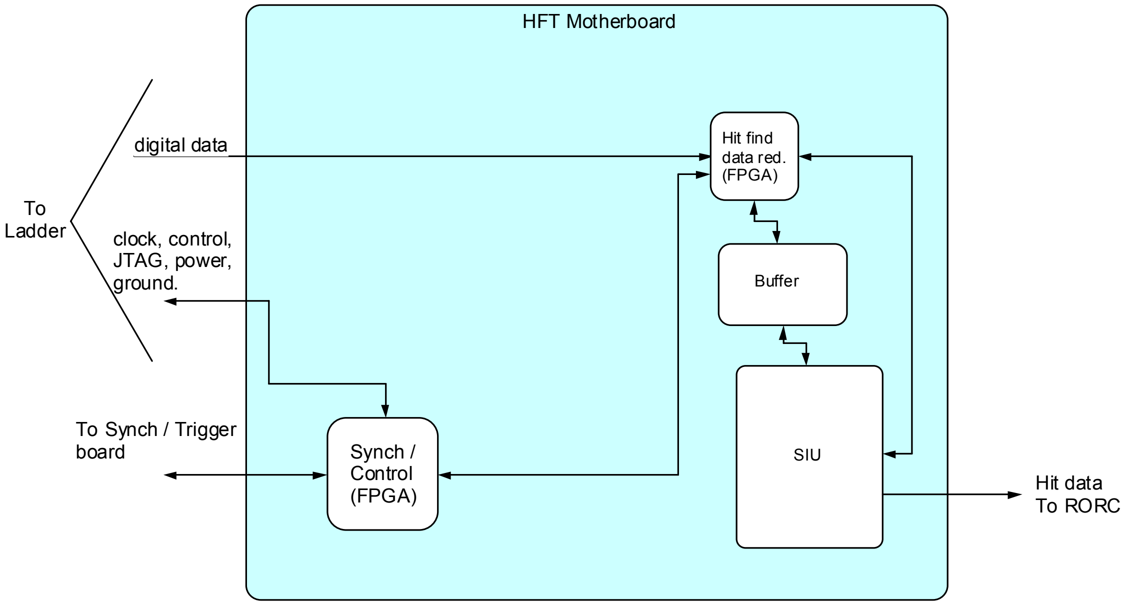

Figure 63: Functional block diagram for Ultimate sensor based readout system.

4.18.1 Data Flow

The Ultimate sensor readout system is a parallel system of 33 ladders, each with the same readout, thus the readout system for a single ladder is presented as the basic building block of the system. In this readout design, the sensors are as described above and are triggered. Triggers, clock, JTAG, Synchronization and markers are provided from the readout board. After receiving a trigger, the sensors perform a high/low threshold compare to the CDS value for each pixel and send a serial stream of the logic values results of this threshold comparison through LVDS buffers located at the end of the ladder (out of the low mass region) to the readout board via low mass twisted pair cable. On the readout board the data is transferred into high speed memory located in an FPGA. This memory now contains the full contents of each pixel on the sensor represented by a 2 bit string with the hot pixel map implemented as a mask. The sensor threshold data is then run through a cluster finder with the same form as previously described in our readout system and the resulting center address is passed to a cluster FIFO. The contents of these cluster FIFOs are built into an event with header and event ID information and the resulting event is passed to DAQ via the DDL.

4.18.2 Timing and Implementation

The proposed time structure of the readout is shown in Figure 64.

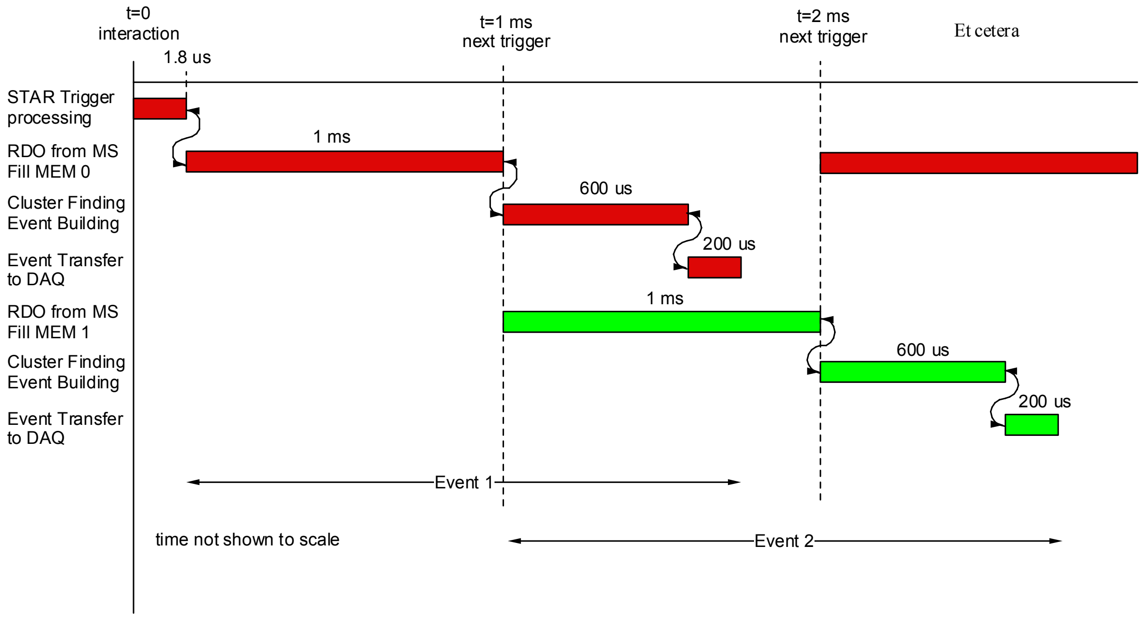

Figure 64: Proposed time structure of the MIMOSTAR Ultimate readout. To meet the 1 KHz trigger requirement, we require two memory buffers to allow for immediately retriggered readout of the sensor.

The requirement of servicing a 1 kHz trigger combined with the 1 ms readout time of the sensors drives us to implementing two full sensor readout buffers in a ping-pong configuration. Data resorting, if required, will be implemented in the memory controller to give a raster scan data image in the memory. The hot pixel map will also be implemented as a mask in the memory. Unlike the synchronous analog readout cluster finder, which operates on the readout clock (50 MHz), the cluster finding for the Ultimate sensor can run at implementation speed in the FPGA which is significantly faster. The event building readout into the event buffer similarly will run at FPGA implementation speed. Data transfer through the DDL is fast and additional event FIFO buffers can be implemented if needed. Both, read-out time and deadtime can be improved by moving zero-suppression on the chip. Future designs will reflect this.

It is important to note that current FPGAs have significant memory block resources. The Xilinx Virtex-5 can be purchased in configurations that have 11.664 Mbit of block memory and 550MHz internal clock distribution.[136] We could implement the entire RDO system for one ladder on two Xilinx Virtex-5 FPGAs in the current technology. By the time this design will be implemented we expect to see further improvements in FPGA technology.

4.19 Data Rates for the Ultimate RDO

We use the same parameters as used in the prototype system data rate calculations but scale the occupancy to reflect the much smaller 200 μs integration time. The rates shown for each RDO system are for comparison under common input parameters, the rates shown may be scaled with luminosity. The data rate from each 640 × 640 Ultimate detector is 102 MB/s. The total rate of raw data entering the processing chain in the detector is thus approximately 3.38 GB/s. Pixel addressing within a sector still requires 18 bits and is padded to 32 bits in our event format. Combining this with the occupancy per layer, the average number of pixels / cluster, and the readout rate of 1 kHz gives an event size of 57 KB and data rate from the detector of 57 MB/s. Figure 65 shows this graphically.

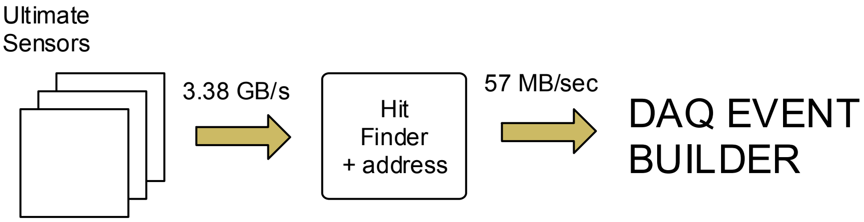

Figure 65: Data rates in ULTIMATE PIXEL readout.

4.20 Prototype Telescope

Several different prototype readout electronics boards have been constructed and tested that are very similar to the proposed prototype readout electronics described above. In Figure 66 one can see the prototyping results of a low mass flex PCB on a ladder with MIMOSA-5 detectors. This prototype flex cable has the signal trace configuration that we expect to use (except in copper conductor rather than aluminum) for the final readout for both the prototype and Ultimate ladder readout.

A prototype readout system for reading the MIMOSTAR-2 sensors was also constructed. The MIMOSTAR-2 sensor is a preliminary prototype for the MIMOSTAR-4 and contains the basic interface and functionality that we expect to have in the first stage prototype detector.[137] We are developing a three MIMOSTAR-2 sensor telescope for test during the 2007 beam run at RHIC. Our goal is to test functionality of a prototype MIMOSTAR-2 detector in the STAR environment. We anticipate gathering information on:

- Charged particle environment near the interaction region in STAR.
- Performance of our cluster finding algorithm.
- Performance of the MIMOSTAR-2 sensors.
- Functionality of our tested interfaces to the other STAR subsystems.

- Performance of our hardware and firmware as a system.
- The noise environment in the area in which we expect to put the final pixel detector.

Figure 66: A prototype ladder showing low mass PCB, MIMOSA5 detectors and driver electronics bonded to a mechanical carbon fiber and reticulated vitreous carbon foam based carrier.

To realize this goal we are assembling a prototype telescope and the mechanical infrastructure and positioning system to allow us to place a 3 MIMOSTAR-2 detector telescope into the STAR magnet near the interaction region. This plan presents challenges in the mechanical, electronics, firmware and infrastructure aspects of assembling and integrating a prototype system into the STAR environment.

Three separate MIMOSTAR-2 chips are mounted in a telescope configuration. This system is controlled and read out into a motherboard mounted to a Stratix development board.[138] Trigger, clock, and DC power come from the STAR TPC detector subsystem cables. This system is meant to be a functional test of our intended prototype PIXEL readout system. A block diagram of the test system is shown in Figure 67.

In this test, the basic data flow is as follows. Triggers are received from the STAR triggering system into the motherboard and processed in the FPGA on the daughter card. MIMOSTAR-2 configuration (JTAG), latch up protected power, clock, sync and reset are provided via shielded CAT-5 cables from the motherboard.[139] The MIMOSTAR-2s will be running in parallel with multidrop LVDS clock and only 1 marker signal is brought out for synchronization. The analog signals and marker signals are transferred from the MIMOSTAR-2 detectors mounted on the flex PCBs[140] via the same CAT-5 cables back to the motherboard and routed to the daughter card[141] for ADC conversion, data resorting, CDS and cluster finding. Cluster addresses or full frame data (raw or CDS) is then routed from the daughter card through the motherboard into the Stratix development board and to our data acquisition Linux PC via the CERN ALICE DDL/RORC modules.

From the DAQ Linux PC, the events are built into the STAR event structure and/or into our own event files.

The hardware used in this test consists of 3 MIMOSTAR-2 detectors mounted on 25 micron Kapton flex PCBs, a motherboard, daughter card, Stratix development board, DDL, DAQ Linux PC and configuration PC. Photographs of the assembled motherboard, daughter card, Stratix development board and DDL, and of the assembled cable are shown in Figure 68 and in Figure 69.

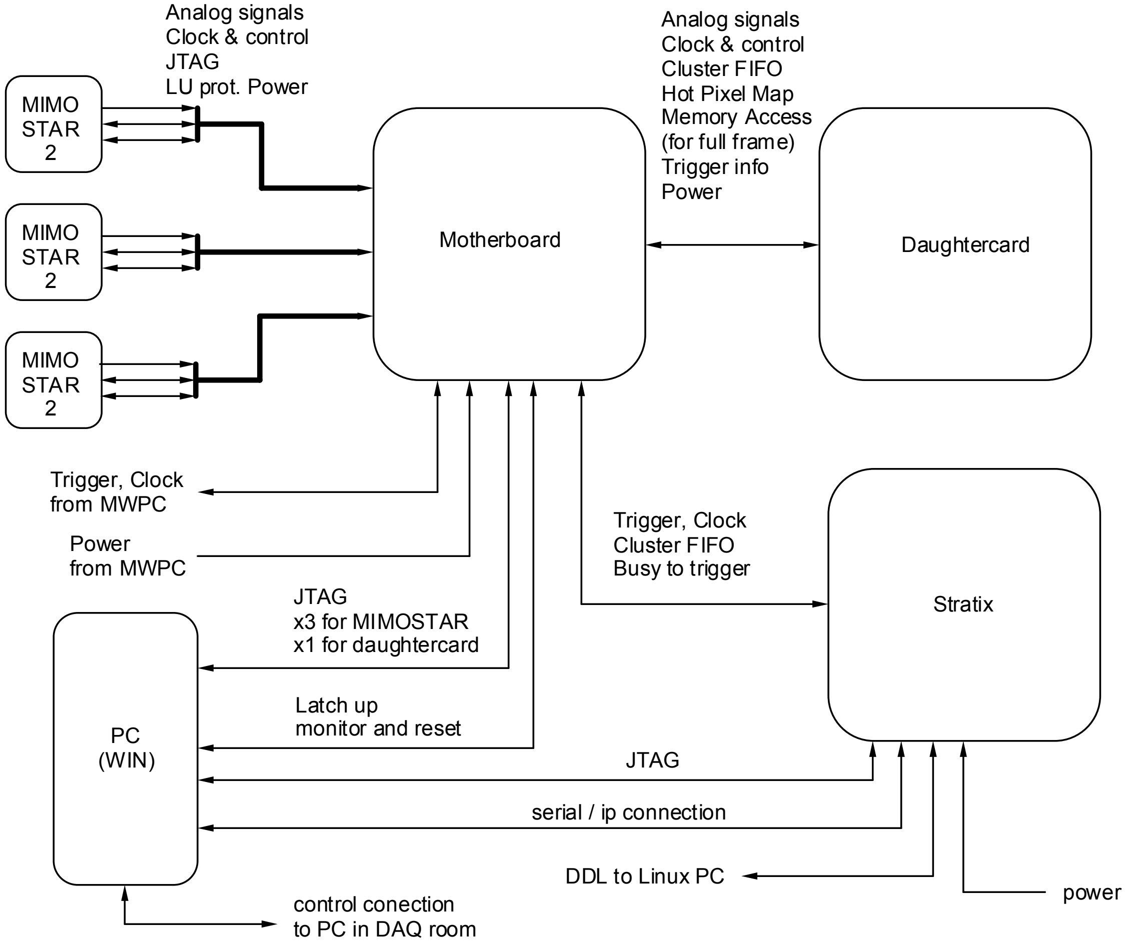

Figure 67: Block diagram for the PIXEL MIMOSTAR-2 three detector telescope to be tested in the STAR 2007 beam run.

The firmware required for this test includes most all of the functionality of the final firmware needed for the full detector. The following basic functionality is required:

Implemented on daughter card

- Accept and respond appropriately to triggers in the STAR trigger system
- SRAM memory controller
- 50 MHz 12-bit ADC serial interface

- Data re-sorter
- CDS
- Full frame readout
- Cluster finding
- Cluster FIFO building

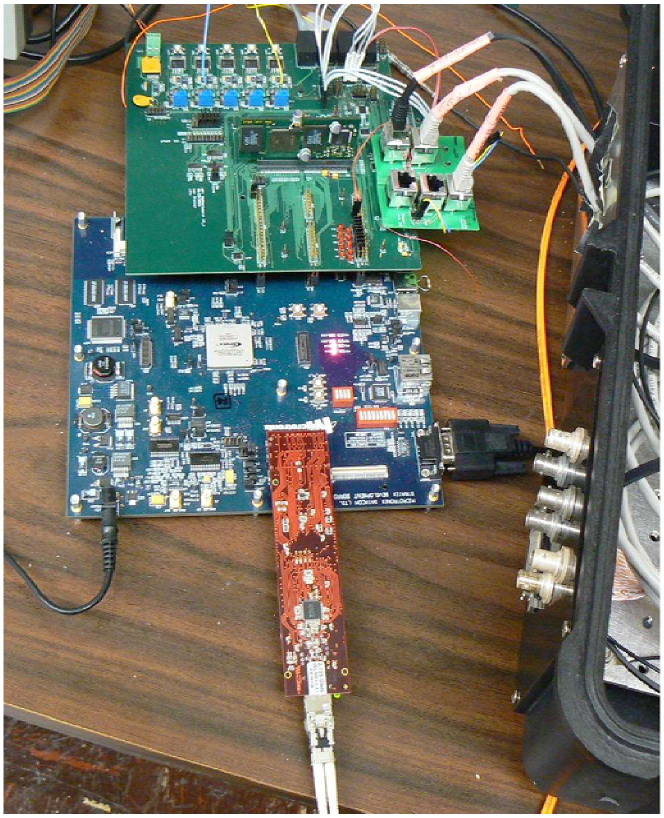

Figure 68: Photograph of PIXEL prototype readout system containing motherboard, daughter card, Microtronix Stratix development board and CERN DDL fiber optic interface module.

Implemented on Stratix board

- Event building
- JTAG configuration of the chained MIMOSTAR-2 chips from the Stratix board
- Interface to control shell
- DDL control and interface
- Latch-up detection and remote reset

Some significant effort is required to insert this telescope into the STAR experiment close to the interaction point. An insertion system, electronics control box and cooling system have been designed and fabricated. The basic system is shown in Figure 70 and in Figure 71.

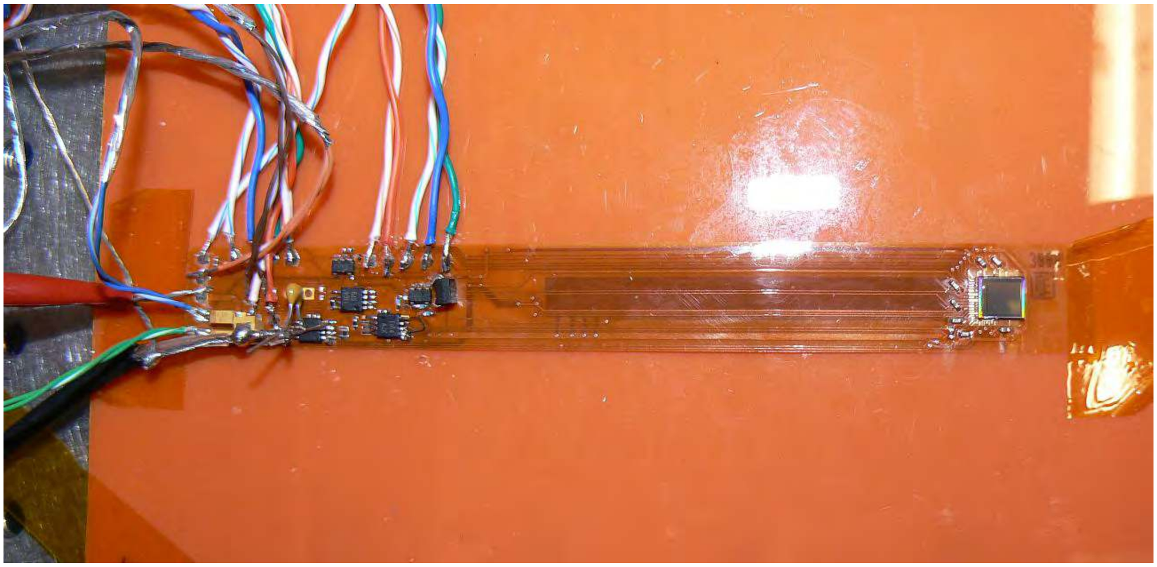

Figure 69: 25 µm Kapton flex cable with MIMOSTAR-2 sensor mounted and bonded. Three of these will be stacked to form a telescope.

Figure 70: Telescope mechanical housing and positioning head. The MIMOSTAR-2 flex cables will be glued to the aluminum support and positioning brackets.

In this diagram, the insertion tube that carries our telescope to a point near the interaction region is shown with respect to the STAR magnet pole tip. The electronics box is mounted in the hole in the pole tip above the beam pipe. Cooling is provided by a vacuum system that draws air past the MIMOSTAR-2 detectors through a tube that also carries our signal cables. The MIMOSTAR-2 detectors on their flex cables will be mounted into a positioning assembly (shown below) that will hold position and protect the telescope as it is slid into the insertion tube.

One can see that this test contains almost all of the required firmware development and experiment interfaces required for both generations of detector.

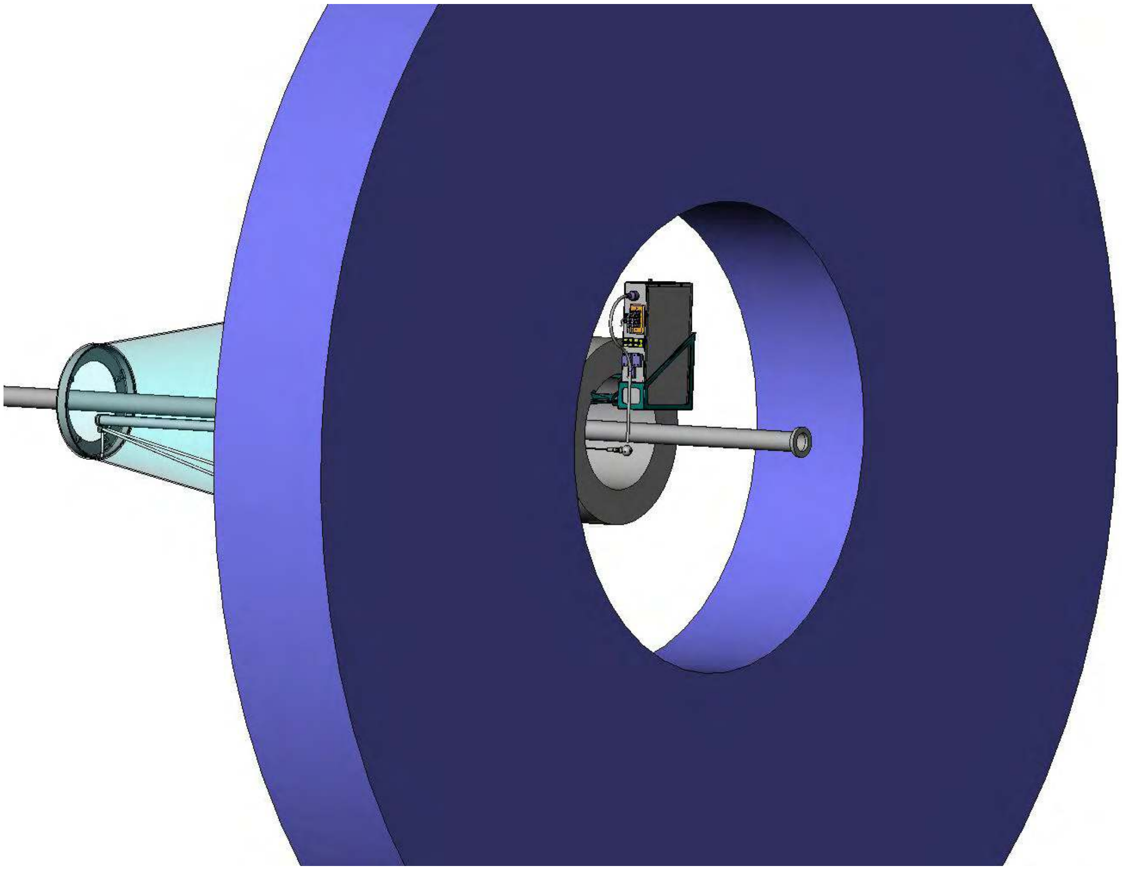

Figure 71: Solid model of telescope insertion system and electronics box position. The large blue toroid is the magnet endcap. The insertion tube is shown below the beam pipe.

5 The Strip Detector (IST)

5.1 Overview

To reach the full physics capabilities of the HFT, PIXEL requires tracks with good pointing resolution at its outer layer. TPC tracks alone provide a pointing resolution of around 1000 μm at the outer layer of PIXEL. The existing SSD yields an improvement only in the r-ϕ direction because of its modest resolution in the z-direction. The SSD layer (at a radius of 23 cm) is relatively far from the outer layer of the PIXEL (at a radius of about 7 cm), which is not optimal for the pointing resolution.

The Intermediate Silicon Tracker (IST) will provide space points with high accuracy in r-ϕ and z. The IST consists of two concentric layers between the PIXEL and the SSD, as shown in Figure 19.

The IST makes use of a combination of standard silicon strip sensors and silicon striplet sensors. The striplet sensors are very similar to the strip sensors but the strip length is halved by an equatorial divide of the sensor to lower the double hit probability. Various technical details draw to a large extent from previous experience on the design and operation of silicon tracker systems such as the PHOBOS silicon tracker stations. The construction of the IST will make use of existing equipment and infrastructure from the PHOBOS silicon tracker through the MIT group.

5.2 Proposed Configuration

The requirements leading to the proposed design come from the overview of the HFT in Section 3.2 and 3.4.

The Intermediate Silicon Tracker (IST) consists of two concentric layers as shown in Figure 72. Each layer will be assembled from ladders. Ladders are the smallest building block of the IST. There are two ladder types, their length determined by the layer they are located in. Having the ladders only cover the rapidity range of interest is the most cost effective solution, but 2 different ladders does complicate the design and production of the ladders. The inner ladders carry one layer of silicon sensors with striplets. The outer ladders carry 2 layers of silicon sensors arranged back to back. Radii, number of sensors per ladder and number of ladders per layer can be found in Table 20.

	Layer 1	Layer 2	Total
Radius sensor [mm]	120	170	
No. of sensors per ladder	10	26	
No. ladders	19	27	
No. sensors per layer	190	702	892
No. readout chips	1,900	3,510	5,410
No. channels	243,200	449,280	692,480

Table 20: Overview of IST layout parameters.

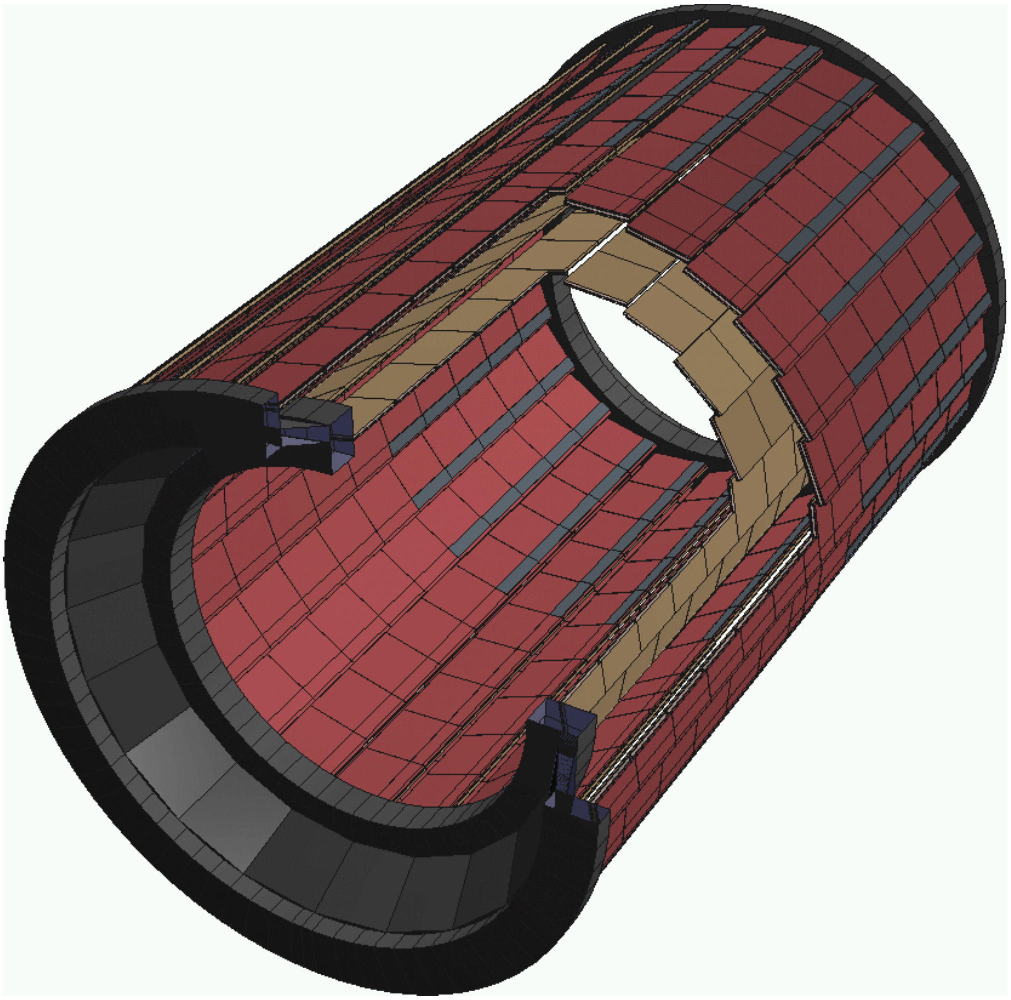

Figure 72: Geometry drawing of the two IST layers.

The anticipated material budget for the two IST layers is shown in Figure 73 and Figure 74. The top plot gives the observed radiation length versus rapidity and averaged over ϕ. The bottom plot is for the radiation length versus ϕ at mid-rapidity. These results where obtained by propagating 100,000 GEANT events through the IST geometry using GEANT 3.21/08 with a realistic estimate for the ladder material and readout cables. The support structures are simplified but should still give an adequate measure of the amount of material. Figure 75 gives the total material budget for the two layers of the IST. The asymmetry in the rapidity plots in Figure 73, Figure 74, and Figure 75 is caused by the readout cables all running in the positive rapidity direction.

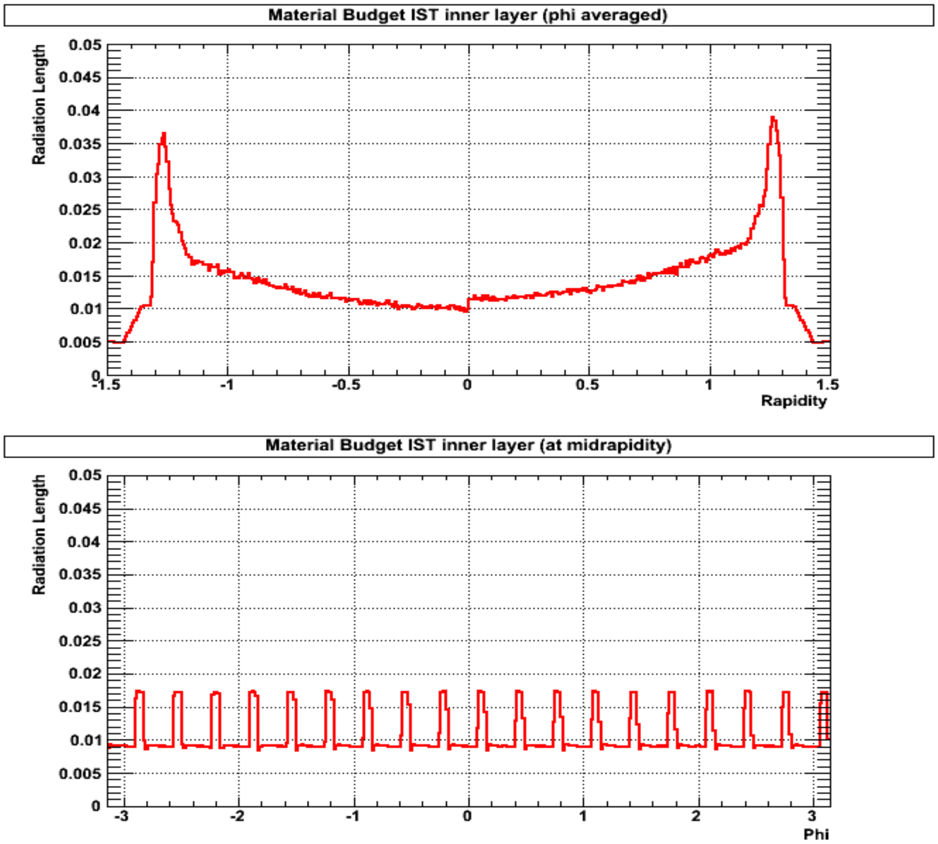

Figure 73: Material budget versus rapidity (top) and ϕ (bottom) for the inner layer of the IST.

5.3 Support Structure

The support structure of the Intermediate Silicon Tracker (IST) will be both mechanically stable and at the same time based on light-weight materials. The amount of dead material determines how performance will be affected by processes like multiple scattering, conversions, delta rays, and nuclear interactions. On the other hand it has to provide a mechanically and thermally stable support for the detector elements. In order to carry out maintenance work and to accommodate a possible staged installation schedule, the structure will be highly modular.

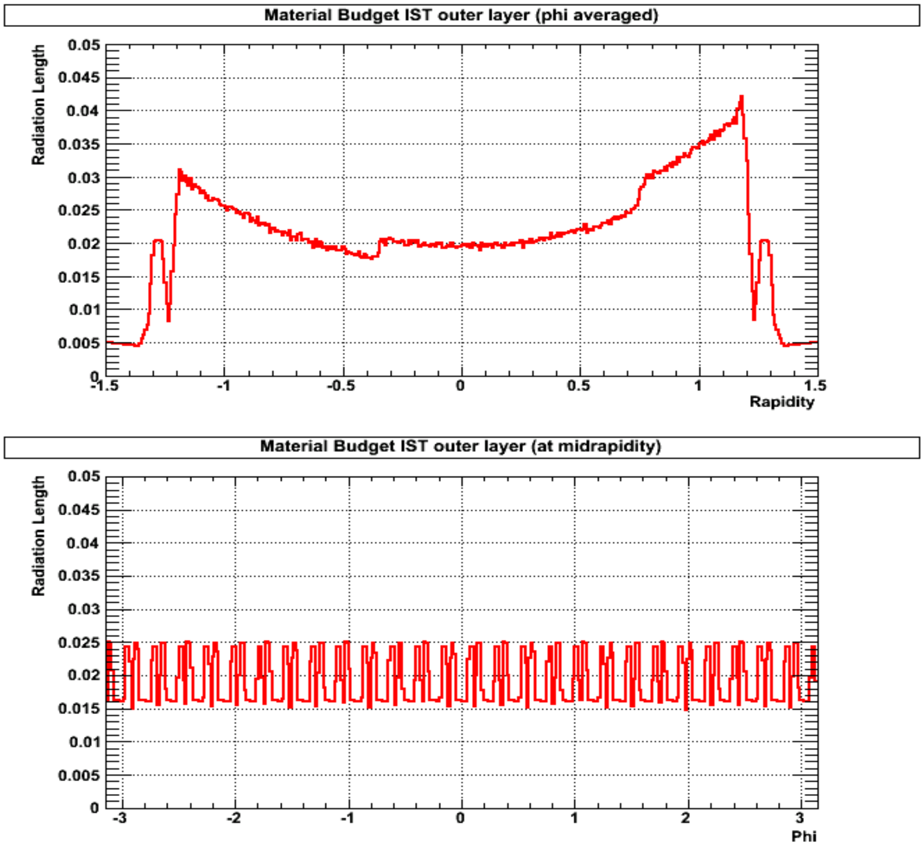

Figure 74: Material budget versus rapidity (top) and ϕ (bottom) for the outer layer of the IST.

The mechanical support structure will be manufactured with an overall accuracy of 100 μm. Locally, the structure supporting the IST requires an accuracy of less than 100 μm. For instance, the mounting surfaces of the sensor modules will have to be flat to within 50 μm to avoid stress, and possibly breakage, of the sensors.

It is not foreseen that the detector will be operated other than at room temperature, both during lab testing and while installed in STAR. However, thermal excursions will be accommodated in the choice of materials. For instance, sensor ladders can be mounted only rigidly on one side while the other side is seated in sapphire mounts which make longitudinal expansion possible. Also special care will be taken in the choice of adhesives and avoiding 'bimetal' effects during construction of various parts. A structure made out of carbon fiber composites is the most promising choice. Many groups are using this material to build highly accurate trackers.

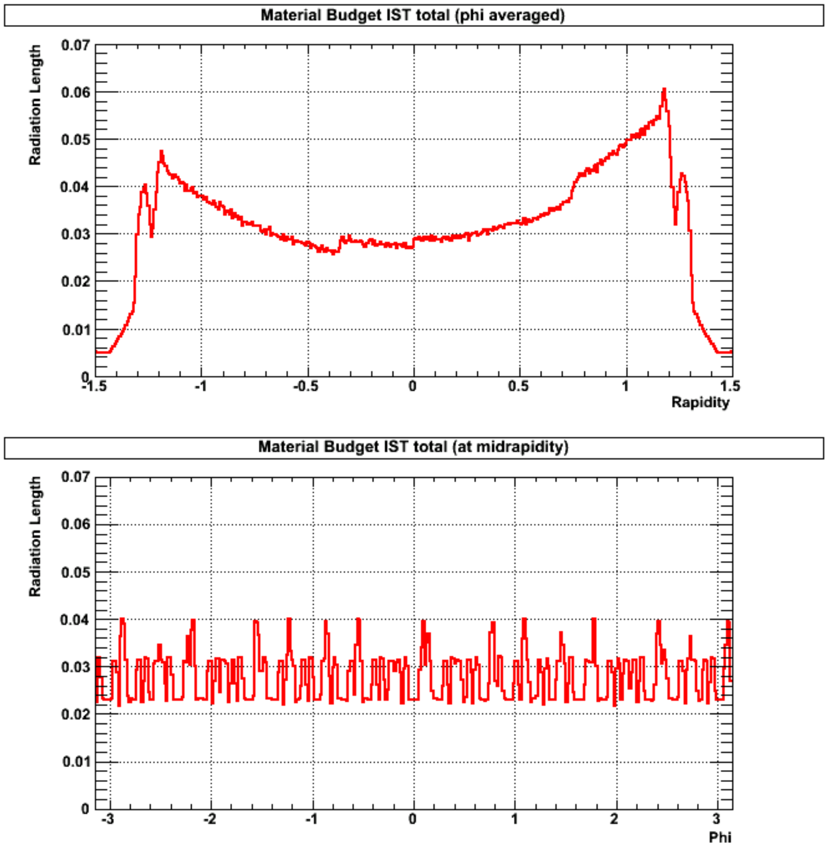

Figure 75: Total IST material budget versus rapidity (top) and ϕ (bottom).

5.4 Silicon Sensors

The manufacturing techniques for silicon strip sensors are well established and are mastered by several manufacturers. Silicon strips have been and remain the first choice for a wide range of high-energy experiment trackers.

The preference is to produce single sided devices with p^+ implants on n-bulk silicon and poly-silicon biased. They are relatively easy to produce with high yields and can also be handled without much difficulty in a standard semi-conductor lab. In contrast, double-sided devices have lower yields (thus more expensive) and need special equipment to handle them. For convenience we would prefer to have all sensors have the same dimensions and the same strip pitch of 60 μm.

Central Au+Au collisions at 200 GeV lead to a particle density of about 1 per cm^2 at the inner IST barrel near mid-rapidity. At the outer barrel the particle density will be a factor of 2 lower. For the outer barrel we will use reasonably standard silicon strip sensors, i.e. with strips running over the whole length of the sensor. There will be two layers of silicon sensors in the outer barrel with the sensors mounted back-to-back on the ladders. The sensors on the outside of this barrel have their strips running parallel to the beam-axis, giving a good r-ϕ resolution. This orientation is the same as for the SSD and provides redundancy. The sensors on the inside of the barrel are identical to the ones on the outside but rotated by 90 degrees, which results in a good z resolution. The chosen sensor size of 4 x 4 cm^2 gives acceptable double hit probabilities for the outer barrel. Using the same sensors in the inner barrel would lead to unacceptable double hit levels. Therefore, we have decided to adapt the sensors of the outer barrel to the higher particle density by dividing the strips in half at the middle of the sensor. The resulting striplets run parallel to the beam-axis and give good r-ϕ resolution.

From the manufacturing point of view all the designs under investigation are reasonably standard. Preliminary discussions with Hamamatsu showed that they are able to make the outer barrel sensors as we proposed to them within the proposed budget. We will need to determine the price and feasibility of the proposed silicon striplet sensors.

Table 3 provides information about the sensors that are needed. Figure 76 shows the two designs for the strips and striplets in the intermediate silicon tracker (IST).

5.5 Ladders and Cooling System

A substantial amount of R&D is required to develop a low mass and stable ladder structure on which the silicon sensors can be mounted. The best candidate for the ladder material is thermally conductive carbon foam developed by Oak Ridge National Laboratory. It combines very low density with high strength and a thermal conductivity close to that of aluminum.

The inner layer of the tracking system will dissipate about 3 watt per sensor assuming 10 APV25-S2 readout chips per sensor. Since the radiation levels are not an issue the system can be kept at room temperature. This avoids problems with condensation and makes maintenance of the system much less complicated.

Current R&D plans on using air cooling channels through a ladder made out of the thermally conductive carbon foam. By internally shaping the cooling channels an increased turbulence will make the cooling more efficient than just blowing air over the sensors.

5.6 Dry Air System

It is preferable to keep the ladders and especially the sensors of the IST in a low humidity environment. We propose to copy the PHOBOS dry air system which has kept the

PHOBOS silicon system at about 10% relative humidity for the duration of the PHOBOS operation. This is a very simple system which boils off liquid nitrogen from a supply tank and feeds it into the almost airtight enclosure of the PHOBOS silicon system. The flow is just enough to maintain a slight overpressure in the enclosure to keep the higher humidity air from the experimental area out of the system. The pressure is regulated by one valve which provides just enough nitrogen boil off to maintain the required overpressure. The system has proven to be very reliable.

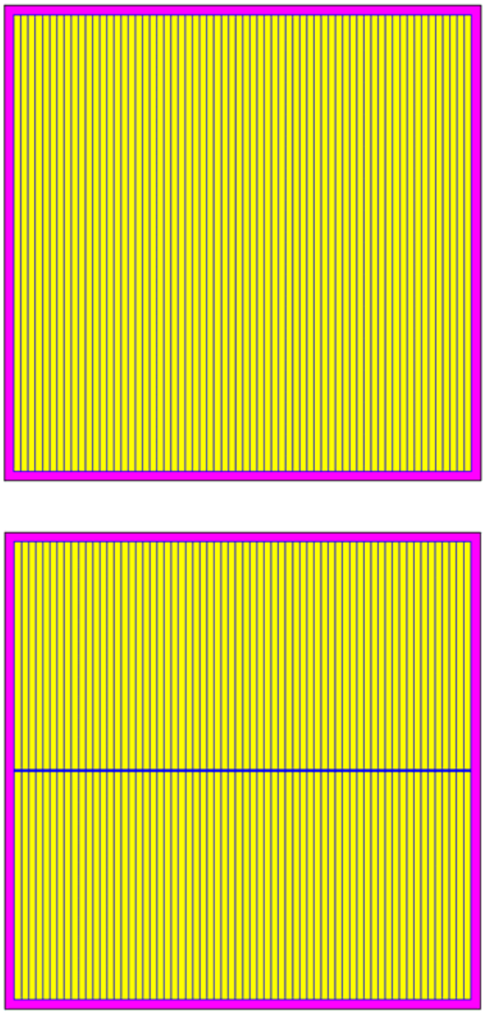

Figure 76: Schematic design of the IST silicon strip (top) and striplet (bottom) sensors.

5.7 Front-end Electronics and DAQ System

About 700,000 channels will be read out in the IST. Readout chips with the necessary requirements for this system are already being used for similar purposes by other experiments.

The best candidate so far is the APV25-S1 readout chip which was designed for the CMS silicon tracker and of which about 75,000 will be used in CMS. Each channel of the APV25-S1 chip consists of a charge sensitive amplifier whose output signal is sampled at 40 MHz which accounts for the LHC interaction rate. The samples are stored in a 4 μs deep analog pipeline. Following the trigger the data in the pipeline can be processed by an analog circuit, mainly de-convoluting the amplifier response from the actual signal and associating the signal with a certain interaction (or rather beam crossing at LHC). The resulting analog data can then be multiplexed and sent to digitizer boards. Although the analog data leads to higher data volumes at the front-end, it is an enormous advantage that charge sharing between strips and common mode noise can be studied in detail, which greatly improves the understanding and performance of the detector. The Equivalent Noise Charge (ENC) of the APV25-S1 depends on the capacitance of the strips and the de-convolution algorithm used, but, for our purposes, it is better than 2000 electrons. With 300 μm thick silicon sensors this will give a signal-to-noise ratio of better than 11:1 when we take the most probable energy deposition by a minimum ionizing particle (MIP). The power consumption of the APV25-S1 is about 2 mW/channel, i.e. about 0.25 Watt/chip. The chips are fabricated in the radiation hard deep sub-micron (0.25 μm) process. Figure 77 shows a close-up view of the APV25-S1 chip.

A prototype readout system for the APV25-S1 chips has been designed and is currently being tested. This is part of the triple-GEM prototype effort for the STAR Forward GEM Tracker (FGT) upgrade. More details on the overall readout system will be presented in Section 5.13.

The STAR radiation environment is less harsh than that of CMS: it could well be that the front-end digitizers can be located much closer to the detector and that there is no need for 100 meter long analog optical links. The preference is that the readout system be kept the same as for the FGT, which is also utilizing the APV25-S1 readout chip. Considering that about 700,000 analog channels have to be digitized there is also need for a zero-suppression system as part of the readout system.

5.8 Flex Cable and Hybrid

To keep the material budget as low as possible a new Kapton cable/hybrid cable is under investigation. This flexible cable combines the hybrid, which carries the readout chips, with the long readout cable. This cable is made out of Kapton with a total thickness of about 100 μm. The hybrid end is glued down on the sensor, the other end plugs into the readout unit, which will be located just outside of the central TPC area. Figure 78 shows one of the prototype cables, which are currently being used for building an IST prototype module.

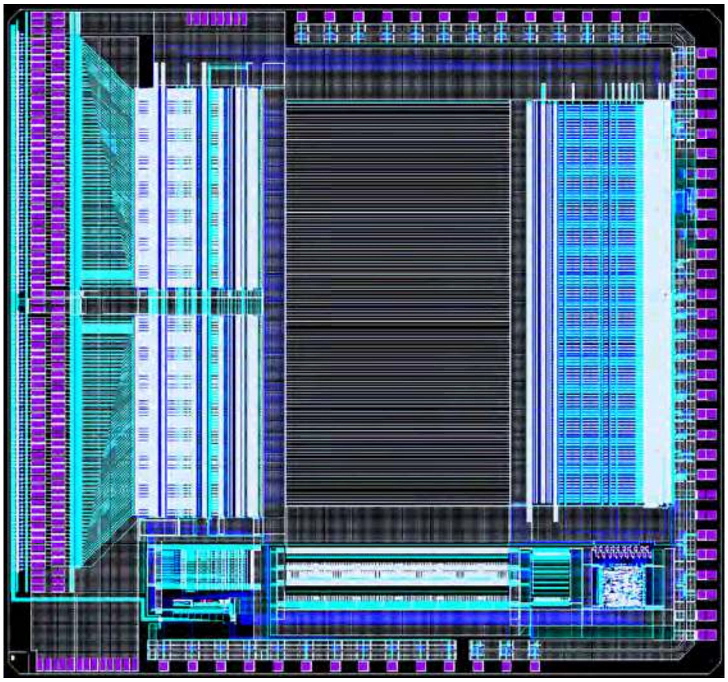

Figure 77: Picture of the APV25-S1 die. On the left are the input pads; on the right are the output pads and control pads. The whole die measures 8.055 by 7.100 mm^2.

5.9 High-Voltage and Low-Voltage System

Considering the standard requirements both for the high voltage and low voltage system, the hardware can likely be obtained as almost off the shelf components. Since these systems will be located relatively close to the detector there is the need for remote control and monitoring. Companies like Wiener can build these systems to the desired specifications, including a CANBUS interface.

5.10 Alignment System

The final alignment of the inner silicon tracker will have to be obtained from reconstructed tracks. Usually this is done through an iterative residual method. For this method to work the positions of the strips will need to be known with an accuracy comparable to their width, i.e. 60 μm, which is challenging, requiring very careful and precise assembly.

Figure 78: Prototype cable/hybrid, equipped with readout chips and mounted on a Type 1 PHOBOS silicon pad sensor.

Finding the position of each detector element on a ladder is relatively straightforward. An optical surveying system, which is available at MIT, makes it possible to do this with accuracy of about 10 μm in the plane of the sensors and about 50 μm to 100 μm perpendicular to the plane of the sensors.

While the ladders are being assembled into barrel layers the next survey step has to be taken. It is very unlikely that the MIT optical surveying station will be able to handle the size of the assembled barrel layers. Logistically it is preferable that the barrel assembly takes place at BNL to avoid shipping of these vulnerable structures. The optical survey station and touch probe system which were used for the STAR SVT should be able to determine the ladder positions within the inner barrel structure with an accuracy of 50 μm or better. The assembly requires survey in 3 stages: after assembly of the innermost layer as well as after assembly of the second and then the third layer.

The whole structure has to be stiff enough to retain the surveyed positions after installation in the STAR magnet. A system with very accurate positioning pins and surfaces is required to position the whole system with respect to the Heavy Flavor Tracker.

5.11 Slow Control Systems

A slow control system has to measure all working parameters of the IST. The temperature of the hybrids and the currents and voltages of the components on the hybrids need to be monitored continuously. Also cooling water temperatures and water flow rates and dry air flow rates need to be recorded regularly. All these monitored values will be entered into a database. In case the values get out of predefined operating values alarms will alert the shift crew and interlocks will be activated if necessary.

Although STAR is using EPICS as its standard slow control system there is a slight preference to use LabVIEW instead. LabVIEW provides the user with virtually any instrument driver and has a very convenient user interface. LabVIEW runs on several operating systems. It is relatively simple to interface LabVIEW and EPICS. However, at the moment, both options are still open.

5.12 Installation Procedures

It is foreseen to assemble the complete inner tracking system including a new beam pipe in the STAR experimental hall. This would include a system test using a cosmic ray test setup. This would also allow one to test the integration into the STAR DAQ system. This step has been proven by many experiments as a critical step for a successful operation after installation. After completion of a complete system test, the inner tracking system including a new beam pipe would then be installed as one unit inside STAR.

5.13 Readout System

A prototype readout system, based on the APV25-S1 readout chip, has been completed. The following section provides a brief description of this prototype and how the anticipated readout system will be integrated into the STAR DAQ environment.

Data from prototype detectors are read out by the APV25-S1 readout system which consists of the following components:

- Signal Boards
- APV Module

- Control Unit

The signal board collects the charge from the detector. The signal board has two sets of an integrated bus system as part of the communication and data collection between the APV module and control unit. Figure 79 shows a schematic design of the readout system.

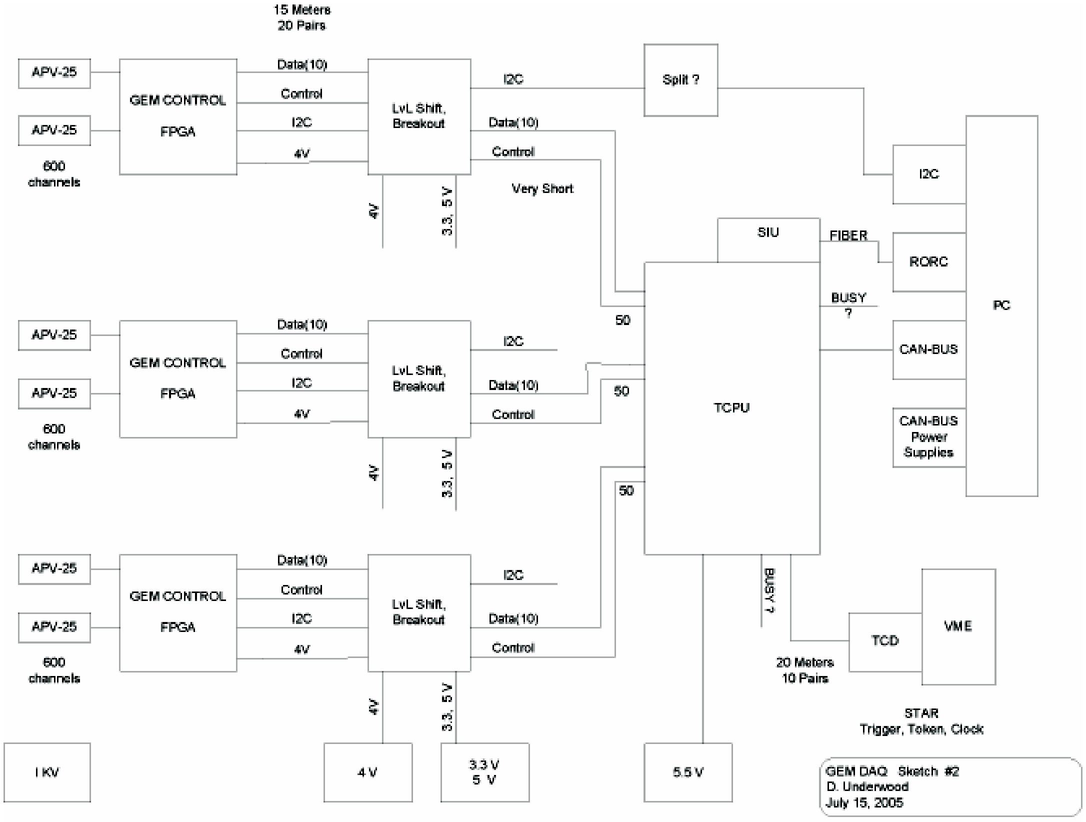

Figure 79: Schematic design of the APV25 chip readout system and STAR DAQ integration based on the FGT prototype setup.

The APV module in the prototype version has an on-board glued APV25-S1 chip which is fabricated in submicron process (0.250 micron) and is connected to 68 sensor channels. In the final version each APV module will be connected to 128 channels. The APV25-S1 chip is operated with a clock frequency of 40 MHz and read out with 20 MHz. The APV25-S1 chip is set up using the I2C Philips Standard. Calibration pulses can be generated directly on board to feed each channel. The Control Unit is the main control system for the readout electronics, i.e. for ADC, FIFO, and data formatting. It also maintains communication between the APV25 modules and the DAQ system. A Xilinx CPLD is the heart of each Control Unit. This Xilinx component is fabricated in a deep submicron process (0.095 micron). In radiation tests which were carried out at the Bates Linear Accelerator Center, it was found that radiation hardness of the Xilinx CPLD component is beyond 1 Mrad. The advantage of the Xilinx CPLD is based on the flexibility in re-programming to any desired configuration. Each Control Unit contains for each APV25-S1 an ADC and a FIFO, with the ADC continuously running and converting incoming signals from the APV25-S1. Upon a positive trigger decision, the data are converted and written in parallel into all FIFOs and then in sequence these data are sent out FIFO by FIFO in LVDS standard to the STAR DAQ system. These actions are controlled by the Xilinx CPLD device which is programmed in VHDL language. The Control Unit is connected with the outside environment only through one twenty-wire pair flat ribbon cable. Each Control Unit has all required voltage regulators on board. The power distribution requires only one +4V power supply using one wire pair. The signal board, APV25 module and control unit form one compact unit without cables and wires. All connections are realized through PC board printed layer connections. This guarantees that the system will have very low noise. We have already made good progress in integrating the APV25 readout into the STAR environment.

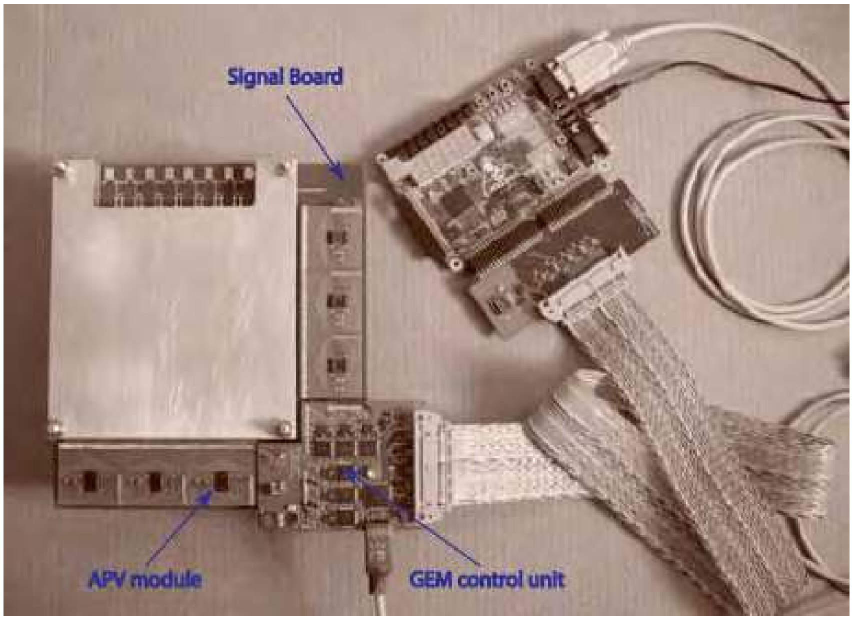

Figure 80: Prototype APV25-S1 readout system adapted to the STAR Forward-GEM Tracker (FGT) prototype chamber. The location of the APV module, GEM control unit and signal board is indicated.

We have a prototype system which utilizes the STAR Trigger and Token distribution through the TCD module, and also reads out the data using an ALICE DDL link, as will be used in STAR TOF and future upgrades. This prototype system was constructed by modifying an Altera Stratix FPGA based controller, called a TCPU, developed for the STAR Time-of-Flight system, and by adding some interfacing for the MIT controller, and other systems such as I2C for the APV25, and CANBUS for the Stratix TCPU board. The complete readout system was successfully operated during a test beam experiment at FNAL to evaluate the performance of prototype triple-GEM detectors. The prototype system is shown in Figure 80.

6 Integration with STAR

6.1 Mechanical Support

The current inner region of STAR is designed to accommodate the SSD and the SVT. The employed structure consists of two symmetric cones supporting the SSD at the large radius and the thick SVT at a smaller radius. Presently, one FTPC module is placed at each end of the cone structure. With the HFT detector a new concept that minimizes the material in the inner region and incorporates means for precise relative positioning will be implemented. The overall structure will also allow for the proposed Forward GEM Tracker (FGT) to be installed in one end of STAR.

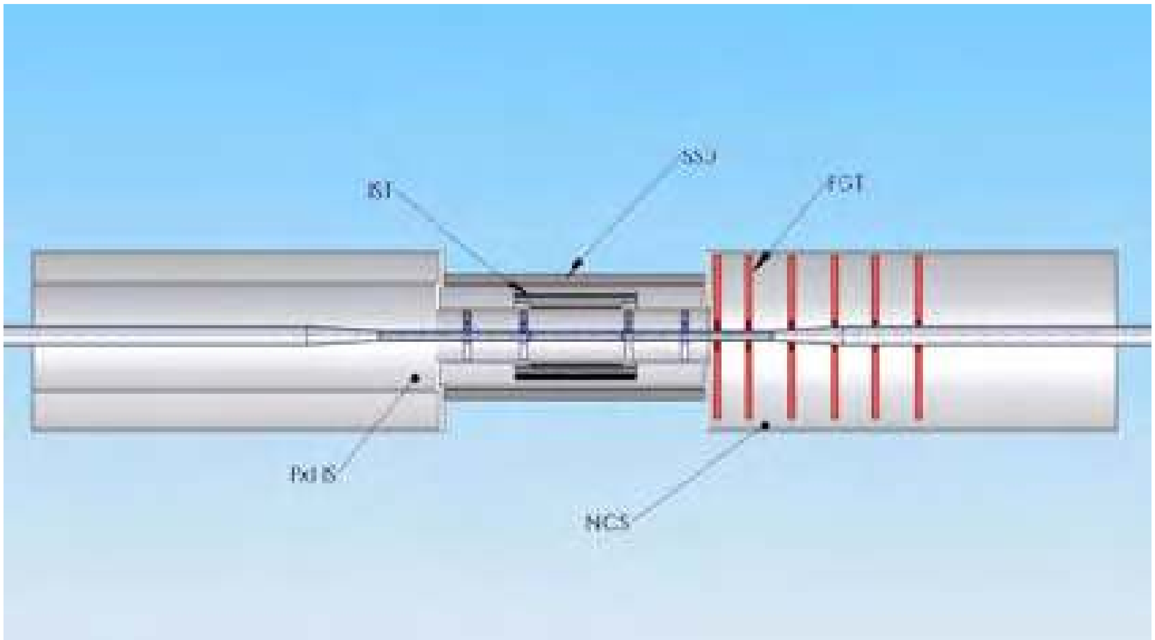

Figure 81: Schematic layout drawing of the supporting structure for the HFT. The layout shows two cone structures: the inner support barrel and the ladders of the IST and SSD. The PIXEL mount will be brought in through the PIXEL insertion volume (Pxl IS).

A schematic concept of how the mounting may be achieved is depicted in Figure 81 as a cut along the beamline. The PIXEL and IST will be mounted from the one side (left, STAR West). The inner barrel structure provides support for the beam pipe and for the PIXEL detector support carriage. The carriage is designed as discussed in Section 4.8 to allow for rapid removal and replacement of PIXEL sensors. The IST ladders are mounted outside the inner barrel structure. The fixpoints for the IST ladders will be at the west end. The services (signals, electric and cooling) for the PIXEL detector will come through the support carriage. The IST will be served in the outside part of the west cone.

In recognition of difficulties encountered in previous experiments, we are adopting design requirements for rapid insertion and removal of the PIXEL vertex detector, rapid calibration and calibration transfer and multiple detector copies. By addressing these issues early in the design cycle the requirements can be met without major cost impact. The mechanical design makes significant use of carbon composite material, which has nearly the same radiation length as beryllium. This allows us to take advantage of the extensive work going on at LBNL for the ATLAS pixel detector. It is clear that significant R&D is necessary to achieve a low mass system.

6.2 Beam Pipe

The PIXEL vertex detector extends the measurement radius down to 25 mm from the interaction axis and will require a new small radius beam pipe for STAR. The design concept for this pipe is shown in Figure 82.

Figure 82: Beam pipe.

The beam pipe is constructed from 60 mm diameter aluminum tubes that taper down to a 40 mm diameter beryllium beam pipe with 1 mm thick walls. The central region where the HFT is located is a 40 mm diameter beryllium pipe with a 0.5 mm thick wall. The beam pipe is supported in the center with the same shell that carries the pixel detector. The shell provides gravitational support as well as isolating the thin central region from handling stresses from the long extended pipe. The central support is shown in Figure 83. The outer shell has been made transparent in the figure to show the inner structure.

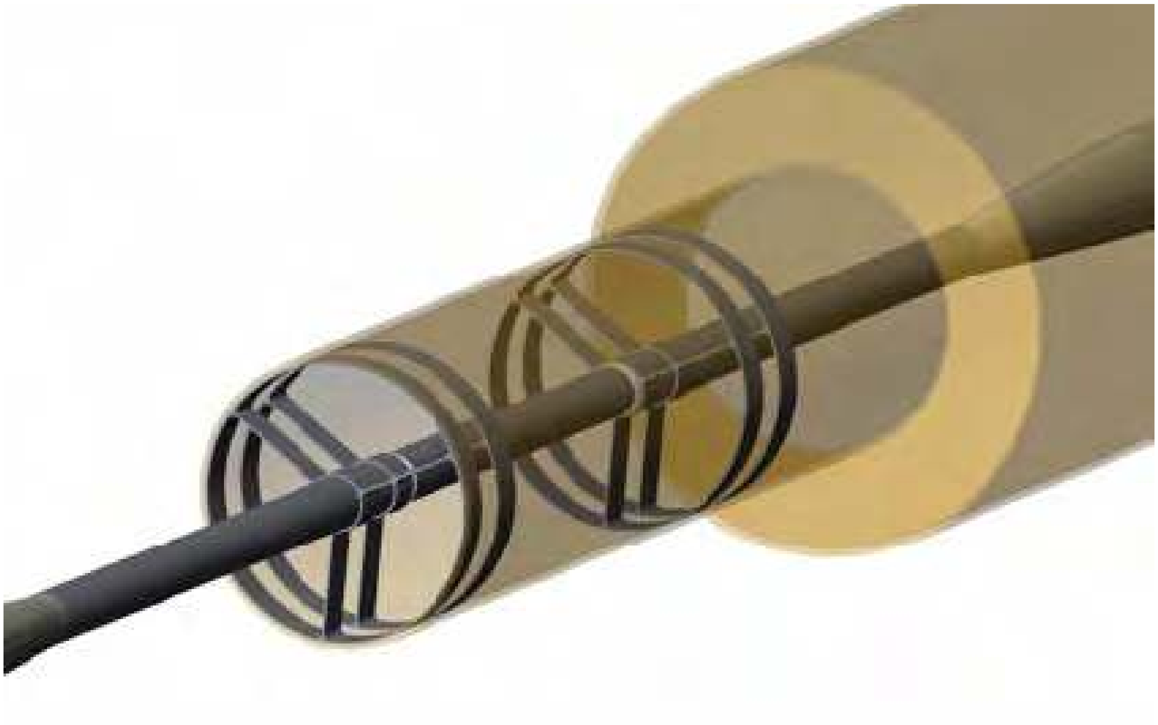

Figure 83: View of the beam pipe mid-section with central support.

6.2.1 Minimum Beam Pipe Radius

We have chosen a minimum radius for the beam pipe which, now that the RHIC optics has stabilized, is reasonable conservative. From the standpoint of beam pipe interaction with beam optics, the beam pipe wall should, according to accelerator physicists at BNL, have a minimum radius of 6 σ while 10 σ is very conservative.[142] Here σ is the size of the beam envelope at injection. For STAR at injection the beam emittance is 15 π mrad·mm, β^* is 10 m, βγ is 10.52, which gives σ = 1.5 mm plus a 5 mm beam offset at injection.[142, 143, 144, 145] For proton injection σ is smaller and therefore less of a constraint. We have chosen an inner beam pipe radius of 20 mm or ~ 10 σ. This is satisfactory for RHIC operation and it is larger than the limiting aperture, leaving PIXEL clear of uncontrolled beam aborts.[145]

6.2.2 Beam Pipe Radius - Vacuum Considerations

The dimensions of the beam pipe sets limits on pumping speed and the expected pressure at the center of the interaction region in STAR. The 1700 mm long central section, with a 40 mm diameter, joins a larger 80 mm diameter pipe, which extends 4000 mm to the pumping section. A simple analysis was performed[146,147,148] which gives a pressure increase at the center in the interaction region of ~ 10^{-11} torr. This is the pressure increase above the pressure at the pumping station and it is based on a surface out-gassing rate of 5.3×10^{-11} W/m^2 and a conservative estimate of the pipe conductance.[147] This pressure is well within the requirements. The greatest uncertainty in this estimate is the outgassing rate, but a factor of 10 greater value is still tolerable. If an active NEG coating is used the inner section will be a pumping surface rather than an outgassing surface.

6.2.3 Supporting Section

The support barrel, which carries the PIXEL ladders and supports the beam pipe through the spoke structure, is shown in Figure 83. This permanent support provides mechanical isolation of the central thin section of the beam pipe such that it carries only the load of the vacuum and is not subjected to forces from loads on the rest of the beam pipe. It is supported by the west cone, and provides support for the IST ladders on the outside. The spokes that couple the beam pipe to the outer support barrel allow insertion of the vertex detector into the center region. The detector modules move to a larger radius during insertion to clear the spokes.

6.2.4 Central Beam Pipe Thin Window Section

The current plan for the thin central region is to use a beryllium pipe with a 0.5 mm wall thickness. It is believed that this will provide the minimum Coulomb scattering while maintaining a reasonable structural safety margin. Preliminary analysis indicates a 50:1 safety margin for buckling.[149] There is a structure failure limit imposed by the degree of roundness of the cylinder. A stress analysis indicates that a 1 mm deviation from a cylinder (1 mm difference between major and minor axis of an ellipse) sets a 20:1 safety margin for material failure.

6.2.5 RF Background from the Wake Field

It is believed that the beam pipe in STAR will be sufficient to suppress wake field signals in the detector to well below the expected signal. The evidence for this belief comes from experience with the gas jet polarimeter and carbon strip polarimeter located at the 12 o'clock intersection region of RHIC. These polarimeters have silicon detectors located inside the beam pipe close to the beam and it has been found that a few microns of conductor are sufficient to shield these detectors from the wake field.[150]

The PIXEL detector will be located outside the beam pipe and will benefit from the RF shielding this pipe provides. The pipe will be constructed from at least 500 microns of beryllium. The maximum beam in RHIC will be 1×10^9 gold ions per bunch.[§§] This gives a wake field current of 110 mA (counting both beams), which with a 1 μm skin depth will generate a resistive potential drop of only 7 mV. A more sophisticated calculation should include induction, rise time and skin depth and detector filtering, since our bandwidth cutoff will be closer to the wake field GHz frequency than the polarimeter detector cutoff.

6.2.6 Beam Pipe Insertion and Removal

We are currently investigating the removal and insertion of the beam pipe. We anticipate replacing the current center section of the STAR beam pipe with the components described above. This will likely entail a period of refit and installation to install the new beam pipe after which removal and reinsertion should not be necessary during the normal course of running and detector repair.

6.2.7 Bake-Out

Beam pipe bake out is still under discussion. It is expected that the same form of NEG coating will be used and there are two possibilities in how this will be treated. It may either be a minimum bake out to remove primarily water as it is done now with a hot dry nitrogen scrub gas at 150 C to 110 C or it could be a full activation of the NEG coating turning it into a pumping surface.[151] This later case requires baking at 150 C to 200 C with vacuum. This could impose additional constraints on beam pipe materials and would require additional thermal isolation from the other detectors. If it is decided that the less aggressive bake out procedure is adequate then carbon composites can be used in the construction of the beam pipe support spokes. In either case the pixel detector will be withdrawn during bake out from its location to isolate it from the heated beam pipe.

6.3 Compatibility with the SSD and Other Cone Mounted Detectors

The SSD will be supported by the common structure outside the PIXEL and IST space. The FTPCs will be removed. The proposed Forward GEM Trackers will be mounted at the other end and serviced exclusively from there. The PIXEL and IST detectors will be supported and installed from one end only. There will be no other detectors requiring support or access at this end. Other detectors requiring cone support will be outside of the PIXEL space.

[§§] RHIC has achieved $1.1\text{x}10^9$, but the design of RHIC-II calls for $0.5\text{-}1.0\text{x}10^9$ ions per bunch.

7 Management Plan

This section provides the proposed management organization and delineates responsibilities within the HFT project. Figure 84 shows a preliminary management organizational chart.

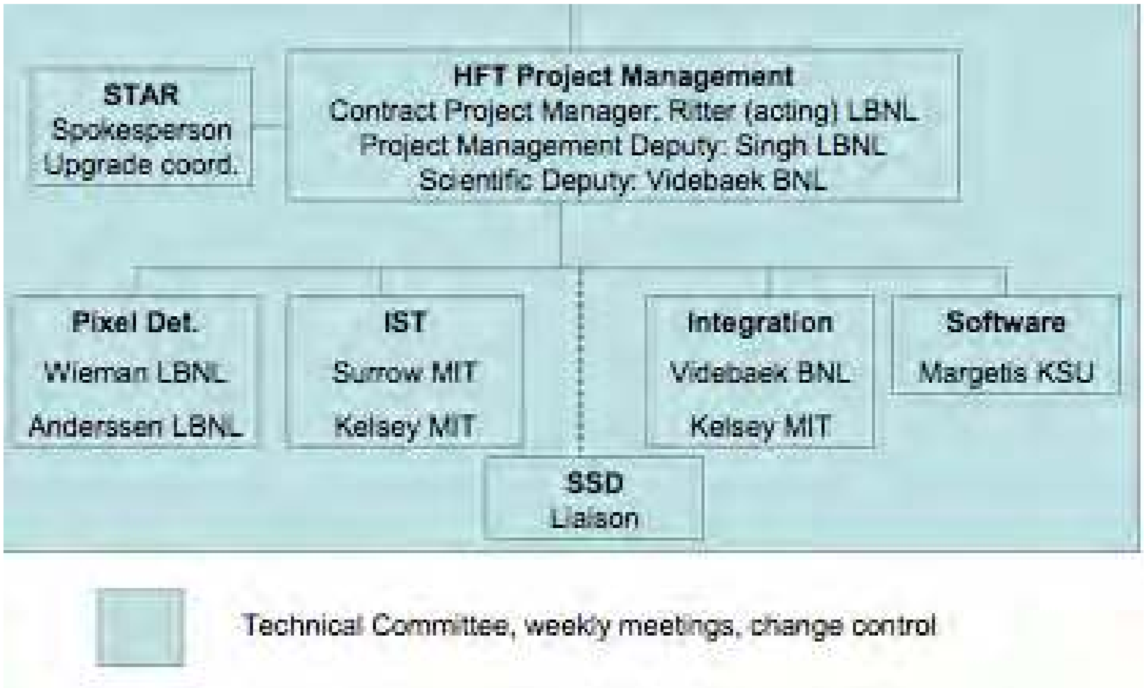

Figure 84: Proposed management structure and Technical Committee. The structure above the HFT Project Management, involving BNL and DOE, will be defined later.

7.1 Host Laboratory

The Host Laboratory is defined as the lead laboratory that is fully responsible for the construction of the overall HFT upgrade and assumes fiscal responsibility for the MIE. LBNL will be the Host Laboratory during the R&D, construction and testing of HFT and will be responsible for ensuring that the manpower and necessary infrastructure are provided.

7.2 Director of the Nuclear Science Division at LBNL

Funding for this project will be directed through the LBNL Nuclear Science Division. Thus, ultimate fiscal and management Contractor responsibility for the fabrication of HFT will reside with the Director of the Nuclear Science Division, James Symons.

7.2.1 Responsibilities

The Director of the Nuclear Science Division at LBNL shall be administratively and fiscally responsible for the entire R&D effort and the MIE. In particular he/she must provide the following:

- Provides overall management oversight for all aspects of the MIE.
- Appoints the Contractor Project Manager.
- Approves key personnel appointments made by the Contractor Project Manager.
- Approves major subcontracts recommended by the Contractor Project Manager.
- Ensures that adequate staff and resources are available to complete HFT in a timely and cost effective manner (within constraints of the funding provided by DOE).
- Ensures that HFT has demonstrated that it meets the functional requirements.
- Provides documentation and access to information necessary for operation of HFT at BNL.
- Ensures the work is performed safely and in compliance with the Integrated Safety Management (ISM) rules

7.3 Contractor Project Manager (CPM)

The Director of the Nuclear Science Division at LBNL has appointed H. G. Ritter (LBNL) as the acting HFT Contractor Project Manager.

7.3.1 Responsibilities

The CPM shall report directly to the Director of the Nuclear Science Division at LBNL and will be in charge of the overall management of HFT project. The CPM shall appoint the key staff needed for the MIE with the approval of the Director of the Nuclear Science Division at LBNL. The Contractor Project Manager also will have the following responsibilities:

- Responsible and accountable for the successful execution of contractor’s MIE scope of HFT.
- Supports Federal Project Director in implementing DOE project management process.
- Provides input on project documentation.
- Implements contractor performance measurement system.
- Delivers project deliverables as defined in this project execution plan.
- Identifies and ensures timely resolution of critical issues within contractor’s control.
- Responsible for HFT functionality requirements
- Allocates the contingency funds according to the procedure defined in the Baseline Change Control Procedures.
- Acts as the spokesperson for the project to the DOE, the Host Laboratory, other participating institutions, and the scientific community at large. Keeps the

Collaboration informed on the status of the HFT project by regular updates at collaboration meetings.

- Appoints the Deputy Contractor Project Managers with the concurrence of the Director of the Nuclear Science Division at LBNL
- Collaborates with the Director of the Nuclear Science Division at LBNL and Deputy Contractor Project Managers to assemble the staff and resources needed to complete the project.
- Advises the Director of the Nuclear Science Division at LBNL on the selection of non-host-site construction teams and sub-contractors and in defining the areas of collaboration and the relationship between LBNL and other institutions participating in HFT through Memoranda of Understanding (MOU).
- Recommends major subcontracts to the Director of the Nuclear Science Division at LBNL for approval.
- Ensures the work is performed safely and in compliance with the ISM rules.
- Appoints the Quality Assurance Manager (QAM) in consultation with the Deputy Contractor Project Managers.
- Produces necessary ES&H documentation (e.g., Hazards Analysis Documents).
- Recommends baseline changes up to Level 2.

7.4 Deputy Contractor Project Managers

The HFT CPM, with the approval of the Director of the Nuclear Science Division at LBNL, has appointed two Deputies: R. P. Singh (LBNL) as the Project Management Deputy, and Flemming Videbaek (BNL) as the Scientific Deputy. The two Deputies will report to the CPM.

The two Deputies support the function of the CPM by way of both shared and specific responsibilities. The following are responsibilities that the two Deputies share:

7.4.1 Shared Responsibilities

- Under the direction of and by delegation from the Contractor Project Manager, executes contractor's MIE scope of HFT, and supplies the deliverables on time and within budget.
- Collaborates with the Contractor Project Manager to assemble the staff and resources needed to complete HFT.
- Collaborates with the Contractor Project Manager in the technical direction of HFT project.
- Contributes to the preparation of regular reports and project reviews as required by DOE and LBNL.
- Collaborates with the Contractor Project manager to ensure that work is performed safely and in compliance with the ISM rules.

Specific Responsibilities are delegated individually to the two Deputies

7.4.2 Responsibilities for Project Management Deputy

- Develops and maintains the HFT documentation.
- Communicates the functional requirements to the subsystem managers
- Responsible for the development of the HFT system design requirements, including interfaces between subsystems, and methods and practices for achieving these requirements.
- Controls changes in the HFT system design requirements, including interfaces between subsystems.
- Responsible for overall engineering safety of project design
- Carries out monthly project review and reports results to the Contractor Project Manager.
- Participates in the preparation of project quarterly reports to the DOE.
- Supervises the LBNL staff of the HFT project.
- Oversees the effort from other institutions participating in HFT.
- Identifies and ensures timely resolution of critical issues within Deputy Contractor Project Manager's control.
- Identifies and collaborates with the Contractor Project Manager in mitigating project risks.
- Maintains project files.
- Additional responsibilities as delegated by the Contractor Project Manager.

7.4.3 Responsibilities for Scientific Deputy

- Represents the project in discussions with the collaborations (see section 7.2) concerning physics requirements and functionality requirements as may arise in the change control process.
- Responsible for simulations that establish and support functionality requirements and CD-4 acceptance criteria.
- Communicates the functional requirements and their relation to physics requirements to the Collaboration.
- Provides supervisory oversight in the preparation of the HFT CDR, TDR and other major HFT reports.
- Participates in the preparation of project quarterly reports to the DOE.
- Identifies and ensures timely resolution of critical issues within Deputy Contractor Project Manager's control.
- Identifies and collaborates with the Contractor Project Manager in mitigating project risks.
- Additional responsibilities as delegated by the Contractor Project Manager

7.5 Subsystem Managers

Separate HFT Subsystem Managers are responsible for each of the four major HFT subsystems: Pixel Detector, Strip Detector (IST), Integration and Software, as shown in Table 21.

HFT Subsystem	Subsystem Manager
Pixel Detector	Howard Wieman (LBNL)
Strip Detector (IST)	Bernd Surrow (MIT)
Integration	Flemming Videbaek (BNL)
Software	Spiros Margetis (KSU)

Table 21: HFT subsystems and subsystem managers.

Subsystem Managers report directly to the CPM and will be responsible for the design, construction, installation, and testing of their respective subsystem, in consultation with the CPM and in accordance with the performance requirements, schedule, and budget. In particular, all subsystem managers have the following general responsibilities:

7.5.1 Responsibilities

- Collaborates with the CPM and his Deputies to assemble the staff and resources needed to complete the subsystem.
- Communicates the system design requirements to the sub-system staff.
- Ensures that subsystems meet the HFT system design requirements, including interfaces.
- Responsible for carrying out the design, construction and assembly of the subsystem in accordance with the scope, schedule and budget, assuming funding and resources as described in the PEP.
- Provides regular reports on the status of the subsystem to the Contractor Project Manager.
- Ensures the work is performed safely and in compliance with the ISM rules.

In addition to these general responsibilities, the subsystem managers have specific responsibilities.

Pixel Detector

The HFT CPM has appointed Howard Wieman (LBNL) as Subsystem Manager for the Pixel Detector subsystem. As the Subsystem Manager of the Pixel Detector, he oversees all aspects of the R&D, conceptual design, detailed design, construction, testing and installation of the Pixel Detector.

Strip Detector (IST)

The HFT CPM has appointed Bernd Surrow (MIT) as Subsystem Manager for the IST subsystem. As the Subsystem Manager of the IST, he oversees all aspects of the R&D, conceptual design, detailed design, construction, testing and installation of the IST.

Integration

The HFT CPM has appointed Flemming Videbaek (BNL) as Subsystem Manager for the Integration subsystem of the HFT into the STAR detector. As the Subsystem Manager of the Integration subsystem, he oversees all aspects of this subsystem.

Software

The HFT CPM has appointed Spiros Margetis (Kent State University) as Subsystem Manager for the Software subsystem. As the Subsystem Manager of the IST, he oversees all aspects of this subsystem.

SSD Liaison

The SSD Liaison is responsible for the coordination of the SSD upgrade with the HFT mounting structure and with the software.

7.6 Quality Assurance Manager (QAM)

R. P. Singh (LBNL) will assume the duties of the interim QAM for the HFT project until a permanent QAM can be appointed.

7.6.1 Responsibilities

- Collaborates with the CPM to ensure the quality of HFT.
- Ensures that the quality control system is established, implemented, and maintained in accordance with the HFT Quality Assurance Plan.
- Provides oversight and support to the partner labs and institutions to ensure a consistent quality program.

7.7 Integrated Project Team

The composition of the HFT Integrated Project Team (IPT) is given in Table 22. Its responsibilities are described in DOE Order 413.3A. The team plans to meet quarterly or as needed. The DOE FPD will chair the IPT.

7.8 PARTICIPATING INSTITUTIONS

LBNL will be responsible for the fabrication of this MIE instrument. In additional to LBNL personnel, members of the Collaboration from U.S. Universities and National Laboratories will share major responsibilities for the design, fabrication and installation of the HFT subsystems. These institutions have expertise and past experience in designing and fabricating similar subsystems. A MOU will define the relationship between the institution and LBNL. In addition, scientists will provide leadership for the various subsystems comprising the HFT.

List of participating institutions:

- Brookhaven National Laboratory
- Institut Pluridisciplinaire Hubert Curien, Strasbourg, France
- Kent State University
- Lawrence Berkley National Laboratory
- Massachusetts Institute of Technology
- Nuclear Physics Institute, Prague, Czech Republic
- University of California, Irvine, California
- University of California, Los Angeles, California
- Purdue University
- University of Washington, Seattle

DOE Federal Project Director	TBD (chair)
LBNL Contractor Project Manager	H. G. Ritter
LBNL Deputy Contractor Project Manager	R. P. Singh
BNL Deputy Contractor Project Manager	F. Videbaek
DOE Contracting Officer	TBD
LBNL Contracting Officer	TBD
LBNL ES&H Lead Lead/HFT EH&S Liaison	TBD
DOE EH&S	TBD

Table 22: HFT Integrated Project Team.

8 Cost and Schedule

The HFT has been organized into a Work Breakdown Structure (WBS) for purposes of planning, managing and reporting project activities. Work elements are defined to be consistent with discrete increments of project work. Project Management efforts are distributed throughout the project, including conceptual design and R&D. The HFT has 6 WBS Level 2 components:

WBS	Title
1.1	Conceptual Design and R&D
1.2	Pixel Detector
1.3	Strip Detector (IST)
1.4	Integration
1.5	Software
1.6	Project Management

8.1 Schedule

The Gantt chart view of the project schedule is shown in Figure 85. The schedule is fully integrated to include all the major subsystems comprising the HFT upgrade to the STAR detector.

8.2 Milestones

The following list is a preliminary schedule of milestone dates for the HFT MIE. Additional level 2 milestones will be established prior to CD-2. Critical Decision-0 (establishing mission need) is planned for Q4 FY 2007, to get the project started.

Milestones are assigned to different levels depending on their importance and criticality to other milestones and the overall Project schedule. In this document we summarize only Level-1 (Critical Decision) and Level-2 (Project Control) milestones. These are listed in Table 23.

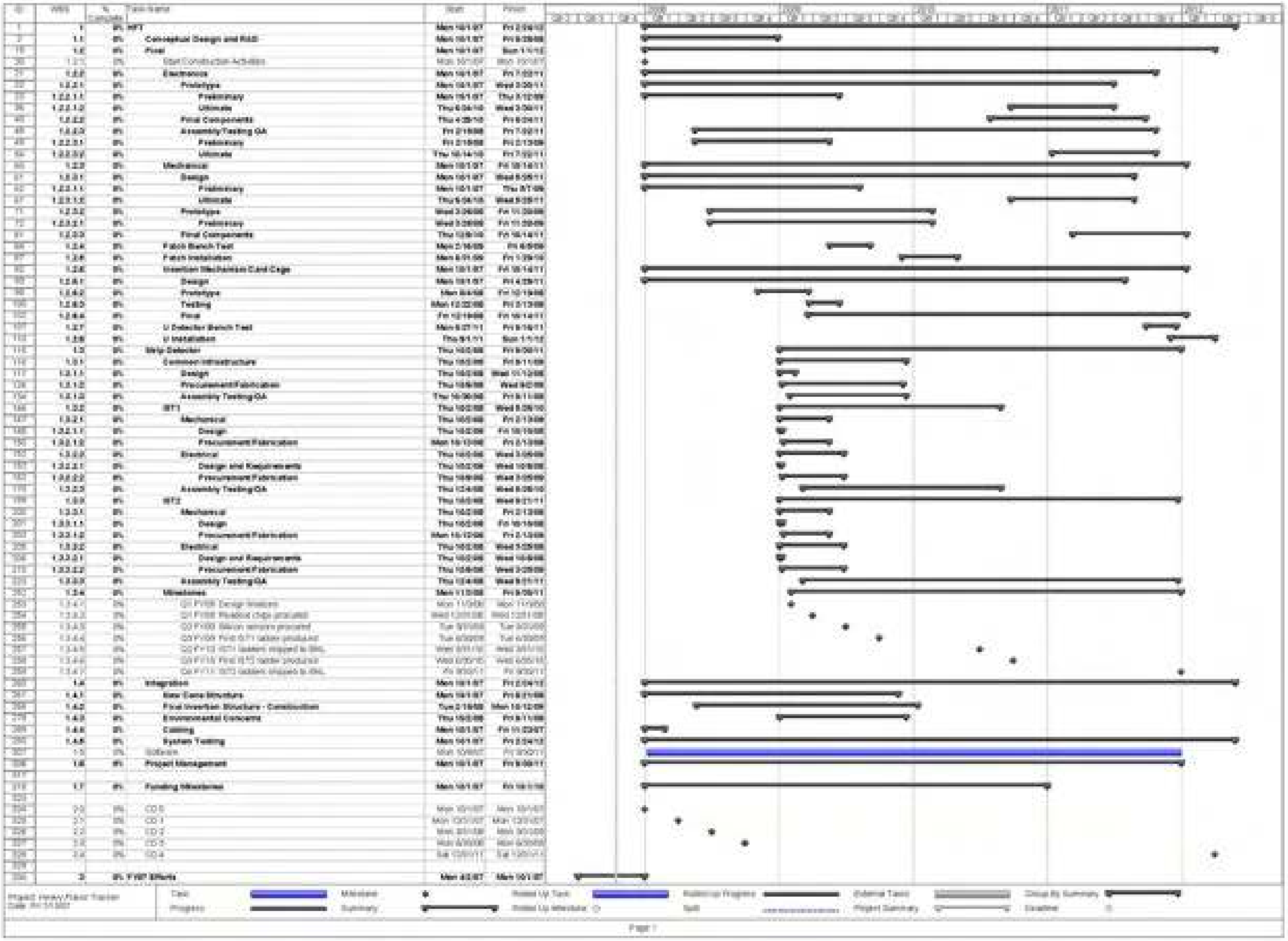

Figure 85: Schedule of the high level WBS elements.

Level 1	Date
CD 0	Q4 FY07
CD 1	Q2 FY08
CD 2	Q3 FY08
CD 3	Q4 FY08
CD 4	Q4 FY11
Level 2	**Date**
Prototype Telescope Analysis Complete	Q1FY08
Patch Silicon Fabricated	Q4FY08
Final Design and Safety Review Complete	Q1 FY09
Readout chips procured for IST	Q1 FY09
Silicon Sensors procured for IST	Q2 FY09
First IST1 ladder produced	Q3 FY09
Ultimate design complete	Q3 FY09
Patch Pixel detector installed	Q4 FY09
Ultimate final fabrication complete	Q2 FY10
IST1 ladders shipped to BNL	Q2 FY10
First IST2 ladder produced	Q3 FY10
Pixel installed	Q4FY11
IST2 ladders shipped to BNL	Q4 FY11

Table 23: Critical Decision dates and Level 2 Milestones.

8.3 Cost Range

The estimated TPC range at CD-0 for the project is \$15.1M – \$16M. The preliminary TPC for the project is \$15.1M, in Current Year Dollars. The upper bounds recognize the risk at this early stage of the project of unknown unknowns. Such items as the chips for the Pixel Detector remain at high risk.

The estimated budget of \$15.1M includes all DOE base costs developed from the appropriate WBS level. The costs shown by fiscal year in Table 24 are base costs (no contingency). The total contingency for each fiscal year by WBS ID is shown in a separate column in Table 25, and totals \$4.3M or 40% of the base cost.

The elements of the HFT could have a useful life of up to fifteen years. The components of a total life-cycle cost include: (a) Fabrication, as described in this document; (b) Operation; and (c) Decommissioning costs. The estimated yearly cost of operation is less than \$20,000 and does not include management and operations (M&O) support for the U.S. research program under the conditions set by HFT management and the required M&O and annual replacement costs for computing resources. The decommissioning of

HFT covers the disposal of standard electronic, computer, and experimental lab equipment, which must follow accepted standard procedures for disposal of these items. The decommissioning activities are not anticipated to be complex or cost prohibitive, and would likely be carried out by U.S. researchers, as is commonly done for pieces of scientific instrumentation. Although a detailed analysis has not been carried out, it is estimated that the decommissioning is likely less than $100,000. The estimated life-cycle cost is less than $17 million.

WBS	Title	Total Budget	FY08	FY09	FY10	FY11	FY12
1.1	Conceptual Design and R&D	862	862	0	0	0	0
1.2	Pixel Detector	3,294	1,295	629	688	682	0
1.3	Strip Detector (IST)	3,539	0	3,139	246	154	0
1.4	Integration	1,777	407	1,351	0	3	16
1.5	Software	0	0	0	0	0	0
1.6	Project Management	1,384	343	351	358	332	0
	Subtotal	10,857	2,907	5,470	1,293	1,171	16
	Contingency - 40%	4,286					
	HFT Est. TPC	**15,143**					

Table 24: CD-0 TPC estimate.

8.4 Funding

The HFT MIE project will be entirely funded by DOE-NP. Labor contributed by Institut Pluridisciplinaire Hubert Curien, Strasbourg, France, is expected to develop the final version of the MIMOSTAR 4 chip to be used for the patch Pixel detector in 2009 – 2011, and the final version of the Ultimate chip to be used in the final version of the full Pixel detector for the CD4 phase of the project.

The estimate for the DOE TPC at CD-0, as shown in Table 24, is $15.1M.

8.5 Contingency

Contingency funds will be managed in conformance with the policies contained in DOE Manual 413.3-1 and as defined in the Baseline Change Control section of this document.

8.5.1 Contingency evaluation for CD-0 cost estimate

At the present pre-CD-0 phase (Establish Mission Need), traditional contingency percentages that varied from a low of 20% for well-understood and well-defined tasks, and escalating to 60% for tasks with high associated risks were used. These contingency percentages were based on expert judgment and were applied at the appropriate WBS level. Based on previous experience with similar projects, this level of contingency is considered conservative but acceptable at this phase.

The contingency assignment per WBS element resulting from the contingency analysis is shown in Table 25. These contingency amounts were utilized to develop the overall project contingency.

WBS	Title	Total Budget	Cont	%
1.1	Conceptual Design and R&D	862	0	0%
1.2	Pixel Detector	3,294	1,956	59%
1.3	Strip Detector (IST)	3,539	1,275	36%
1.4	Integration	1,777	1,055	59%
1.5	Software	0	0	0%
1.6	Project Management	1,384	0	0%
	Subtotal	10,857	4,286	39%
	Contingency -	4,286		
	HFT Est. TPC	15,143		

Table 25: Contingency assignment per WBS element.

9 Summary

Probing charm quark flow, thermal equilibration, and partonic energy loss will be the critical measurements in characterizing the strongly interacting matter created at RHIC. Furthermore, measuring the energy loss of high transverse momentum heavy (c, b) quarks while traversing the medium will help disentangle between energy loss scenarios in cold nuclear matter and in partonic matter. Measuring charm and bottom in polarized p+p collisions will serve as a reference and will determine production cross sections and their spin dependence. The HFT is designed to tackle these tasks by precisely measuring open charm hadron yields, spectra and elliptic flow (v_2) and by measuring the displaced vertex of the electrons produced by high transverse momentum bottom hadrons. The design requirements are fulfilled by having two thin ($\leq 0.28\%$ radiation length) layers of Active Pixel Sensors (APS) with a resolution of 10 μm at the front surface of the detector. APS technology is the only option that fits these requirements without compromising the efficiency or the readout speed. Indeed, an APS can be thinned down to 50 μm and their low power consumption allows us to use air-cooling. The mechanical support will be carefully designed so that the detector can be easily retracted. This feature allows the PIXEL detector to be externally aligned, repaired and upgraded. The IST consisting of two layers of single-sided strips fabricated with a well established technology, provides the additional needed pointing resolution together with the existing SSD to enable connection of track in the STAR TPC with the PIXEL detector. By combining cutting edge sensor and readout technologies of the PIXEL with a flexible and robust mechanical design, the HFT will provide the high precision data on heavy flavor hadrons that are crucial to understand the nature of the medium formed in Au+Au collisions at RHIC.

10 Appendix I – The Silicon Strip Detector (SSD)

10.1 Introduction

The STAR Silicon Strip Detector[93] (SSD) is the outermost layer of the HFT. Installed between IST-2 and the TPC, the SSD will enhance the tracking capabilities of the STAR experiment by measuring accurately the two-dimensional hit position and energy loss of charged particles. It aims specifically at improving the extrapolation of TPC tracks to the IST. As a result, the tracking efficiency is significantly improved. The SSD resides at a distance of 230 mm from the beam axis and covers a pseudorapidity range of $|\eta| < 1.2$. It has a total silicon surface of about 1 m^2.

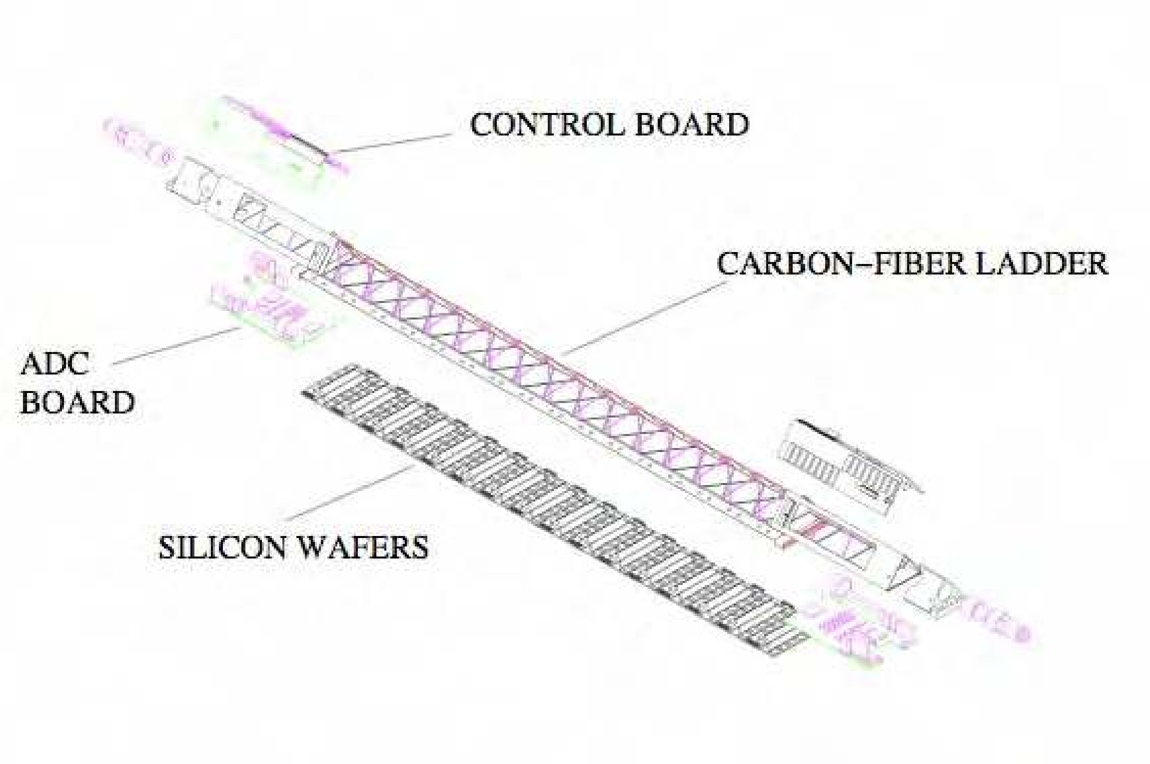

Figure 86: An SSD ladder showing separately its components.

The design of the SSD has two clam shells. Each clam shell supports 10 carbon fiber ladders. Each of these ladders (see Figure 86), supports 16 wafers using double-sided silicon strip technology (768 strips per side). These wafers are connected to the front-end electronics (6 ALICE 128C chips per side) by means of the Tape Automated Bonded

(TAB) technology.[152] The ladders are tilted with respect to their long axis, allowing the overlap of the detectors in the transverse plane for better hermiticity and alignment. A bus cable transports the analog signals along the ladder to a 10-bit ADC board, which is installed at each end. After digitization, the signals are sent to Readout Boards, which are linked to the DAQ system through Giga-link optical fibers.

The whole system is remotely controlled to monitor power and temperature and also to calibrate and tune the front-end electronics. The cooling system uses airflow through the ladder, which is enclosed in a Mylar sheet. The total radiation length of each ladder is approximately 1%.

10.2 Current Readout

The current readout chain can be viewed in Figure 87. There, 10 ADC boards are daisy chained to one readout board. As each of the 20 ladders has two ADCs, then a total of four RDO boards can digitize the full detector.

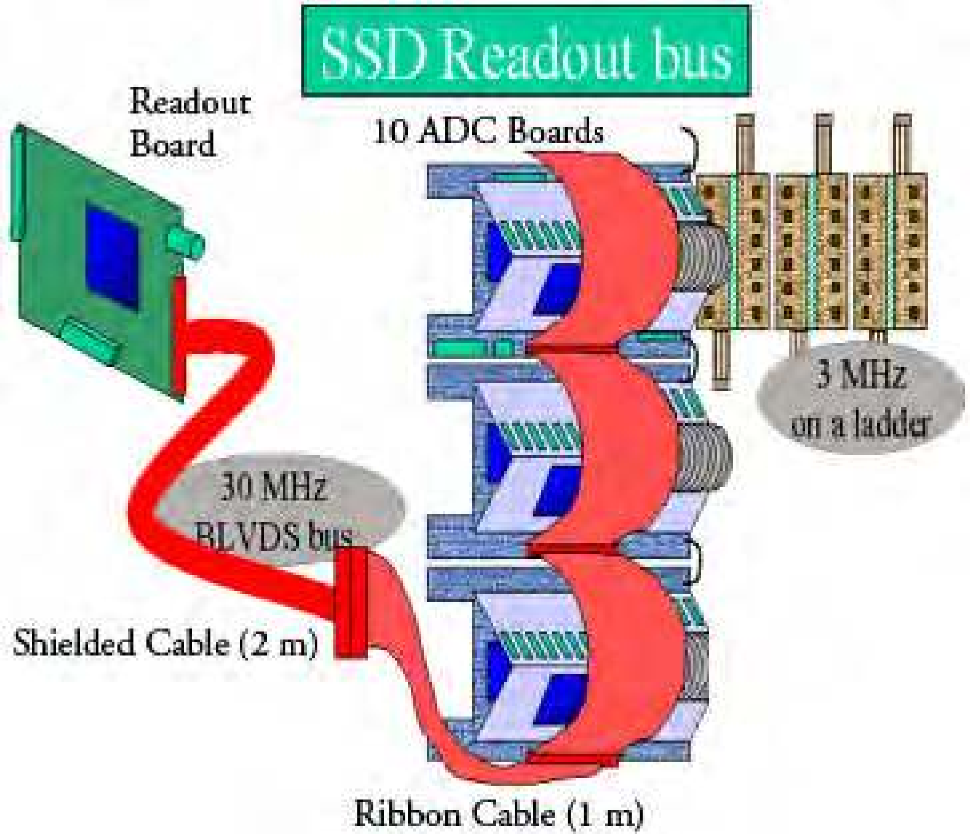

Figure 87: Module layout of the electronics.

The current FEE runs at 3 MHz. As there are 768 strips/wafer and 16 wafers/ADC Board, then it takes 4.1 ms to read out a ladder into the ADC Board. Each RDO, which runs at 30 MHz controls 10 ADC boards. Therefore, it takes a similar time, 4.1 ms, to read out each RDO. Due to a quick fix to match the TPC format, there is an extra 3 ms needed to readout extra 0s. Nevertheless, that SSD readout time is less than the TPC, so no special effort has been made to eliminate this superfluous data. When needed, this extra data transfer can be eliminated.

10.3 Future Readout

The existing ADC, which is Analog Devices model AD 9200,[153] can operate at 10 MSPS as its maximum speed is 20 MSPS. However, the fundamental limitation to increasing the readout speed to match DAQ1000 is the custom made ALICE128 ASIC.[154] This device has a maximum speed of 10 MHz. In principle, the ladder should work at this maximum speed, so that the SSD readout out speed can be increased to 800 Hz. In order to achieve this rate, the number of readout cards needs to be increased from 4 to 14. However, because of the significant effort required to produce this new hardware, we feel it is much wiser to replace the complete readout hardware.

The new readout chain will use an architecture which makes use of the PC-based PCI-RORC cards connected by DDL fiber-optic links. As this architecture is identical to that used in the upgraded TPC DAQ, the development time and effort will be reduced. This endeavor also requires redesigning the SSD readout cards, which are mounted inside the magnet. The ADC card on the SSD ladders will be replaced with a new design utilizing more modern components. As a result, the speed limitation imposed by the existing multi-drop cable connecting the ADC cards to the readout cards will be eliminated. Interleaving the readouts of pairs of modules to one ADC allows conversion at 12 MHz. As a result of these modifications, the new SSD event readout rate will be in excess of 1 kHz and matched to DAQ1000.

10.4 Cooling

The SSD is cooled by room temperature air, which greatly reduces the material budget. Air-cooling has been shown that it can keep the SSD as a proper operating temperature. However, experience has shown that with the existing SVT, there is a tangle of cables. When the pole tip of the STAR magnet is closed, it is very difficult to maintain an adequate supply of air. Therefore, when the PIXEL detector, IST and SSD are integrated in one structure, great care will be taken to provide adequate cooling that can be maintained when STAR is operating.

References

---

[1] F. Karsch, *Nucl. Phys.* A699, 199c (2002).
[2] K.H. Ackermann et al. (STAR Collaboration), *Phys. Rev. Lett.* 86, 402 (2001).
[3] J. Adams et al. (STAR Collaboration), *Phys. Rev. Lett.* 91, 172302 (2003).
[4] C. Adler et al. (STAR Collaboration), *Phys. Rev. Lett.* 90, 082302 (2003).
[5] J. Adams et al. (STAR Collaboration), *Nucl. Phys*. A757, 102 (2005).
[6] J. D. Bjorken, *FERMILAB-Pub-82/59-THY*.
[7] X. N. Wang, M. Gyulassy, I. Vitev, and B. Zhang, *nucl-th/0302077*.
[8] D. Schiff, R. Baier, and B. Zakharov, *Ann. Rev. Nucl. Part. Sci.*, 50, 37 (2000).
[9] J.J. Aubert et al., *Phys. Lett.* B123, 275 (1983).
[10] J. Ashman et al., *Phys. Lett.* B206, 364 (1988).
[11] J. Ashman et al., *Nucl. Phys.* B328, 1 (1989).
[12] B.L. Combridge, *Nucl. Phys.* B151, 429 (1979).
[13] B. Mueller, nucl-th/0404015.
[14] R. Vogt, hep-ph/0203151.
[15] K.J. Eskola, V.J. Kolhinen, and R. Vogt, *Nucl. Phys*. A696, 729 (2001).
[16] P. Levai, B. Mueller, and X.N. Wang, *Phys. Rev.* C51, 3326 (1995);
P. Levai and R. Vogt, *Phys. Rev*. C56, 2707 (1997)
[17] K. Adcox et al. (Phenix Collaboration), *Phys. Rev. Lett.* 88, 192303 (2002).
[18] J. Adams et al. (STAR Collaboration), *Phys. Rev. Lett*. 94, 062301 (2005); nucl-ex/0407006.
[19] T.Sjöstrand, Comp. Phys. Commun. 82, 74 (1994).
[20] PYTHIA 6.152 was used with the parameter settings: MSEL=1, CTEQ5M1. Bottom contribution was estimated to be 20-30% in p_T=2-3 GeV/c, 40-50% in 3-4 GeV/c to the total non-photonic electrons, and negligible at lower p_T.
[21] R. Vogt, Private Communication.
[22] S. Batsouli et al. *Phys. Lett*. B557, 26 (2003).
[23] X. Dong, "Open Charm Production at RHIC" QM2005, nucl-ex/0509038.
[24] J. Adams et al. (STAR Collaboration), *Phys. Rev. Lett*. 95, 122301 (2005).
[25] J. Adams et al. (STAR Collaboration), *Phys. Rev. Lett*. 92, 052302 (2004).
[26] K. Schweda et al. (STAR Collaboration), *J. Phys*. G 30, S693 (2004).
[27] J. Castillo et al. (STAR Collaboration), *J. Phys*. G 30, S1207 (2004).
[28] J. Adams et al. (STAR Collaboration), *Phys. Lett*. B616, 8 (2005).
[29] E. Shuryak, *Phys. Lett*. B78, 150 (1978).
[30] R. Rapp and J. Wambach, *Adv. Nucl. Phys*. 25, 1 (2000).
[31] R. Rapp, *Phys. Rev*. C63**,** 054907 (2001); R. Rapp, hep-ph/0201101;
R. Rapp and J. Wambach, hep-ph/9909229.
[32] U. Heinz and P.F. Kolb, *Nucl. Phys*. A702**,** 269c (2002).
[33] H. Sorge, *Phys. Rev. Lett*. 78, 239 (1997); H. Sorge, *Phys. Rev. Lett*. 8**2,** 2048 (1999).
[34] C. Adler et al. (STAR Collaboration), *Phys. Rev. Lett.* 87, 262301 (2001).
[35] C. Adler et al. (STAR Collaboration), *Phys. Rev. Lett*. 89, 132301 (2002).
[36] P. Huovinen et al. *Phys. Lett*. B503, 58 (2001).
[37] M. Kaneta (PHENIX Collaboration), *J. Phys. G: Nucl. Part. Phys*. 30, S1217 (2004).
[38] V. Greco, C.M. Ko, and R. Rapp, *Phys. Lett*. B595, 202 (2004)
[39] J. Stachel, *Nucl. Phys*. A654, 119c (1999).
[40] P. Braun-Munzinger, D. Magestro, K. Redlich, and J. Stachel, *Phys. Lett*. B518**,** 41 (2001).
[41] P. Braun-Munzinger, K. Redlich, and J. Stachel, nucl-th/0304013.
[42] E. Schnedermann, J. Sollfrank, and U. Heinz, *Phys. Rev*. C48**,** 2462 (1993).
[43] P. Braun-Munzinger and J. Stachel, *Phys. Lett*. B490**,** 196 (2000).
[44] P. Braun-Munzinger and J. Stachel, *Nucl. Phys*. A690**,** 119c (2001).

---

[45] A. Andronic, P. Braun-Munzinger, K. Redlich, and J. Stachel, *Phys. Lett.* B571, 36 (2003).
[46] http://www-h1.desy.de/psfiles/confpap/EPS2003/H1prelim-02-076.ps
[47] http://www-zeus.desy.de/physics/phch/conf/eps03/564/paper.pdf
[48] B.I. Abelev et al. (STAR Collaboration), *Phys. Rev. Lett.* 98, 192301 (2007).
[49] M. Djordjevic, M. Gyulassy, and S. Wicks, Phys. Rev. Lett. 94, 112301 (2005).
[50] Y.L. Dokshitzer and D.E. Kharzeev, *Phys. Lett*. B519, 199 (2001).
[51] N. Armesto, A. Dainese, C.A. Salgado, U. Wiedemann, *Phys. Rev*. D71, 054027 (2005).
[52] S. S. Adler et al. (PHENIX Collaboration), *Phys. Rev. Lett.* 91, 072301 (2003).
[53] S. S. Adler et al. (PHENIX Collaboration),)., *Phys. Rev. Lett.* 91, 241803 (2003).
[54] M. Gyulassy and M. Plümer, *Nucl. Phys.* A527, 641c (1991).
[55] H. Büsching et al. (PHENIX Collaboration), *Nucl. Phys*. A774, 103 (2006).
[56] J. Dunlop et al. (STAR Collaboration), *Nucl. Phys*. A774, 139 (2006).
[57] A. Adare et al. (PHENIX Collaboration), *Phys. Rev. Lett.* 98, 172301 (2007).
[58] J. Adams et al. (STAR Collaboration), *Phys. Rev. Lett*. 91, 072304 (2003).
[59] M. Djordjevic, M. Gyulassy, R. Vogt, and S. Wicks, *Phys. Lett*. B632, 81 (2006).
[60] H. van Hees, V. Greco, and R. Rapp, nucl-th/0508055.
[61] K. Abe et al. (Belle Collaboration), *Phys. Rev. Lett*. 89, 142001 (2002).
[62] S. Baek, P. Ko, J. Lee, and H.S. Song, *J. Korean Phys. Soc*. 33, 97 (1998).
[63] P.L.Cho and A.K. Leibovich, *Phys. Rev*. D54, 6690 (1996).
[64] F. Yuan, D.F. Aiao, and K.T. Chao, *Phys. Rev*. D56, 321 (1997).
[65] B.L. Ioffe and D.E. Kharzeev, *Phys. Rev*. D69, 014016 (2004).
[66] D.E. Kharzeev and K. Tuchin, *Nucl. Phys*. A753, 316 (2005).
[67] R. Rapp, *Phys. Rev.* C63, 054907 (2001).
[68] X. Dong, P. Sorensen, and N. Xu, in preparation.
[69] A. Marín et al., *J. Phys. G: Nucl. Part. Phys*. 30, S709 (2004).
[70] D. Adamova et al. (CERES Collaboration), *Phys. Rev. Lett*. 91, 042301 (2003).
[71] R. Arnaldi et al. (NA60 Collaboration), *Phys. Rev. Lett*. 96, 162302 (2006).
[72] G. David, R. Rapp, Z. Xu, nucl-ex/0611009.
[73] R. Rapp, *Phys. Rev.* C63, 054907 (2001).
[74] R. Rapp, *Pramana* 60, 675 (2003).
[75] R. Rapp, nucl-th/0204003.
[76] M. Cacciari, P. Nason, and R. Vogt, hep-ph/0502203; *Phys. Rev. Lett*. 95, 122001 (2005).
[77] See e.g. M Cacciari, hep-ph/0407187; M.L. Mangano, hep-ph/0411020.
[78] B.A. Kniehl, G. Kramer, I. Schienbein, and H. Spiesberger, hep-ph/0508129; *Phys. Rev. Lett*. 96, 012001 (2006).
[79] http://www-hera-b.desy.de/general/talks/05/had05_charm_faccioli.pdf
[80] R. Vogt, private communication, 2007.
[81] M. Cacciari, M. Greco, and P. Nason hep-ph/9803400; *JHEP* 9805, 7 (1998).
[82] Z. Xu, nucl-ex/0607015; A.A.P. Suaide, nucl-ex/0702035.
[83] B.I. Abelev et al. (STAR Collaboration), *Phys. Rev. Lett*. 97, 252001 (2006).
[84] K.J. Eskola et al, *Nucl. Phys*. B535, 351 (1998), *Eur. Phys. J*. C9 (1999) 61, hep-ph/0703104.
[85] M. Hirai et al, *Phys. Rev*. D64, 034003 (2001), *Phys. Rev*. C70, 044905 (2004).
[86] D. de Florian and R. Sassot, *Phys. Rev*. D69, 074028 (2004).
[87] B. Lampe and E. Reya, hep-ph/9810270; *Phys. Rept*. 332, 1 (2000).
[88] M. Karliner and R.W. Robinett, *Phys. Lett*. B324, 209 (1994).
[89] I. Bojak and M. Stratmann, *Phys. Rev*. D67, 034010 (2003).
[90] X.-D. Ji, *Phys. Lett*. B284, 137 (1992); J. Soffer, M. Stratmann, and W. Vogelsang, *Phys. Rev*. D65, 114024 (2002).
[91] http://rhicii-science.bnl.gov/spin/program/talks/sudoh-2.pdf

---

[92] K.H. Ackerman et al. (STAR Collaboration), *Nucl. Instr. and Meth*. A499, 624 (2003); M. Anderson et al. (STAR Collaboration), *Nucl. Instr. and Meth*. A499, 659 (2003).

[93] L. Arnold et al., *Nucl. Instr. and Meth*. A499, 652 (2003).

[94] P. Billoir, *Nucl. Instr. and Meth*. A225, 352 (1984).

[95] R. Fruhwirth, *Nucl. Instr. and Meth*. A262, 444 (1987); D. Liko, STAR Note SN0087.

[96] H.H. Wieman, private comm. http://rnc.lbl.gov/~wieman/HitDensityMeasuredLuminosity7.htm

[97] K. Hencken, G. Bauer, and D. Trautmann, *Phys. Rev*. C69, 054902 (2004).

[98] http://www-rnc.lbl.gov/~wieman/HitFinding2DXsq.htm

[99] http://rnc.lbl.gov/~wieman/GhostTracks.htm

[100] http://rnc.lbl.gov/~wieman/HitFindingPadVsStrip.htm

[101] *GEANT -- Dectector Description and Simulation Tool*, The CERN computing center. CERN Program Library Long Writeup W5013, and Technical Report:
http://www.star.bnl.gov/STAR/comp/simu/newsite/gstar/Manual/manual_index.html

[102] K. Abe *et al., Nucl. Instr. and Meth.* A400, 287 (1997).

[103] J. Janesick, *Scientific Charge-Coupled Devices,* SPIE Press, Bellingham, WA, 2001.

[104] K.D. Stefanov, *Nucl. Instr. and Meth*. A549, 93 (2005).

[105] C.J.S. Damerell, *Rev. Sci. Instr*. 69, 1549 (1998).

[106] J. Kemmer and G. Lutz, *Nucl. Instr. and Meth*. A253, 365 (1987).

[107] G. Lutz, Nucl. *Instr. and Meth*. A549, 103, (2005).

[108] E. R. Fossum, IEEE Trans. On Electron Devices, 44, 1689 (1977).

[109] http://ireswww.in2p3.fr/ires/recherche/capteurs/

[110] R. Turchetta et al., *Nucl. Instr. and Meth*. A458, 677 (2001).

[111] M. Winter et al., *Proc. of the 8th ICATPP, Como Italy* (2003).*lear Science Symposium, Portland* Or.

[112] MIMOSA: Standing for Minimum Ionizing particle MOS Active pixel sensor.

[113] M. Devaux et al., *Nucl. Instr. and Meth*. A512, 71 (2003).

[114] W. Dulinski et al., *Proc. IEEE Trans. Nucl. Sci*. (2003).

[115] http://www.lbnl.leog.org/thinned_mimosa_testing.htm

[116] Technical report, http://ireswww.in2p3.fr/ires/recherche/capteurs/index.html

[117] H. S. Matis et al., *IEEE Trans. on Nucl. Sci*. 50, 1020 (2003).

[118] S. Kleinfelder et al., Proceedings of the SPIE, Hard X-Ray and Gamma Ray Detector Physics IV, July 2002, Vol. 4784, pp 208.

[119] H.S. Matis et al., *Nucl. Instr. and Meth*. A549, 130 (2005).

[120] S. Kleinfelder et al., LBNL 59121, Submitted to the Proceedings of Pixel 2005, Bonn, Germany (2005).

[121] S. Kleinfelder et al*., IEEE Trans. Nucl. Sci*. 51, 2328 (2004).

[122] N.H. Xuong et al., *SPIE* 5301, 242 (2004).

[123] Technical report, http://www-lepsi.in2p3.fr/~huch/MimoStar181203.pdf

[124] Technical report, http://www-rnc.lbl.gov/~wieman/RadiationLengthsProposal.htm

[125] http://www-rnc.lbl.gov/~wieman/radiationdoseinapsDulinskiValue.htm

[126] http://doc.cern.ch/yellowrep/2001/2001-006/p1.pdf

[127] http://www.lbnl.leog.org/writeup.htm

[128] Technical report, http://www-rnc.lbl.gov/~wieman/StiffnessLadder1.htm

[129] Technical report, http://www-rnc.lbl.gov/~wieman/StiffnessLadder1.htm

[130] TV Holography System at LBNL, courtesy of Eric Anderssen and the ATLAS project.

[131] Technical report, http://www.lionprecision.com/modular/probes.html

[132] Technical report, http://www.lbnl.leog.org/writeup.htm

[133] Technical report, http://www.lbnl.leog.org/ir prelim writeup.htm

[134] Technical report, http://www.lbnl.leog.org/cable constraints.htm

[135] Technical report, http://www.lbnl.leog.org/crossing_lines_measurement_first_look.htm

[136] http://direct.xilinx.com/bvdocs/publications/ds100.pdf

[137] MIMOSTAR-2 Manual, http://www.lbnl.leog.org/rdo/MimoStar2_1_1.pdf

---

[138] User Guide http://www.pg.infn.it/home/imbergam/microtronix_stratix/Getting%20Started%20Guide.pdf

[139] Schematic, http://www.lbnl.leog.org/rdo/mimostar2_mb_prelim_v4.pdf

[140] Schematic, http://www.lbnl.leog.org/rdo/mimostar2_cable_sept_test_final.pdf

[141] Schematic, http://www.lbnl.leog.org/pdf/hft-daughterboard.pdf

[142] Steve Peggs and Steve Tepikian, Private Communication.

[143] S. Tepikian, Twiss functions and beam sizes of the RHIC intersection. *RHIC/AP25* (1994).

[144] Technical report, http://www-rnc.lbl.gov//~wieman/BeamPipeRadiusLimitsRHICAP25.htm

[145] Technical report, http://www-rnc.lbl.gov/~wieman/WolframFisherApertureNote.htm

[146] Technical report, http://www-rnc.lbl.gov/~wieman/BeamPipeVacuumShortAns.htm

[147] John O'Hanlon, *A User's Guide to Vacuum Technology*. John Wiley and Sons, second edition (1989).

[148] Seth Wieman, Private Communication.

[149] Technical report, http://www-rnc.lbl.gov/~wieman/TopThinPipeAnalysis.htm

[150] Sandro Bravar, Private Communication.

[151] Dan Weiss, Private Communication 30-Nov-2004.

[152] S. Bouvier, Proceedings of the workshop on electronics for LHC experiments, Rome, Sept. 1998.

[153] http://www.analog.com/en/prod/0,,AD9200,00.html

[154] L. Hebrand et al., Proceedings of the Eleventh Annual IEEE International ASIC Conference, 89 (1998).

Addendum to STAR HFT proposal

January 22, 2008

Introduction

The STAR HFT upgrade proposal was submitted to BNL in the summer of 2007. It describes the configuration and proposed design of the detector as of that time[1]. Since then the simulation work and the R&D effort have continued. In particular, we have improved the design and geometry of the PIXEL detector and we have simplified the IST design and geometry. We have also made substantial improvements to the electronics readout scheme for the PIXEL detector. In part due to these changes, the overall cost range of the proposal has come down.

We have also reviewed our plans for a PIXEL engineering prototype. Instead of planning for a full detector with slow sensors (a different technology than our final sensor) we will now implement a small detector patch with prototype sensors that are a milestone on the path towards a final sensor chip.

This addendum highlights the important changes that have resulted from the work in the past year and it describes the most important consequences for the expected performance of the HFT. At the CD0 review the concept introduced here will be presented in detail. The reader is advised to read this addendum first. Each chapter of this document will reference the chapter in the proposal that is being amended or superseded.

Changes to the PIXEL Detector Geometry

This amends chapter 4 of the proposal.

The support and geometry for the pixel sensors have been modified and the new layout is shown in Figure 1. The sensors will be mounted on a trapezoidal ‘box beam’ (similar to the ALICE and CMS detector designs) and we will no longer use individual ladders to support a row of sensors. Each carrier assembly now has 3 rows of outer sensors for each inner row of sensors. The inner layer of sensors will be located at 2.5 cm radius and the outer layer will sit at an average radius of 8 cm. This is a small increase over the ~7 cm outer radius quoted in the proposal.

We have also changed the way the detector is assembled around the beam pipe. We have adopted a clam shell design rather than a three part assembly (section 4.8.1 page 105) which is easier to design and fabricate.

PIXEL Read-out and Engineering Prototype

This supersedes sections 4.12 – 4.19 in the proposal and amends sections 4.5 and 4.6.

---

[1] The version is labeled “hft_final_submission_version”

Recent changes in the development path for the PIXEL sensors have resulted in a plan which delivers sensors with enhanced capabilities sooner than the ones described in the original proposal. With these new capabilities comes a new set of requirements for the readout system.

We intend to approach the completion of the final PIXEL detector for STAR as a two stage development process with the readout system requirements tied to the stages of sensor development effort in France at IPHC. In the new development path, the first available set of prototype sensors will have digital outputs and a 640 μsec integration time. We will use these sensor prototypes to construct a limited engineering prototype detector system for deployment at STAR during the summer of 2010. A CAD model of this prototype is shown in Figure 2. This prototype system will employ the same mechanical design planned for the final PIXEL detector as well as a readout system that is designed to be a prototype for the expected final readout system. The final electrical and mechanical systems are expected to be deployed with the final sensors at the end of FY11. In this revised development plan a 4 msec sensor as described in the previously submitted proposal will not be deployed at any point and the new development path for the readout and DAQ systems will proceed in a linear way without diversions.

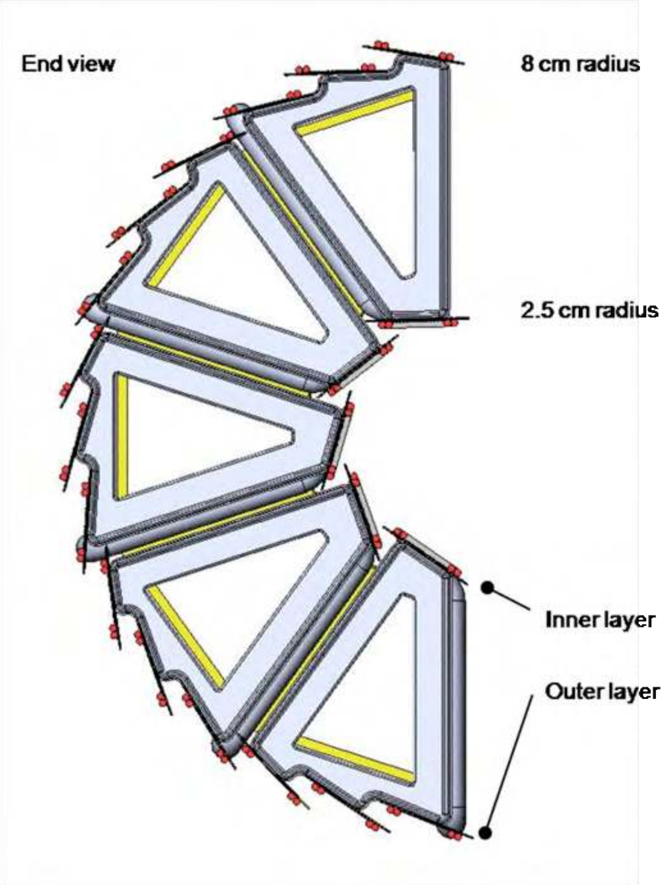

Figure 1: End view of the new PIXEL geometry. The figure shows the inner and outer sensor layers at their new locations of 2.5 cm and 8.0 cm, respectively.

A complete write-up describing the updated sensor development plan and readout system is available at:

http://rnc.lbl.gov/hftcd0/Addendum_rdo_2007_12_26.pdf

It is intended that the linked document serve as a replacement for the readout section of the submitted proposal (sections 4.12 – 4.19).

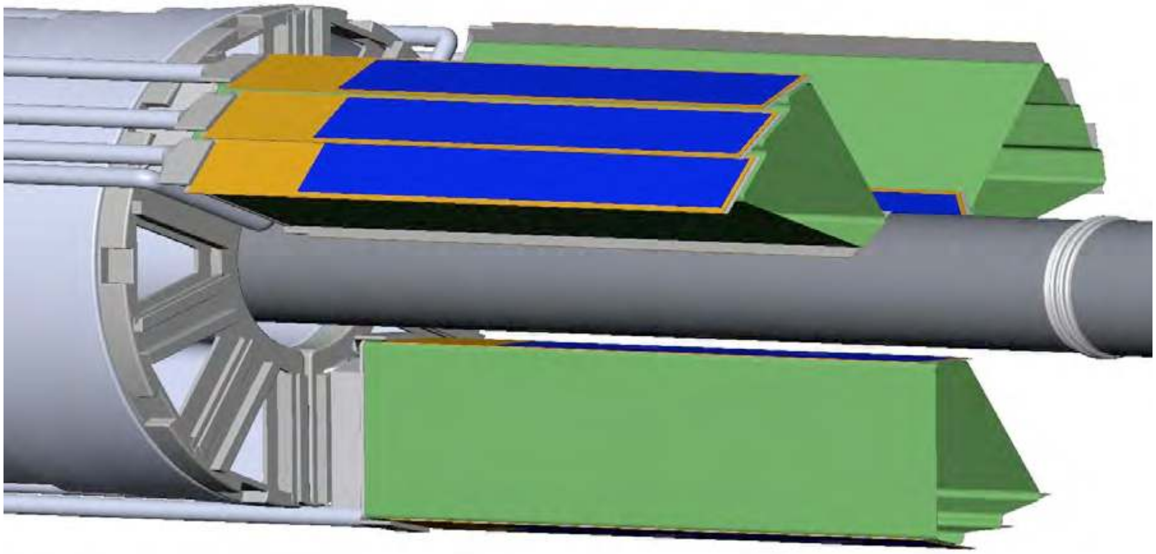

Figure 2: An oblique view of the new detector assembly. Three sensor-assemblies are shown. The detector will be deployed in this configuration for the engineering prototype. Putting the detectors in a 120° configuration maximizes their acceptance for catching the charged-daughter particles from a D^0 decay. The final detector configuration will cover the full 2π azimuth.

IST Geometry

This amends chapter 5 of the proposal.

The layout of the Intermediate Silicon Tracker has been optimized by investigating a large number of different detector geometries with different numbers of layers at different radii, and with different pad sizes to maximize the single-track efficiency for the system as a whole. Another goal was to ensure redundancy in case of failures of either the SSD or the IST sensors.

The old layout (proposal configuration) had three silicon layers at two radial locations. The new layout employs one layer of silicon at one radial location. This design minimizes the number of silicon layers and thus minimizes the number of channels (number of readout chips) and reduces the cost. The current design consists of a single layer at a radius of 14 cm, with 23 ladders, and has a length of 44 cm with 11 sensor modules per ladder. Each Silicon pad sensor has a double-metal-layer construction, AC coupled and with an overall size of 4 cm by 4 cm. The final structure is still being optimized; but pad dimensions of 400 μm x 1 cm are currently anticipated (Section 5.2 page 129-130).

The new configuration has many fewer sensors and readout chips and results in an overall reduction in heat load on the system; but the new scheme requires the use of the more expensive double-metal sensors. A schematic drawing of the new IST geometry and layout is shown in Figure 3.

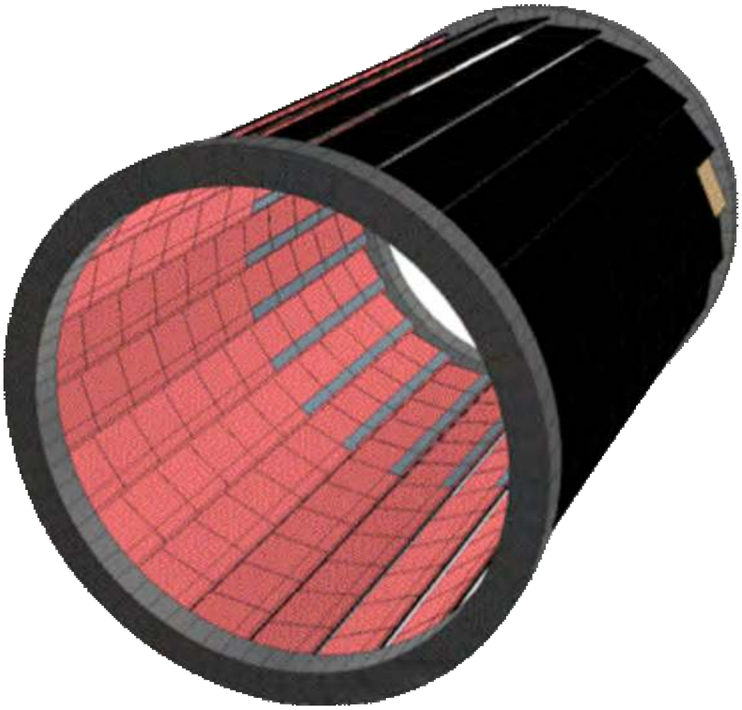

Figure 3: Geometry of the new single layer IST. There are 23 ladders at an average radius of 14 cm; each with 11 Si sensor modules per ladder and 5 APV 25 readout chips per module.

Simulations

This amends chapter 3 of the proposal.

We have completed a detailed set of simulations for the HFT at RHIC II luminosities using GEANT and ITTF. The new feature in these simulations is the fact that they include pile-up from overlapping events. The pile-up calculations were not available at the time the proposal was submitted to BNL and so this is a new result. However, due to the slow pace of performing GEANT simulations, we have only been able to do these simulations, with pile-up, for the configuration described in the proposal. We have not yet completed a full set of simulations for the new detector geometry that is described in this addendum to the proposal. Instead, we have investigated the performance of the new geometry with a compact series of 'hand-calculations' and we have found that the new detector's performance will modestly exceed the performance of the old detector.

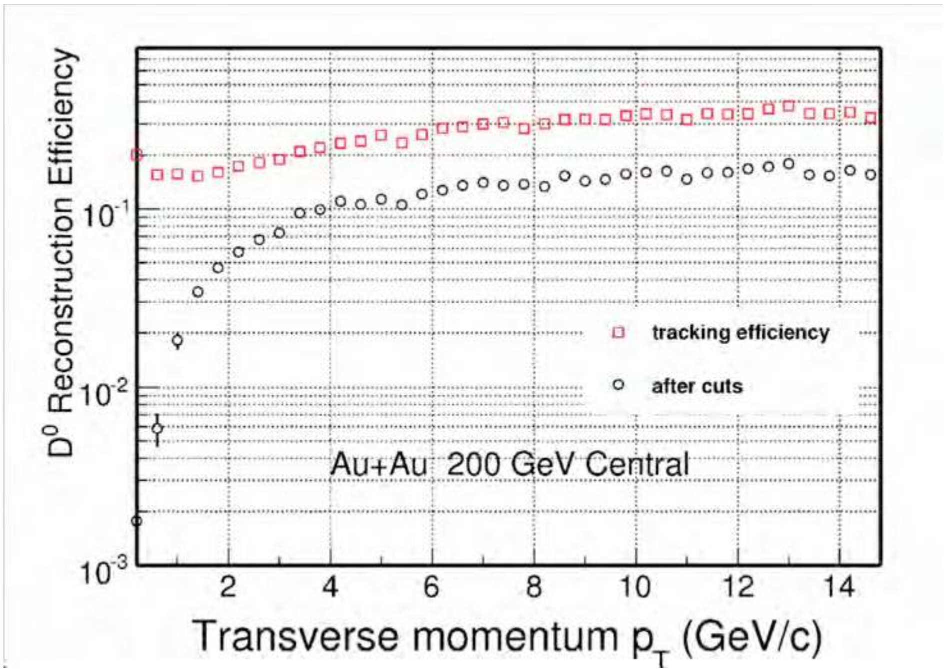

Figure 4: The total efficiency for reconstructing D^0s in the HFT (proposal configuration). These simulations include pileup and were done with GEANT and ITTF and include the finite geometric acceptance of the TPC and SSD. The red squares show the probability that a D^0 is seen by the HFT and the black squares show the absolute efficiency for finding the D^0 after all of the requisite software cuts have been applied to the data. A flat spectrum of D^0s, as a function of p_T, was assumed in the simulation.

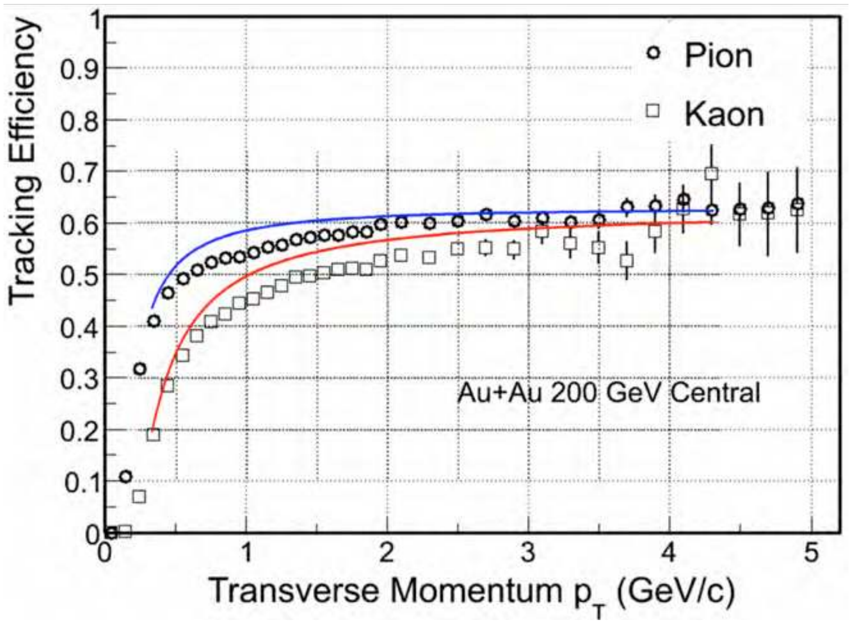

Figure 5: The total efficiency for reconstructing pions and kaons in the HFT (proposal configuration). The simulations include the effects of pileup in the HFT. The data points are from a full GEANT/ITTF simulation that includes the finite acceptance of the TPC and the SSD. The blue and red lines are the result of calculating the same quantities with the hand-calculations. The agreement is surprisingly good in view of the fact that the hand calculations involve a number of simplifications in order to make the calculations tractable with modest tools.

The simulation chain that is referred to in the previous paragraph is the complete STAR software chain that we are developing for physics analysis with the proposed detector. These simulations include the effects of pile-up in Au-Au collisions and, as a critical figure of merit, we have now shown that even for RHIC-II luminosities we can achieve good efficiencies and reasonable signal to background ratios. See Figure 4.

We have also studied the performance of the old detector configuration and the new configuration using hand-calculations. These calculations are based on a simplified Kalman Filter that is closely related to the tracking algorithm implemented in ITTF.

The calculated efficiency for reconstructing pions and kaons in the HFT using GEANT/ITTF and the hand-calculations is compared in Figure 5.

In view of the fact that the hand-calculations agree with the GEANT/ITTF simulations in most critical areas, we are confident that the new detector geometry will also perform well. The results of the hand calculations, for the new geometry, are not substantially different than the results shown in Figure 4.

Cost Estimate

This amends chapter 8 in the proposal. The table represents a new cost range. More details will be given in the presentations at the CD0 review.

The simplification of the HFT design results in a reduced cost compared to the proposal configuration. The table, below, gives the new cost range and the cost for the sub-systems with an estimate of the contingency for each level two WBS item.

WBS	Task Name	Cost (estimate) in K$	Average % Cont.	Cont. in K$	Lower Range in K$	Upper Range in K$
1.1	Research and Design	1,461	0	0	1,461	1,461
1.2	Pixel	1,985	46	1,125	3,110	4,354
1.3	Strip Detector	2,293	36	859	3,152	4,255
1.4	Integration	1,665	41	946	2,611	3,656
1.5	Software	0	60	0	0	0
1.6	Project Management	785	0	0	785	941
Total		8,189	29	2,930	11,119	14,668

LG 10/18/2007

Updated 12/26/2007

Addendum to the PIXEL read-out section of the STAR HFT proposal

This document is intended as an update to sections 4.12 - 4.19 of the Heavy Flavor Tracker for the STAR proposal to the DOE. Recent changes to the development path of the MAPS sensors have resulted in a plan which delivers sensors with enhanced capabilities as compared to the ones described in the original proposal. With these new capabilities comes a new set of requirements for the readout system. In this document we intend to describe the newly agreed sensor development path, the accompanying readout system and provide a preliminary system analysis. This document supersedes the sensor readout and development discussion and analysis presented in section 4.12 – 4.19 of the HFT proposal.

Development and Deployment Plan

We intend to approach the completion of the final PIXEL detector for STAR as a two stage development process with the readout system requirements tied to the stages of sensor development effort at IPHC. In the new development path, the first available set of prototype sensors will have digital outputs and a 640 μs integration time. We will use these sensor prototypes to construct a limited prototype detector system for deployment at the STAR detector during the summer of 2010. This prototype system will employ the mechanical design to be used for the final PIXEL detector as well as a readout system that is designed to be a prototype for the expected final readout system to be deployed with the final PIXEL sensors in a complete detector in the 2012 time frame.

MAPS Sensor Development at IPHC

The initial sensor development path for the PIXEL detector sensors was tailored to follow the development path of the technology as it was set by the IPHC group. In this path, MAPS sensors with multiplexed serial analog outputs in a rolling shutter configuration were envisioned as the first generation of sensors for a prototype or demonstrator patch of PIXEL detector with a more advanced final or ultimate sensor that had a digital output(s). This path is well described in the previous RDO section of the proposal. The new sensor development path moves to digital binary readout from MAPS with fine grained threshold discrimination, on chip correlated double sampling (CDS) and a fast serial LVDS readout. A diagram showing the current development path and with the attendant evolution of the processing and readout requirements is shown in Figure 1.

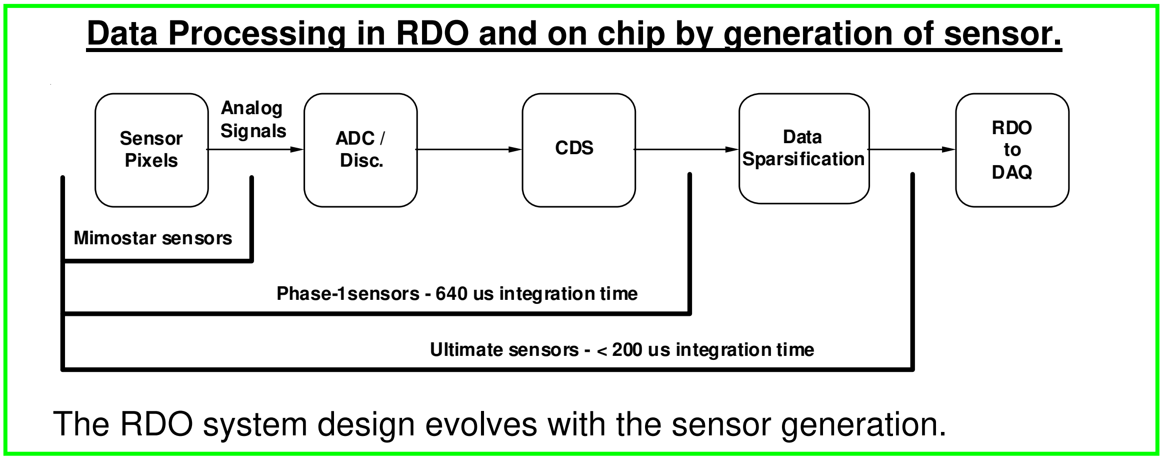

Data Processing in RDO and on chip by generation of sensor.

The RDO system design evolves with the sensor generation.

Figure 1 Diagram showing the sensor development path of sensors for the STAR PIXEL detector at IPHC in Strasbourg, France. The readout data processing required is shown as a function of sensor generation. The first generation Mimostar sensors are read out via a rolling shutter type analog output. The next generation Phase-1 sensor integrates CDS and a column level discriminator to give a rolling shutter binary readout with a 640 µs integration time. The final generation Ultimate sensor integrates data sparsification and lowers the readout time to < 200 µs.

The Mimostar series sensors are the generation of sensors that have been fabricated and tested. These are 50 MHz multiplexed analog readout sensors with 30µm × 30µm pixels in variously sized arrays depending on generation. This generation has been tested and characterized and, with the exception of some yield issues, appears to be well understood. These sensors are well described in the existing RDO section of the proposal.

The next generation is named "Phase-1". This sensor will be based on the Mimosa-8 and Mimosa-16 sensors and will contain on-chip correlated double sampling and column level discriminators providing digital outputs in a rolling shutter configuration. The Phase-1 will be a full sized 640 × 640 array resulting in a full 2 cm × 2 cm sensor size. In order to achieve a 640 µs integration time, the Phase-1 sensor will be equipped with four LVDS outputs running at 160 MHz. The first delivery of wafers of this sensor design is expected in late 2008.

The final sensor is named "Ultimate". The Ultimate sensor contains all of the attributes of the Phase-1 sensor with the pixel sub-arrays clocked faster to give a <200 µs integration time and the integration of a run length encoding based data sparsification and zero suppression circuit. There is one data output from the sensor and the data rates are low thanks to the newly included data sparsification circuitry. The first prototypes of this design are expected to be delivered in the 2010 time frame.

Sensor Series Specifications

The specifications of the sensors under development are shown in the table below.

	Phase -1	**Ultimate**
Pixel Size	30 μm x 30 μm	30 μm x 30 μm
Array size	640 x 640	640 x 640
Active area	~ 2 x 2 cm	~ 2 x 2 cm
Frame integration time	640 μs	100 – 200 μs
Noise after CDS	10 e-	10 e-
Readout time / sensor	640 μs	100 – 200 μs
Outputs / sensor	4	1
Operating mode	Rolling shutter with all pixels read out.	Rolling shutter with data sparsification.
Output type	Digital binary pixel based on threshold crossing.	Digital addresses of hit pixels with run length encoding and zero suppression. Frame boundary marker is also included.

Table 1 Specifications of the Phase-1 and Ultimate sensors.

The Phase-1 is a fully functional design prototype for the Ultimate sensor which results in the Phase-1 and Ultimate sensors having very similar physical characteristics. After successful development and production of the Phase-1 sensors, a data sparsification system currently under development at IPHC will be integrated with the Phase-1 design. With the additional enhancement of design changes allowing for faster clocking of the sub-arrays, the resulting sensor is expected to be used in the final PIXEL detector. In addition to the specifications listed above, both sensors will have the following additional characteristics;

- Marker for first pixel
- Test output pattern JTAG selectable for binary readout troubleshooting. (at least 2 alternating patterns)
- Independent JTAG settable thresholds
- Radiation tolerant pixel design.
- Minimum of 3 fiducial marks / sensor for optical survey purposes.
- All bonding pads located along 1 side of sensor
- Two bonding pads per I/O of the sensor to facilitate probe testing before sensor mounting.

Architecture for the Phase-1 Sensor System

The requirements for the Phase-1 prototype and final readout systems are very similar. They include;

- Triggered detector system fitting into existing STAR infrastructure and to interface to the existing Trigger and DAQ systems.
- Deliver full frame events to STAR DAQ for event building at approximately the same rate as the TPC (~ 1 KHz for the STAR DAQ1K upgrade).
- Reduce the total data rate of the detector to a manageable level (< TPC rate)

We have designed the prototype data acquisition system to read out the large body of data from the Phase-1 sensors at high speed, to perform data compression, and to deliver the sparsified data to an event building and storage device.

The proposed architecture for the readout of the Phase-1 prototype system is shown in Figure 2 with the physical location and separation of the system blocks shown in Figure 3.

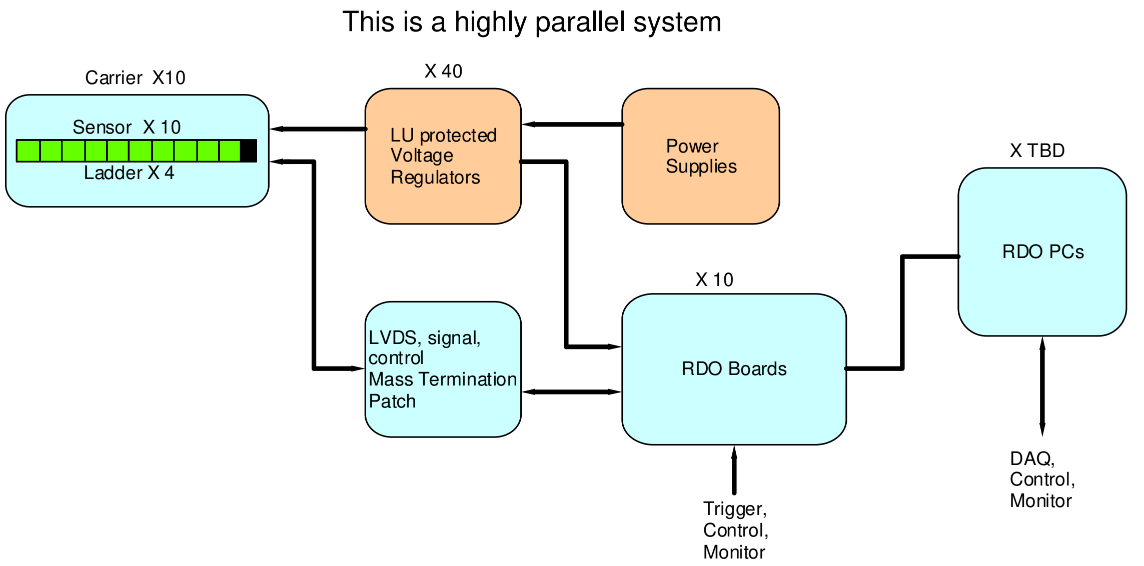

Figure 2 Functional block schematic for the readout for the Phase-1 prototype system. The detector ladders and accompanying readout system have a highly parallel architecture. One system unit of sensor array / readout chain is shown. There are ten parallel sensor array / readout chain units in the full system.

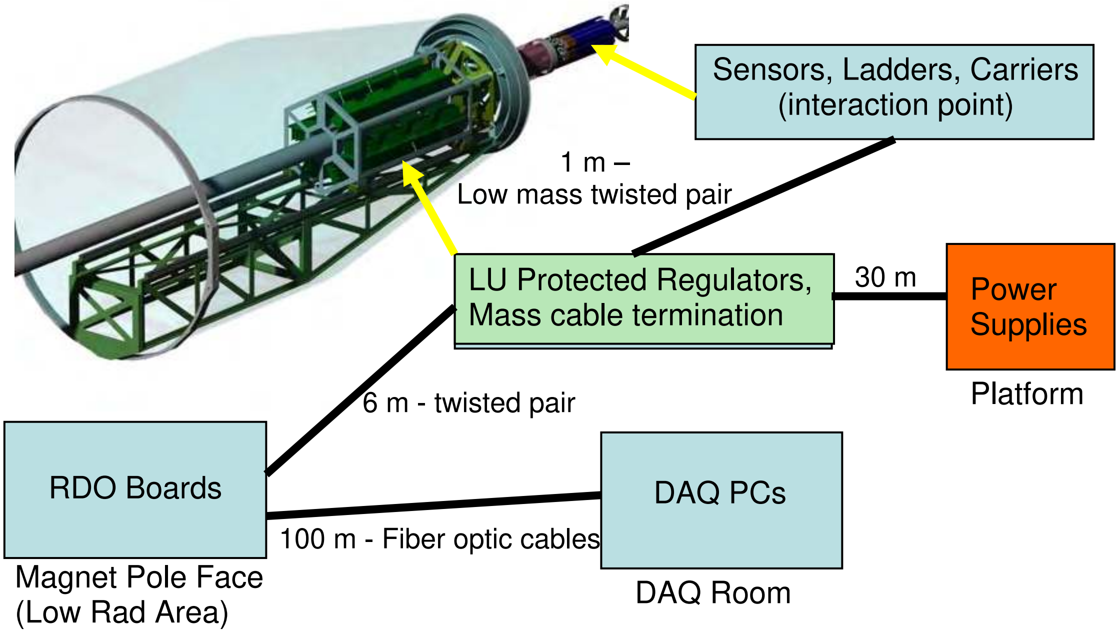

Figure 3 Physical layout of the readout system blocks. This layout will be the same for both the Phase-1 based patch and the final PIXEL detector system.

The architecture of the readout system is highly parallel. Each independent readout chain consists of a four ladders mechanical carrier unit with each ladder containing ten Phase-1 sensors. The current plan is to install a patch of Phase-1 sensors consisting of at least two carrier units mounted with the final mechanical positioning structure and positioned with a 120 degree separation. The readout system will be described as if all carriers will be installed since this architecture also extends to the final PIXEL system.

The basic flow of a ladder data path starts with the APS sensors. A PIXEL ladder contains 10 Phase-1 APS sensors, each with a 640 × 640 pixel array. Each sensor contains four separate digital LVDS outputs. The sensors are clocked continuously at 160 MHz and the digital data containing the pixel threshold crossing information is read out, running serially through all the pixels in the sub-array. This operation is continuous during the operation of the Phase-1 detectors on the PIXEL ladder. The LVDS digital data is carried from the four 160 MHz outputs in each sensor in parallel on a low mass flex printed circuit board to discrete LVDS buffers located at the end of the ladder and out of the low mass detector region. This electronics portion of the ladder also contains the buffers and drivers for the clocks and other control signals needed for ladder operation.

Each Phase-1 sensor requires a JTAG connection for register based configuration, power, ground, a 160 MHz readout clock and a synchronization signal to begin the readout. These signals and latch-up protected power as well as the LVDS outputs and synchronization and marker signals from the detectors are carried via low mass twisted pair cables from the discrete electronics at the end of the ladder to a power / mass termination board located approximately 1 meter from the PIXEL ladders. There is one readout board per PIXEL carrier (40 sensors). A diagram of a ladder is shown in Figure 4.

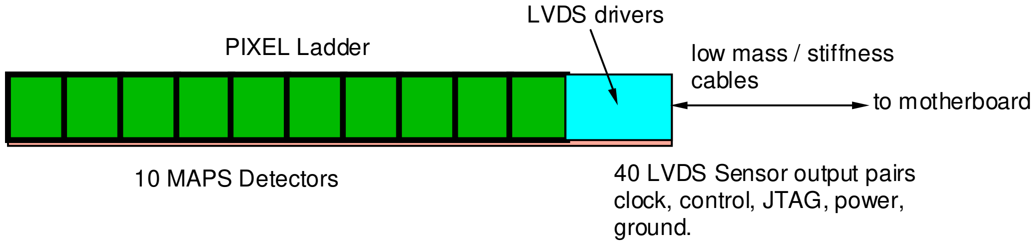

Figure 4 Assembly of sensors on a low radiation length kapton flex cable with aluminum conductors. The sensors are connected to the cable with bond wires along one edge of the ladder.

The flex cable parameters are shown below;

- 4 layer - 150 micron thickness
- Aluminum Conductors
- Radiation Length ~ 0.1 %
- 40 LVDS pair signal traces
- Clock, JTAG, sync, marker traces.

The connection to the driver end of the ladders will be made with very fine 150 µm diameter twisted pair wire soldered to the cable ends. These wires are also very low stiffness to avoid introducing stresses and distortions into the mechanical structure. The other ends of these fine twisted pair wires will be mass terminated to allow connection to the Power / Mass-termination (PM) board located approximately 1 meter away.

Latch-up protected power is provided to the sensors from the PM boards. Each ladder has independently regulated power with latch up detection circuitry provided by a power daughter card that plugs into the PM board. There are four regulation and latch-up daughter cards per PM board and a total of ten PM boards are needed for the complete detector system readout. A block diagram for the PM board is shown in Figure 5.

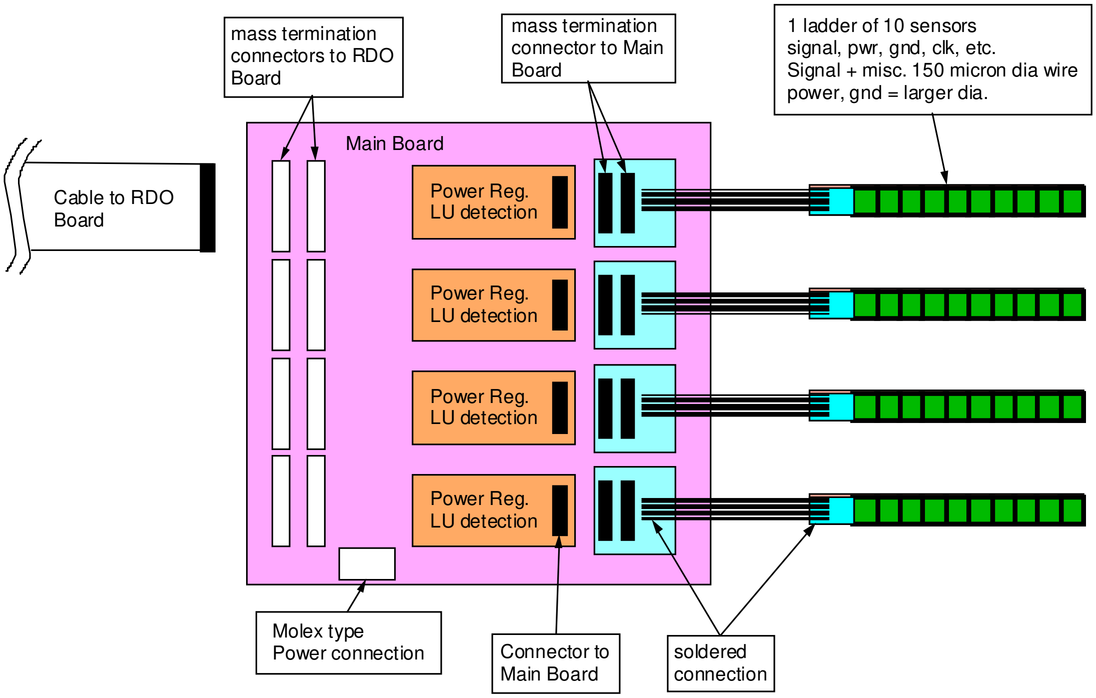

Figure 5 Power and mass-termination board block diagram. The digital signals to and from the sensors are routed through the main board and carried to mass termination connectors for routing to the readout boards. Latch-up protected power regulation is provided to each ladder by a power daughter card mounted to the main board. The main power supplies are located in the STAR racks.

The digital sensor output signals are carried with a 160 MHz clock to from the PM board to the readout boards (RDO) which are mounted on the magnet iron of the STAR magnet structure approximately 6 meters away. A diagram describing the attributes of the two PCBs that make up the RDO system can be seen in Figure 6. A functional block diagram of the RDO can be seen in Figure 7.

Two board System – Virtex-5 Development board mated to a new HFT motherboard

Xilinx Virtex-5 Development Board

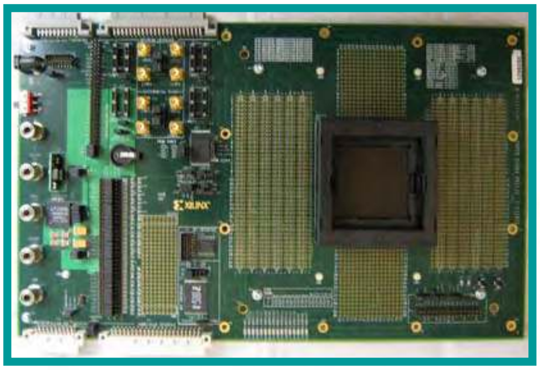

- FF1760 Package
- 800 – 1200 I/O pins
- 4.6 – 10.4 Mb block RAM
- 550 MHz internal clock

\+

New motherboard

- Digital I/O LVDS Drivers
- 4 X >80 MHz ADCs
- PMC connectors for SIU
- Cypress USB chipset
- SODIMM Memory slot
- Serial interface
- Trigger / Control input

Note – This board is designed for development and testing. Not all features will be loaded for production.

Figure 6 Readout board(s). The readout system consists of two boards per carrier of 40 sensors. A commercial Xilinx Virtex-5 development board is mated to a custom motherboard that provides all of the I/O functions including receiving and buffering the sensor data outputs, receiving the trigger from STAR and sending the built events to a STAR DAQ receiver PC via fiber optic connection.

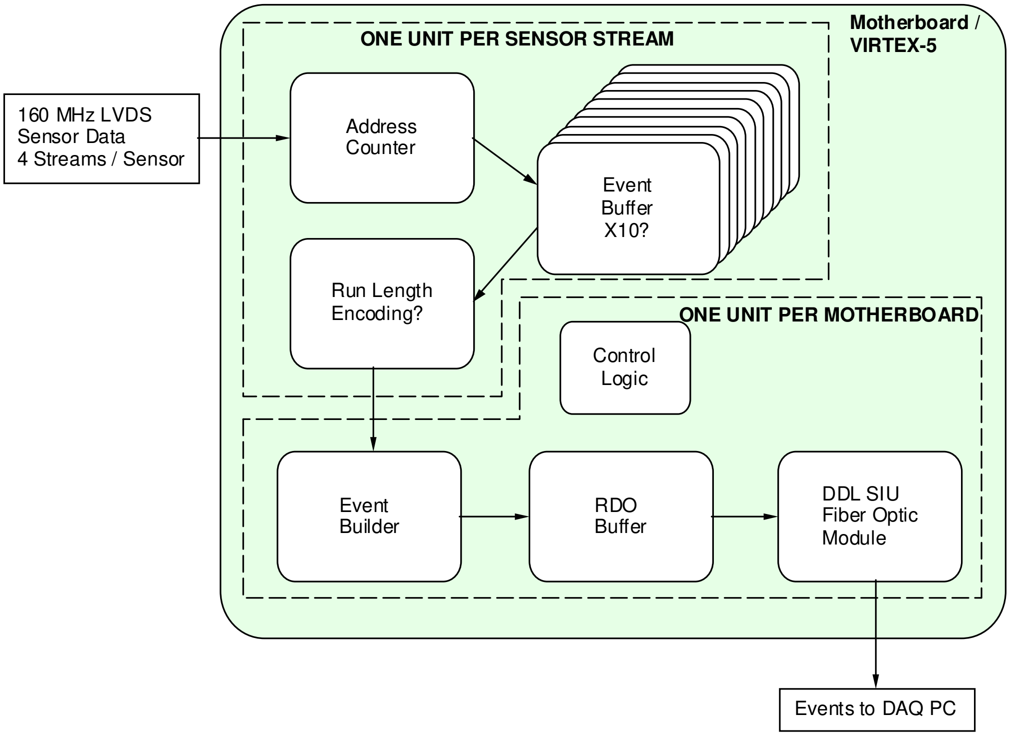

Figure 7 Functional block diagram of the data flow on the RDO boards.

The RDO boards are based on a fast Xilinx Virtex-5 FPGA development board which is mated to a custom motherboard that provides LVDS buffering into the FPGA, the STAR trigger input, PMC connectors for mounting the CERN developed fiber optic Detector Data Link (DDL), SRAM, and various ADCs and I/O to be used in testing. The data processing path is as follows. The sensor output signals are buffered and then fed into the FPGA. In the FPGA the data is resorted to give a raster scan, after which hits registered on pixels are converted to pixel addresses using an address counter. This mechanism of zero suppression, the conversion of hits to addresses in a relatively low multiplicity environment, is the main mechanism for data reduction used in this readout system. The efficiency and accidental rate of a simple threshold on pixel signal is shown in Figure 8.

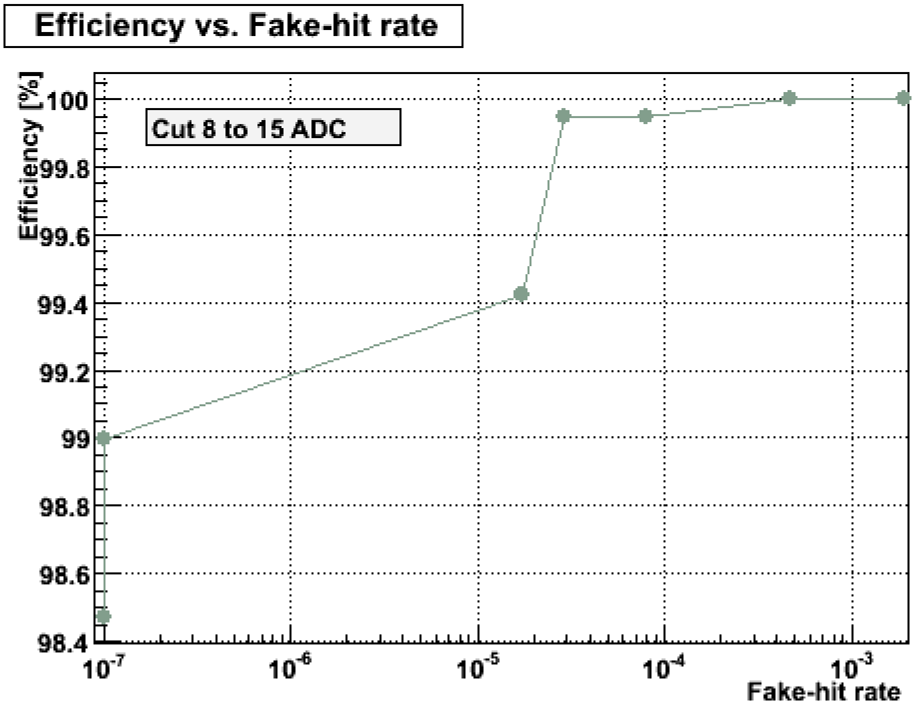

Figure 8 Efficiency and fake hit rate for a simple threshold cut on pixel signal level. This figure is obtained from beam data taken with Mimostar-2 sensors.

When a trigger is received, one of a bank of event buffers is enabled for one frame (409,600 pixels). After the frame has been recorded in the event buffer, the results of that frame are sent to an event builder. The event builder gathers all of the addresses on the RDO from that trigger and builds them into an event which is then passed via fiber optic links to the STAR DAQ receiver PCs. We intend to use the Source Interface Unit (SIU) and Readout Receiver Cards (RORC) developed for ALICE as our optical link hardware to transfer data to and from the STAR DAQ system. These links have been chosen as the primary readout connections for the new STAR TPC FEE. Leveraging existing hardware and expertise in STAR allows for a faster and more reliable design than developing our own custom solution. The complete system consists of a parallel set of carrier (4 ladder / carrier) readouts consisting of 10 separate chains. A system level functionality block diagram is shown in Figure 9.

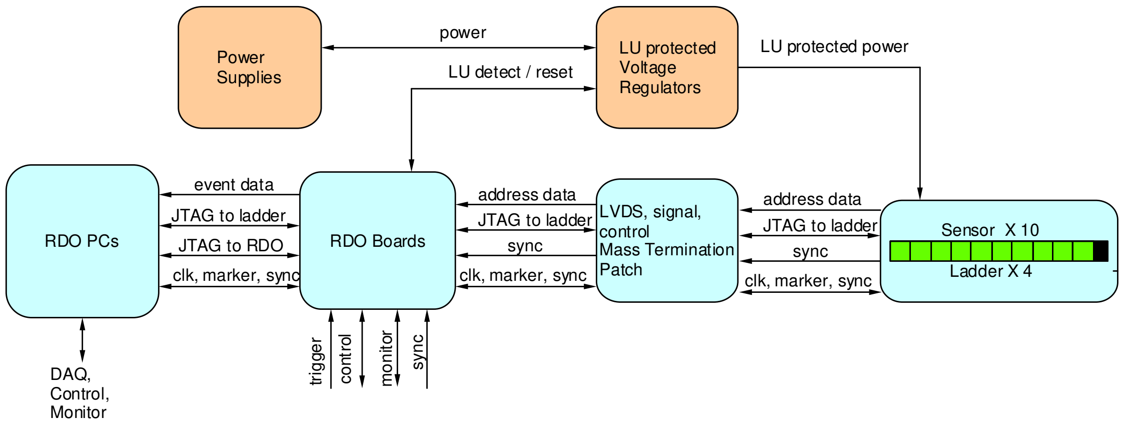

Figure 9 System level functionality diagram of the readout of the PIXEL sensors. One of ten parallel readout chains in shown.

Data Synchronization, Readout and Latency

The readout of the prototype PIXEL sensors is continuous and hit-to-address processing is always in operation during the normal running of the detector. The receipt of a trigger initiates the saving of the found hit addresses into an event buffer for 1 frame (409,600 pixels). The PIXEL detector as a whole will be triggered via the standard STAR TCD module. Since 640 μs are required to read out the complete frame of interest, the data will be passed to DAQ for event building ~ 640 μs after the trigger is received. We will provide for multiple buffers that will allow the capture of temporally overlapping complete frames. This will allow us to service multiple triggers within the 640 μs readout time of the sensor. In this system, the hit address data is fanned out to 10 event buffers. A separate event buffer is enabled for the duration of one frame upon the receipt of a trigger from the TCD. Subsequent triggers enable additional event buffer until all of the event buffers are full and the system goes busy. The resulting separate complete frames are then passed to the event builder as they are completed in the event buffers. This multiple stream buffering gives a system that can be triggered at a rate above the expected average rate of the STAR TPC (approximately 1 kHz) after the DAQ1K upgrade. Furthermore, since the addition of buffers is external to the sensors, the capability for the addition of large amounts of fast SRAM will be included in the RDO board design allowing for flexibility in our readout system configuration. This multiple event buffer architecture will result in the duplication of some data in frames that overlap in time, but our data rate is low and the duplication of some data allows for contiguous event building in the STAR DAQ, which greatly eases the offline analysis. In addition, synchronization between the ladders/boards must be maintained. The PIXEL will receive triggers and the STAR clock via the standard STAR Trigger and Clock Distribution module (TCD). We will provide functionality to allow the motherboards to be synchronized at startup and any point thereafter.

Triggering Considerations

The primary tracking detector of the STAR experiment is the TPC with the Heavy Flavor Tracker upgrade designed to add high resolution vertex information. The PIXEL detector is part of a larger group of detectors that make up the HFT upgrade at STAR. The other tracking detector components of the HFT include the SSD and the IST. Since the HFT is a system of detectors, in order to maximize efficiency, the trigger response and dead time characteristics of the each detector in the HFT system should be matched, as much as possible, to the others. As the main detector, the post DAQ-1K TPC sets the effective standard for the other detectors in the system. In the current understanding of the system, the PIXEL detector information is only useful in conjunction with the external tracking detectors and thus the PIXEL detector will only be triggered when the TPC is triggered.

The triggers in STAR are produced essentially randomly with a 110 ns crossing clock spacing. The behavior of the TPC is to go dead for 50 μs following the receipt of a trigger. This means that the TPC, and by extension the PIXEL detector, will receive random triggers spaced by a minimum of 50 μs. An additional constraint is imposed by the fact that the DAQ 1K contains 8 buffers at the front end. This allows for the capability of the TPC to take a quick succession of 8 triggers (separated by 50 μs) but then the TPC will go busy until the data has been transferred and buffers cleared. The time required for this depends on the event size. (Some of these numbers can be found at http://drupal.star.bnl.gov/STAR/daq1000-capabilities others are private communication with Tonko Ljubicic). This behavior provides the basis for the assessment of the trigger response characteristics of the detectors in the HFT system. In general, HFT detector readout systems should provide for the acquisition of up to 8 successive triggers separated by 50 μs with some, as yet uncharacterized, clearing time. The goal is to have the HFT detectors "live" whenever the TPC is "live". In appendix 1 we show some analysis of the trigger response characteristics of the PIXEL detector.

System Performance for the Phase-1 Prototype Sensor System

The raw binary data rate from each Phase-1 sensor is 80 MB / s. For the 400 sensors that make up the PIXEL detector this corresponds to 32GB / s. This raw data rate must clearly be reduced to allow integration into the overall STAR data flow. Zero suppression by saving only addresses of hit pixels is the main mechanism for data volume reduction. The parameters used to calculate the data rates are shown below in Table 2.

Item	Number
Bits/address	20
Integration time	640 μs
Luminosity	3×10^{27}
Hits / frame on Inner sensors (r=2.5 cm)	295
Hits / frame on Outer sensors (r=8.0 cm)	29
Phase-1 sensors (Inner ladders)	100
Phase-1 sensors (Outer ladders)	300
Event format overhead	TBD
Average Pixels / Cluster	2.5
Average Trigger rate	1 kHz

Table 2 Parameters used to calculate data rates from a Phase-1 based system.

Based on the parameters given above, the average data rate (address only) from the sensors in the prototype Phase-1 detector is 237 kB / event which give an average data rate of 237 MB / s. It is possible to reduce the data rate further using a run length encoding scheme on the addresses as they are passed from the event buffer to the event builder as indicated in Figure 7. We are currently investigating this option, though the data rate reduction from this approach is expected to be moderate. The raw data rate reduction from the hit pixel to address conversion is given graphically below as Figure 10.

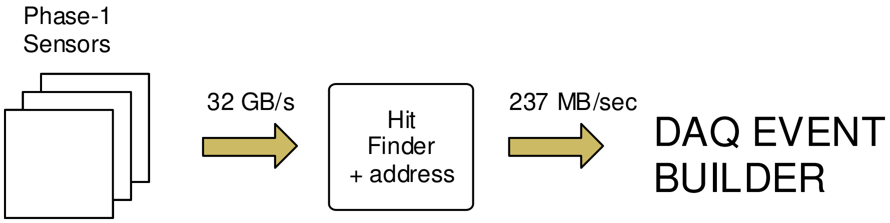

Figure 10 Data rate reduction in the Phase-1 readout system.

Architecture for the Ultimate Sensor System

The most significant difference between the Phase-1 and Ultimate sensors is the integration of zero suppression circuitry on the sensor. The ultimate sensors provide zero suppressed sparsified data with one LVDS output line per sensor. In addition, the sub-frame arrays are clocked faster to give a <200 μs integration time and a frame boundary marker is added to the data stream to allow for the demarcation of frame boundaries in the absence of hits in the sensor and to allow for synchronization with the RDO system. The upgrade from the Phase-1 to the Ultimate sensors in the system is expected to involve the fabrication of new sensor ladders using the same mechanical design used in Phase-1 but with the addition of new Ultimate series sensors and a redesign of the kapton readout cable. The Ultra sensor kapton readout cable will require significantly fewer (10 LVDS pairs instead of 40) traces for readout and the new cable design should have a lower radiation length. The task of reading out the Ultimate series sensors is actually less challenging than the readout of the Phase-1 sensors since the data reduction functionality is included in the sensor. **The readout hardware described above for the Phase-1 readout system remains the same for the Ultimate readout system.** Some reconfiguration of the functionality in the FPGA is required for readout of the Ultimate sensor PIXEL detector. A functional block diagram for the RDO boards is shown in Figure 11.

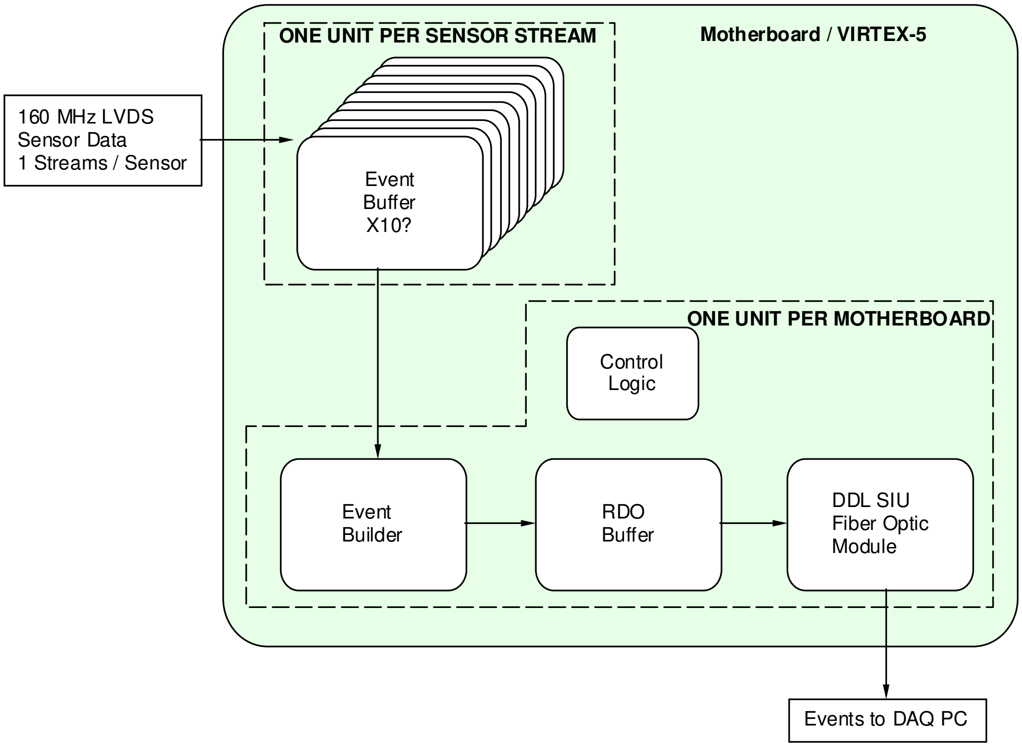

Figure 11 Functional block diagram of the RDO boards for the readout of the Ultimate detector based PIXEL detector.

The Ultimate sensor operates in the same rolling shutter readout mode as the PHASE-1 sensor. The address data clocked out of the Ultimate chip has understood latencies that we will use to keep track of triggered frame boundaries and will be able to verify using synchronization markers from the sensors. The first pixel marker from the sensor corresponds to the actual scan of pixels through the sensor. The frame boundary marker delineates frame boundaries in the sparsification system on the sensor. Using this information and knowing the internal latencies in the sensor, we can generate the internal logic in the FPGA to implement the same multiple buffering technique that was previously described.

System Performance for the Ultimate Sensor System

The parameters used to calculate the data rates for this system are shown below in Table 3

Item	Number
Bits/address	20
Integration time	200 μs
Luminosity	8×10^{27}
Hits / frame on Inner sensors (r=2.5 cm)	246
Hits / frame on Outer sensors (r=8.0 cm)	24
Phase-1 sensors (Inner ladders)	100
Phase-1 sensors (Outer ladders)	300
Event format overhead	TBD
Average Pixels / Cluster	2.5
Average Trigger rate	1 kHz

Table 3 Parameters used to calculate data rates from a Ultimate sensor based system.

From these parameters, we calculate an average event size of 199 kB giving an address data rate of 199 MB / s from the Ultimate sensor based PIXEL detector.

A more detailed analysis of the readout chain including parameters such as the size of buffers and the internal FPGA functions is included as appendix 1.

Appendix 1

Detailed System Description of the HFT PIXEL RDO System

This document is an extension of the PIXEL RDO addendum to the HFT proposal. It is intended to give detailed parameters of the function of the PIXEL readout system that will allow for the understanding of the logic and memory and requirements and the functionality of the readout system. We will present the designs of the Phase-1 and Ultimate readout systems under periodic triggering conditions. The simulation of the system response to random triggering of the type expected to be seen at the STAR experiment is ongoing and will be available upon completion. The readout design is highly parallel and one of the ten parallel readout systems is analyzed for each system.

Phase-1 Readout Chain

The Phase-1 detector will consist of two carrier assemblies, each containing four ladders with ten sensors per ladder. The readout is via parallel identical chains of readout electronics. The relevant parameters from the RDO addendum are reproduced below.

Item	**Number**
Bits/address	20
Integration time	640 μs
Hits / frame on Inner sensors (r=2.5 cm)	295
Hits / frame on Outer sensors (r=8.0 cm)	29
Phase-1 sensors (Inner ladders)	100
Phase-1 sensors (Outer ladders)	300
Event format overhead	TBD
Average Pixels / Cluster	2.5

Table 4 Parameters for the Phase-1 based detector system used in the example calculations shown below.

The functional schematic of the system under discussion is presented below

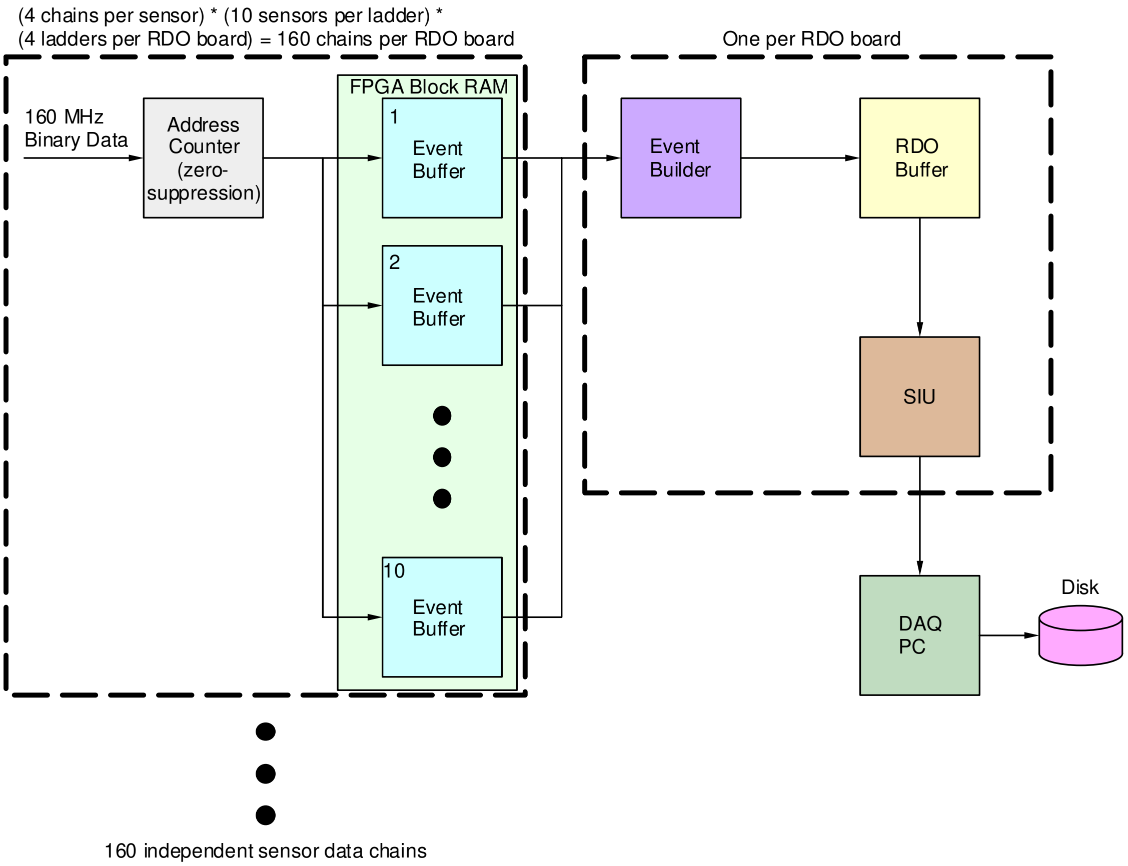

Figure 12 Functional schematic diagram for one Phase-1 sensor based RDO board. Each RDO board services one inner ladder and 3 outer ladders. Each ladder contains 10 sensors.

We will show the system function for two cases. The first is for a periodic trigger rate of 1 kHz. The second is for a periodic trigger rate of 2 kHz. These cases make the scaling clear. In both cases we will use the average (pile-up included) event size. We are currently simulating the dynamic response of the system to the triggering and event size fluctuations seen at STAR and will make this information available after the simulations are completed. It is important to note that the system is FPGA based and can be easily reconfigured to maximize the performance by the adjustment of buffer sizes, memory allocations, and most other parameters. The relevant parameters of the system pictured above are described below;

<u>Data transfer into event buffers</u> – The binary hit data is presented to the address counter at 160 MHz. The corresponding hit address data from the adders counter is read synchronously into the event buffers for one full frame of a 640 × 640 sensor at 160 MHz. This corresponds to an event buffer enable time of 640 μs.

<u>Event Buffers</u> – Each sensor output is connected to a block of memory in the FPGA which serves as the storage for the event buffers. Each block of memory is configured as dual ported RAM and. The overall FPGA block RAM used per sensor output is sized to allow for storage of up to ten average events with event size fluctuation. This leads to a total buffer size that is 20 × the size required for the average sized event (different for

inner and outer sensors). The FPGA block RAM will be configured with pointer based memory management to allow for efficient utilization of the RAM resources. The average inner sensor has 295 hits / event. There are 4 outputs per sensor so the average inner sensor event address length is (0.25 sensor area) × (295 hits) × (20 bits) × (2 factor for event size fluctuations) × (2.5 hits per cluster) = 7,375 bits**.** Multiplying this event buffer size by 10 gives the size of the RAM required for the full set of event buffers required. **The event buffer block RAM size for each inner sensor output is 73,750 bits or 3,688 20-bit addresses**.

For outer sensors, the event buffer size is calculated similarly. The average outer sensor has 29 hits / event. There are 4 outputs per sensor so the average inner sensor event address length is (0.25 sensor area) × (29 hits) × (20 bits) × (2 factor for event size fluctuations) × (2.5 hits per cluster) = 725 bits**.** Multiplying this event buffer size by 10 gives the size of the RAM required for the full set of event buffers required. **The event buffer block RAM size for each outer sensor output is 7250 bits or 363 20-bit addresses**.

<u>Data transfer into the RDO buffer via the event builder</u> – This process is internal to the FPGA, does not require computational resources, and can run at high speed. In the interests of simplicity, we will assume a 160 MHz clock to move data in 20-bit wide address words. The event builder first adds a 128 Byte header that contains the trigger ID and other identifying information into the RDO buffer, and then moves the address data from the event buffers into the RDO buffer in 20-bit words. The average carrier event size is [(29 hits / sensor (outer)) × (10 sensors) × (3 ladders) + (295 hits / sensor (inner)) × (10 sensors) × (1 ladders)] × (2.5 hits / cluster) = **9550 address words (20-bit)**. The RDO buffer is 5 × the size required for an average event and is thus **955 kb** in size. The full time required to transfer the address data into the RDO buffer (in 20-bit per clock transfers) is then **59.7 µs**.

<u>Data transfer from the RDO buffer over the DDL link</u> – The RDO buffer is dual-ported and thus readout from the SIU to the RORC can proceed as soon as the RDO buffer begins filling. The data transfer rates for the SIU – RORC combination as a function of fragment size are shown below.

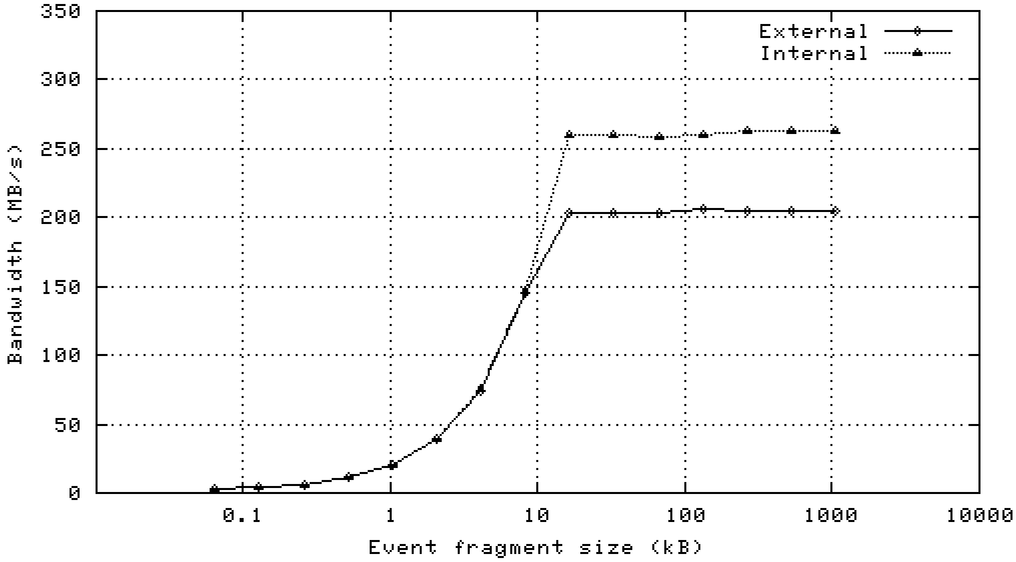

Figure 13 Bandwidth of a single channel of the SIU - RORC fiber optic link as a function of event fragment size with an internal and external (DDL) data source using two D-RORC channels. From the LECC 2004 Workshop in Boston.

In this case, we will assume that we are padding the 20-bit address data to 32-bit word lengths for DDL transfer. The event size is then (32 bits) × (9550 address words) **= 305.6 kb or 38.2 kB.** In this example, our transfer rate is ~ 200 MB / s. This transfer then takes **191 µs.**

Data transfer to the STAR DAQ for event building – The event data is buffered in the DAQ PC RAM (>4GB) until only accepted events are written to disk and then transferred via Ethernet to an event building node of the DAQ system. Level 2 trigger accepts are delivered to the RDO system and transferred via the SIU – RORC to the DAQ receiver PCs. Only the events that have been accepted by level 2 are then built into an event. In this way, the buffer provided by the DAQ PC RAM provides for the elasticity needed for an average event acceptance of 1 kHz

The results of these calculations and discussion are presented below in the following chronograms.

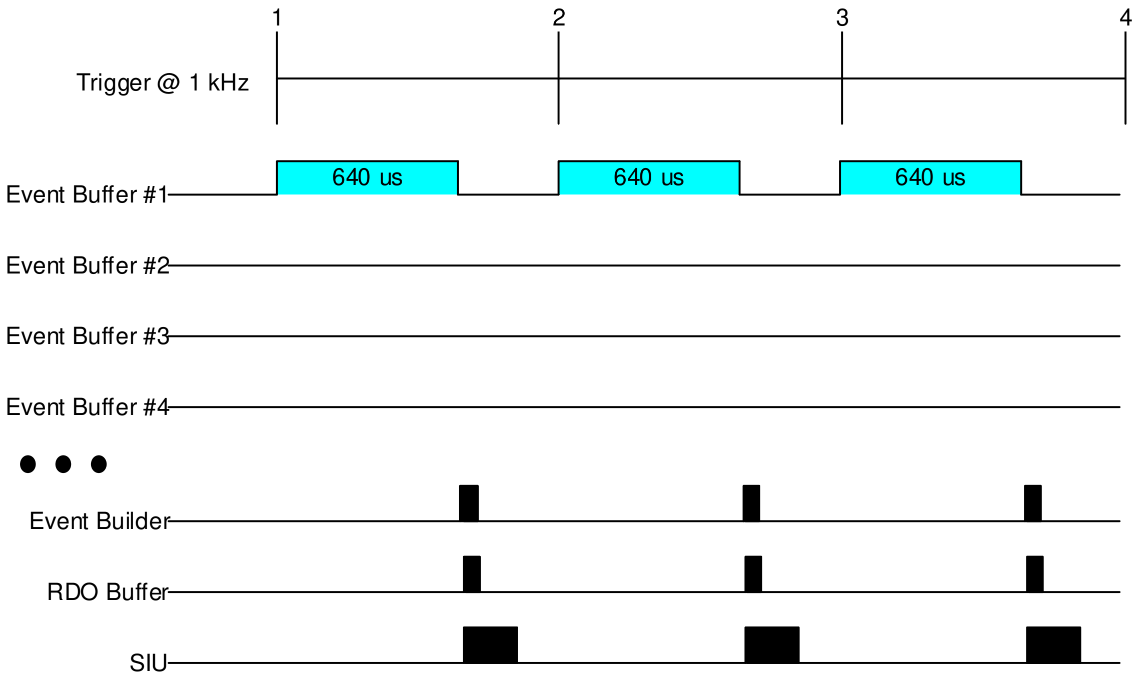

Figure 14 Chronogram of the Phase-1 based readout system functions for a 1 kHz periodic trigger.

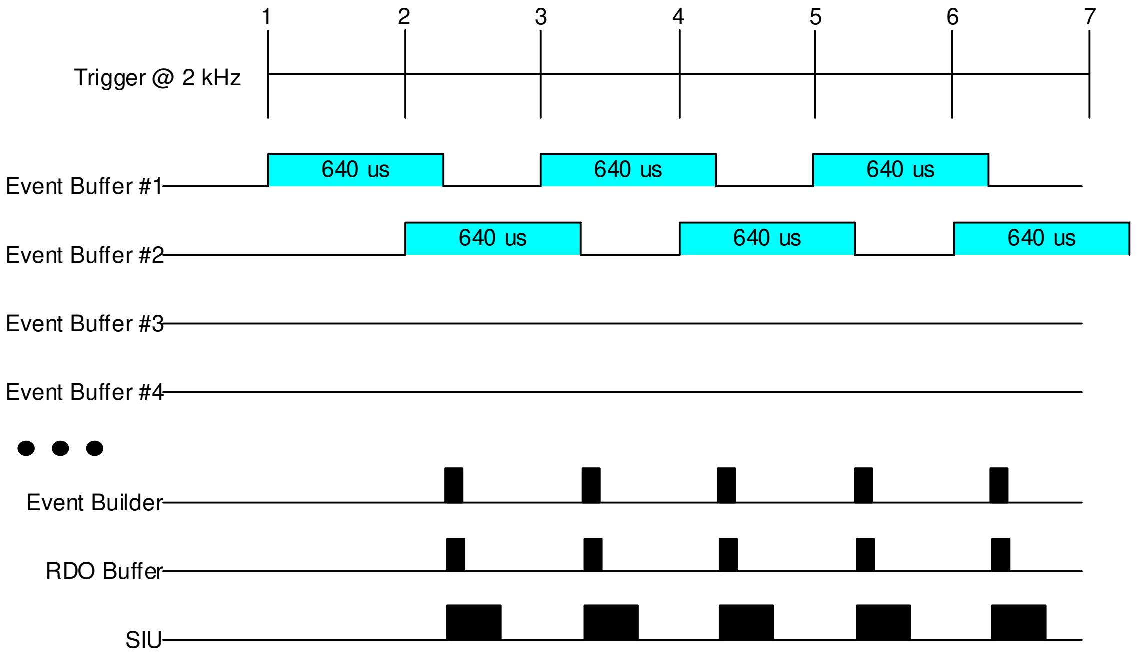

Figure 15 Chronogram of the Phase-1 based readout system functions for a 2 kHz periodic trigger.

The memory resources required in the FPGA / motherboard combination for this readout design are (120 outer sensor readout buffers) × (7.25 kb per event buffer) + (262.5 kb for the RDO buffer) + (40 inner sensor readout buffers) × (73.75 kb per event buffer) + (955 kb for the RDO buffer)= **4775 kb**. The Xilinx Virtex-5 FPGA used in our design contains 4.6 – 10.4 Mb of block RAM so the entire design should fit easily into the FPGA.

Ultimate Sensor Detector Readout Chain

Again, the Ultimate sensor readout system consists of ten parallel readout chains. The main difference between the Phase-1 sensors and the Ultimate sensors is the inclusion of zero suppression circuitry in the Ultimate sensor, thus only addresses are read out into the RDO boards. In addition, the integration time of the Ultimate sensor is 200 μs and there is one data output per sensor. These differences lead to the functional schematic of the readout system shown below.

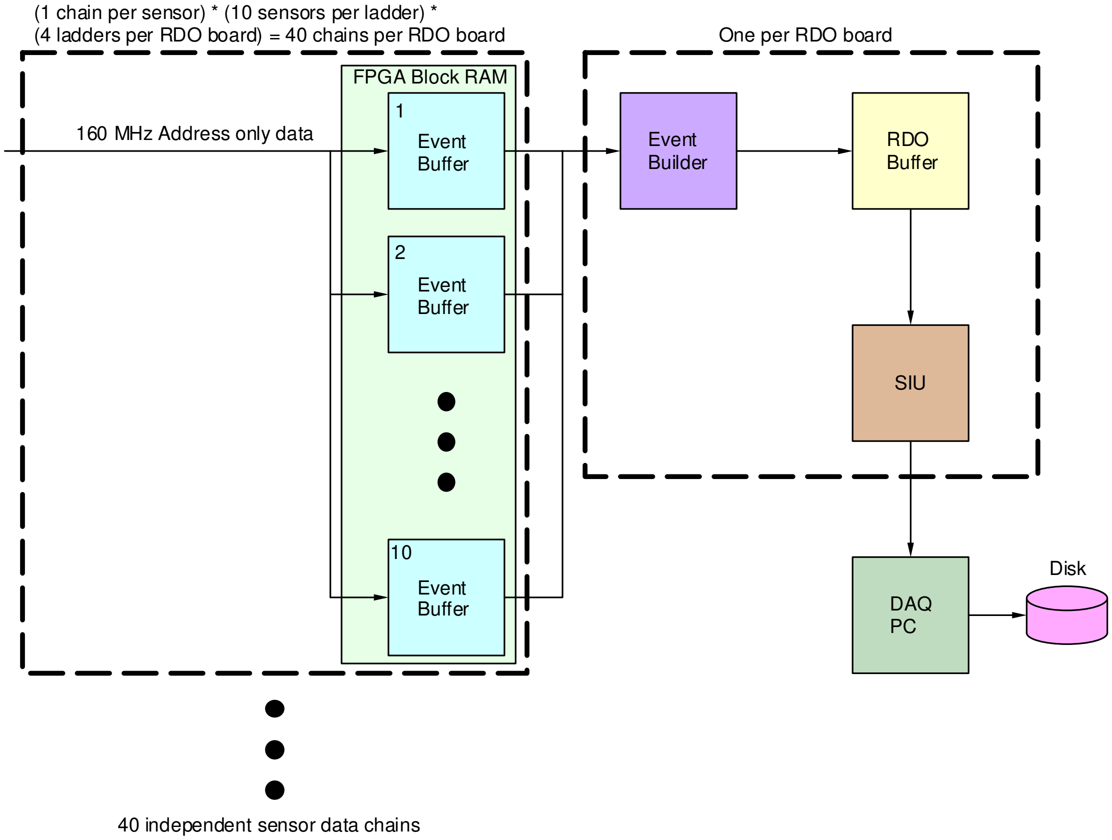

Figure 16 Functional schematic diagram for one Ultimate sensor based RDO board. Each RDO board services one inner ladder and 3 outer ladders. Each ladder contains 10 sensors.

We will show the system function for the same two cases as shown for the Phase-1 readout system. The first is for a periodic trigger rate of 1 kHz. The second is for a periodic data rate of 2 kHz. Again, in both cases we will use the average (pile-up included) event size. The relevant parameters of the Ultimate sensor based system pictured above are described below;

Item	Number
Bits/address	20
Integration time	200 µs
Hits / frame on Inner sensors (r=2.5 cm)	246
Hits / frame on Outer sensors (r=8.0 cm)	24
Ultimate sensors (Inner ladders)	100
Ultimate sensors (Outer ladders)	300
Event format overhead	TBD
Average Pixels / Cluster	2.5
Average Trigger rate	1 kHz

Table 5 Parameters for the Ultimate sensor based detector system used in the example calculations shown below.

Data transfer into event buffers – The 20-bitaddress data is presented to the event buffer 160 MHz. The integration time is now 200 µs giving an event buffer enable time of 200 µs.

Event Buffers – Again, we will calculate the amount of FPGA block RAM required for the event buffering. The average inner sensor has 246 hits / event. There are 4 outputs per sensor so the average inner sensor event address length is (0.25 sensor area) × (246 hits) × (20 bits) × (2 factor for event size fluctuations) × (2.5 hits per cluster) = 6150 bits**.** Multiplying this event buffer size by 10 gives the size of the RAM required for the full set of event buffers required. **The event buffer block RAM size for each inner sensor output is 61,500 bits or 3,075 20-bit addresses**.
For outer sensors, the event buffer size is calculated similarly. The average outer sensor has 24 hits / event. There are 4 outputs per sensor so the average inner sensor event address length is (0.25 sensor area) × (24 hits) × (20 bits) × (2 factor for event size fluctuations) × (2.5 hits per cluster) = 600 bits**.** Multiplying this event buffer size by 10 gives the size of the RAM required for the full set of event buffers required. **The event buffer block RAM size for each outer sensor output is 6000 bits or 300 20-bit addresses**.

Data transfer into the RDO buffer via the event builder –We will again assume a 160 MHz clock to move data in 20-bit wide address words. The event builder first adds a 128 Byte header that contains the trigger ID and other identifying information into the RDO buffer, and then moves the address data from the event buffers into the RDO buffer in 20-bit words. The average carrier event size is [(24 hits / sensor (outer)) × (10 sensors) × (3 ladders) + (246 hits / sensor (inner)) × (10 sensors) × (1 ladders)] × (2.5 hits / cluster) = **7950 address words (20-bit)**. The RDO buffer is 5 × the size required for an average event and is thus **795 kb** in size. The full time required to transfer the address data into the RDO buffer (in 20-bit per clock transfers) is then **49.7 µs**.

<u>Data transfer from the RDO buffer over the DDL link</u> – The RDO buffer is dual-ported and thus readout from the SIU to the RORC can proceed as soon as the RDO buffer begins filling. Again, we will assume that we are padding the 20-bit address data to 32-bit word lengths for DDL transfer. The event size is then (32 bits) × (7950 address words) **= 254.4 kb or 31.8 kB.** In this example, our transfer rate is ~ 200 MB / s. This transfer then takes **159 µs.**

<u>Data transfer to the STAR DAQ for event building</u> – Again, only the events that have been accepted by level 2 are then built into an event. In this way, the buffer provided by the DAQ PC RAM provides for the elasticity needed for an average event acceptance of 1 kHz

The results of these calculations and discussion are presented below in the following chronograms.

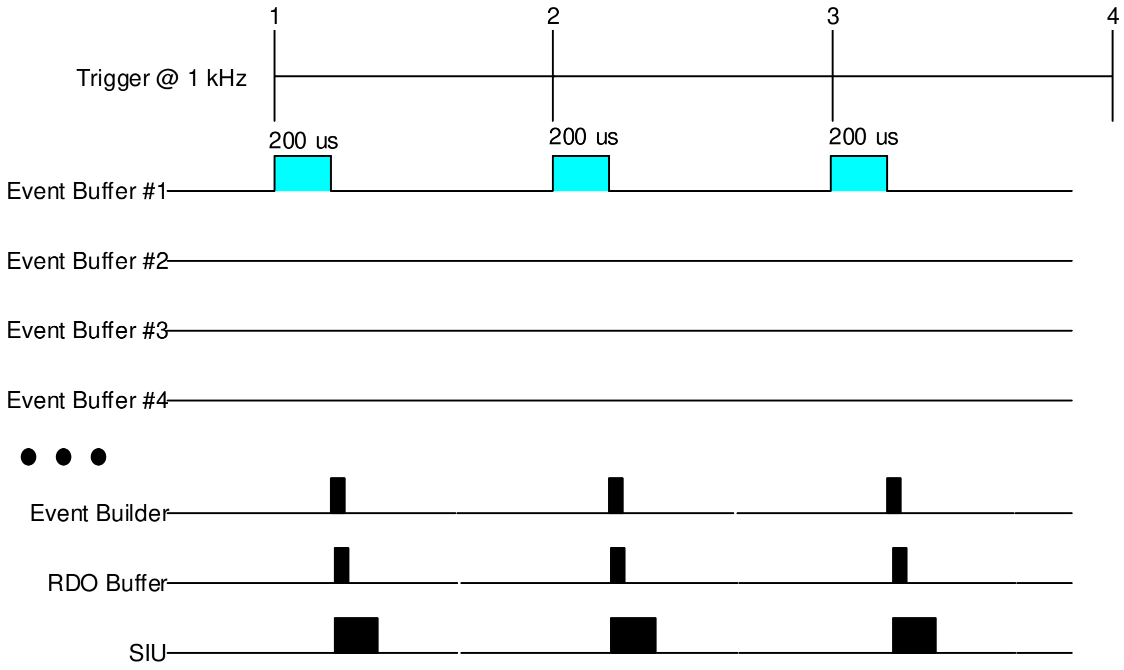

Figure 17 Chronogram of the Ultimate sensor based readout system functions for a 1 kHz periodic trigger.

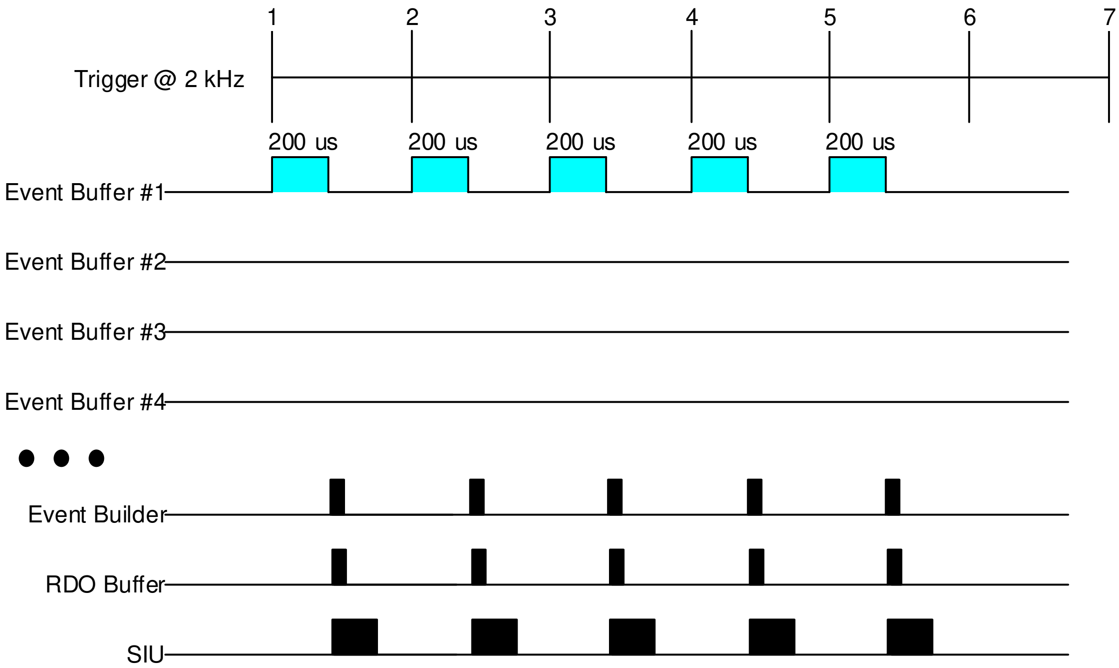

Figure 18 Chronogram of the Ultimate sensor based readout system functions for a 2 kHz periodic trigger.

The system memory resource requirements are somewhat less than those required for the Phase-1 RDO system. This fits easily into the memory resources of the Virtex-5 FPGA.